High Sensitivity Search for Neutrinoless Double-Beta Decay in KamLAND-Zen with Double Amount of 136Xe

博士論文

High Sensitivity Search for Neutrinoless Double-Beta Decay in KamLAND-Zen with Double Amount of ^{136}Xe

(^{136}Xeを倍増したKamLAND-Zenでのニュートリノを伴わない二重ベータ崩壊の高感度探索)

尾﨑 秀義

令和元年

Doctoral Dissertation

High Sensitivity Search for Neutrinoless Double-Beta Decay in KamLAND-Zen with Double Amount of ^{136}Xe

by Ozaki Hideyoshi

University of Tohoku

A thesis submitted for the degree of

Doctor of Science

2020

Abstract

Majorana nature of neutrinos is an important piece of the theories explaining the matter dominant universe and the extremely light masses of neutrinos. In this dissertation, the first result of the search for neutrinoless double-beta($0\nu\beta\beta$) decay in KamLAND-Zen 800 is reported. KamLAND-Zen is a search for ^{136}Xe $0\nu\beta\beta$ decay with the large liquid scintillator detector KamLAND, seeking the Majorana nature of neutrinos. The Xe-loaded liquid scintillator was filled in an ultra-low radioactivity container "inner-balloon" at the center of KamLAND. KamLAND-Zen completed the phase of using about 383 kg of Xe (KamLAND-Zen 400) in 2015. Aiming to increase ^{136}Xe isotope mass and reduce ^{214}Bi backgrounds from the inner-balloon film, a cleaner and larger volume inner-balloon was newly created and installed. In the new phase called KamLAND-Zen 800, 745 kg Xe gas 91% enriched in ^{136}Xe, which is about double Xe amount of the previous KamLAND-Zen 400, was loaded. The observation started in January 2019, and the lower limit of the ^{136}Xe $0\nu\beta\beta$ decay half-life was obtained by $T^{0\nu}_{1/2} > 5.8\times10^{25}$ yr (90% C.L.) with 145 days livetime (219 days runtime). The 90% C.L. limit sensitivity for the KamLAND-Zen 800 145 days observation was obtained to be $T^{0\nu}_{1/2} > 8.1\times10^{25}$ yr (90% C.L.), and it is the most sensitive measurement fo ^{136}Xe $0\nu\beta\beta$ decay half-life and the effective Majorana mass $\langle m_{\beta\beta}\rangle$ in the world. The combined results with the KamLAND-Zen 400 gives the strictest limit on the $0\nu\beta\beta$ decay $T^{0\nu}_{1/2} > 12.7\times10^{25}$ yr (90% C.L.). It corresponds to the limit on the effective Majorana mass $\langle m_{\beta\beta}\rangle <$ (49-150) meV with the matrix elements in [1]. Although it depends on the model of the nuclear matrix element, the result was the first in the world to reach the band created by the inverted mass hierarchy region at $\langle m_{\beta\beta}\rangle$. KamLAND-Zen 800 is the first $0\nu\beta\beta$ decay search experiment that has the possibility to perform a $0\nu\beta\beta$ decay search in the band of the inverted hierarchy region.

Acknowledgements

First and foremost, I express my great appreciation to Prof. Kunio Inoue, the spokesperson of the KamLAND/KamLAND-Zen experiments. He made me interested in the KamLAND-Zen experiment, and I am very grateful that he entrusted me with the responsible parts for both hardware and analysis of the important project, KamLAND-Zen 800. Assoc. Prof. Itaru Shimizu gave me brilliant guidance in the analysis. He also gave me very polite answers, even if how stupid the question it is. I am indebted for his patience with the improvement of my poor English dissertation. Former Prof. Junpei Shirai has instructed me since my master's course. His curiosity always inspired me to do a better study. Assoc. Prof. Masayuki Koga has been taking care of my hardware research. He taught me the importance of confirming the details in each step, and the insight coming from the experience. Dr. Kengo Nakamura conscientiously instructed me on the Xe system. He was in charge of the HV modules, and the very comprehensive information was useful for the analysis. At the time of distillation, dissolving Xe, and for regular DAQ shift in Kamioka, I could have a good time thanks to their kindness. Assoc. Prof. Koji Ishidoshiro helped my hardware study, and I thank his valuable advice and instructions. Assoc. Prof. Tadao Mitsui gave me various opinions on the analysis, and it was helpful. He was in charge of the HV reductions and worked hard to maintain the hardware status. Prof. Yasuhiro Kishimoto provided important advice on the dissertation and the analysis. I also significantly appreciate many experts. I am proud to be able to study together when fabricating the inner-balloon with the balloon experts, Drs. Yoshihito Gando, Haruo Ikeda, Hiroko Watanabe, Kota Ueshima, Azusa Gando, Keishi Hosokawa, Shuhei Obara, Takahiko Hachiya, Shingo Hayashida, Saori Umehara. This dissertation was completed, thanks to the fact that we have always been the best since the first inner-balloon production, even in the toughest times. The Xe system experts, Drs. Kengo Nakamura, Kota Ueshima, Keishi Hosokawa, Sei Yoshida, Yasuhiro Takemoto, Shingo Hayashida instructed me since the retrieve of KamLAND-Zen 400. I had a valuable experience through the handling of the Xe system. Special thanks to colleague Takahiko Hachiya; he gave me many advice and suggestions every time. He worked on developing the light spallation isotope veto tools and made a significant contribution to the dissertation. Drs. Sei Ieki, Itaru Shimizu, Haruo Ikeda contributed to the simulation and estimation on the long-lived spallation, and they gave me helpful advice

on the invention of the long-lived veto. The KamLAND/KamLAND-Zen collaborators, Drs. Patrick Decowski, Brian Fujikawa, Yuri Efremenko, Jason Detwiler, Sanshiro Enomoto, Lindley Winslow, Bruce Berger, Chris Grant, and Atsuko Ichikawa gave me many wise comments and suggestions during the collaboration meeting. Many researchers and engineers contributed to the launch of KamLAND-Zen 800, and I thank everyone. Also, the analysis of KamLAND-Zen 800 is based on that of KamLAND-Zen 400, which many pioneers invented and developed. I appreciate all those people. Finally, I thank my family for supporting me from afar for a long time.

Contents

List of Figures

List of Tables

Chapter 1

Introduction

Whether neutrinos are Dirac particles or Majorana particles has not been revealed yet. In 1937, Italian physicist E. Majorana created the theory of a Majorana particle. Since its anti-particle is the same as the particle, it is a theory that can only be applied to particles that have no charge. Only neutrinos are charge-less fermions in the standard model of physics, so only neutrinos can be Majorana particles.

Since the observations of neutrino oscillations proved that neutrinos have finite masses, which had been assumed to be exactly "Zero" in the standard model, neutrinos have been promised as the portal to the physics beyond the standard model. The neutrinos still have unknowns such as the CP violation phase, mass hierarchy, and absolute mass. In contrast, the mixing angles and mass squared differences were observed. Also, having a Majorana mass or not is interesting. If the neutrinos are Dirac particles in the standard model, their Yukawa coupling constants must be very tiny $Y \leq 10^{-11}$ ($Y \sim 10^{-6\sim 0}$ for other particles) and right-handed neutrinos which do nothing must be introduced. This seems to be "unnatural".

If the neutrinos are Majorana particles, the seesaw mechanism naturally explains the light neutrino masses with massive right-handed neutrinos [2]. Also, Majorana neutrinos are crucial in leptogenesis theory [3], which links the reason for the present matter dominant universe with the lepton number violation by the decay of the massive right-handed neutrinos. Majorana neutrinos can explain the mystery of particle physics and the origin of matter.

Neutrinoless double-beta ($0\nu\beta\beta$) decay search is the most prominent way for verifying the Majorana nature of the neutrinos. $0\nu\beta\beta$ decay occurs only in limited nuclei causing double-beta decay, only when neutrinos are Majorana particles. $0\nu\beta\beta$ decay has not yet been discovered because of its tiny decay rate. At present, many experiments are searching for this decay mode using various types of detectors and multiple isotopes of tens to hundreds of kg. Most stringent limits are obtained by KamLAND-Zen, CUORE, and GERDA for ^{136}Xe, ^{130}Te and ^{76}Ge, respectively.

The experiment using the largest number of $0\nu\beta\beta$ decay nuclei was KamLAND-Zen 400, which is the Xe-loaded organic liquid scintillator detector, and used about 326 kg of ^{136}Xe isotope at first. The ^{136}Xe isotope mass was increased to about 346 kg.

In this dissertation, the first result of the $0\nu\beta\beta$ decay search in KamLAND-

Zen 800, which doubles the isotope to 745 kg of Xe ($\sim$ 676 kg ^{136}Xe), is reported. KamLAND-Zen started experiments using a low radioactivity Xe-loaded liquid scintillator container "inner-balloon" with a radius of 1.5 m and Xe gas of about 330 kg from 2011. By collecting data up to October 2015 with some Xe mass increase and purification campaigns, KamLAND-Zen 400 provided the most stringent limit on the half-life of ^{136}Xe $0\nu\beta\beta$ decay more than 10^{26} yr. KamLAND-Zen achieved the most sensitive search for $0\nu\beta\beta$ decay by having the extremely low radiation environment, and by using a large number of decay nuclei. In 2015, we retrieved the loaded Xe and the 1.5-m-radius inner-balloon from the KamLAND detector and started preparations to introduce twice the amount of ^{136}Xe isotopes. In May 2018, we installed the new inner-balloon with the radius of 1.9 m and 1/10 times radioactive impurities with respect to the previous inner-balloon.

In January 2019, KamLAND-Zen 800 started taking data with 745$\pm$3 kg of xenon. Data for about 7 months until September 2019 were analyzed. The new spallation background rejection techniques were also introduced. The sensitivity for 90% C.L. upper limit on the ^{136}Xe $0\nu\beta\beta$ decay half-life by the data set was 8.1×10^{25} yr, which is about 1.5 times that of the whole data set in KamLAND-Zen 400 and the highest sensitivity search for $0\nu\beta\beta$ decay in the world. The obtained limit on the $0\nu\beta\beta$ decay half-life was over 5.8×10^{25} yr (90% C.L.).

This dissertation is organized as follows. Majorana neutrino and theory on double-beta decay are described in Chapter 2. Current $0\nu\beta\beta$ decay search experiments and the former KamLAND-Zen 400 are summarized in Chapter 3. Chapter 4 introduces the KamLAND and KamLAND-Zen detector. Chapter 5 is about upgrade from KamLAND-Zen 400 to KamLAND-Zen 800. Data analysis and event selections are summarized in Chapter 6. The detector calibration and MC simulation tuning are described in Chapter 7. The background model is explained in Chapter 8. Chapter 9 is on the $0\nu\beta\beta$ decay search analysis. This paper is concluded in Chapter 10.

Chapter 2

Majorana Neutrino

Neutrinos are the only neutral fermions among matter particles, and their masses are remarkably lighter than the other particles. In the framework of the standard model, all the matter particles are Dirac particles, and the neutrino masses are assumed to be precisely Zero. However, the discovery of the neutrino oscillations revealed that more than one of three neutrinos have finite masses. Since neutrinos do not have any charges, it is possible that they are not Dirac particles but Majorana particles, in which particles are identical with their anti-particles.

2.1 Neutrino Physics

2.1.1 Neutrino Oscillation

Neutrino oscillations were firstly discovered by the disappearance of atmospheric neutrinos in 1998 [4], then the flavor change of solar neutrinos by SNO [5]. KamLAND observed the reactor neutrino oscillation and established the large mixing angle solution [6]. The observations of neutrino oscillations are the evidence of finite neutrino masses. The neutrino oscillation is a phenomenon in which a flavor change periodically occurs between generated neutrinos and observed neutrinos with a certain probability. It is caused by the fact that the flavor and mass eigenstates of neutrinos are different. Here, we describe neutrino oscillations among three generations. The mass eigenstates of neutrinos are $\nu_i (i = 1, 2, 3)$, and the eigenstates of flavors are ν_l $(l = e,\ \mu,\ \tau)$ Then, using the Maki-Nakagawa-Sakata (MNS) mixing matrix $U_{\rm MNS}$, the neutrino flavor stats are described with neutrino mass states by

$$\begin{pmatrix} \nu_e \\ \nu_\mu \\ \nu_\tau \end{pmatrix} = U_{\rm MNS} \begin{pmatrix} \nu_1 \\ \nu_2 \\ \nu_3 \end{pmatrix}, \tag{2.1}$$

where $U_{\rm MNS}$ is

$$
\begin{aligned}
&U_{\rm MNS} \qquad (2.2)\\
&= \begin{pmatrix} 1 & 0 & 0 \\ 0 & c_{23} & s_{23} \\ 0 & -s_{23} & c_{23} \end{pmatrix} \begin{pmatrix} c_{13} & 0 & s_{13}e^{-i\delta} \\ 0 & 1 & 0 \\ -s_{13}e^{i\delta} & 0 & c_{13} \end{pmatrix} \begin{pmatrix} c_{12} & s_{12} & 0 \\ -s_{12} & c_{12} & 0 \\ 0 & 0 & 1 \end{pmatrix} \\
&\quad \times \mathrm{diag}(e^{i\alpha 1/2}, e^{i\alpha 2/2}, 1) \\
&= \begin{pmatrix} c_{12}c_{13} & s_{12}c_{13} & s_{13}e^{-i\delta} \\ -s_{12}c_{23} - c_{12}s_{13}s_{23}e^{i\delta} & c_{12}c_{23} - s_{12}s_{13}s_{23}e^{i\delta} & c_{13}s_{23} \\ s_{12}c_{23} - c_{12}s_{13}s_{23}e^{i\delta} & -c_{12}s_{23} - s_{12}s_{13}c_{23}e^{i\delta} & c_{13}c_{23} \end{pmatrix} \\
&\quad \times \mathrm{diag}(e^{i\alpha 1/2}, e^{i\alpha 2/2}, 1).
\end{aligned}
$$

δ is the CP phase, α_1 and α_2 are 2 Majorana phases, c_{ij} and s_{ij} are $\cos\theta_{ij}$ and $\sin\theta_{ij}$ which means a mixture between i-th and j-th generations , and θ_{ij} is the mixing angle. Note that the Majorana phases vanish in the neutrino oscillations whose are always calculated with $UU^\dagger$. The time evolution of mass eigenstates are described by modifying the Schrödinger equation,

$$i\frac{\partial}{\partial t}|\nu_i\rangle = E_i|\nu_i\rangle \tag{2.3}$$

by changing eigenstates like,

$$|\nu_i(t)\rangle = e^{-iE_it}|\nu_i(0)\rangle. \tag{2.4}$$

The time evolution of the flavor eigenstates and the mass eigenstates are related by,

$$|\nu_\alpha(t)\rangle = \sum_{i=1}^{3} U^*_{\alpha i} e^{-iE_it}|\nu_i(0)\rangle. \tag{2.5}$$

The oscillation probability between two flavors $\mathrm{P}(\nu_\alpha \to \nu_\beta)$ is

$$
\begin{aligned}
P(\nu_\alpha \to \nu_\beta) &= |\sum_{i=1}^{3} U^*_{\alpha \mathrm{i}} U_{\beta \mathrm{i}} e^{-i\frac{m_i^2}{2E_\nu}L}|^2 \\
&= \delta_{\alpha\beta} - 4\sum_{i>j} \mathrm{Re}(U^*_{\alpha \mathrm{i}} U_{\alpha \mathrm{j}} U_{\beta \mathrm{i}} U^*_{\beta \mathrm{j}}) \sin^2\left(\frac{\Delta m^2_{ij}}{4E_\nu}L\right) \\
&\quad +2\sum_{i>j} \mathrm{Im}(U^*_{\alpha \mathrm{i}} U_{\alpha \mathrm{j}} U_{\beta \mathrm{i}} U^*_{\beta \mathrm{j}}) \sin\left(\frac{\Delta m^2_{ij}}{2E_\nu}L\right).
\end{aligned} \tag{2.6}
$$

Here, $E_i = \sqrt{p_i^2 + m_i^2} \simeq E_\nu + m_i^2/2E_\nu$ was used. E_ν is neutrino energy, L is travel distance of the neutrinos, $\Delta m^2_{ij} \equiv m_i^2 - m_j^2$ (i, j = 1, 2, 3,$i > j$) are squared mass differences. In the case of anti-neutrinos, U changes to a complex conjugate and as a result, the sign of the third terms is changed. The difference between the neutrino and anti-neutrino oscillation probabilities is

$$\Delta P = P(\nu_\alpha \to \nu_\beta) - P(\bar\nu_\alpha \to \bar\nu_\beta) = -16 J_{\alpha\beta} \sin\Delta_{12} \sin\Delta_{23} \sin\Delta_{31}, \tag{2.7}$$

where $\Delta_{ij} = \frac{\Delta m^2_{ij} L}{4E}$, $J \equiv \mathrm{Im}(U_{\alpha 1} U^*_{\alpha 2} U^*_{\beta 1} U_{\beta 2}) = \pm J_{\mathrm{cp}}$, and $J_{cp} \equiv s_{12}c_{12}s_{23}c_{23}s_{13}c^2_{13}\sin\delta$. The sign is positive if it is e, μ, τ cycle, and it is negative if it is a reverse cycle. It is possible to measure CP violation from the difference between the neutrino and anti-neutrino oscillation probability. Experimental searches for the CP violation phase δ are ongoing for example NOνA [7] and T2K [8].

2.2 Majorana Neutrino and Neutrino Mass Origin

2.2.1 Majorana Neutrino

This section is based on [9]. Majorana particles are massive fermions that are their own anti-particles described by Ettore Majorana in 1937 [10]. Majorana particles must be genuinely natural. A particle-anti-particle conjugate operator $\hat{C}$ effects fermion field ψ satisfying the Dirac equation $(i\gamma^\mu\partial_\mu - m)\psi = 0$ like,

$$\hat{C} : \psi \to \psi^c = C\bar{\psi}^t \tag{2.8}$$

Here, $\bar{\psi}^t\gamma_0$. Matrix C is particle-anti-particle matrix. ψ^c satisfies the same Dirac equation as ψ. $\hat{C}$ flips its chirality.

$$\hat{C} : \psi_L \to (\psi_L)^c = (\psi^c)_R,\ \psi_R \to (\psi_R)^c = (\psi^c)_L \tag{2.9}$$

Here ψ_L and ψ_R are left-handed and right-handed chiral fields. They satisfy two coupled equations:

$$(i\partial_0 - i\sigma\cdot\nabla)\psi_L - m\psi_R = 0 \tag{2.10}$$

$$(i\partial_0 + i\sigma\cdot\nabla)\psi_R - m\psi_L = 0 \tag{2.11}$$

The Eq. (2.9) means that the anti-particle of a left-handed particle is right-handed. The Dirac Lagrangian of the spin-1/2 particle is

$$\mathscr{L} = \bar{\psi}(i\gamma^\mu\partial_\mu - m)\psi. \tag{2.12}$$

The mass term of this Lagrangian is written as

$$-\mathscr{L}_{mass} = m\bar{\psi}\psi = m(\bar{\psi}_L\psi_R + \bar{\psi}_R\psi_L). \tag{2.13}$$

The mass term needs both left-handed and right-handed chiral fields.

Here, there are 2 possibilities. We can construct the Dirac field with independent 2-component left-handed field ψ_L and right-handed field ψ_R: $\psi = \psi_L + \psi_R$. Also, we can construct a Majorana field with only one 2-component field. In this case, the right-handed field is just its $\hat{C}$-conjugate: $\psi_R = (\psi_L)^c = (\psi^c)_R$ and,

$$\psi = \psi_L + (\psi_L)^c = \psi_L + (\psi^c)_R \tag{2.14}$$

This field satisfies Majorana condition which means,

$$\hat{C} : \psi \to \psi^c = (\psi_L)^c + ((\psi^c)_R)^c = (\psi_L)^c + \psi_L = \psi \tag{2.15}$$

This formula shows that Majorana particles are their own anti-particles. Majorana neutrino's mass term is described as,

$$\mathscr{L}_{mass} = -\frac{m}{2}[\bar{\psi^c_L}\psi_L + \bar{\psi}_L\psi_L)^c] = \frac{m}{2}[\psi^T_L C^{-1}\psi_L + h.c.] \tag{2.16}$$

2.2.2 Neutrino Mass and Seesaw Mechanism

Consider n left-handed neutrino fields $\nu_{\alpha L}$ in $SU(2)_L$ and k right-handed neutrino fields $\nu_{\beta R}$ that are electroweak singlets. General mass term contains the Majorana masses m_L, m_R, and Dirac mass m_D.

$$\mathscr{L}_{mass} = \frac{1}{4}\overline{(\psi_L)^C} m_L \psi_L - \frac{1}{4}\overline{(\psi_R)^C} m_R \psi_R - \frac{1}{2}\bar{\psi_R} m_D \psi_L + h.c. \tag{2.17}$$

Here m_R and m_L are k×k and n×n matrices. m_D is a k×n matrix. The total mass matrix M has the form,

$$M = \begin{pmatrix} m_L & m_D^T \\ m_D & m_R \end{pmatrix}. \tag{2.18}$$

Assuming 2×2 matrix for the simplicity, which means there are right-handed Majorana neutrinos and left-handed Majorana neutrinos, m_D,m_L, and m_R are just indices. Neutrino mass eigenvalues are

$$m_{1,2} = \frac{m_L + m_R}{2} \pm \sqrt{(\frac{m_L - m_R}{2})^2 + m_D^2}. \tag{2.19}$$

Since the right-handed neutrino is an electroweak singlet, Majorana mass term does not need to relate to the electroweak scale. Right-handed neutrino mass should rather relate to a new physics beyond the standard model. If right-handed neutrino mass is greater than the Dirac mass scale($m_L, m_D \ll m_R$), the eigenvalues are

$$m_1 \simeq m_L - m_D^2/m_R, \quad m_2 \simeq m_R, \tag{2.20}$$

and rotation angle $\theta \simeq m_D/m_R \ll 1$. Eigenstates are

$$\nu_1 \simeq \nu_L + \eta_1(\nu_L)^c, \nu_2 \simeq \nu_R + \eta_2(\nu_R)^c. \tag{2.21}$$

$\eta_{1,2} = 1$ or -1 for $m_{1,2} > 0$ or < 0. We have a light Majorana mass state composed of a left-handed active neutrino ν_L and its $\hat{C}$-conjugate $(\nu_L)^c$ and a heavy Majorana mass state composed of a right-handed sterile neutrino ν_R and its $\hat{C}$-conjugate $(\nu_R)^c$. The admixture of the sterile neutrino and the active neutrino are suppressed by order of $m_D/m_R \ll 1$. The general case which includes n left-handed and k right-handed case is described using n×n matrix $\tilde{m_L}$ and k × k matrix which are block-diagonarized matrix of M ($VV^T MV$=diag(m_L, M_R)).

$$\tilde{m_L} \sim m_L - m_D^T M_R^{-1} m_D \tag{2.22}$$

$$\tilde{M_R} \sim M_R \tag{2.23}$$

The admixture of the active neutrinos is also suppressed with the heavy right-handed sterile neutrinos by order of $m_D/M_R \ll 1$. Since heavy right-handed Majorana masses make the masses of other neutrinos small, this neutrino mass mechanism is called seesaw mechanism [2], [11], [12]. There are many scenarios for seesaw mechanisms.

Type I Seesaw

As shown in the last chapter, right-handed neutrinos, which transform as a singlet(1,1,0) in the standard model gauge group $SU(3)_C SU(2)_L U(1)_Y$, are added in the standard model. They have large Majorana masses($m_D \ll M_{\nu_R}$) and there is no left-handed Majorana mass($m_L = 0$). The light neutrino masses are given by $\sim y_0^2 v_0^2 / M_{\nu_R}$. y_0 is Yukawa coupling. If $y_0 = 1$, M_{ν_R} should be 10^{14}-10^{15} GeV.

Type II Seesaw

In the case of the type-II seesaw, scalar triplet $\Delta_L(1,3,2)$ is introduced. Δ_L does not couple to any quarks, but it couples to higgs and gives the neutrino mass. $m_\nu \sim Y_\nu \mu v_0^2 / \sqrt{2} M_\Delta^2$. Here, μ is a dimensionful parameter. The light neutrino mass depends on M_Δ.

Type III Seesaw

The type-III seesaw adds fermionic multiplet Σ_L, which is a $SU(2)_L$ triplet(1,3,0) in the standard model. The new seesaw partner must be mass of the new leptons M_Σ.

2.2.3 Neutrino Mass Measurements

Current observational knowledge on the neutrino masses is shown.

Squared Mass Differences from Oscillation Experiments

Neutrino oscillation experiments give the neutrino squared mass differences ($\Delta m_{ij}^2 = m_j^2 - m_i^2$). Considering the case of only 2 generations, the survival probability of electron neutrinos is written as

$$P(\nu_e \to \nu_e) = 1 - \frac{1}{2} \sin^2 2\theta_{12} \sin^2 (\frac{\Delta m_{21}^2}{4E} L), \tag{2.24}$$

where, E is neutrino energy, and L is the distance of the baseline. Solar neutrino and reactor neutrino oscillation experiments give,

$$\Delta m_{solar}^2 \simeq 7.4 \times 10^{-5} \text{ eV}^2. \tag{2.25}$$

Also, atmospheric neutrino experiments provide,

$$\Delta m_{atm}^2 \simeq 2.5 \times 10^{-3} \text{ eV}^2. \tag{2.26}$$

Although now we know two squared mass differences of the neutrinos, the absolute value of the neutrino masses and if normal hierarchy ($m_1 < m_2 < m_3$) or inverse hierarchy ($m_3 < m_1 < m_2$) are not revealed. See Fig. 2.1.

At present, the neutrino mass hierarchy is being observed by the long baseline measurements [7], [8], atmospheric neutrino oscillation with the effects of scattering inside the earth [13], and normal is preferred, and it will also be measured in future precision measurements of the reactor neutrino oscillation.

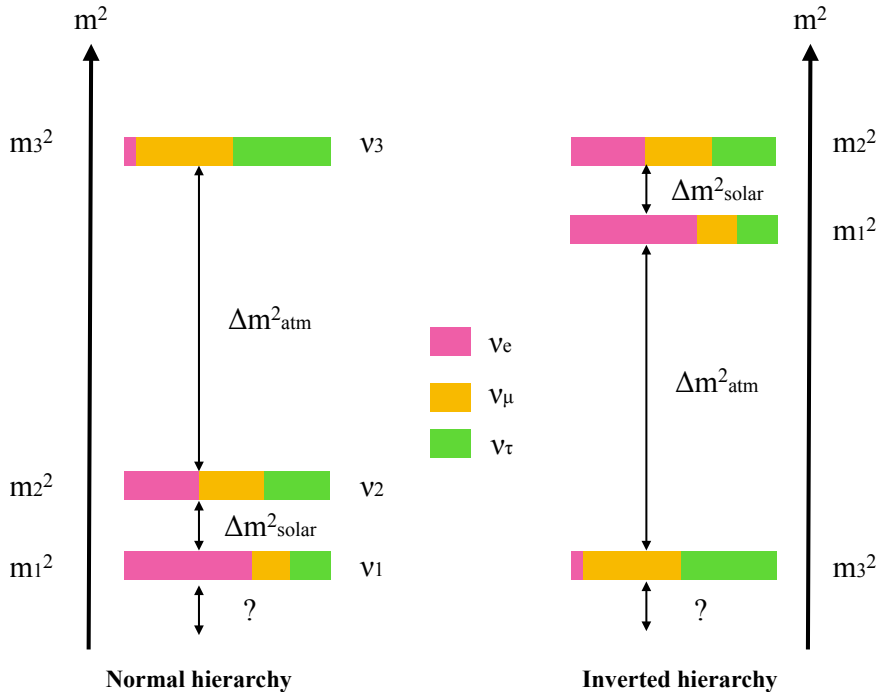

Figure 2.1: Neutrino mass hierarchy
The neutrino mass orderings of the normal mass hierarchy (left side) and the inverted mass hierarchy (right side) are shown. The three colors represent the three flavors, respectively. Two differences of the absolute mass measured in the atmospheric neutrino oscillation and the solar and reactor neutrino oscillations are shown in each hierarchy.

Search for Electron Neutrino Mass

The most reliable and model-independent way to determine the absolute neutrino masses is through beta decay. The electron neutrino mass search can be performed by measuring the distortion of the endpoint of the beta decay energy spectrum because a fraction of the decay energy goes into the emitted neutrino mass.

$$\langle m_e \rangle \equiv \sqrt{\sum_i \left(m_i^2 \left| U_{\mathrm{ei}} \right|^2 \right)} \tag{2.27}$$

Currently, $\langle m_e \rangle$ <1.1 eV(90% C.L.) is given from the KATRIN experiment, which uses ^{3}H(E_0=18.57 keV) and started the first observation run in 2019 [14]. KATRIN aims at the sensitivity of ∼0.2 meV in 5 years.

Cosmological Limits

Neutrinos affect background evolution of the universe and the evolution of cosmological perturbations. We can derive the neutrino properties from observations of the anisotropes in the cosmic microwave backgrounds (CMB) and fluctuations in the matter field with many cosmological parameters. The cosmological observations can limit the total neutrino mass defined by,

$$\Sigma_\nu \equiv \sum_i m_i. \tag{2.28}$$

The tightest limit from a single observable come from the CMB anistoropy observation by the Plank satellite [15]. The total neutrino mass parameter is correlated with other parameters such as Hubble constant, but using multiple probes breaks the degeneracy of each parameter, and the limit can be improved. Combining final Plank results with the BAO observations gives $\Sigma_\nu < 0.16$ eV(95% C.L.) [16]. Note that the upper limit is only valid within the ΛCDM model, although it fits the CMB anisotropies, distant Supernovae Ia, and galaxy clustering data very well. The analysis of the cosmological observations can include the IH/NH parameter, though it does not have enough sensitivity yet. It is a probable scenario that the cosmological effects eliminate the IH by setting the limit to the total neutrino mass below 0.1 eV (See Fig. 2.2). Next-generation detectors such as CMB-S4 and the DESI large-scale-structure survey will have a sensitivity of $\sigma(\sum_i m_i)$ ∼0.015 eV [17]. Even in the normal hierarchy scenario, the minimal mass can be detected at 3σ. Future cosmological observations will clearly reveal neutrino properties.

Effective Majorana Mass from Neutrinoless Double-Beta Decay Search

In the $0\nu\beta\beta$ decay search described later, it is possible to measure the effective Majorana mass $\langle m_{\beta\beta} \rangle$, if we assume three generations of light neutrino exchanges and Majorana neutrinos. In this case, the observation results can determine the vertical

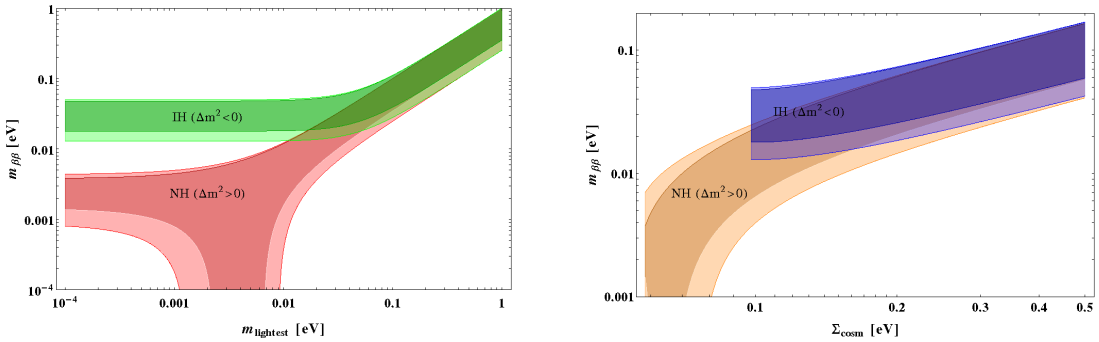

Figure 2.2: Neutrino mass plots
The figures are from [20]. In the left picture, green area is the inverted hierarchy (IH), and red area is the normal hierarchy (NH). In the right picture, purple area is the IH, and orange area is the NH. Light colors represent 3σ errors from the neutrino parameters. The $0\nu\beta\beta$ search experiments can determine or limit the vertical value in the figures. The accelerator experiments, atmospheric neutrino experiments, and cosmological observations will determine the neutrino mass hierarchy. The cosmological observations and direct search can determine or limit the horizontal axis.

value of Fig. 2.2, which can provide insight into the neutrino mass hierarchy and absolute mass.

$$\langle m_{\beta\beta} \rangle \equiv \left| \sum_i m_i {U_{\mathrm{ei}}}^2 \right| \tag{2.29}$$

The tightest limit against $\langle m_{\beta\beta} \rangle$ is currently obtained from [18], which is $\langle m_{\beta\beta} \rangle <$ 61-165 meV, and also gives the limit for the lightest neutrino mass $m_{lightest}$ <(0.18-0.48) eV. The correlations between total neutrino mass Σ_ν and $\langle m_{\beta\beta} \rangle$, and $m_{lightest}$ and $\langle m_{\beta\beta} \rangle$ are shown in Fig. 2.2. The $0\nu\beta\beta$ decay can be observed only when the neutrinos are the Majorana particles. We can know that the mass hierarchy is normal if the effective Majorana neutrino mass is observed, and it is less than $\sim$10 meV. If it is observed at above 10 meV, the information of mass structure can not derived only from the $0\nu\beta\beta$ decay experiment. In 10 meV - 40 meV region of $\langle m_{\beta\beta} \rangle$, we may be able to identify the mass hierarchy to be inverted hierarchy with the restrictions on $m_{lightest}$ or Σ_ν from cosmological observations or the end-point measurements of the beta decay spectrum. Also, if the effective Majorana neutrino mass is not observed above $\sim$10 meV, and the mass hierarchy is identified to be inverted hierarchy by other observations, we can know the neutrinos are the Dirac particles, although global analysis of the three flavor neutrino oscillations preferred the normal mass hierarchy more than 3σ [19].

2.3 Leptogenesis

Leptogenesis is the most promising model to explain the matter dominant universe [21] [3]. Leptogenesis postulates that baryon asymmetry in the universe stems from

lepton number violation. Almost all scenarios of the leptogenesis require that neutrinos are Majorana particles.

2.3.1 Matter Dominant Universe

The number of baryons in the present universe is not equal to anti-baryons. It does not seem to be an initial condition, since the baryon asymmetry needs fine-tuning. Another reason is that microwave background radiation suggests that the inflation took place in the history of the universe and diluted the primordial baryon asymmetry. So, some mechanism to create the baryon asymmetry is needed after the inflation. There is more than two observable evidence for the present baryon dominant universe. The first one is through the big bang nucleosynthesis (BBN). Abundance of D, ^{3}He, ^{4}He and ^{7}Li depend on η [22], and the observation gave,

$$\eta = \frac{n_B - \bar{n}_B}{n_\gamma}|_{t_0} \sim (5.6 - 6.6) \times 10^{-10}. \tag{2.30}$$

Here, n_B is matter density, $\bar{n}_B$ is anti-matter density, n_γ is radiation density, and t_0 means the present time of the universe. The amount of matter and anti-matter, which are equal to each other at the opening of the universe, are unbalanced at this value.

The second one is measurements of CMB anisotropies, which provide the relative baryon energy density of the universe. [23] gives

$$\eta = \frac{n_B - \bar{n}_B}{n_\gamma}|_{t_0} \sim 6 \times 10^{-10}. \tag{2.31}$$

The baryon asymmetry would be diluted by inflation. It is difficult to make the baryon asymmetry after the BBN. So, the baryon asymmetry will be made somewhere in between them.

2.3.2 Baryogenesis and Sakharov's Condition

Original baryogenesis requires that the baryon asymmetry is generated dynamically. Sakharov pointed out the requirements for successful baryogenesis, which is called Sakharov's conditions in [24].

I. B violation process
   The primary B violation is needed.

II. C and CP violation
   When C and CP are preserved, the baryon asymmetry cannot be created because the particle and anti-particle processes occur equally.

III. Out of equilibrium dynamics
   If it did not leave the equilibrium, the inverse reaction will occur, and the symmetry will not be broken.

Although the Kobayashi-Maskawa complex phase can make CP violation, it is not enough to explain the quantities of baryon asymmetry.

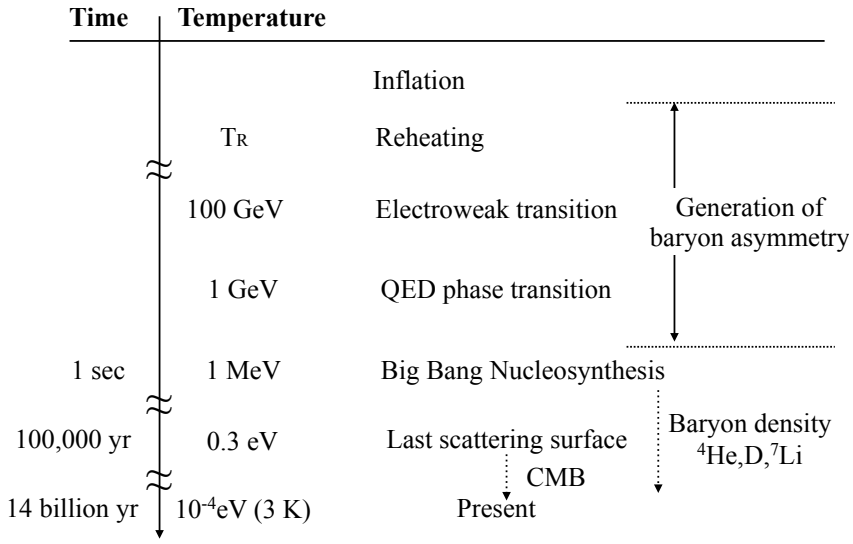

Figure 2.3: Baryon asymmetry generation in the history of universe
The generation of the baryon asymmetry is thought to be taken place from just after reheating to before the BBN.

2.3.3 Leptogenesis

Currently, various leptogenesis scenarios are considered, most of which predict $0\nu\beta\beta$ decay. The most standard scenario is thermal leptogenesis. The standard leptogenesis will be explained in this section.

Sphaleron

There is a baryon and lepton number violating process within the standard model of physics, called sphaleron. The sphaleron is effective at high-temperature T > 100 GeV and believed to be in thermal equilibrium. The sphaleron process involves 9 quarks and 3 leptons and still conserve B−L number. This means that if the B−L conserving process makes the baryon asymmetry in the early universe, it must be washed out by the sphaleron process. However, a B−L number breaking process can make the baryon asymmetry universe [21].

Laptogenesis

Standard leptogenesis [3] predicts that the decay of heavy Majorana neutrino creates the B-L number violation. At first, the lepton number violation was made at T $\sim$ M_R.

$$\Gamma(N \to lh) \neq \Gamma(N \to \bar{l}h) \tag{2.32}$$

The L violation made by the heavy Majorana neutrino decay translated to the B violation via the sphaleron process. The baryon density of the universe is expressed in [25] as,

$$\frac{n_B}{s} \sim 0.3 \times 10^{-10} \left(\frac{\kappa}{0.1}\right) \left(\frac{M_1}{10^9 \text{ GeV}}\right) \left(\frac{m_3}{0.05 \text{ eV}}\right) \delta_{\text{eff}}. \tag{2.33}$$

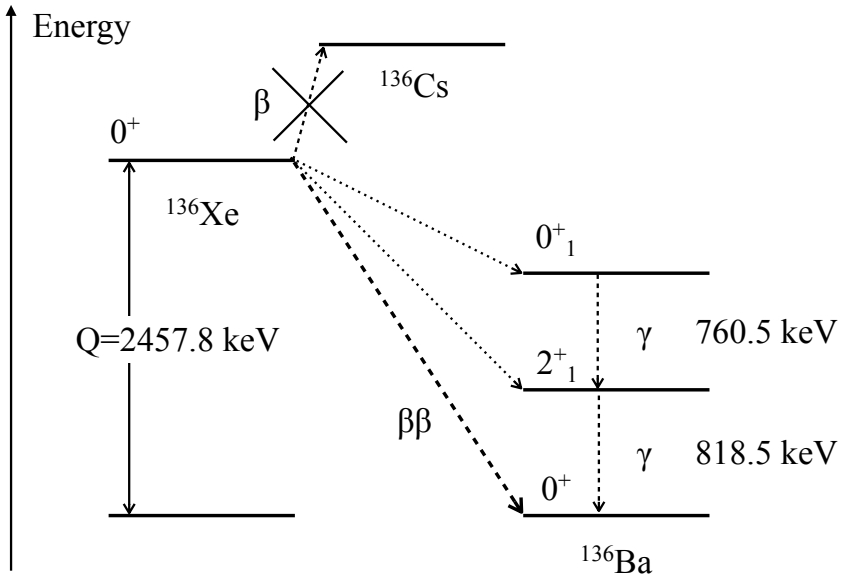

Figure 2.4: Double-beta decay of ^{136}Xe
The level diagram of ^{136}Xe double-beta decay is shown.

Here, κ is wash-out efficiency factor depending on the right-handed neutrino interaction strength, M_1 is the heavy Majorana neutrino mass, m_3 is the heaviest light neutrino mass and δ_{eff} is the effective CP violation phase. Observed value of the Eq.(2.33) is $\sim 0.87\times10^{-10}$ [26]. This formula shows that leptogenesis works if heaviest Majorana neutrino mass is heavier than $10^{9\text{-}10}$ GeV. If we consider 3-flavor leptogenesis, M_1 could be smaller, but $M_1 < 10^6$ GeV is not realistic because a fine-tuning is needed [27].

2.4 Double-Beta Decay Theory

2.4.1 Double-Beta Decay with Neutrino Emission

Double-beta decay($2\nu\beta\beta$), which is proposed by Mayer in 1935 [28], is observed in only some even-even nuclei in which usual beta decay is energetically forbidden or strongly suppressed (See Fig. 2.4 in the case of ^{136}Xe). Two beta decays simultaneously happen in the nuclei, and 2 anti-neutrinos and 2 electrons are emitted (See Fig. 2.5). $2\nu\beta\beta$ decay is a very rare phenomenon because it is a second-order process of weak interaction. The decay half-lives are more than $\sim10^{19}$ yr.

$$(A, Z) \rightarrow (A, Z+2) + 2e^- + 2\bar{\nu}_e \tag{2.34}$$

The half-life is calculated within the standard model and does not depend on the

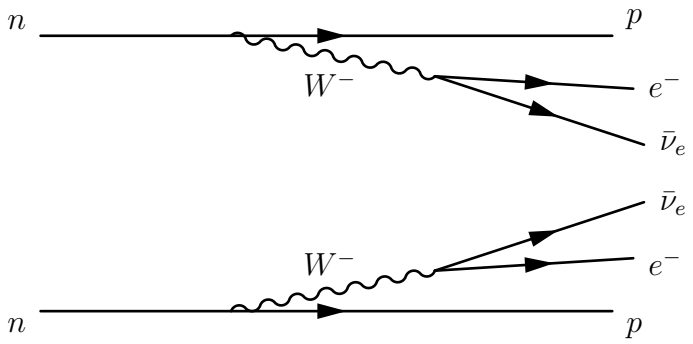

Figure 2.5: Feynman diagram of $2\nu\beta\beta$ decay
Two neutrons turn into protons inside the nucleus. Two electrons and two anti-electron neutrinos are emitted by the decay.

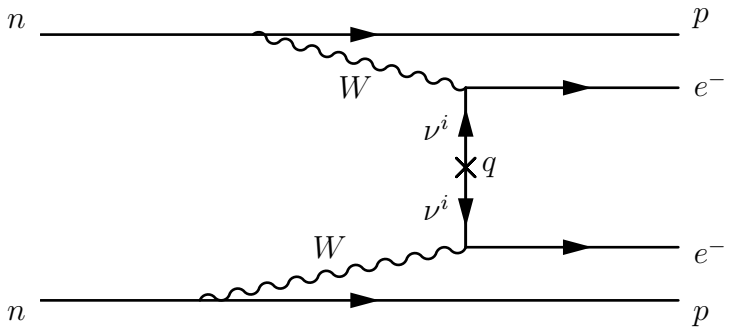

Figure 2.6: Feynman diagram of $0\nu\beta\beta$ decay
Two neutrons turn into protons inside the nucleus. Two electrons are emitted by the decay, and neutrinos are not emitted.

neutrino mass or charge conjugation properties.

$$[T^{2\nu}_{1/2}]^{-1} = G_{2\nu}(Q,Z)|M^{2\nu}_{GT} - \frac{g_V^2}{g_A^2}M^{2\nu}_F|^2 \tag{2.35}$$

where $G_{2\nu}(Q,Z)$ is the phase-space factor for $2\nu\beta\beta$ decay.

2.4.2 Neutrinoless Double-Beta Decay

If neutrinos are Majorana particles, as suggested by Furry[29], it is possible to cause $0\nu\beta\beta$ decay that does not emit neutrinos as in the Eq.(2.36) and Fig. 2.6.

$$(A,Z) \rightarrow (A,Z+2) + 2e^- \tag{2.36}$$

The half-life of $0\nu\beta\beta$ decay is described by

$$(T^{0\nu}_{1/2})^{-1} = |\Sigma_i \sqrt{G_i} g_i^2 M_i \eta_i|^2. \tag{2.37}$$

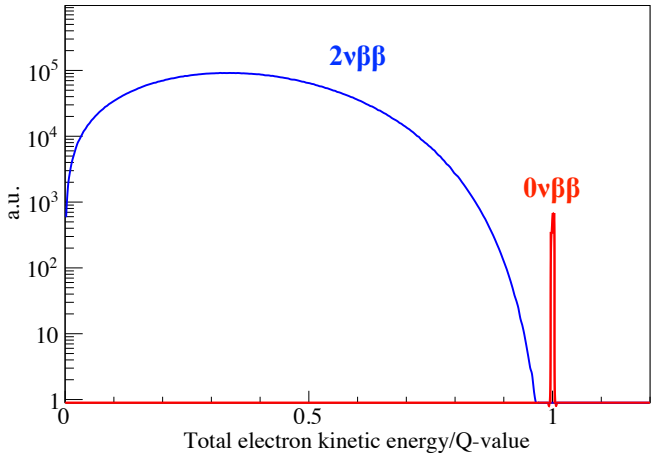

Figure 2.7: Energy spectra of $0\nu\beta\beta$ decay (red peak) and $2\nu\beta\beta$ decay (continuous blue spectrum)

Subscript i indicates a physics mechanism causing $0\nu\beta\beta$ decay. G is the phase space factor, g is the hadronic coupling, M is the nuclear matrix element, η is corresponding new physics mass. Considering that the exchange of light neutrinos is the main contribution, Eq.(2.37) becomes,

$$(T^{0\nu}_{1/2})^{-1} = G_{0\nu}|M_{0\nu}|^2\langle m_{\beta\beta}\rangle^2. \tag{2.38}$$

Here, $G_{0\nu}$ is the phase space factor, which is recently recalculated using the exact Dirac wave function with finite nuclear size, and electron screening is taken into account. Recent calculation results can be seen in [30], [31] and [32]. A matrix element M is theoretical calculation and currently has a large model uncertainty.

Since there is no energy loss by neutrinos, the total kinetic energy of the two electrons emitted by $0\nu\beta\beta$ has a monochromatic peak at the Q-value like Fig. 2.7. The experiments on $0\nu\beta\beta$ decay search are going to detect the peak.

Neutrinoless double-beta decay occurs by not only the light neutrino exchange. However, [33] showed even if the underlying particle physics model does not contain tree-level Majorana mass, observation of the neutrinoless double-beta decay is a proof of the existence of non-zero Majorana mass (See Fig. 2.8). The neutrino mass generated by this diagram is too small to explain the neutrino mass observed in the neutrino oscillation because it is a 4-loop level, but the observation of $0\nu\beta\beta$ decay process is the evidence of the Majorana mass. Moreover, extended black box theorem [34] showed that if neutrinos are Majorana particles, current neutrino oscillation data implies there must be the non-zero double-beta decay rate.

Effective Field Theory(EFT) Aproach for Lepton Number Violation Processes

Study from the EFT approach is underway to link the underlying lepton number violation operator with $0\nu\beta\beta$ decay. The observable beyond standard model physics

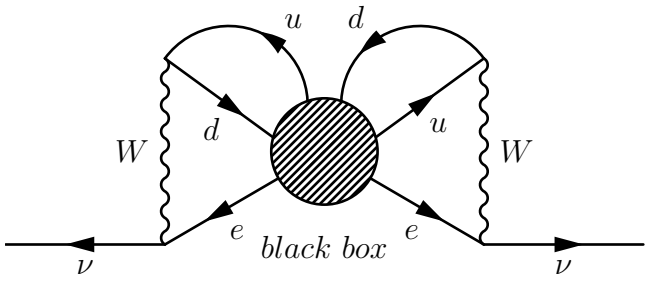

Figure 2.8: Black box theorem
The black box in the middle of the figure represents any $0\nu\beta\beta$ decay process. Whatever the process in between, the diagram shows that the neutrino flips anti-neutrino, and it means that the neutrino is a Majorana particle.

energy Λ at $0\nu\beta\beta$ decay search experiments was investigated up to dim-9 (partly dim-11). The contribution to the of $0\nu\beta\beta$ decay amplitude (A) is roughly

$$A \sim (\frac{1}{\Lambda^{d-4}}). \tag{2.39}$$

Here, d is dimension. The dim-5 term provides the mass mechanism by the light Majorana neutrino exchange. If the operator of dim-7 or dim-9 is the main contribution, the constraints by future double-beta decay experiments will becomes $\Lambda > 10(100)$ TeV, and it can exceed the searchable level of the LHC search ($pp \rightarrow 2l + 2jets$) and decays of mesons or leptons ($l \rightarrow l$'$+\gamma$, lN$\rightarrow l$'N). The many non-standard mechanisms up to dim-11 cause washout of the lepton number violation, and the most baryogenesis via leptogenesis will become ineffective [35].

2.4.3 Nuclear Matrix Elements

Nuclear matrix elements are determined by theoretical calculations because they are not actually measured. The uncertainty on the model dependence of the theoretical calculations is still large, which is the largest uncertainty when determining the effective Majorana mass from the $0\nu\beta\beta$ decay experiment. Currently, there are several calculation methods with advantages and disadvantages. Each feature is summarized.

- Shell model(SM, NSM)
  The shell model can provide exact solutions, and its reliability is high. However, the model space is limited only on the Fermi surface, and some spin orbit partners are not considered.

- Quasi-particle random phase approximation(QRPA)
  QRPA uses intermediate states with large number single particle orbits. The neutron-proton correlation can be handled. The problem is that two sets of intermediate states must be created and matched artificially. Also, the result depends on the parameterized proton-neutron interaction.

- Interacting boson model(IBM)
  The model space is larger than the shell model with fewer correlations. The IBM is more phenomenological than others, and the results depend on adjustment of parameters and matching with experimental results.

- Energy density functional theory and generator coordinate methods(EDF,GCM)
  The result tends to be larger than others. Wide model space is used, but limited correlations are considered. And, the result depends on the considered correlation. The calculation of odd-odd nucleus is difficult because of the closure approximation.

In addition, Fig. 2.9 summarizes the NME calculations of each nucleus. The difference is about 3 times at maximum, and we can know only the absolute value of ^{48}Ca is small. The deference in the NME by factor 3 corresponds to about one order for the half-life, considering the Eq. (2.38). Also, the phase-space factors are summarized in Fig. 2.10.

2.4.4 Axial-Vector Coupling Constant

The theoretical uncertainty of $0\nu\beta\beta$ decay experiment results is even greater when the g_A problem is considered. There is a discrepancy in the g_A between the observed beta decay and the theoretical value, and this difference is phenomenologically eliminated by correcting the g_A. The g_A tends to be small "quenching", and the corrected g_A is called effective g_A, which is 0.6-0.8 times in beta decay. The reason why effective g_A is necessary is not clear yet, and it is not known whether it is necessary for $0\nu\beta\beta$ decay or $2\nu\beta\beta$ decay. The possible causes are assumed to be some nuclear many-body correlations missed in the calculation and many-nucleon weak currents. If the cause is many-body correlation effects, the current matrix elements are too large. In the other case, the difference in the matrix elements is less than factor 2 [1] because the effect by the two-body currents at the high momentum transfer in $0\nu\beta\beta$ decay is smaller, unlike $2\nu\beta\beta$ decay. A theory to explain this g_A quench in beta decay has recently been proposed [36]. In the study, the cause of the g_A quench is considered to be 2(3) body-current. If the quench is stemmed in it, the quenching effect of the double-beta decay is less about 10% [37], compared to the one of beta decay about 20% [38].

Also, a study to test the effective g_A is proposed though $2\nu\beta\beta$ decay spectrum shape analysis measured by $0\nu\beta\beta$ decay search experiments [39], although it is different from $0\nu\beta\beta$ decay. KamLAND-Zen 400 performed the $2\nu\beta\beta$ decay shape analysis in [40].

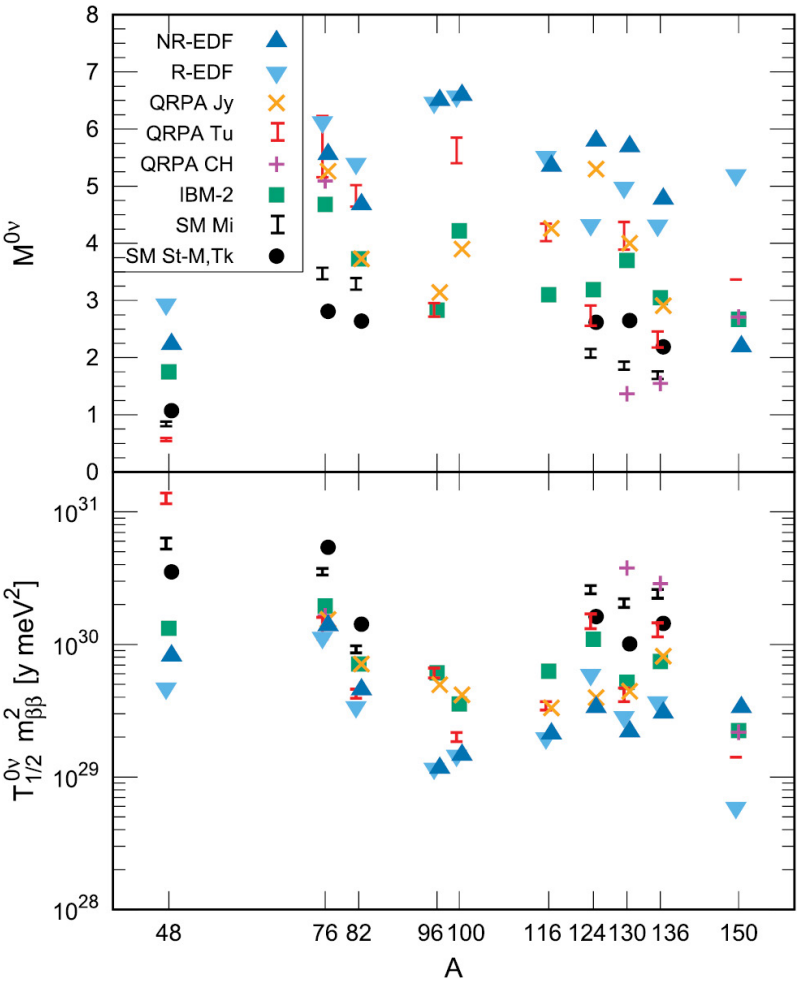

Figure 2.9: NME summary
The figure is from [1]. The top figure is the NMEs for $0\nu\beta\beta$ decay with their mass number in the different models. The bottom figure is the $0\nu\beta\beta$ decay half-lives scaled by the unknown $\langle m_{\beta\beta}\rangle$.

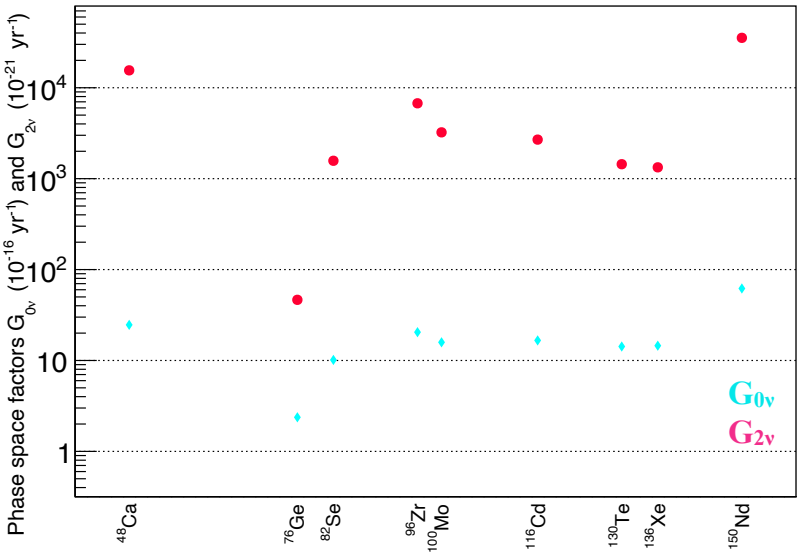

Figure 2.10: Phase-space factors for each nucleus in [30] are summarized for $2\nu\beta\beta$ decay and $0\nu\beta\beta$ decay. The phase-space factors for ^{76}Ge are smaller than the others, which gives the larger effective Majorana mass if the same half-life is obtained.

Chapter 3

Double-Beta Decay Experiments

3.1 Double-Beta Decay Experiments

Experiments on the $0\nu\beta\beta$ decay search are performed and planned using various nuclei around the world. The main results from them are summarized in Table 3.1. Although there are few ten $2\nu\beta\beta$ decay nuclei, not all of them are suitable for $0\nu\beta\beta$ decay search. The selection of the nuclei is performed according to the following criteria.

- High abundance of isotopes
  Generally, $2\nu\beta\beta$ decay nuclei do not exist with vast enrichment in nature. The highest one ^{130}Te has about 30% natural abundance. Therefore, if a nuclear enrichment method has not been established, the cost for the isotopes could be exceptional to prepare in large quantities. Also, the isotopes that can be used in low radioactivity detectors must be selected.

- High Q value
  The higher Q-value is vital because the background events due to natural radioactivities can be avoided. The 2.615 MeV gamma, which is the highest natural single gamma-ray released by ^{208} Tl decay from ^{232}Th decay chain, is a troublesome background. If the Q-value is high enough to avoid ^{214}Bi(Q=3.270 MeV), a daughter nucleus of ^{222}Rn, the experiments can get great benefits. Also, the energy resolution is better with higher energy. ^{48}Ca has the highest Q-value of 4.27 MeV.

- Long $2\nu\beta\beta$ decay rate
  One of the inevitable backgrounds is the high energy tail of $2\nu\beta\beta$ decay, which cannot be separated to $0\nu\beta\beta$ due to the detector energy resolution. The isotopes which have long $2\nu\beta\beta$ decay half-life are preferred, especially by detectors with poor energy resolution.

Experiments using various detectors are conducted all over the world, such as high-purity Ge semiconductors, cryogenic bolometers, loaded-organic scintillator detectors, time-projection chambers, and tracking chambers. $0\nu\beta\beta$ decay is a very rare decay

Table 3.1: Summary of double-beta decay experiments
The phase space factors on $0\nu\beta\beta$ decay in [30] and the nuclear matrix elements in [1] were used. The g_A is assumed to be 1.27.

Nucleus	Q-value (MeV)	$T^{2\nu\beta\beta}_{1/2}$ ($\times 10^{18}$ yr)	$<T^{0\nu\beta\beta}_{1/2}$ ($\times 10^{25}$ yr)	$> \langle m_{\beta\beta} \rangle$ (meV)	Experiments
^{48}Ca	4.267	64	6.2×10^{-3}	(1.50-2.76)$\times10^{3}$	CANDLES[41] NEMO-3[42]
^{76}Ge	2.039	1926	9	111-244	GERDA[43],[44]
^{82}Se	2.996	86.0	0.35	311-638	NEMO-3[45] CUPID-0[46], [47]
^{100}Mo	3.034	6.8	0.11	364-615	NEMO-3[48], CUPID-MO[49]
^{130}Te	2.528	790	3.2	73-343	CUORE[50], [51]
^{136}Xe	2.458	2210	10.7	54-165	KamLAND-Zen[18] EXO[52]

with a long half-life, so it is necessary to create an ultra-low background detector with large isotopes in order to find a small number of signals. For this reason, an experimental device is usually located underground and covered with active or passive shields. Besides, each experiment has unique technologies and features as follows:

- **Low radioactivity**
  The main backgrounds come from natural radioactivities. The detector source and material containing low radioisotopes are selected. KamLAND-Zen achieved an extremely low radioactivity environment by using the KamLAND liquid scintillator.

- **High energy resolution**
  Background counts can be reduced by increasing energy resolution because the region of interested (ROI) energy can be narrowed. In particular, the tail of $2\nu\beta\beta$ decay can only be reduced by increasing energy resolution.

- **Particle identification (PID)**
  If the detector can separate beta rays from gamma rays and alpha rays, backgrounds can be reduced strongly. Most of the high energy natural radioactivity are gamma rays, including 2.6 MeV gamma from ^{208}Tl. Many detectors are working on the PID using the pulse shape discrimination. Also KamLAND-Zen studies PID using the difference of the scintillation T-Q waveform with neural network [53].

- **Tracking (using event topology)**
  If the two betas of $0\nu\beta\beta$ decay can be tracked, the backgrounds other than $2\nu\beta\beta$ will hardly be eliminated. Notably, the elastic scattering of the electron by ^{8}B solar neutrino can be distinguished, which can not be removed by the PID. Detecting Cerenkov light is almost the only method using event topology in LS detectors such as KamLAND-Zen, and R&D is on going.

Generally, the detector sensitivity is expressed by the following formula,

$$T^{0\nu}_{1/2} \propto \begin{cases} \varepsilon M t & \text{(background free)} \\ \varepsilon \sqrt{\frac{Mt}{B\Delta E}} & \text{(with background)} \end{cases} \tag{3.1}$$

Here $T^{0\nu}_{1/2}$ is half life of the $0\nu\beta\beta$ decay, M is mass of the isotope, B is background counts in ROI, ΔE is the energy resolution, t is observation time and ε is the detector signal efficiency such as fiducial volume and analysis cut. The sensitivity is proportional to the observation time and mass, if the experiment is background free. It is proportional to $\sqrt{t}$ or $\sqrt{M}$ in the experiments with backgrounds.

Following sub-sections describe some $0\nu\beta\beta$ decay search experiments which are running or planned.

3.1.1 GERDA/LEGEND

GERDA is the GERmanium Detector Array located at Gran Sasso National Laboratory in Italy. High purity Germanium(HPGe) semiconductor detectors enriched in ^{76}Ge by $\sim$ 87% are used. Advantages of using HPGe detectors are good energy resolution ($\sigma(E)/E < 0.1\%$ at Q-value 2039 keV) and no intrinsic beckground thanks to the high purity. The background count is $< 10^{-3}$ cts/keV/kg/yr. The latest result on the $0\nu\beta\beta$ decay half-life is $>0.9\times10^{26}$ yr(90% C.L.), and the sensitivity is 1.1×10^{26} yr [43].

LEGEND is the next generation HPGe detector for the $0\nu\beta\beta$ decay search experiment, and it combine technology and materials with MAJORANA, which is also a similar HPGe detector. LEGEND-200 is upgrade of existing infrastructures with 200 kg of Ge. The goal of the background count is 0.6 cts/(FWHM ton yr), and it plans to start observation in 2021 with the sensitivity of $\sim 10^{27}$ yr in 5 years. The future plan LEGEND-1000 will search up to the sensitivity of 10^{28} yr using 1000 kg of Ge.

3.1.2 CUORE/CUPID

Cryogenic Underground Observatory for Rare Events (CUORE) uses ^{130}Te for $0\nu\beta\beta$ decay isotopes with 988 TeO_2 crystals, which are $5\times5\times5$ cm^3 each. Total crystal mass is 742 kg TeO_2 (natural Te) and ^{130}Te mass is 206 kg. Crystals operated as bolometers in a cryostat capable of reaching T<10 mK. The energy deposition is converted into a temperature rise. The energy resolution is 5 keV at Q-value(2.528 MeV). The experiment started observation in 2017, and the recent result on the $0\nu\beta\beta$ half-fife provides 3.2×10^{25} yr (90% C.I.) [50]. The sensitivity of the half-life is 7×10^{25} yr (90% C.L.) in 5 years.

Future upgrade of the CUORE is Cuore Upgrade with Particle IDentification (CUPID) with new scintillating bolometer. Heat plus light detection gives capability of PID. Background count in the ROI will be 100 times lower than COURE. Now, 25 crystals of $Zn^{82}Se$ with 5.5 kg of ^{82}Se was operated as first demonstrator of the dual readout technology (CUPID-0). Then, the sources were replaced with 20 Mo crystals ($Li_2^{100}MoO_4$ with 2.264 kg of ^{100}Mo), and started the observation (CUPID-Mo). The

^{100}Mo isotope has higher Q-value, and can avoid gammas coming from contamination in the cryostat and shields. The sensitivity will be $\sim 10^{27}$ yr in the future full detector [54].

3.1.3 EXO/nEXO

EXO is a liquid-Xenon time projection chamber (TPC) located at Waste Isolation Pilot Plant (WIPP) in Carlsbad, NM, USA. EXO-200 began the operation in Sept. 2011 with ∼175 kg Xe and the operation of EXO-200 concluded in December 2018. The energy resolution(σ/E) is 1.15 ± 0.02% with 12 kV cathode HV, and the particle identification using multi site (γ-like) and single site (β-like) recostruction was performed. Also, α event is identified by its large scintillation and ionization signal ratio. The result with full data set was published in [52] and they obtained the $0\nu\beta\beta$ half-life limit by 3.5×10^{25} yr. The sensitivity was 5.0×10^{25} yr. The next-generation Enriched Xenon Observatory (nEXO) is proposed to search for the $0\nu\beta\beta$ decay with a target half-life sensitivity of $\sim 10^{28}$ yr using 5×10^3 kg of liquid-Xenon in a time projection chamber. The detection technology is based on EXO-200. Also, the energy resolution will be improved about half of that in EXO-200.

3.1.4 KamLAND-Zen 400

KamLAND-Zen 400 (Zero-neutrino) uses Xe loaded liquid scintillator contained in 25-μm-thick nylon inner-balloon (IB). The inner balloon is suspended at the center of the KamLAND 13-m-diameter large balloon. The electron kinetic energies are transformed into scintillation photons and detected with 1897 17-inch and 20-inch PMTs. KamLAND-Zen 400 started the observation with ∼ 320 kg of Xe in October 2011[55]. The period up to June 2012 is called Phase-I. In this phase, the ^{110m}Ag background (β^- decay: τ =360 days, Q=3.01 MeV) was found around the Q-value (2.458 MeV) of ^{136}Xe (See Fig. 3.1). Therefore, the Xe loaded liquid-scintillator was replaced with a new one and purified by distillation and liquid-liquid extraction. Xe gas is also extracted and purified by distillation to reduce the backgrounds.

Phase-II was started in November 2013. ^{110m}Ag backgrounds were almost disappeared in Phase-II (See Fig 3.2). Furthermore, the amount of Xe was increased to 383 kg. The observation of this phase was completed in October 2015, and the stringent upper limit on the half-life of ^{136}Xe $0\nu\beta\beta$ decay ($T^{0\nu\beta\beta}_{1/2}$ >1.07×10^{26} [18]) was obtained. Converting this limit to the effective Majorana neutrino mass yields $\langle m_{\beta\beta}\rangle < (61 - 165)$ meV [18].

3.2 Discovery Potential

The discovery possibility of $0\nu\beta\beta$ decay was investigated by Bayesian global analysis in [58]. The inputs are known parameters, neutrino mass squared, mixing angles and constraints on the Majorana effective mass, electron neutrino mass, and the sum of neutrino masses. Unknown parameters are assumed to be uniform distributions for

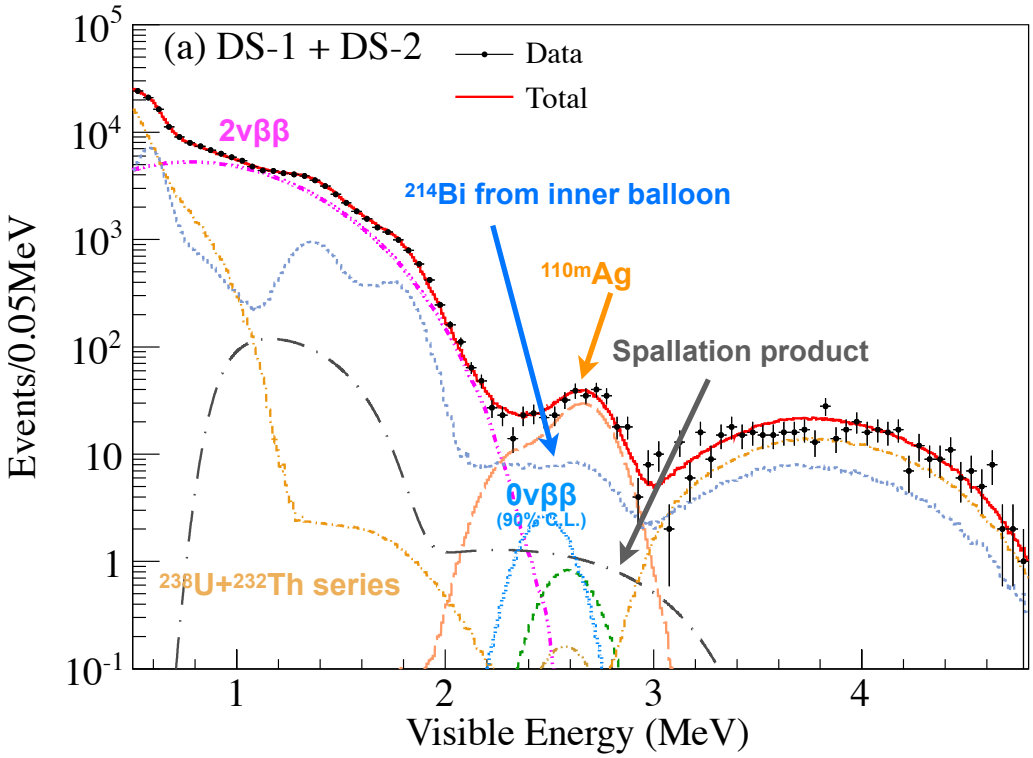

Figure 3.1: Phase-I result [56]
The figure shows the energy spectrum with the best fit results within the 120 cm radius in Phase-I. 90% C.L. upper limit rate of the $0\nu\beta\beta$ decay is also drawn. Many ^{110m}Ag events were seen in the $0\nu\beta\beta$ decay energy region.

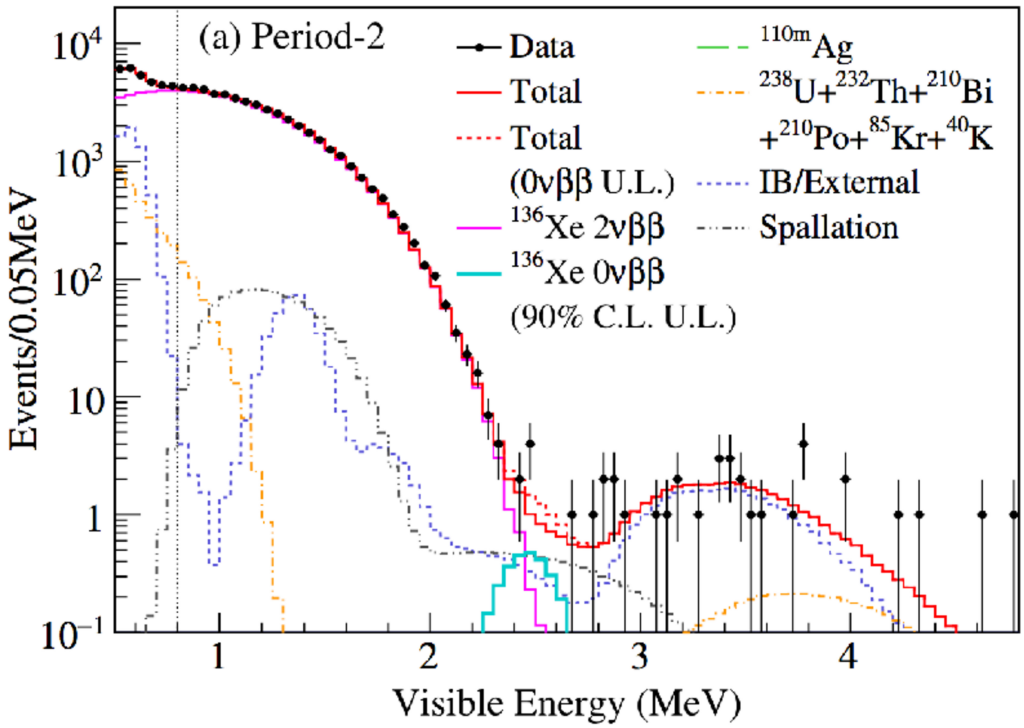

Figure 3.2: Phase-II result [18]
The energy spectrum in the latter period of Phase-II within the low background volume (R <1.26 m for z >0 and R <1.06 m for z <0) is shown. ^{110m}Ag is not seen after the purification. The remaining backgrounds are spallation products and contamination of the inner-balloon (IB).

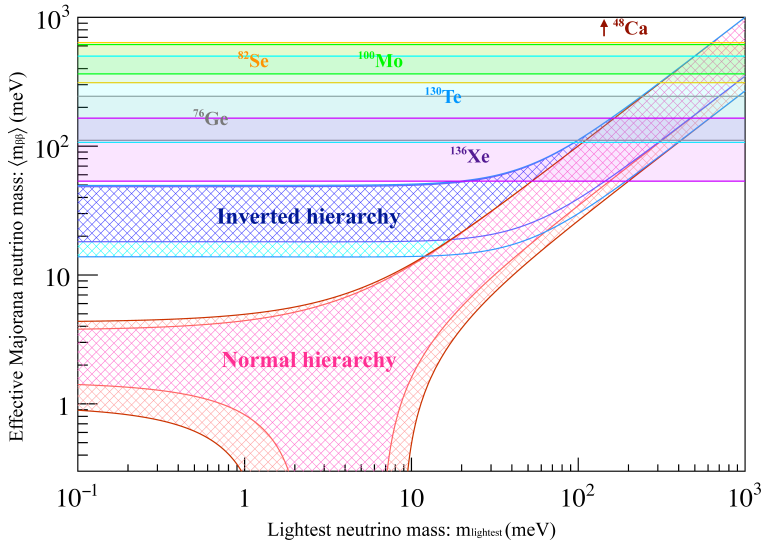

Figure 3.3: Effective Majorana mass and lightest neutrino mass
The blue band represents the inverted mass hierarchy and the red band is the normal mass hierarchy. Light colors mean 3σ errors from the current global oscillation analysis [57]. Each experimental result in Table 3.1 is drawn by the colored bands with the NME uncertainties.

δ and Majorana phases, and logarithmic distribution for the neutrino masses. Fig. 3.4 shows the probability density of $\langle m_{\beta\beta} \rangle$ and the lightest neutrino mass. The small value of $\langle m_{\beta\beta} \rangle$ in the normal hierarchy is unlikely because they need fine-tuning of the Majorana phases. Future $0\nu\beta\beta$ decay search experiments, which will start in the next 5-10 years, are going to cover almost all the inverted hierarchy ($\sim$10-20 meV). If neutrinos are Majorana particles and the inverted mass hierarchy, they have more than 95% chance to the discovery, and even if the normal hierarchy, they still have $\sim$50% chance to the discovery. In order to cover all the inverted hierarchy, it is necessary to perform ton-scale experiments. ^{136}Xe can be easily extended to the ton scale; in fact, KamLAND-Zen 800 introduced a more than half-ton isotope. Once $0\nu\beta\beta$ decay is found, it becomes crucial to improve the accuracy of the measured effective Majorana mass and to access the physics behind the $0\nu\beta\beta$ decay. Currently, nuclear matrix elements and effective g_A have large uncertainty. The theoretical approach alone is not enough to eliminate the uncertainty, but multi-isotope measurements can help reduce it. Also, the mechanism that derive $0\nu\beta\beta$ decay is not only standard light neutrino exchange, but other mechanisms can lead the $0\nu\beta\beta$ decay, for example, L-R symmetry, R-parity violation, and Zee model. Whether the standard mass mechanism or something else lead the $0\nu\beta\beta$ decay can be verified by measuring with various isotopes [59], examining the angle and the energy distribution of two electrons with a tracking detector.

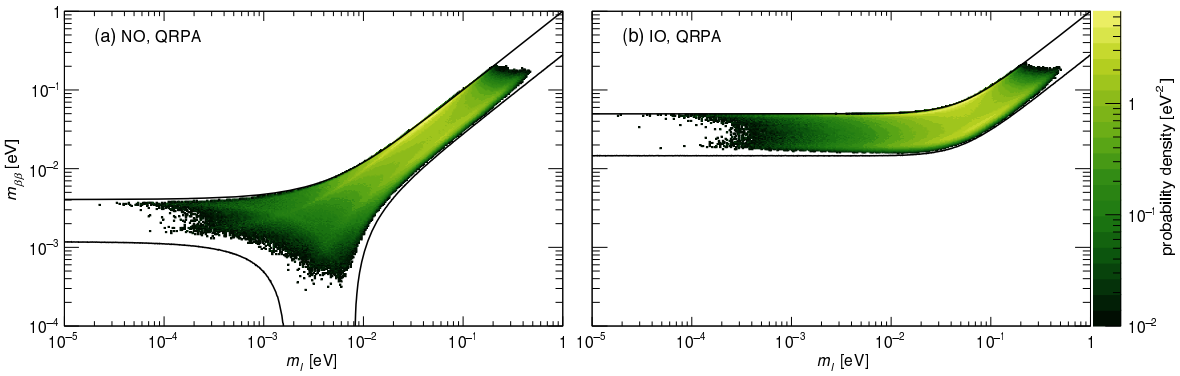

Figure 3.4: Probability density distribution of $\langle m_{\beta\beta} \rangle$ in the normal hierarchy(left) and inverted hierarchy(right). The figure is from [58]. The light color means high probability. The lower value in the normal hierarchy is unlikely because fine-tuning in the Majorana phases is needed.

Chapter 4

Detector

KamLAND(**Kam**ioka **L**iquid-scintillator **A**nti-**N**eutrino **D**etector) is a large size liquid scintillator detector for a reactor antineutrino oscillation experiment. It is located at 1000 m underground of Mount Ikenoyama, Gifu prefecture, Japan.

4.1 Site

Fig. 4.1 shows the KamLAND site 1000 m underground of Mount Ikenoyama. On-site shifters monitor the data acquisition and detector conditions in a control room. There exists equipment for purification by liquid-liquid extraction of water and organic liquid scintillator, and by nitrogen purge in 1st purification area. 2nd purification area and 25 m^3 tank area are in the left outside of Fig. 4.1. The distillation system for the liquid scintillator exists in the 2nd purification area. A dome area is above the KamLAND detector. The dome area itself is a class 10,000 cleanroom and has an electronics hut in it. The top of the KamLAND chimney is in the class 100-1000 clean booth. The clean booth is extended for the inner-balloon installation in August 2016 and May 2018. There exists a Xe distillation tower in front of the 4th access tunnel and Xe handling system in the former 3rd access tunnel.

4.2 KamLAND

4.2.1 Inner-Detector

KamLAND consists of a liquid scintillator inner detector (ID) and water Cherenkov outer detector (OD). Fig. 4.2 shows the KamLAND detector. The ID is made of 18-m-diameter stainless steel sphere tank, 1,325 17-inch PMT, 554 20-inch PMT, and 13-m-diameter outer-balloon. Outside of the outer balloon is filled with non-scintillating buffer oil. The acrylic panel separates the buffer oil to 2 parts, the inner buffer oil (IBO) and the outer buffer oil (OBO). The acrylic panel also prevents the radon from PMT glass to move into the inner part.

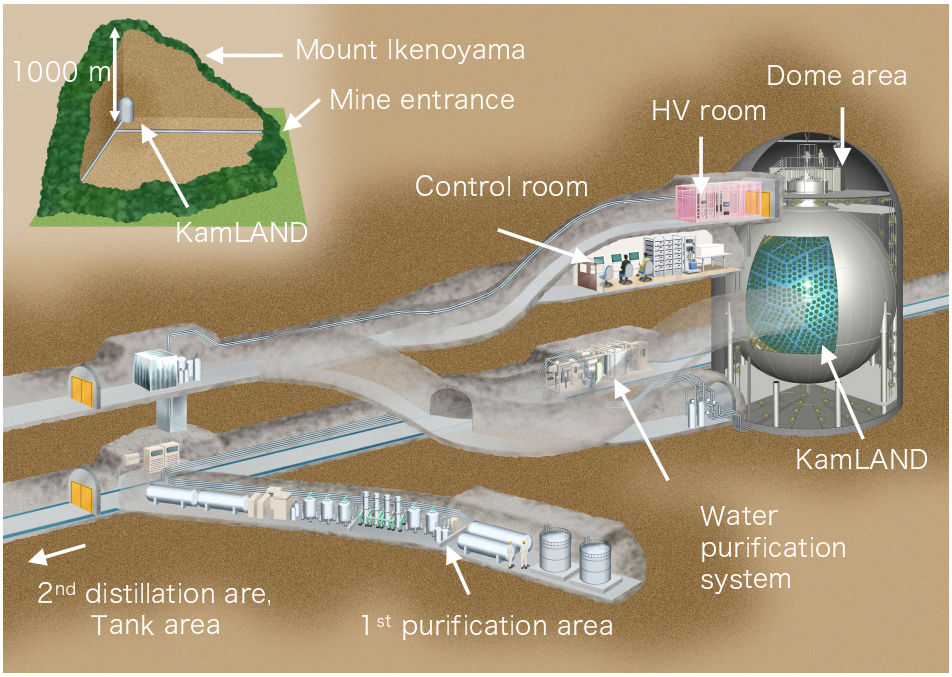

Figure 4.1: KamLAND site

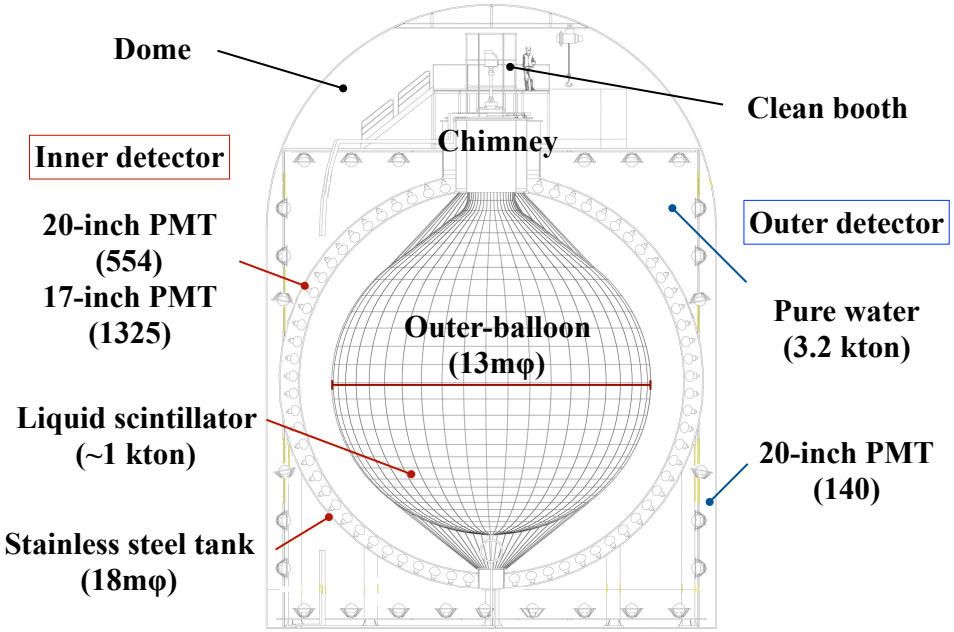

Figure 4.2: KamLAND

Table 4.1: Components of KamLAND LS

	D12	PC	PPO
Molecular formula	$C_{12}H_{26}$	C_9H_{12}	$C_{15}H_{11}NO$
Density[g/cm^3]	0.7526	0.8796	-
Boiling point[°C]	216	169	360
Melting point[°C]	−10	−44	72
Flash point[°C]	83	54	-

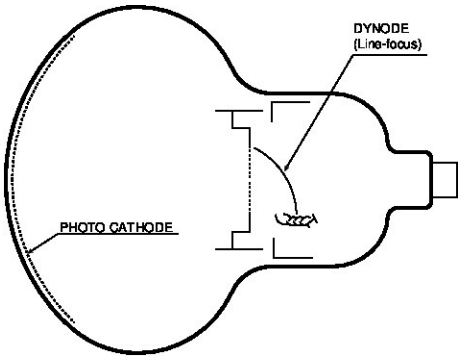

Figure 4.3: 17-inch PMT
The dynode is box&linear focused type and the photocathode is masked to 17-inch diameter.

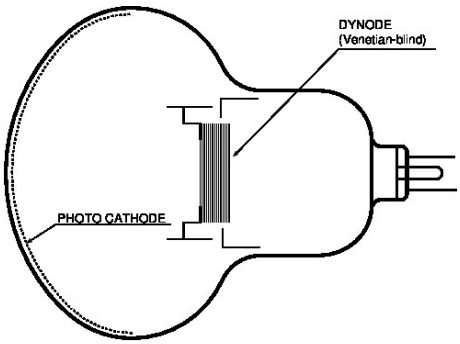

Figure 4.4: 20-inch PMT
The dynode is Venetian blind type and the photo-cathode is not masked.

4.2.2 Liquid Scintillator

KamLAND has about 1,200 m^3 liquid scintillator(KamLAND LS) in the outer balloon. The KamLAND LS composed of 80.2% normal-dodecane (D12), 1,2,4-trimethylbenzene 19.8% (pseudocumene,PC) and 1.36 ± 0.03 g/L 2,5-diphenyloxazole(PPO), which takes an role of the scintillation agent. After the liquid scintillator purification campaign in 2007-2009, very low ^{232}U and ^{238}Th concentrations had been achieved respectively $5.0 \pm 0.2 \times 10^{-18}$ g/g and $1.3 \pm 0.1 \times 10^{-17}$ g/g [60]. They are evaluated with ^{214}Bi-^{214}Po decay of U series, ^{212}Bi-^{212}Po decay of Th series, assuming radioactivity equilibrium.

KamLAND buffer oil is made of 53% normal paraffin($C_{12}H_{26}$) and 47% isoparaffin (C_nH_{2n+2},n∼14). The buffer oil does not emit scintillation light. It has the role of shielding gamma rays and particles coming from outside materials such as the PMTs and acrylic panels.

4.2.3 PMT

PMT (photomultiplier tube) is an optical sensor that can detect a single photon signal with excellent timing resolution. A photon is converted into a photoelectron on the photocathode and collected by the electric field into dynodes, which are electron

Table 4.2: Performance of 17-inch and 20-inch PMTs

	17-inch	20-inch
Effective photocathode area (diameter)	430 mm	460 mm min.
Dynode structure	Box&Linear focused	Venetian blind
	10 stages	13 stages
Quantum efficiency	23% at 390 nm	23% at 390 nm
T.T.(Transit Time)	110 ns	90 ns
T.T.S.(T.T Spread, FWHM)	3.5 ns	7.7 ns
PV ratio	2.5	not seen
Dark pulse rate	22 kHz	40 kHz
After-pulse rate	$\sim 3\%$	$\sim 1\%$

multipliers. One photoelectron is amplified to $10^{6\text{-}7}$ times in the dynodes, and they are read out through the anode. The current of the photoelectrons is converted into a voltage by a coupling capacitor and sent to the data reading circuit. Inner detectors include 1,325 17-inch PMTs (R7250) and 554 20-inch PMTs (R1449 or R3600). Both photocathodes use bialkali, which is sensitive to wavelengths of 300-650 nm within the emission wavelength range of the PPO. Fig. 4.5 shows the quantum efficiency of the PMT. The 17-inch PMT is a PMT developed for the KamLAND detector, which has better timing resolution than that of 20-inch PMT. Unlike the 20-inch PMT has the Venetian blind type dynode, the dynode structure is a box & linear focused type (See Fig. 4.3 and Fig. 4.4). The box type first dynode makes CE (Collection efficiency) better, and the line focus type dynodes in the second and subsequent stages provide better T.T.S. (Transit time spread). The glass structure of 17-inch PMT is the same as the 20-inch PMT, however the outer radius region with poor time resolution is masked to 17-inch. The 20-inch PMTs are reused from the Kamiokande experiment. The regular performance of 17-inch PMT and 20-inch PMT (R1449) is listed in Table 4.2. The total photocathode coverage of 17-inch PMT and 20-inch PMT at the ID is about 34%. The performance of the large-diameter 17-inch and 20-inch PMT can deteriorate due to influence of the $\sim$450 mG geomagnetic. The entire KamLAND detector is covered with the geomagnetic compensation coils to suppress the magnetic field in the inner detector PMT. The magnetic fields with the coils are calculated to be less than 50 mG in all the ID PMTs. The PMT performance was guaranteed within this range.

In order to detect cosmic ray muons passing through the chimney part at the top of the detector, eight 8-inch PMTs between the stainless steel tank and the acrylic layer (OB 8-inch PMT) and between the acrylic layer and the balloon (IB 8-inch PMT) are installed respectively at the position of $z = 9.35$ m facing the zenith. In addition, six 5-inch PMTs are attached to the flange that closes the KamLAND hatch on the top of the chimney.

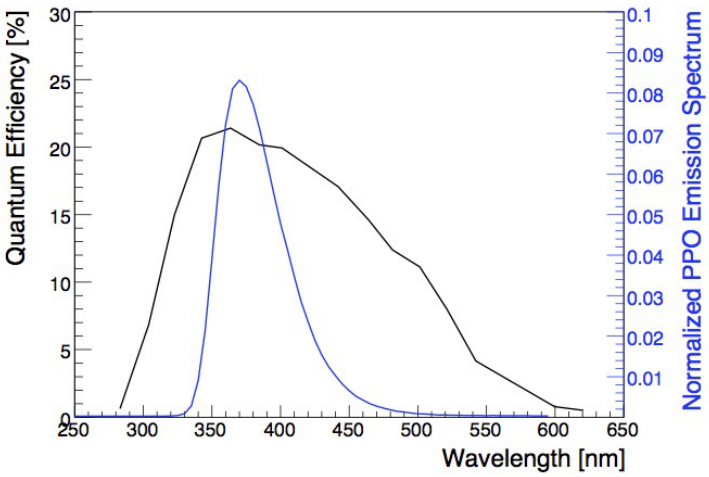

Figure 4.5: Quantum efficiency of the PMT and wavelength dependence of the PPO emission light. The figure is from [61]

4.2.4 Outer-Detector

KamLAND is located at about 1,000 m (2,700 m water equivalent) underground. The muon flux originating from cosmic rays is mitigated to 1/100,000 compared to the ground level. Still, the cosmic ray muon event rate in the whole ID remains about 0.3 Hz. In order to reduce background events generated by cosmic ray muons, the outside of KamLAND is covered with a water Cherenkov detector. The outer water tank is a cylindrical cavity with a diameter of about 20 m and a height of about 20 m, which is filled with about 3,200 m^3 pure water (See Fig. 4.2). The OD was refurbished in 2016 [62], and 140 new 20-inch PMTs (R3600) were installed inside the cavity. The wall of the outer tank and the outer surface of the ID stainless steel spherical tank are covered with high reflective Tyvek sheets (Tyvek 1073B and 1082D) to collect as much light generated in the water as possible into the PMT. The role of the outer water detector is to reduce muon derived background events using cosmic ray muon tags, to shield radiations and fast neutrons from the outer rock, and to stabilize the temperature of the ID.

4.3 Data Acquisition

4.3.1 KamLAND DAQ

In KamLAND, two data acquisition (DAQ) systems are running in parallel. One is a DAQ system using KamFEE (KamLAND Front-End Electronics), which has been used since the start of the KamLAND observation, and the other is a DAQ system using MoGURA (Module for General-Use Rapid Application). MoGURA is a data acquisition circuit developed to eliminate deadtime just after cosmic ray muons. An overview of the data acquisition at KamLAND is shown in Fig. 4.6.

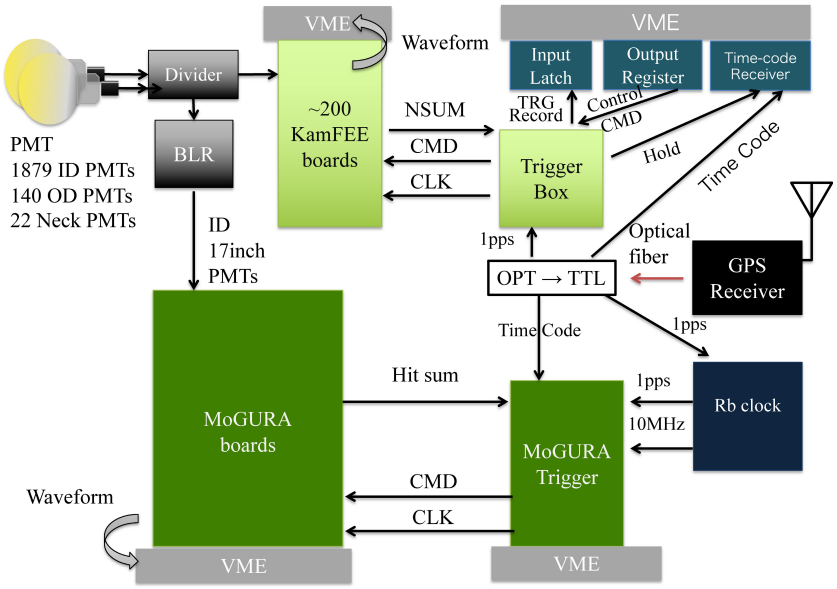

Figure 4.6: KamLAND DAQ system
The PMT signals branch at the divider, and they go through BLR to the MoGURA boards or go directly to the FBE boards.

4.3.2 KamFEE DAQ

The data collection system using KamFEE is controlled by KamDAQ, written in KiNOKO (Kinoko is Network-distributed Object-oriented KamLAND Online system) script. KamDAQ reads data and starts and stops Run, which is the unit of the data. Also, it determines the condition of Run at the beginning of the DAQ and send it to the trigger board and KamFEE. KamFEE is a VME 9U size board that operates with 40 MHz clock. 12 PMTs can be connected to one board at maximum. The signal waveform of PMT is digitized by two ATWDs (Analog Transient Waveform Digitizer) per channel on KamFEE. ATWD digitizes waveforms at 10-bit resolution. The sample interval is about 1.5 nsec, and the number of samples is 128 per waveform; a waveform length corresponds to about 200 nsec. ATWD samples waveforms at three types of gains (20 times, 4 times, 0.5 times), and the data can be acquired at 120 μV/count with the maximum gain. A hit determination is performed by a discriminator set to $\sim$1/6 amplitude of a single photoelectron in each channel, and hit information is sent as Nsum to the trigger circuit for 125 nsec. Then, the ATWD stops signal waveform recording of the hit channel temporarily and waits for the data acquisition command from the trigger board for about 1 μsec. Digitizing a signal waveform with ATWD takes 25 μsec, so in order to reduce deadtime by digitization, two ATWDs are working alternately in one channel.

The hit information is sent to the trigger board as NSUM consisting of 4-bit hit sum counted on each KamFEEs. The trigger board accumulates NSUM of all KamFEE boards and instructs to digitize the waveform of the hit channel according to the number of hits. There exist forcible data acquisition triggers as needed, such as acquiring baselines of signal cables or the laser calibration. The main trigger types

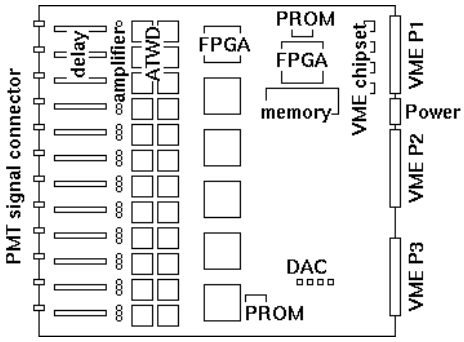

Figure 4.7: KamFEE layout

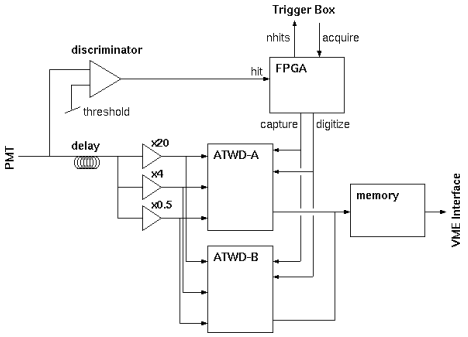

Figure 4.8: KamFEE diagram

and their descriptions are listed in Appendix A Table A.1. Simultaneously with sending the trigger command to KamFEE, the trigger circuit records information on the number of PMT hits, trigger timing (TimeStamp), and trigger type. The number of hit PMTs is the entire ID(N_{ID}), each section of the OD (N_{top}, N_{middle}, N_{bottom}, the entire OD N_{ODglobal}), and 5-inch PMT (N_5). The trigger circuit is also responsible for supplying a 40 MHz clock to all KamFEEs.

4.3.3 MoGURA DAQ

MoGURA (Module for General-Use Rapid Application) is a data collection circuit developed for eliminating dead time caused by high-rate afterpulses and overshoots after cosmic ray muons. MoGURA has four gains (P-gain: $\times$120, H-gain: $\times$24, M-gain: $\times$2.4, L-gain: $\times$0.24). P-gain uses 1 nsec sampling Flash-ADC, and the rests use 5 nsec sampling Pipeline-ADC. The signal that has passed through the gain is digitized by a Flash Analog-to-Digital Converter(FADC). The basic design of the MoGURA DAQ system is the same as KamFEE's one. Special features of MoGURA DAQ are the following.

- **Base line restorer(BLR)**
  The signals of PMTs are sent to BLR (BaseLine Restorer) after branching with the KamFEE signal, then entering MoGURA boards. The BLR has the role of reducing missing signals by suppressing overshoot generated in the PMT circuit at a high-intensity signal such as a muon has come.

- **Adaptive mode**
  The adaptive mode was developed for the purpose of tagging neutron capture after nuclear spallation produced by cosmic ray muons. After the cosmic ray muon, many pseudo signals such as afterpulses or ringing are generated. The normal thresholds against the number of the hit PMTs are impossible to discriminate between physical events and fake hits generated by afterpulses. The event determination is performed by providing a threshold for the differential PMT hits in the adaptive mode. Special launch trigger is issued when muon events come (Nhit>$\sim$800). The adaptive mode is valid for 1 msec after the launch trigger.

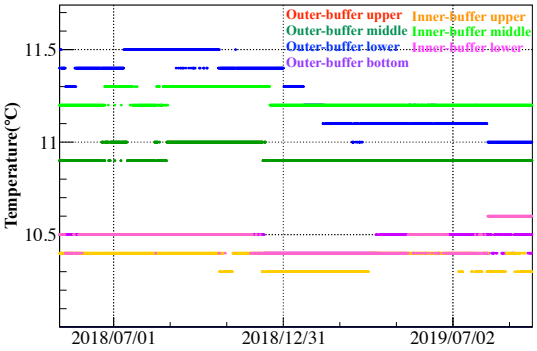

Figure 4.9: Temperature monitor
The colors represent different places, and temperature is stable within 0.5°C with all monitors.

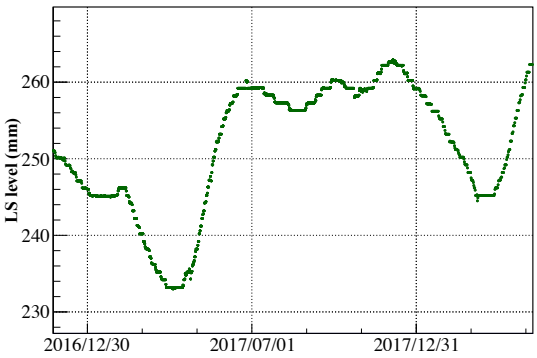

Figure 4.10: LS level monitor
Vertical axis is LS level. 1 mm corresponds to about 10 L of the LS.

Currently, only 17-inch PMTs are connected to 113 MoGURA boards. MoGURA data are mainly used for tagging of spallation products such as ^{10}C, ^{137}Xe, and long-lived Xe products after cosmic ray muons.

4.3.4 Slow Detector Condition Monitor

In order to detect problems of the detector quickly and to perform stable operation, slow detector condition monitor are working all time. It monitors the tension on the outer-balloon and inner-balloon, the LS temperature, the LS level, the OD water level, the water temperature, etc (See Fig. 4.10 and Fig. 4.10).

4.4 KamLAND-Zen Detector

KamLAND-Zen (Zero-neutrino), which is a neutrinoless double-beta decay search experiment, started in 2011. We installed an inner-balloon with a diameter of about 3 m at the center of the outer-balloon in KamLAND. The inner-balloon is filled with a Xe-loaded liquid scintillator. The Xe contains about 91% ^{136}Xe which causes double-beta decay and is disolved about 3 wt% in the LS. In 2018, we updated the inner-balloon to a diameter of about 3.8 m. KamLAND-Zen detector was shown in Fig. 4.11. In this section, components of the KamLAND-Zen detector are introduced.

4.4.1 Inner-Balloon

The inner-balloon is a radiopure vessel to hold the Xe-loaded liquid scintillator in the KamLAND liquid scintillator. In order to reduce radioactivity from the contamination of the materials, the inner-balloon was made of very thin 25-μm thickness

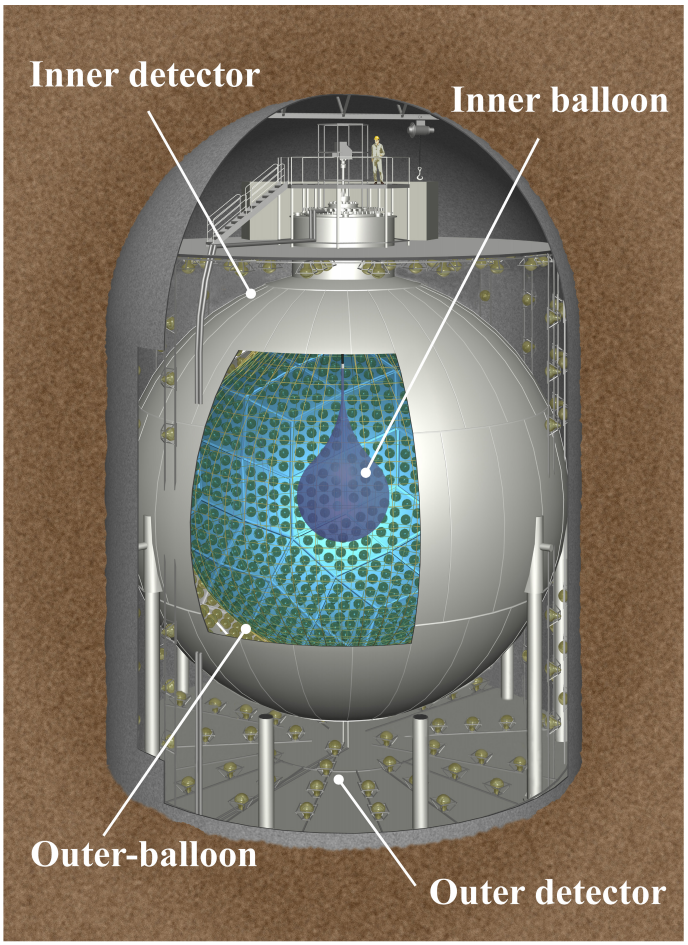

Figure 4.11: KamLAND-Zen detector

Table 4.3: Film contamination
Nylon-6 (washed) is a Nylon-6 film just after washing. The values come from [63]. ^{40}K value of Nylon-6 is calculated assuming a natural abundance 0.0117%. The values in Zen 400 Phase-I and Phase-II refer to [64] and [61].

	^{238}U $[10^{-12}\mathrm{g/g}_{film}]$	^{232}Th $[10^{-12}\mathrm{g/g}_{film}]$	^{40}K $[10^{-10}\mathrm{g/g}_{film}]$
Nylon-6 (washed)	2	6	<0.1
Zen 400 Phase-I	14±1	79±3	(2.1±0.1)×10^3
Zen 400 Phase-II	46.1±0.4	336±2	(4.7±0.5)×10^3(z<0)
Zen 800	3±1	38±2	(0.46±0.03)×10^2(z<0)

nylon-6 film. The raw materials for the nylon-6 film were carefully selected with a low amount of radioactive impurities. The contamination level of the raw nylon material is the order of 10^{-13} g/g in Uranium and Thorium, which were supposed to be introduced in a factory. The contamination level of the nylon-6 film is the order of 10^{-12} g/g. The inner-balloon can be more contaminated during the production, installation, and subsequent works. ^{238}U is the most serious contamination because the daughter nucleus ^{214}Bi have large decay energies high enough to be background events for $0\nu\beta\beta$ decay and can not be tagged with delayed coincidence due to alpha energy loss in the IB film. The amount of ^{238}U was 10^{-11} g/g in KamLAND-Zen 400, and it was reduced in KamLAND-Zen 800. The contamination of the IB are summarized in Table 4.3. The radioactive impurities in the raw material and film are measured by ICP-MS, and the others are calculated based on real events such as ^{214}Bi-Po for ^{238}U and ^{212}Bi-Po for ^{232}Th observed with KamLAND-Zen. The contamination on the film in the KamLAND-Zen 400 Phase-II increased due to the dust contamination by an accident during the liquid scintillator circulation.

IB Support

Inner-balloon was supported by 12 suspending belts and corrugated tubes. See Fig. 4.12 and Fig. 4.13. The top of the inner-balloon was connected to the corrugated tubes by a PEEK(Poly Ether Ether Ketone) connection pipe, which is also used to the connection between corrugated tubes. The suspended belts are to Vectran strings and pulled up to the chimney through the guide ring, which has 12 holes. The suspended belts are connected to the load cells at the clean booth in the dome area and their tensions are monitored .

4.4.2 Xe Loaded Liquid Scintillator (Xe-LS)

Xe liquid scintillator (Xe-LS) is a liquid scintillator filled only inside the inner-balloon for the KamLAND-Zen experiment with a mixture of decane 82%, pseudocumene 18%, $\sim$ 2.5 g/L PPO and $\sim$3 wt% Xe. The concentration of Xe and PPO depends on the phase of the experiment. The PPO concentration is much higher than that of the KamLAND liquid scintillator because Xe quenches the scintillation light. The

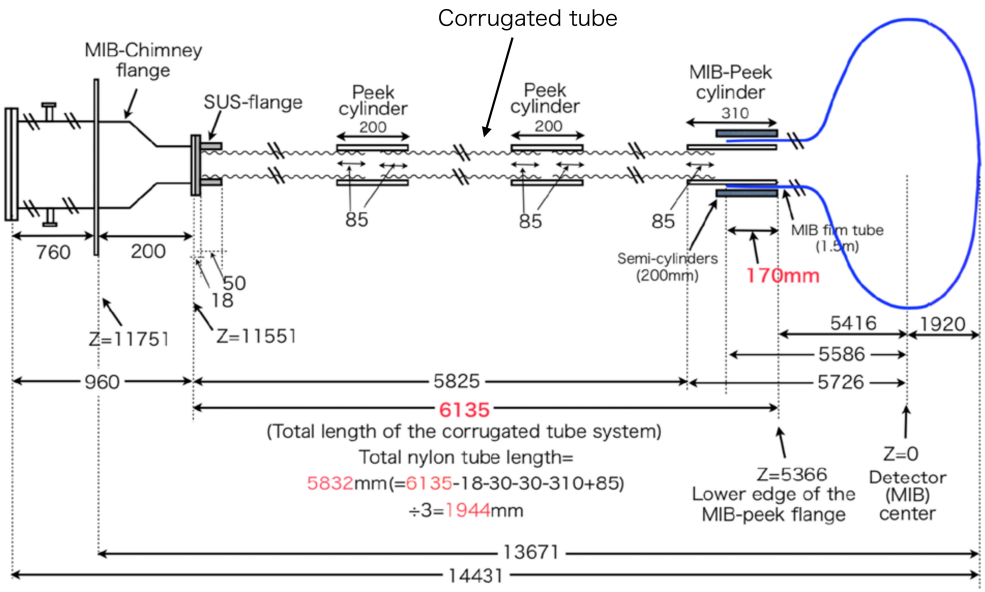

Figure 4.12: IB support: corrugated tube connection
Three corrugated tubes are connected to the inner-balloon with the PEEK cylinder connection pipes.

light yields of the Xe-LS is designed to be comparable to that of the KamLAND LS, but the actual value is about 10% less than the KamLAND LS in visible energy. The components of the Xe-LS were summarized in Table 4.4. The concentration of PPO in Xe-LS of KamLAND-Zen 800 was measured by Gas chromatography. The Xe concentration was calculated from the weight of dissolved Xe gas and the weight of the LS. The decane and PC ratios are calculated values.

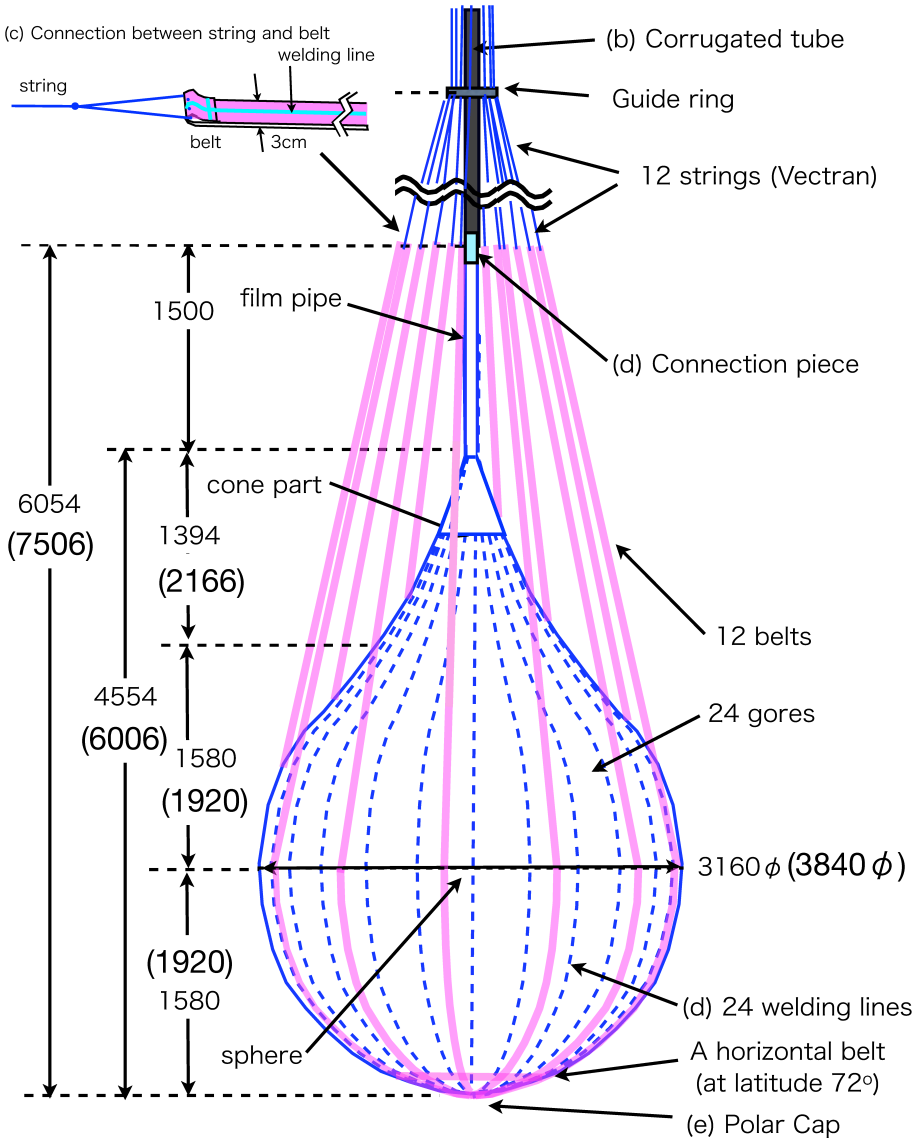

Figure 4.13: IB support: suspending belts and guide ring
Original figure is from [64] and modified. The values in parentheses are for KamLAND-Zen 800.

Table 4.4: Summary of Xe-LS components
The values in Zen 400 refer to [53] and [64]. Two values in the Xe concentration of Zen 400 Phase-I were measured at different times.

Material	Decane	PC	PPO	Xe
	$C_{10}H_{22}$	C_9H_{12}	$C_{15}H_{11}NO$	Xe
Density[kg/m^3]	731	875	-	-
Ratio	unit[%]	unit[%]	unit[g/L]	unit[wt%]
Zen 400 Phase-I	82.3	17.7	2.7	2.44/2.48
Zen 400 Phase-II	80.7	19.3	2.29 ± 0.03	2.91
Zen 800	82.4	17.6	2.38 ± 0.02	3.13

Chapter 5

Upgrade to KamLAND-Zen 800

5.1 KamLAND-Zen 800

We prepared KamLAND-Zen 800 during 2015-2019 to increase Xe amount from about 400 kg to about 800 kg. This chapter describes the upgrade to KamLAND-Zen 800.

5.2 Inner-Balloon Production

5.2.1 Failed Inner-Balloon

The initial plan was to introduce a new inner-balloon and start KamLAND-Zen 800 as soon as KamLAND-Zen 400 was finished. The inner-balloon installed in August 2016 had a LS leak on the IB film. It was uninstalled in November 2016. This failed inner-balloon was summarized in [63].

The signs of LS leak were confirmed by the data disagreement with the ^{222}Rn decay curve in the inner-balloon volume, declination of the load cell value, and fixed-point camera images. Most of them estimated the leak amount to be about 40 L/day. Besides, the components in the Dummy-LS collected when circulating through the filter from October were analyzed by gas chromatography. Dodecane, which is not contained in the initial Dummy-LS but the KamLAND LS, was detected as a component. From these results, we judged that there was a leak in the inner-balloon.

In the spring of 2017, we started making a new inner-balloon that can hold about twice as much liquid scintillator as before in a super-cleanroom, and completed it in the spring of 2018 and installed it into the KamLAND LS.

5.2.2 Cleanroom and Control of Cleanness

Inner-balloon was fabricated in the super-cleanrooms of the Nishizawa Memorial Research Center, Tohoku University since the spring of 2017. The cleanness of the cleanroom is less than class 1; it means that there is less than one 1-micron dust per 1 ft^3. A downflow air through both HEPA-filters and ULPA-filters is supplied to the cleanroom area all the time. We used two super-cleanrooms.

(a) Cleanroom 1

(b) Cleanroom 2

Figure 5.1: Cleanroom 1 and 2
The left figure shows inside of the cleanroom 1, and the right figure is that of the cleanroom 2. The cleanroom 1 was used to fabricate the inner-balloon. The tool washing and changing clean suits were done in the cleanroom2.

- **Cleanroom 1**
  Cleanroom 1 was used to fabricate the inner-balloon, where the strict control of the cleanness was taken. All tools and materials in the cleanroom 1 were washed with ultra-pure water, liquid-soap, and alcohol(ethanol or isopropyl alcohol) before they were brought into the cleanroom. Only people who ware a special clean suit which is washed by every work, double folded gloves and goggles were allowed to enter.

- **Cleanroom 2**
  Cleanroom 2 was also class 1 cleanroom, but it was used to do a little "dirty" works or activities such as washing, changing clean suits, and tests of welding machines.

Cleanness of ultra-pure water, N_2 gas, and He gas used in cleanrooms are all cleanroom standards. The ^{238}U contamination in the ultra-pure water is less than 10^{-13} g/g. The particle contamination in the N_2 gas is rejected by filters, and the residual particles with size of more than 0.1μm are about 10 counts per cubic feet. The He gas is filtered as well. If the air in the cleanroom is dry, dust is adsorbed to the inner-balloon film because it is easy to generate static electricity. It is preferred to be more than 65% humidity, so the fabrication is performed mainly in the rainy season. During the dry season in winter, the humidity in the cleanroom is controlled by the mist generation system (AirAKI®,H.IKEUCHI Co.,Ltd) in the room before the ULPA-filter (See Fig. 5.2). It is also checked that this system did not make any dust. The seasonal modulation in cleanroom humidity is shown in Fig. 5.4, and the control in cleanroom humidity is shown in Fig. 5.5. Also, many static eliminators SJ-F5500 (KEYENCE CORPORATION) were introduced to prevent the generated dust from adhering to the film (See Fig. 5.3).

The leading cause of the inner-balloon contamination is dust carried by people from outside. The particles generated when people moved. Especially many particles came from gloves and the gap between gloves and the sleeve of the clean suits. This

Figure 5.2: Mist generation system
The figure shows the mist generation by the system. The room shown in the figure exists upstream of the ULPA-filter.

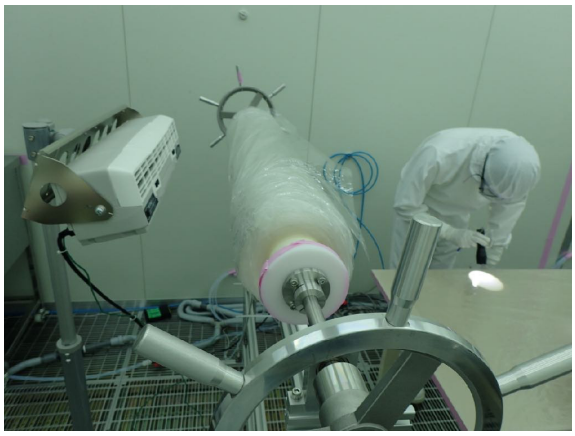

Figure 5.3: Static eliminator
The white machine at the left side of the figure is the static eliminator. It detects the static electricity in the air and send the air with opposite charged ions.

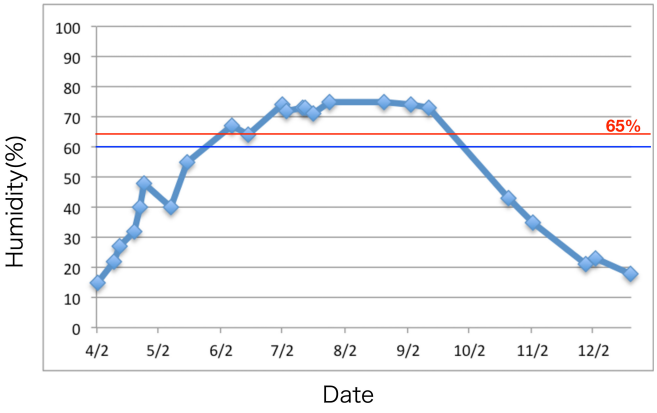

Figure 5.4: Seasonal modulation in cleanroom humidity
The cleanroom humidity in rainy season (from June to October) is more than 65%. Since the humidity in dry season is less than 65%, the mist generation system was used to increase it.

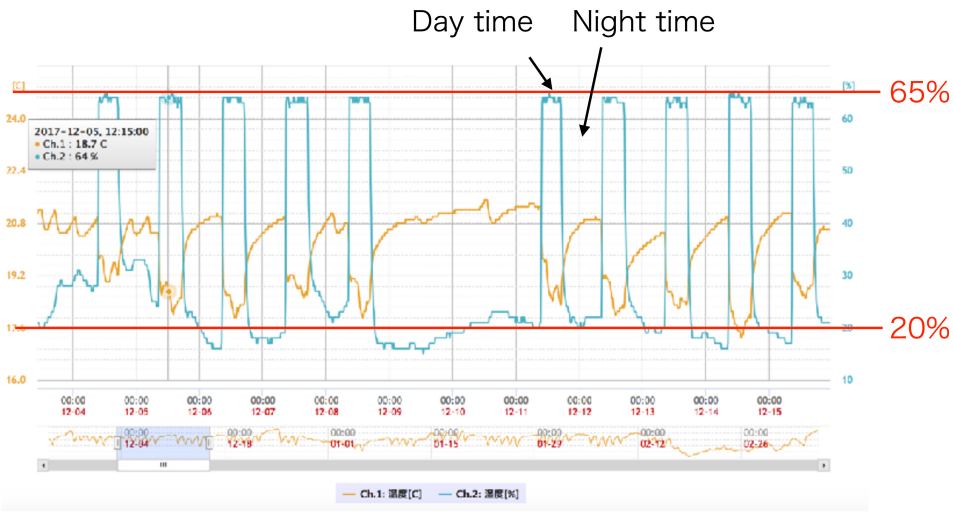

Figure 5.5: Cleanroom humidity with the mist generation system
The cyan graph represents the cleanroom humidity. The cleanroom humidity in the dry season is controlled with the mist generation system. The humidity in the day time was increased to about 65%. The system was off during the night time.

fact was confirmed by visualization of dust with a laser (See Fig. 5.6). It was essential to move slowly and wash our hands before touching the films. The following improvements have been made from the KamLAND-Zen 400 inner-balloon fabrication to prevent dust from humans.

- We changed clothes in the cleanroom 2 from clean suits for class ∼100 to new suits with higher air-tightness. All clean suits used once were washed each time. A clean inner-wear is also adopted.
- Goggles are newly worn to cover the face, and a ventilation hole was on the top for comfort.
- What touches the films most were gloves. Two folded gloves were worn to reduce dust coming from the gap between gloves and clean suits. U and Th contamination in the gloves was measured by ICP-MASS to be 3.5×10^{-9} g/g and 3.3×10^{-9} g/g respectively. The residual gloves in the order of 1 g could be a severe source of background. The hands(gloves) were always washed with ultra-pure water before touching the film.
- Two types of clothes were used in the cleanrooms, SFIDA and Double-cloth. The contamination of these clothes were 2.1×10^{-10} g/g U and 2.4×10^{-10} g/g Th, and 4.6×10^{-10} g/g U and 8.8×10^{-10} g/g Th. The residual clothes in the order of 10 g could be a background source.

Figure 5.6: Dust visualization
The figure shows dust visualization by a laser. The dust was generated by clapping hands. Much dust comes from the gap between the gloves and the sleeve of the clean suit.

5.2.3 Inner-Balloon Components

Inner-balloon was fabricated by cutting a nylon-6 roll with a thickness of 25 μm, a width of 1.1 m. The main body is made of 24 gore, 6 cones, a straight tube, and 12 belt parts for supporting inner-balloon in the LS (See Fig. 5.7). The belt part and the body are not connected, and 12 belts are connected to one ring at the polar part. The belt is connected to the Vectran string from the middle.

The inner-balloon is made by cutting the washed film into this part and connecting them by welding. The inner-balloon after the welding has many pin-holes. They are repaired with patch or welding.

5.2.4 Washing/Cutting

The film was ultrasonically cleaned with ultra-pure water in a stainless bathtub, as shown in Fig. 5.8. All the films were cleaned twice. Dirt spot and scratch are searched for by eyes (See Fig. 5.9). The cleaned films were sandwiched with cover films that were also washed, as shown in Fig. 5.12 in order to suppress the adhesion of dust during the following works. The outlines of Teflon patterns were drawn with a blue pen, and the cover films were marked in the shape of the parts (Fig. 5.10). All three layers were cut out into the inner-balloon parts (Fig. 5.11).

5.2.5 Welding

The KamLAND-Zen 400 inner-balloon was welded by company engineers with a hand welding machine. See left side of Fig. 5.13. Semi-automatic welding machines were

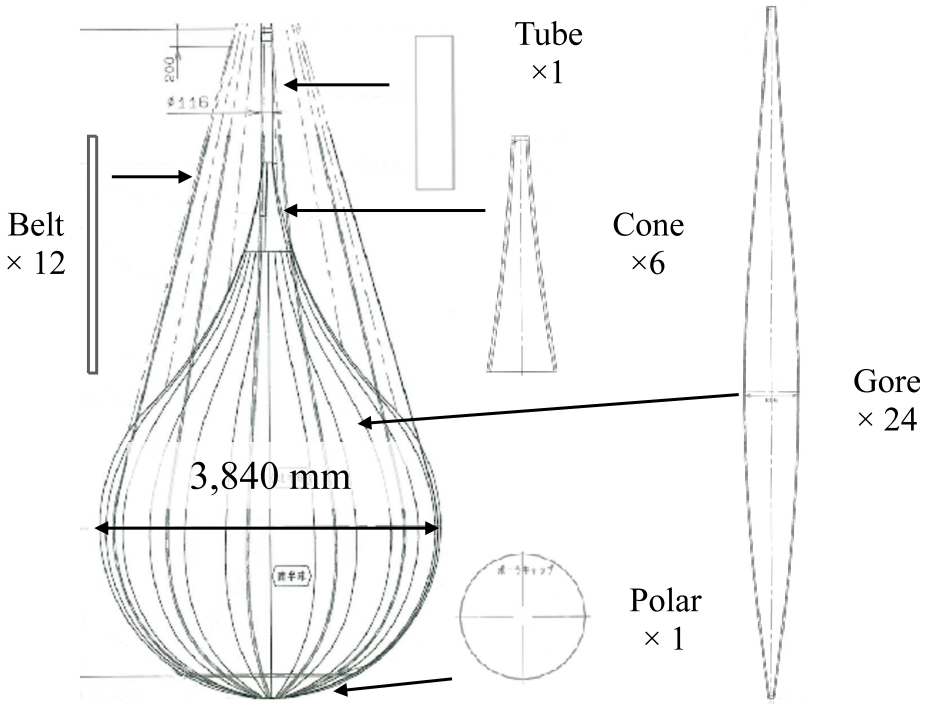

Figure 5.7: Inner-balloon parts
The inner-balloon was composed of a tube, 6 cone parts, 24 gore parts, a polar cap, and 12 belts. The inner-balloon was fabricated by welding these parts.

Figure 5.8: Washing

Figure 5.9: Visual inspection

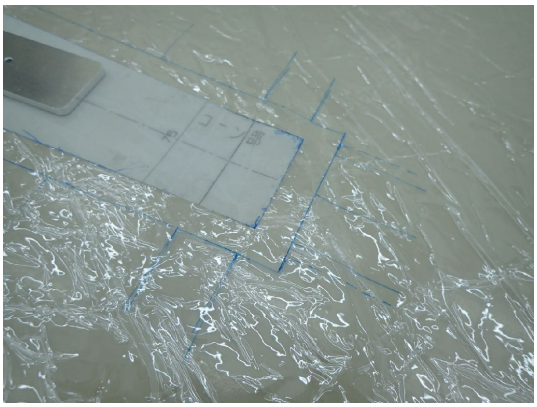

Figure 5.10: Marking

Figure 5.11: Cutting

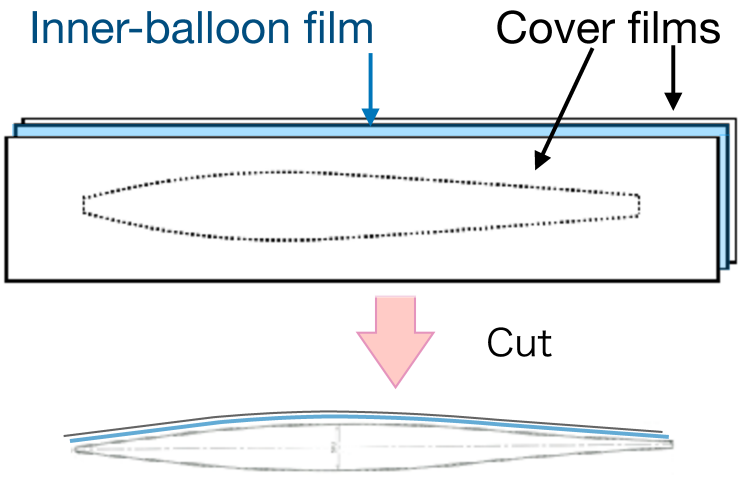

Figure 5.12: Cover film
The main body films were sandwiched with 2 cover films.

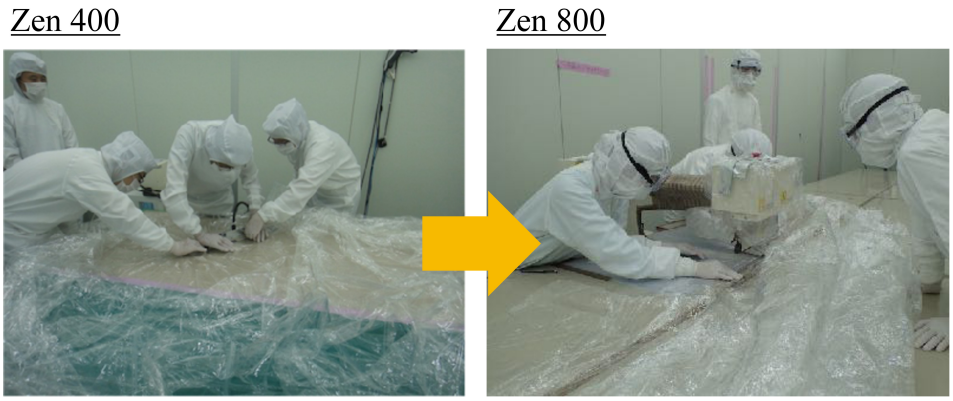

Figure 5.13: Welding methods
The figure shows the hand welding by the company person in KamLAND-Zen 400 inner-balloon production and the semi-automatic welding by scientists in KamLAND-Zen 800 inner-balloon production. Dust drop from humans was suppressed. The work speed was improved because everyone can weld, not only a professional person.

introduced to prevent dust from people and to improve work efficiency. See the right side of Fig. 5.13. The cover films were temporarily removed only when the main film was welded. The welding parameters were 225 °C temperature, 3.5 sec heating time, and 0.4 MPa pressure. The size of the welded line was 310-mm×5-mm (See Fig. 5.15). The welding parameter search was performed in advance because the number of pin-holes and the strength of the welded line changed depending on the parameters. The quality of the welded lines of the inner-balloon was guaranteed during balloon welding for a month by monitoring regularly. As for the complexed parts such as the dense area around the cone and polar, a hand welding machine or a special welding machine for complex parts, of which welding size is 50-mm×5-mm or 100-mm×5-mm, were used (See Fig. 5.14). It also was used for re-welding and reinforcement after closing. The last closing line was welded by a company engineer with a hand welding machine, but the monitor revealed that the strength against peel was not enough. It was reinforced by Krazy Glue and welding with the special welding machine.

The weakest part is the welded line. The strength required for the welded line is more than 10 N/cm, including a safety factor 10. The strength of the welded line was confirmed by a tensile test using a force gauge, and the force gauge system and one sample of the results are described in Fig. 5.16 and Fig. 5.17.

In order to examine the strength and stability of welding, parameters such as temperature, pressure and heating time in welding were searched. The welding machine used for the failed Zen 800 inner-balloon heat from the bottom and apply

Figure 5.14: The figure shows the welding machine used to weld complex area. The length of the heating part is shorter than the other machine.

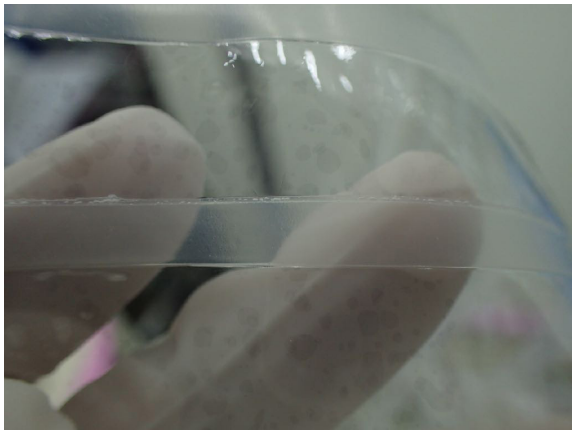

Figure 5.15: Welding line is shown in the middle. The width of the line is ∼5 mm.

Figure 5.16: Force gauge measurement system

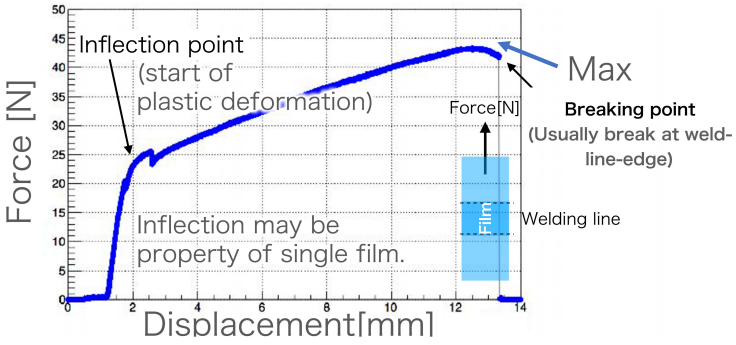

Figure 5.17: Tensile strength of the film
The horizontal axis represents the length displacement of the sample film, which has a 1 cm width. The vertical axis corresponds to the force measured with the force gauge system shown in Fig. 5.16.

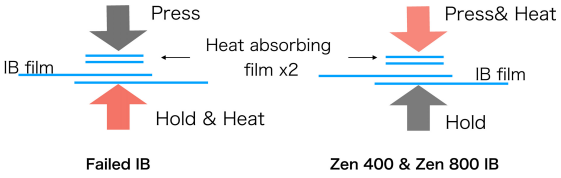

Figure 5.18: Heat methods
The failed inner-balloon was heated from below and applied pressure from above. The KamLAND-Zen 400 and the new inner-balloon was heated from above and also applied pressure from above.

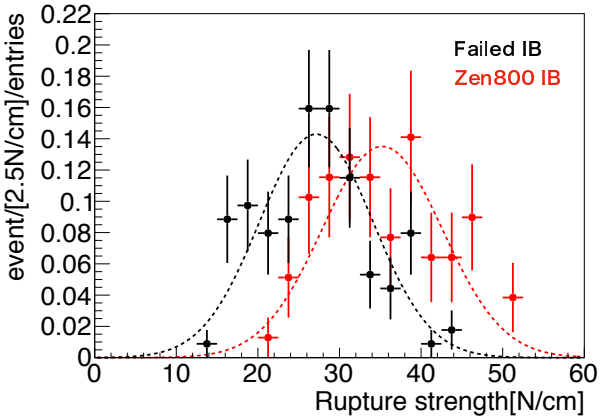

Figure 5.19: Strength of the welded part
The strength of the welded part was measured by force gauge. The strength of the new inner-balloon was enough higher than requirements >10 N/cm.

pressure from the top, so the heat absorption film could not relax the heat well, and the strength of the welded part might be not enough (See Fig. 5.18). Improving the welding method and adjusting the parameters provide a robust way for welding. The strength was improved from 27 N/cm(mean) of the failed inner-balloon to 35 N/cm (mean), as shown in Fig. 5.19.

5.2.6 Leak Check and Repairing

The weld could create holes due to the boiling of water inside the nylon or overheating. Leak point search was done by putting He gas inside the inner-balloon and detecting it from the outside to identify a leak point (See Fig. 5.20 and Fig. 5.21). Small leaks can not be detected with nearby large leaks, so large leaks on the welded lines were searched for and repaired at first. Then, small leaks were explored and repaired. Finally, we peeled off the cover films and searched for leaks all over the films and repaired them. There were two patterns in the leak shown in Fig. 5.22, z-leak is a vertical hole on the weld line, y-leak is a lateral hole between two films. They were repaired with Krazy Glue and patch films. The U and Th contamination of the Krazy Glue is $<5\times10^{-12}$ g/g and $<5\times10^{-12}$ g/g, respectively. The total amount of used Krazy Glue was about the order of 1 g.

Teflon sheets with Double-cloth are put inside the inner-balloon. It was used as a pad because it is clean and does not adhere. Another Teflon sheet and rubber were used on the top, and it was pressed by a person (See Fig. 5.22).

Over about half a year, more than 900 leaks were repaired, and some miss-welded areas, where the welded line was off the heat-absorbing sheet, were repaired by re-welding with the new patch films for heat absorption.

Figure 5.20: Leak hunting
The probe is held by the right hand, and the small monitor is winded around the left wrist.

Figure 5.21: He leak detector
There exists the red He leak detector. The leak value is taken with the camera and sent to the monitor shown in Fig. 5.20.

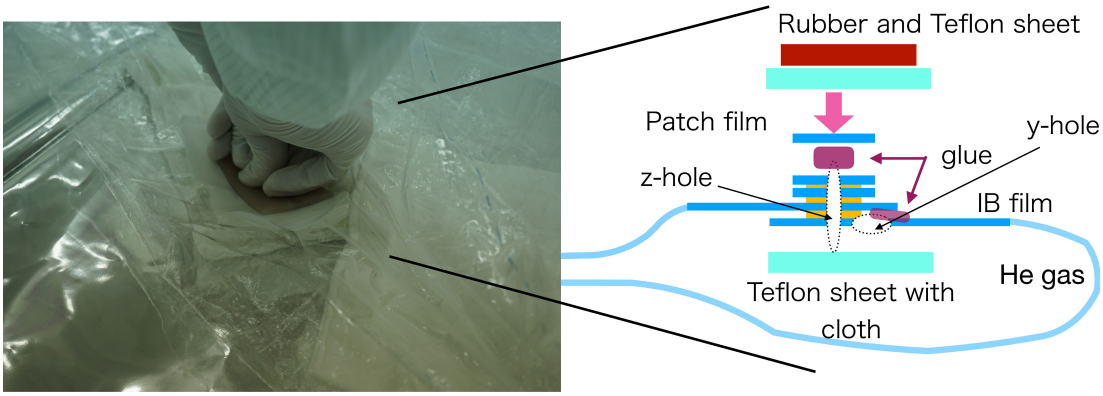

Figure 5.22: Leak repairing
The figure shows the sketch of the leak repairing. The pressure is applied from the upper of the rubber by a human.

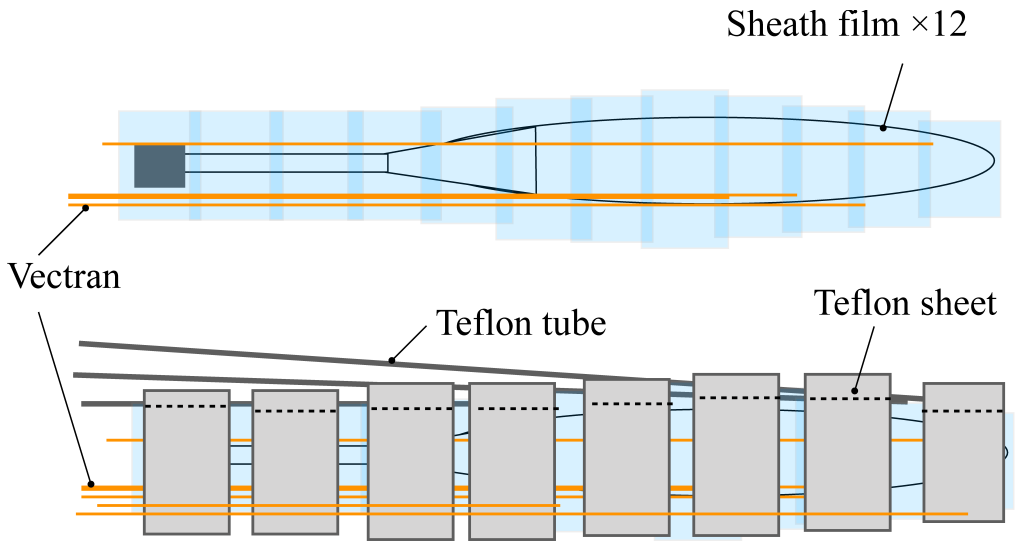

Figure 5.23: Inner-balloon folding
The folded inner-balloon was covered with 12 sheath films, and with 9 Teflon sheets over it. The Teflon sheets have holes, and Teflon tubes are through the holes not to inflate the inner-balloon. There were 3 Teflon tubes, one is for the top 4 sheets, one is for the middle 4 sheets, and the last one is for the most bottom sheet. Two Vectran strings are tied for collecting the Teflon sheets and twelve for collecting the sheath films.

5.2.7 Shipping

The inner-balloon was folded like an umbrella at the non-welded part and covered with 12 sheath films to prevent contamination during the installation(See Fig. 5.23). Furthermore, it was wrapped with Teflon sheets so that it can pass through the 50 cm hole at the top of the KamLAND detector. The sheath films and the Teflon sheets are tied with Vectran string to pull out them after the installation. It was sealed in a gas bag film and a delivery box with super-cleanroom air (class 1 and 65% humidity), and sent to the clean booth in the Kamioka mine. All tools for installation were cleaned and delivered with airtight bags.

5.2.8 Corrugated Tube Connection

In the clean booth on the top of KamLAND, the corrugated tubes were connected to the inner-balloon. The corrugated tube was selected to be strong and flexible in addition to low contamination because limited space was available in the clean booth. The corrugated tubes were cleaned by ultrasonic cleaning with ultra-pure water, and wiped with ethanol in the class 1 cleanroom same as other stuff. Three 2 m corrugated pipes were connected. PEEK connection pipes were used for the connection between a corrugated tube to a corrugated tube and a corrugated tube to the inner-balloon (See Fig. 5.25). The rubber O-ring was inserted between the corrugation and the

Figure 5.24: Inner-balloon delivery
The inner-balloon is tied to the box with the silver gas bag films. The inside of the box is sealed with the gas bag films.

PEEK connection pipe to prevent leakage of Xe gas. The gap between the PEEK connection pipe and a corrugated tube was filled with mixed sealants(Ad-coat).

5.3 Inner-Balloon Installation

The inner-balloon was inserted from the 50 cm hole on the top of the detector, as shown in Fig. 5.26. While the inner-balloon was installed with +0.4% heavier liquid scintillator than the KamLAND liquid scintillator, the Teflon sheets and the sheath films were peeled off in the outer-balloon of the KamLAND detector and pulled up with the Vectran strings. The installation was monitored with two fixed cameras and an endoscope camera (Fig. 5.27).

Monitor Camera

Two fixed monitor cameras, two endoscope cameras, and two LED lights were also cleaned in the class 1 cleanroom. The fixed monitor cameras and LEDs were installed from holes that 5-inch PMTs used at 0.5-m-ϕ before the inner-balloon installation. They were kept until March 2019 to monitor the condition of the inner-balloon during the distillation and Xe dissolving.

LS Transfer Tubes

Two 1/4-inch Teflon tubes were used for feeding and draining. At first, the LS transfer tube without inlet was installed with the inner-balloon. The outlet was at

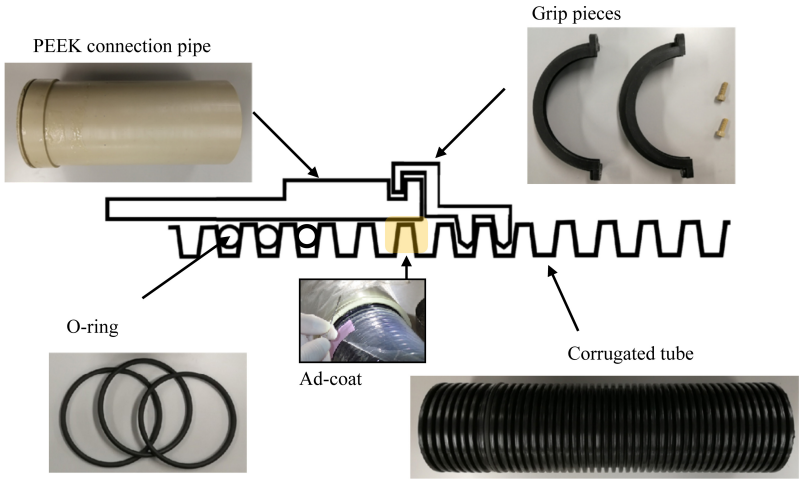

Figure 5.25: The figure shows the connection part of the corrugated tubes.

Figure 5.26: IB installation
The inner-balloon is inserted from the ∼50 cm hole at the top of the KamLAND detector.

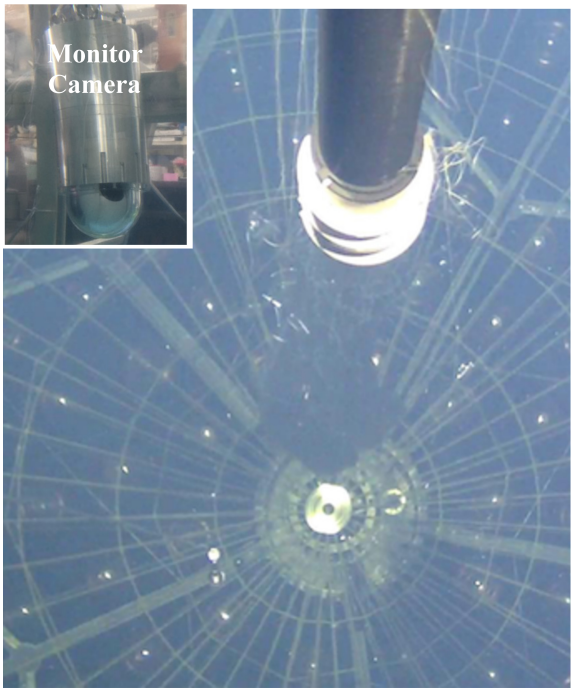

Figure 5.27: Camera view
The figure is the camera view in the inside of KamLAND. The inner-balloon just after installation is shown. The left upper figure shows the camera.

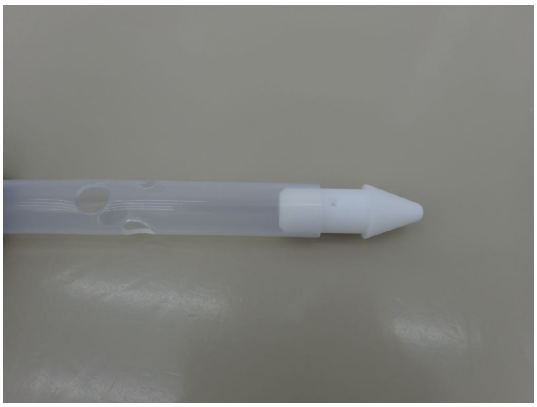

Figure 5.28: The figure shows the LS transfer tube at the IB cone (neck).

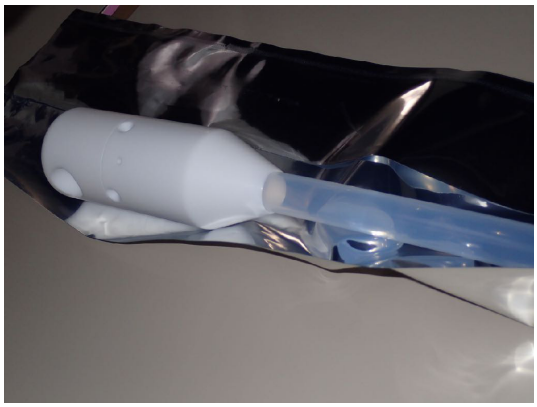

Figure 5.29: The figure shows the LS transfer tube at the IB bottom

the position of the PEEK connection pipe to the inner-balloon. After completely inflating the inner-balloon with liquid scintillator, the 2nd LS transfer tube with an inlet was installed at the bottom, and the 1st one was extended to the inner-balloon neck position. The 1st one was used for draining, and the 2nd one was for feeding during the distillation and Xe dissolving.

Dummy-LS Filling

The liquid scintillator with ∼0.5 g/L PPO without Xe started to be filled just after the installation. During the LS filling, we stopped data taking and inflated it with the image of the camera and the load cell. The inner-balloon fully inflated with 30.5 m^3 of dummy-LS (design value is 31.5 m^3) in 10 days. 30.5 m^3 of the dummy-LS is equivalent to a 190.1 cm inner-balloon radius, although it was 192.0 cm in design. Fig 5.30 shows the inner-balloon after the dummy-LS filling.

5.4 Dummy-LS Distillation

The data of ^{208}Tl (>3 MeV single event), ^{212}Bi-^{212}Po pileup and ^{212}Bi-^{212}Po delayed coincidence suggest that there is $\sim 10^{15}$ g/g ^{232}Th which is larger than our expectation. We decided to purify the LS by distillation before Xe dissolving. The dummy-LS was circulated between the distillation system and the inner-balloon (Fig. 5.31). The distilled dummy-LS was filled from the bottom and made a layer by controlling temperature and density within 0.1% not to damage the inner-balloon film by its weight. The DAQ was working in the distillation. The inner-balloon was monitored continuously with loadcell values and data, and the cameras were used for weekly confirmation. Since the distilled liquid contains ^{222}Rn due to emanation from tanks and pipelines, we could monitor the layers of dummy-LS with ^{214}Bi-^{214}Po delayed coincidence (Fig. 5.33). The 1st distillation campaign was performed from June to August 2018. 119.3 m^3 dummy-LS was circulated. The ^{232}Th amount was not reduced as expected by the 1st distillation. Since PPO tower was considered as the ^{232}Th source,

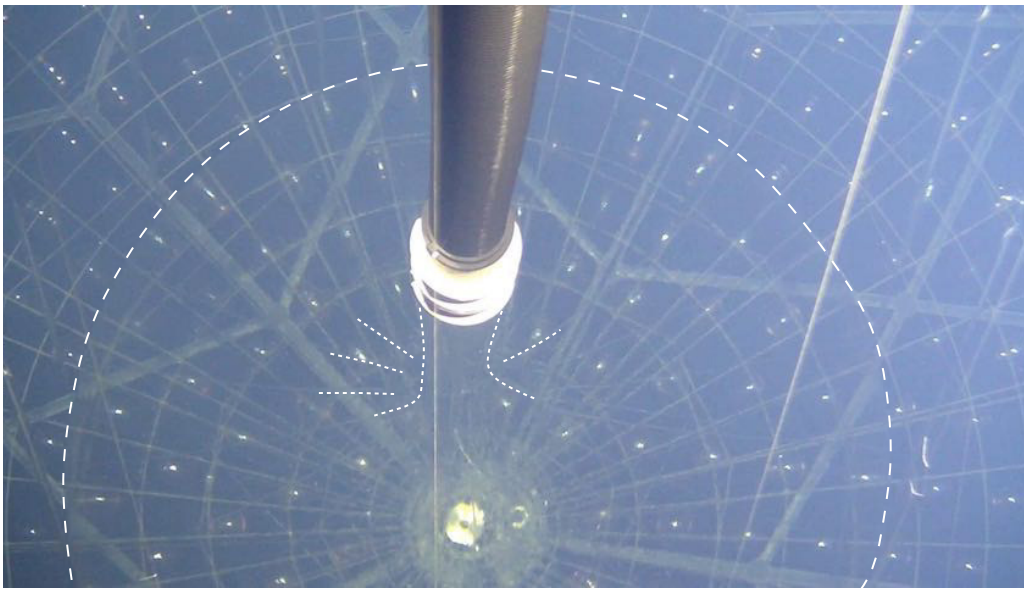

Figure 5.30: Detector inside view after IB installation and dummy LS filling
The dotted line indicates the surface of the balloon. The welding line can be seen.

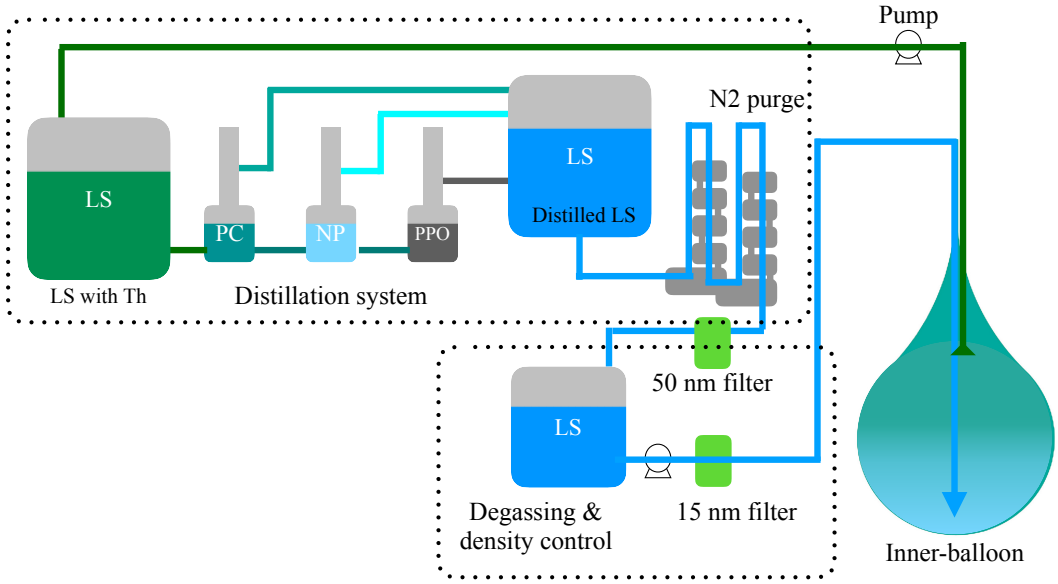

Figure 5.31: LS distillation circulation
The rough schematic of the pipelines during LS distillation circulation is shown.

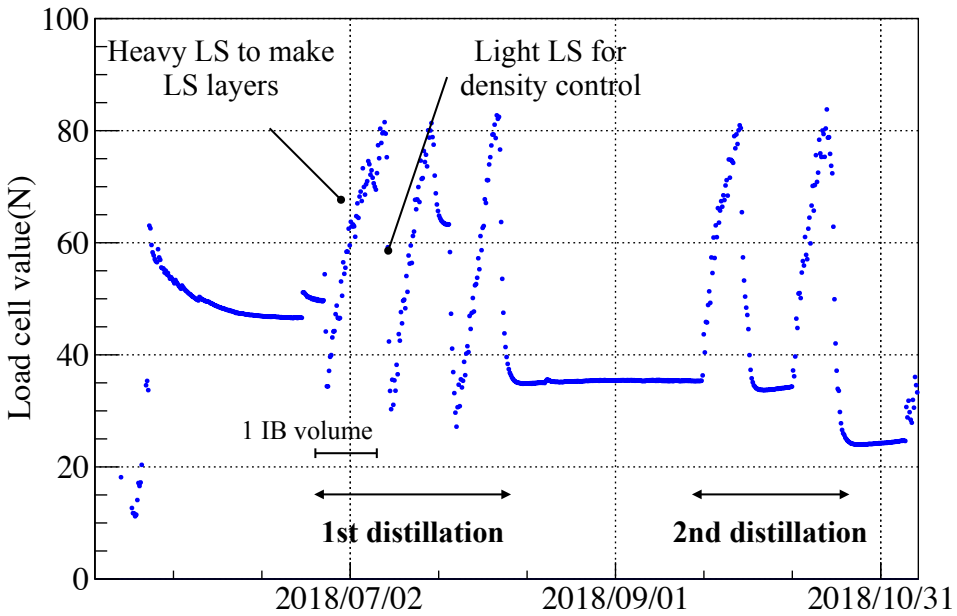

Figure 5.32: Load cell value in LS distillations
The increase in the total load-cell value at first represents dummy-LS filling to the inner-balloon. The increases in the total load-cell value after June were made by heavy LS filling during LS circulation to make LS layers. The value was decreased by filling light LS to adjust the LS density.

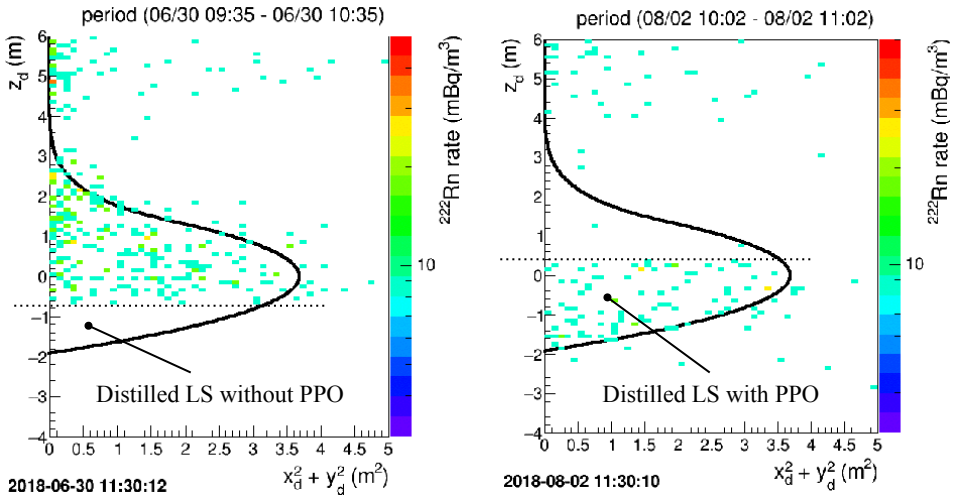

Figure 5.33: ^{222}Rn monitor during LS distillation
The left figure shows ^{222}Rn distribution in the 1st cycle of the 1st distillation campaign. We can see the boundary in the middle of the inner-balloon because distilled LS did not emit scintillation light. The right figure is the last cycle of the first distillation campaign. The dummy-LS with $\sim$ 0.5 g/L PPO was filled from the bottom.

PPO tower and distillation tower were washed with PC, and the impurity concentration was checked by ICP-MS and neutron-activation analysis. The 50-nm-filter before the density control tank in the Xe system tank was also replaced. The results of ICP-MS were ^{238}U: 0.3×10^{-10}g/g and ^{232}Th: 1.6×10^{-10}g/g for PPO before distillation and ^{238}U: $<0.1\times10^{-10}$g/g and ^{232}Th: $<0.1\times10^{-10}$g/g for PPO after distillation, which are the lower detection limit. 30.5 m^3 dummy-LS contains $\sim2.4\times10^{-8}$ g of Th estimated by the ^{212}Bi-^{212}Po delayed coincidence measurement and $\sim$15000 g of PPO, which includes $<1.5\times10^{-7}$ g of ^{232}Th by the ICP-MS measurements. Although the ^{232}Th removal efficiency in the PPO distillation is believed to be better than $\sim$1/100, if worse, the PPO could be the cause of contamination. It was thought that the raw PPO was mixed due to bumping in the PPO tower as the possible cause. The 2nd distillation campaign was from September to November 2018, and 55 m^3 dummy-LS was circulated. Dummy-LS with high PPO concentration $\sim$4 g/L was supplied at the last circulation for Xe dissolving. The 15-nm-filtering circulation by $\sim$141 m^3 was performed to remove contaminated particles in the dummy-LS.

5.5 Xe Dissolving

5.5.1 Xe System

The dissolving of Xe was carried out for about two months from November 2018. In the initial state, there were the dummy-LS with high PPO concentration ∼4 g/L in the inner-balloon. Since the liquid scintillator becomes heavier after dissolving Xe gas, it is necessary to reduce the weight of the dummy-LS with decane and match the density with the KamLAND LS. The density was controlled with the accuracy of the third digit in a density meter and temperature. The 12 load cell values were monitored to prevent inner-balloon from being tensed. Fig. 5.34 shows the Xe system. It is composed of followings.

- **sub-tank**
  A 1.1 m^3 tank for LS. It was used to dissolve Xe gas into LS and send the Xe-LS to the inner-balloon.
- **main-tank**
  Another 1.1 m^3 tank to store the extracted dummy-LS. It was used for degassing the LS.
- **control tank**
  A 0.2 m^3 tank to control the LS density. It stores pure decane or PC. They were refilled from the larger storage tanks at the 2nd purification area. The liquid was fed into the main-tank or the sub-tank by the pressure difference. Nitrogen gas was used to control the pressure of the tank.
- **reservoir tank**
  A 1.1 m^3 tank to store vacuumed Xe and nitrogen gas temporally.
- **25 m^3 tanks**
  There are two 25 m^3 tanks at the entrance of the KamLAND site. Degassed dummy-LS and nitrogen gas were stored in this tank.
- **LS trap**
  A device to remove the evaporated LS contained in vacuumed gas. The temperature was controlled with LN_2 from $\sim -40°C$ to $\sim -50°C$ and solidify the LS.

5.5.2 Xe Dissolving

The replacement from the dummy-LS to the Xe-LS was performed step-by-step.

- **Batch mode**

  I. Xe gas was dissolved to the dummy-LS in the sub-tank. The Xe-LS density was adjusted by adding decane from control tank.

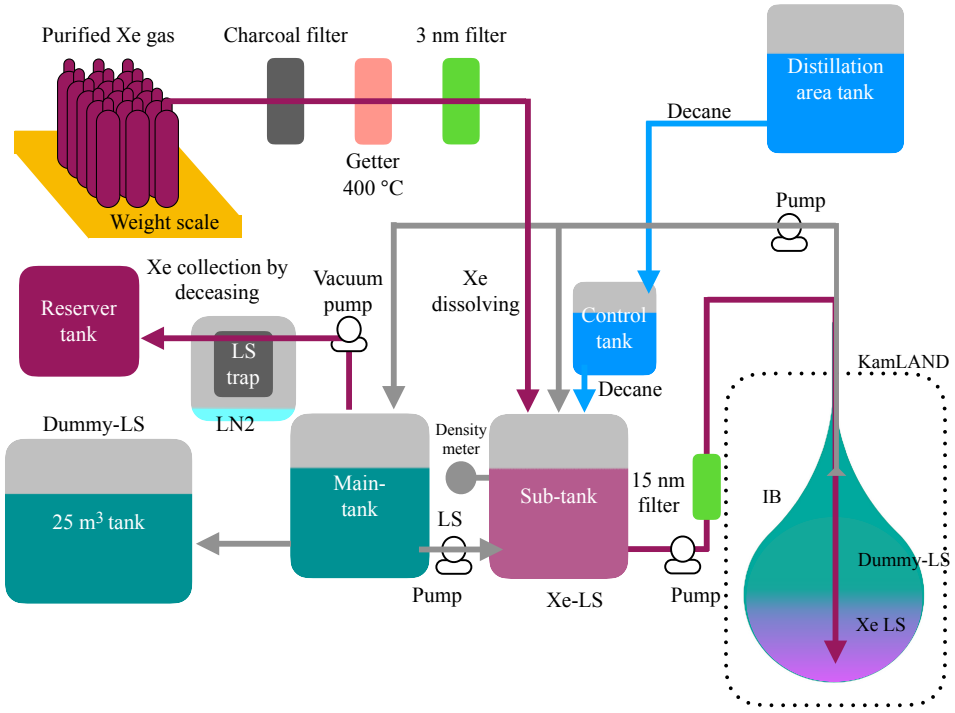

Figure 5.34: Xe system

A schematic drawing of the pipelines in the Xe system is shown. The purple lines are for Xe gas and the Xe-LS. The light blue lines are for Decane. The grey lines are for dummy-LS.

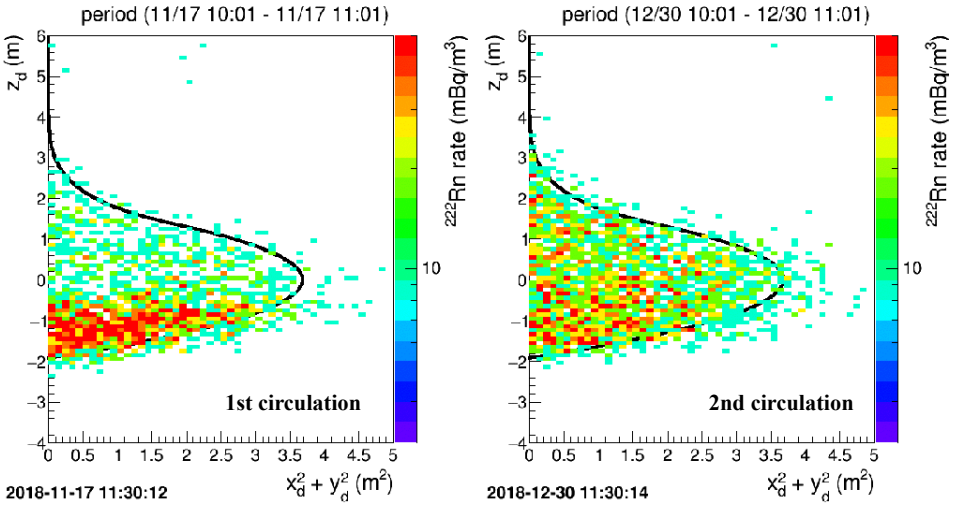

Figure 5.35: ^{222}Rn monitor during Xe-LS filling
The left figure shows the ^{222}Rn events during the Xe-LS filling. The event positions of ^{214}Bi-^{214}Po delayed coincidence are filled to the 2D histogram. Since the Xe-LS contains much ^{222}Rn by the emanation from tanks and pipelines, the Xe-LS layer was seen at the first circulation (left figure). The ^{222}Rn spread throughout and decreased by its decay lifetime as the Xe-LS went up during 2nd circulation(right figure).

II. The Xe-LS was filled to the inner-balloon bottom, while the dummy-LS was extracted from the inner-balloon neck to the main-tank. The Xe-LS density is adjusted to be a little heavier than the dummy-LS to avoid mixing the dummy-LS and the Xe-LS. The layers of the Xe-LS and the dummy-LS is checked with the ^{222}Rn monitor (See Fig. 5.35).

III. Extracted dummy-LS contains Xe gas. The Xe gas was collected by vacuuming the main tank and sent to the reservoir tank. Degassed dummy-LS as much as the added decane amount was sent to the 25 m^3 tank, and others were sent to the sub-tank. This batch mode was repeated 12 times, and $\sim$ 8 m^3 Xe-LS was installed.

- **Circulation mode**
  When returning Xe gas increased, the batch mode was switched to the circulation mode to reduce Xe gas sent to the reservoir tank and to increase speed. Decane and Xe gas were added to the sub-tank while circulating. The Xe-LS density was monitored with load-cells and a density meter and controlled with the amount of adding decane and dissolving Xe gas. The Supplying and draining Xe-LS amount was controlled based on flow meter and KamLAND LS level. Extracted dummy-LS was sent to the sub-tank directly. After Sub-tank became

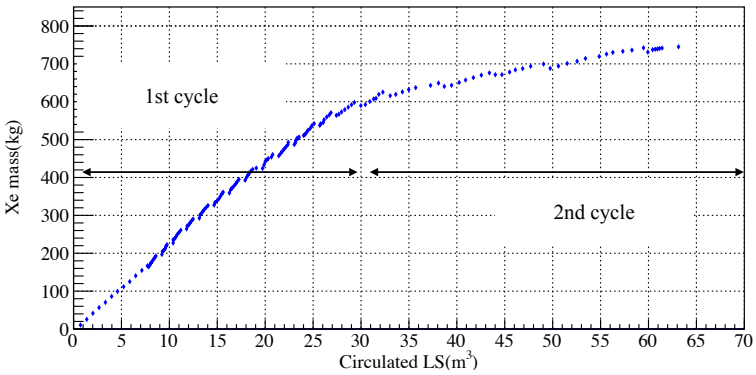

Figure 5.36: Xe mass vs circulated LS volume
The horizontal axis represents the circulated Xe-LS, and the vertical axis shows the Xe mass in the inner-balloon. The decreases in the Xe mass are superficial by degassing the main tank. The increasing rate was low in the 2nd circulation because Xe gas came back with the extracted LS.

full, dummy-LS was collected to the main-tank and sent to the 25 m^3 tank after degassing the main-tank. Because the inner-balloon subduction was observed with the camera view, the density of the filling Xe-LS was adjusted so that the load cell values were slowly reduced in the 2nd circulation.

- **Re-use of Xe gas in the reservoir tank**
  The Xe gas collected in the reserver tank contains nitrogen gas used to the control tank pressurization. It is once solidified in a 10 L bottle with liquid nitrogen, then reused through charcoal filter, N_2 getter, and 3-nm filter.

5.5.3 Xe in Xe-LS and Detector Condition

Xe in Xe-LS

The remaining Xe in the Xe system was collected by the LS-trap and a Xe-trap. Xe amount in the inner-balloon was checked by subtracting the remaining Xe. They are:

I. distilled Xe (total Xe amount): 769±1 kg

II. Xe remained in LS in the sub-tank and pipelines: 16.0±2.0 kg

III. Xe in the drained LS to the 25 m^3 tank (∼15 m^3, 0.05 wt%): 5.5±2.0 kg

IV. Xe in the storage bottles: 1±1 kg

V. Xe trapped by Charcoal filters and lost by sampling: 1.5±0.5 kg

VI. Xe in the inner-balloon(I−(II+III+IV+V)): 745±3 kg

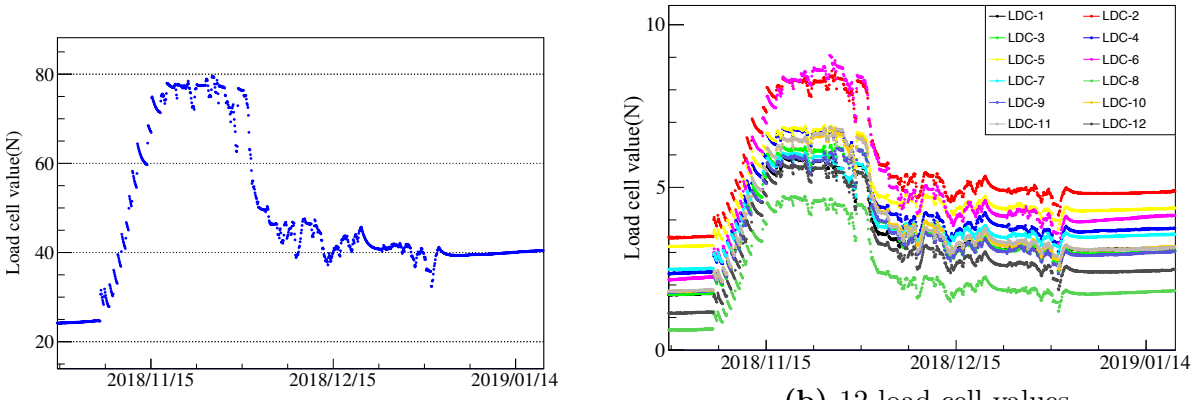

(a) Total load cell value

(b) 12 load cell values

Figure 5.37: Load-cell value during dissolving Xe
The total load-cell value(left) and each 12 load-cell value(right) are shown. The increase from 2018/11/06 to ∼2018/11/20 is made by the heavy Xe-LS filling to make the Xe-LS layer.

Xe-LS Volume

The dummy-LS volume was 30.5±0.3 m^3, which was the measured value of the filled LS with a flowmeter. The LS volume in the inner-balloon was controlled with an LS-level monitor during distillation and Xe dissolving. Fig. 5.38 shows the trend of the LS level after the inner-balloon installation. The LS level was kept constant during the circulations except for the LS filling to the KamLAND LS by an accident. It may have fluctuated due to other factors during the periods, so it may be supplying LS up to 10 mm more or less at maximum to guess from other periods (See Fig. 5.38). 1 mm LS level corresponds to about 13 L LS volume. Hence, the unexpected deviation of the Xe-LS volume during the LS circulations is less than $\sim$ 0.13 m^3.

Limits on Xe Leak

It was checked if there are any leaks of Xe-LS by followings:

- camera view
  The shrinkage of the inner-balloon was checked with the camera view.
- lead-cell value
  The decrease in the load-cell value implies the Xe-LS leak. The load-cell value was stable.
- $2\nu\beta\beta$ decay rate
  The stability of the $2\nu\beta\beta$ decay rate in the Xe-LS was analyzed.
- Xe measurements in the outer KamLAND LS by GC
  The Xe content in the KamLAND LS means the Xe-LS leak.

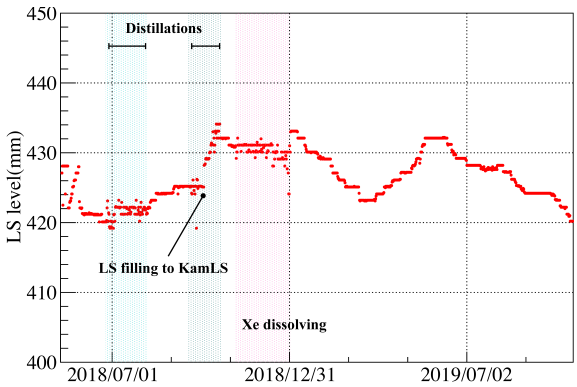

Figure 5.38: LS level in KamLAND-Zen 800
The blue shaded periods are in the distillation campaigns and the pink shaded period is in the Xe dissolving.

Table 5.1: Xe-LS contamination
KamLAND-Zen 400 Phase-I and Phase-II refer [64] and [61]

Phase	^{238}U (10^{-17}g/g)	^{232}Th (10^{-17}g/g)
Zen 400 Phase-I	13 ± 2	190 ± 20
Distiled	5.8 ± 0.3	140 ± 20
Zen 400 Phase-II	17 ± 1	5.5 ± 0.3
Zen 800 Dummy-LS	450	110 ± 20
Zen 800 Xe-LS	1.5 ± 0.4	30 ± 4

The most accurate method is to measure the Xe concentration in the outer LS. The outer LS was sampled from top of the detector and degassed with Nitrogen bubbling. The Xe in the degassed gas was concentrated by a cold trap with LN_2 and measured by gas chromatography. Assuming uniform distribution in the outer LS, an upper limit of <0.068 Xe-LS m^3 (5σ) was obtained for the leak of the Xe-LS [65]. The next accurate method is to check $2\nu\beta\beta$ decay rate, giving an upper limit of <1.1 Xe-LS m^3 in ∼220 days (3σ).

U and Th in Xe-LS

As a result of distillation purification, the ^{212}Bi-^{212}Po pileup background stemming from the amount of ^{232}Th in the Xe-LS became less than the solar neutrino background, which was confirmed by delayed coincidence measurement of ^{212}Bi and ^{212}Po. The amount of ^{238}U was also estimated with ^{214}Bi and ^{214}Po delayed coincidence measurements. Fig. 5.39 shows the ^{212}Bi-^{212}Po and ^{214}Bi-^{214}Po delayed coincidence event rates in the distillation and Xe dissolving periods. Table 5.1 summarizes ^{238}U and ^{232}Th in LS for each period.

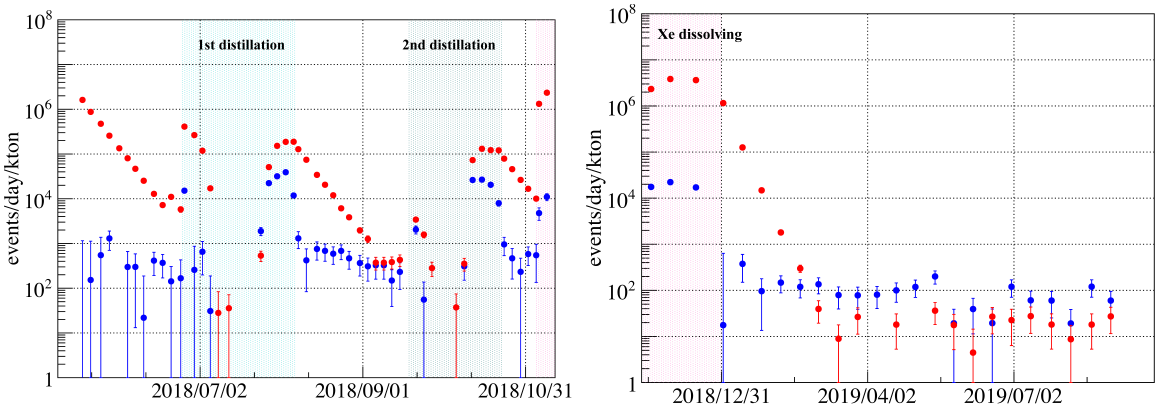

Figure 5.39: ^{212}Bi-^{212}Po and ^{214}Bi-^{214}Po event rates in the inner-balloon LS
The red points represent ^{214}Bi-^{214}Po event from ^{222}Rn decay series, and the blue points represent ^{212}Bi-^{212}Po event from ^{220}Rn decay series.

Chapter 6

Analysis Framework/Event Selections

The flow of the data, procedures of the analysis, and event selections for $0\nu\beta\beta$ decay candidates are described in this chapter.

6.1 Analysis Framework

6.1.1 Data Flow

Fig. 6.1 shows the data flow. PMT signals are digitized in KamFEE or MoGURA and stored as Kinoko Data Format (KDF). The KDF has trigger information and PMT digitized waveforms by TimeStamp. The run condition is also stored in the header. EventBuilder combines the waveforms by event and stores as a serial file(SF). The waveforms are translated to hit time and its charge (TQ) information by a waveform analyzer. The RTQ file has the Raw-TQ information in each PMT. Event vertex and visible energy are derived from the RTQ file via vertex fitters and energy estimators. Also, muon fitter and some other unphysical event selections, such as a flasher veto and a double pulse fit, are applied to the RTQ file. The general vector file (GVF) is usually used to analyze physical events. The GVF file has the following information:

- **run number** run is a unit of the data. A run has usually ∼24 hr data.
- **event number** event number is assigned from 0 at the beginning of the run.
- **TimeStamp** TimeStamp is based on its DAQ clock time, which is 25 nsec for KamFEE and 20 nsec for MoGURA DAQ.
- **unixtime** unixtime is the number of seconds from January 1st in 1970 and used for a veto over a run.
- **trigger type** trigger type records which trigger was issued.

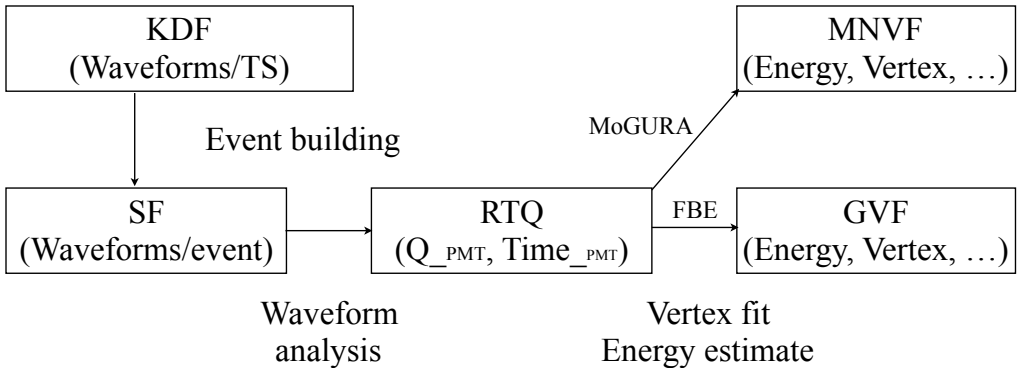

Figure 6.1: The figure shows data flow from raw waveforms to the analysis parameters, such as energy, vertex, total hit PMT number, etc.

- **event vertex (x, y, z, r) and badness** event vertices x, y, z, and a radius from the detector center are stored. The quality of the vertex fit is parameterized as "badness".
- **energy/energy17** visible energies estimated by each energy fitter or estimator are stored. The energy with characters "17" uses only 17-inch PMTs.
- **TotalChargeID/17/OD** they are a sum of the ID PMT or 17-inch PMT, OD PMT charges.
- **numhit/numhit17,NsumMax and N200OD** numhit/numhit17 are the number of hit ID PMTs (17-inch PMTs) in each event. NsumMax is a maximum number of hit PMTs in a TimeStamp within each event. N200OD is a maximum number of hit PMTs in the OD within 200 nsec sequential windows.
- **muon entrance and direction** results of the muon fitter are stored, such as an entrance point and a direction vector.

In the case of the MoGURA, events are associated with muon events acquired with the KamFEE DAQ and stored in a Muon-Neutron Vector File (MNVF) to search for neutron capture events after muons.

6.2 Event Reconstruction

6.2.1 Waveform Analysis

The digitized waveform has 128 samplings. The time width is ∼1.5 nsec, so the time width of one waveform is ∼200 nsec. The time widths of each channel are calibrated run by run using the 25 nsec clock (See Fig. 6.2(b)). The procedure

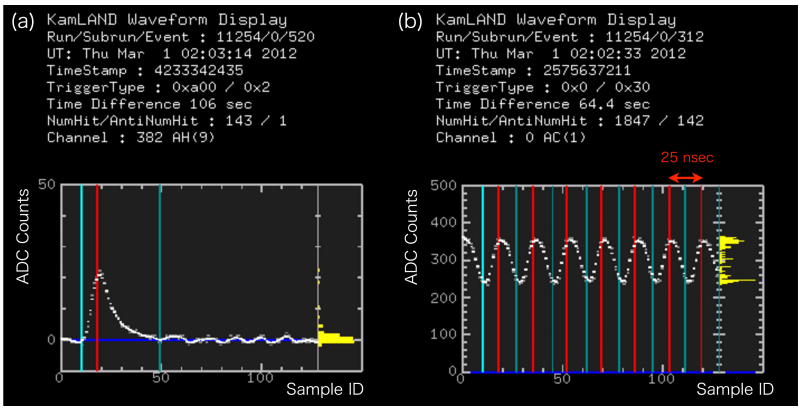

Figure 6.2: Waveform analysis
The figure is from [64]. (a) White dots are ADC counts of data after the baseline subtraction. The left cyan line is a leading-edge, the center red line is a peak position, and the right dark cyan line is a trailing-edge. (b) Clock calibration data is shown. The time interval corresponds to 25 nsec.

for the translation form the waveform to the charge and hit-time by the waveform analysis is the following.

- **Smoothing** The waveform is smoothed using its running-averaged first derivatives.
- **Baseline adjustment** The baseline of each PMT is collected with a forced trigger at the beginning of every run. The waveforms with noise or signals are rejected from the baseline. The baseline is subtracted from the waveform.
- **Searching peaks** Peaks are searched with running-averaged 1st, 2nd, and 3rd derivatives.
- **Searching leading-edge and trailing-edge** A leading-edge is searched from the time, 10 counts ahead of the peak. The leading-edge becomes the hit time (See Fig. 6.2(a)). The trailing-edge is the time when the waveform go back to the baseline.
- **Calculating waveform sum** A charge is a waveform sum from a leading-edge to a trailing-edge.

The waveform analysis allows multiple hits in one PMT. Usually, this is combined into the single hit information, which is the total charge of the multiple hits and the earliest hit time, used in vertex fitter and energy fit. The multiple-hit information is also used in a double-pulse fit and a shower tag, which are described later section.

6.2.2 PMT Corrections

Gain Correction

The PMT gains are corrected run by run with one photoelectron (1 p.e.) charge value. The gains of 17-inch PMTs and 20-inch PMTs are corrected by different methods because 20-inch PMTs do not have a charge resolution of the 1p.e peak.

17-inch PMT Gain Correction

A PMT gain is determined by fitting the 1 p.e. charge distribution of the events with a Gaussian function. The low energy events far from the target PMT are selected to reduce multi-photon events. The event selection criteria are the following.

- run time $\geq \sim$10 hr
- muon event and 2 msec after muon event veto
- 100 μsec veto after all events
- noise event veto
  The definition of noise event is

$$Nhit_{\mathrm{ID}} - N_{100} \geq N_{100} - 50, \tag{6.1}$$

  where $Nhit_{\mathrm{ID}}$ is the number of total hits in the ID and N_{100} is the number of total hit PMTs in the 100-nsec time window, which is optimized to maximize N_{100}. The PMT hit times of the noise event distribute flatly.
- $Nhit_{\text{17-inch}} \geq 120$ and $Nhit_{\text{17-inch}} \leq 230$
  It selects low energy events.
- distance between a target PMT and the event position is larger than 5.56 m
  It selects only events that happen far from the PMT because nearby events yield multiple photons to the one PMT.

Fig. 6.3 shows the result of 1 p.e. fit. The unit of the horizontal axis is one photoelectron (p.e.) charge, which is based on the peak position at a run in 2004. 1 p.e. charge is equivalent to $\sim 5 \times 10^6$ gains at the signal output.

20-inch PMT Gain Correction

The gains of 20-inch PMTs are calibrated by using muon events. The charge ratio ($\mathrm{Q_{Ratio}}$) against the surrounding 17-inch PMTs are fitted to obtain gains of the target 20-inch PMTs (See Fig. 6.4). The difference in the photocathode area is taken into account.

$$Q_{\mathrm{Ratio}} = \frac{Q_{\text{20-inch}}}{\text{Average } Q_{\text{neighbor 17-inch PMTs}}} \left(\frac{17}{20}\right)^2 \tag{6.2}$$

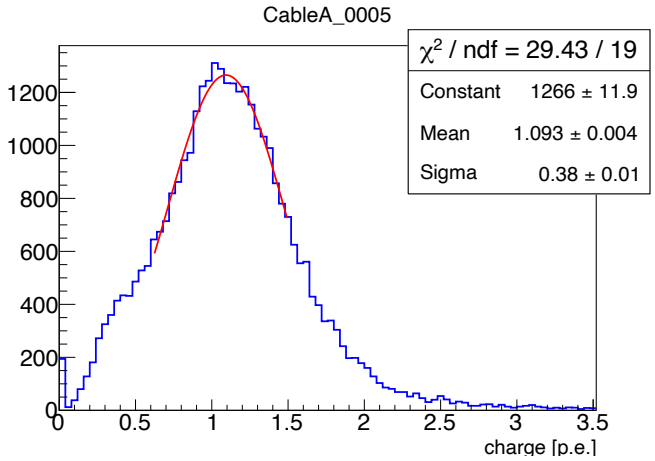

Figure 6.3: 17-inch PMT gain correction
The 1 p.e. peak is fitted with a Gaussian function(red line).

Muon events are selected by muon selection in the following Section 6.2.5. Considering the PMT linearity, events with low average 17-inch PMTs are selected.

$$\text{Average } Q_{\text{neighbor 17-inch PMTs}} < 5,000 \text{ p.e.} \tag{6.3}$$

Low Gain Problem and HV Reductions

The increase in 17-inch low gain channels (gain < 0.4 p.e.) has started since around 2011, as shown in Fig. 6.5. It was suggested by a HV current and voltage monitor (HV monitor) that the PMTs become low impedance sometimes before they become the low gain. The low impedance state is usually recovered by a HV power cycle. The auto HV power cycle by the HV monitor was performed since 2016. It was also observed that the gain decreased repeatedly step by step (See Fig. 6.6). However, the cause is still unknown.

Repeating the low impedance state of the PMTs is suppressed by the HV reduction of the PMT. Occasional HV reductions were performed since 2017 to stabilize the DAQ and to protect the PMTs. Once the PMT became the low impedance state, its HV value was reduced. The reduction values were 50-100 V. Since some channels were reduced more than one time, a total 450 V reduction was performed at the maximum. The decrease in the gain is calculated by $\sim$30% per 100 V reduction. HV reductions after the Xe-LS install were summarized in Table 6.1. 30 V reductions were also performed to healthy PMTs as a precaution in 2019. The low gain channels are not used in the analysis because it cannot detect the 1 p.e. peak position correctly, and they will be used after developing the analysis tool.

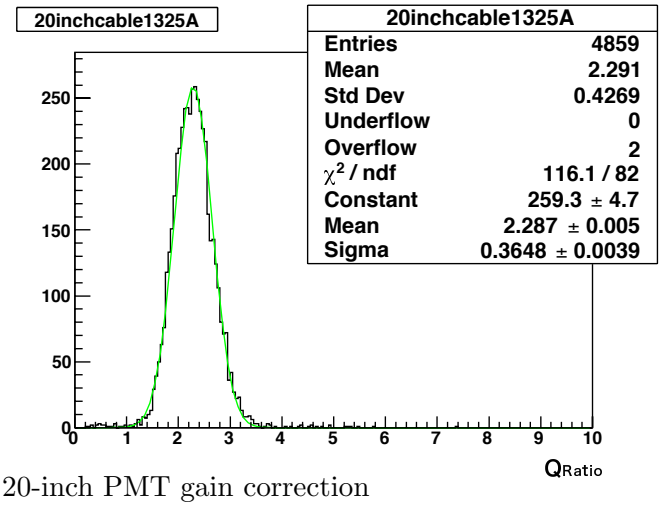

Figure 6.4: 20-inch PMT gain correction
The peak of Q_{Ratio} is fitted with a Gaussian function (green).

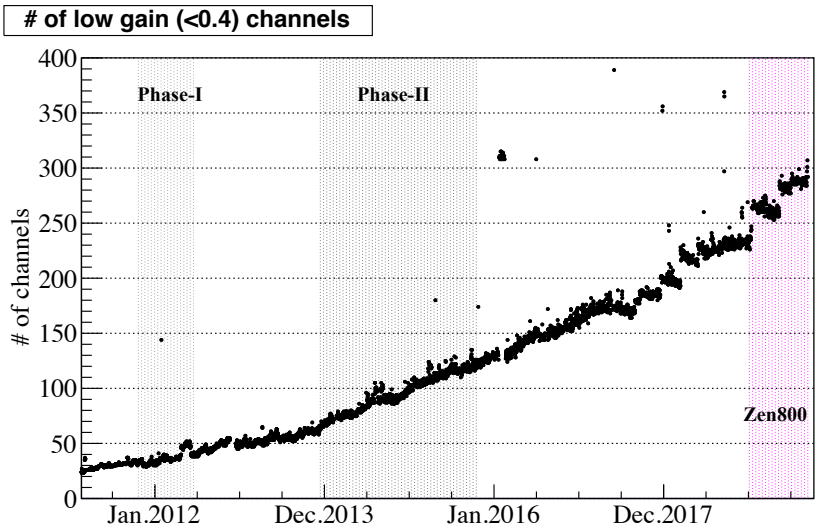

Figure 6.5: The figure shows the trend of low gain 17-inch PMTs. The number of low gain channels increased gradually, and the step increases since 2017 are due to the HV reductions.

Table 6.1: Summary of the HV reductions

No.	Date	First run	Number of reduced PMTs
9th	Jan. 15, 2019	15394	341
10th	May. 13, 2019	15596	394
11th	May. 22, 2019	15608	9
12th	Jul. 03, 2019	15667	275

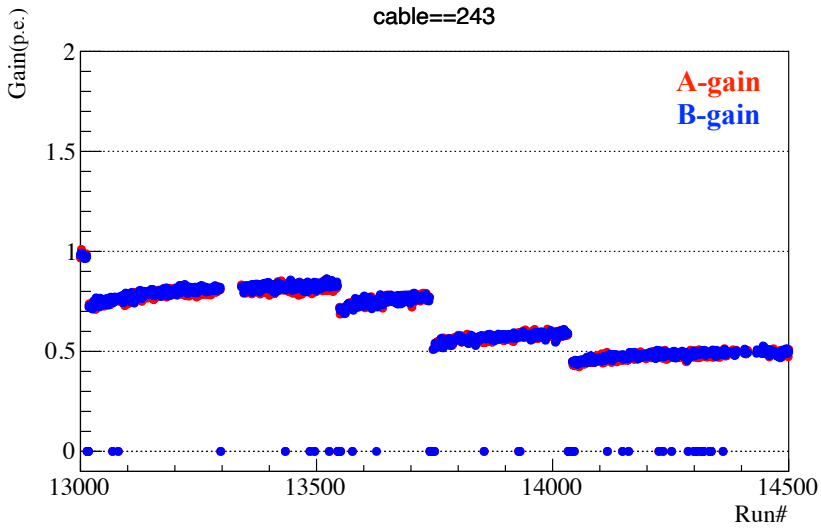

Figure 6.6: Gain decrease in a 17-inch PMT
The trend of the gain in the 17-inch PMT from run013000(April 2015) to run014500(August 2017) is shown. The gain drops step-by-step with repeating low impedance state.

TQ Correction

The raw PMT hit time has some delays and jitters by various factors. It is corrected by the following,

$$T_{\text{correction}} = T_{\text{leading edge}} - T_{\text{laser}} - T_{\text{launch offset}} - T_{\text{cable delay}} - T_{\text{run}}. \tag{6.4}$$

Each correction means,

- $T_{\text{leading edge}}$ is a raw PMT hit timing derived from the waveform analysis.
- T_{laser} is a cable-by-cable time offset measured by Dye-laser calibrations at the center of the detector. The most recent calibration was performed in June 2017. The light intensity was changed from 0.1 p.e./PMT to ∼1,500 p.e./PMT. The correction factor contains charge dependence of the hit timing as,

  $$T_{\text{laser}} = T_0 + T_1 \cdot \log_{10}(\text{ADCsum}) + T_2 \cdot (\log_{10}(\text{ADCsum}))^2. \tag{6.5}$$

  Here, T_0, T_1, and T_2 are cable-by-cable correction factors determined by the calibration. ADCsum corresponds to the observed PMT charge.
- $T_{\text{launch offset}}$ is a trigger launch offset based on its hit TimeStamp information.
- $T_{\text{cable delay}}$ is a time offset caused by cable extension.
- T_{run} is a run-by-run correction of the timing correction. The causes of the time dependence are the changes in the state of PMT, such as gain dropping and HV

reductions, and the replacement of the electronics, etc. The HV reduction and electronics replacement make a large variation in the known specific PMTs. It has been corrected so that there will be no change in the hit time of the specific PMTs in the run before and after that. The events around the balloon surface were used to measure the run-by-run offset.

Bad Channel

There exist noisy PMTs and low hit rate PMTs in KamLAND. They are rejected from the analysis in vertex fitters and energy estimators as "bad channel". The selections of the bad channels are followings:

1. Number of hits is less than 600 in 10,000 events.
   The low hit rate PMTs are removed.

2. Number of hits is less than 80 in 100 high energy muon events.
   The low muon hit rate PMTs are also removed.

3. Number of hits is less than 480 in 10,000 events except for muon events.
   The selection also removes low hit rate PMTs.

4. Number of missing waveforms (Q=0) is larger than 1,000 in 10,000 events.
   The high missing waveform PMTs are removed.

5. Difference between the number of ATWD-A hits (N_A) and the number of ATWD-B hits (N_B) in 10,000 events is large: $\mid N_A - N_B \mid / (N_A + N_B) > 0.18$.

6. High muon charge PMTs are removed from the analysis. The cut condition is

$$\frac{1}{N_{periods}} \sum_{j}^{N_{periods}} \left(\frac{1}{N_{muon\ event}} \sum_{i=0}^{i=N_{muon\ event}} \frac{(Q_{exp} - Q_{real})^2}{Q_{exp}} \right) > 1000\ p.e. \quad (6.6)$$

   Here, Q_{real} is a real charge and Q_{exp} is an expected charge which is derived from the neighbor PMTs. One run was divided into periods. Each period has 100 muon events.

7. Low gain channels and strange gain channels are also masked,

$$\begin{aligned} &\text{gain} < 0.4 \text{ p.e. } \cup \text{ gain} > 4.0 \text{ p.e. for 17-inch PMT and} \\ &\text{gain} < 0.4 \text{ p.e. } \cup \text{ gain} > 6.0 \text{ p.e. for 20-inch PMT.} \end{aligned} \quad (6.7)$$

A PMT corresponding to one or more of the selections is regarded as "bad channel". The trend of the number of the bad channels is shown in Fig. 6.7. The main cause of the increase in the bad channels is the increasing number of low gain channels.

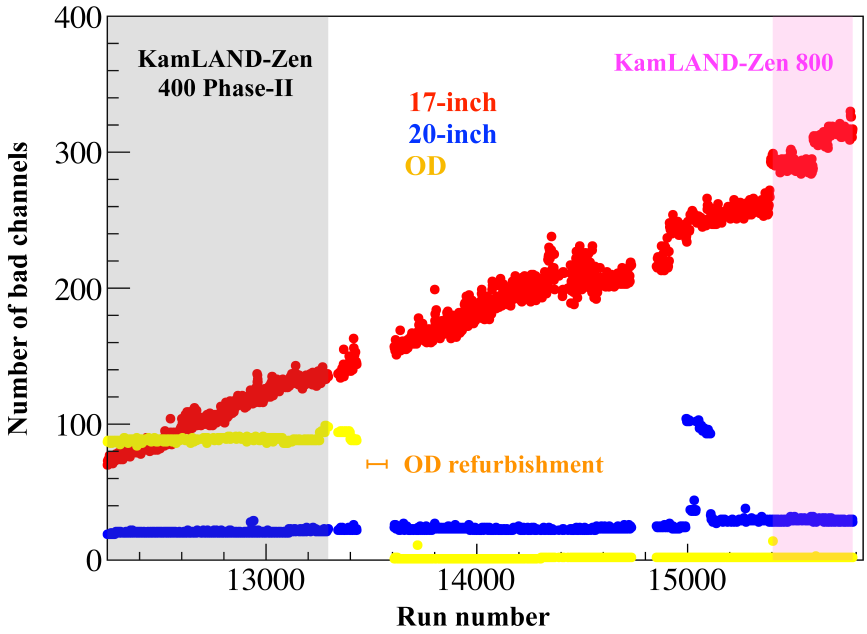

Figure 6.7: Trend plot of the number of bad channels
The number of bad channels increased gradually before KamLAND-Zen 800, and the step-by-step increases in the KamLAND-Zen 800 period are due to the HV reductions.

Dark Hit

The PMTs have several 10 kHz dark hits in the LS. The leading cause of the dark hit is thermal electron emissions and radioactivities in the PMT glass, and so on. The dark rate depends on the detector conditions such as the LS temperature, detector activities, and high voltage values of the PMTs. The charge sum of dark hits "dark charge" and cable by cable dark charge "dark ring" were estimated run by run.

- Event selection by r <2 m except for muon and after muon events.
- Determination of the off-time window 50 nsec before the 50 nsec window that maximizes the number of PMT hits (See Fig. 6.8).
- The dark charge is defined by the mean value of all entries on the charge sum in the off-time windows in a run.
- Flasher events are rejected by (max charge)/(total charge)<0.6 for the estimation of the dark ring. The dark ring is the average value of the dark hits charge in a run.

The time dependence of the dark charge is shown in Fig. 6.9.

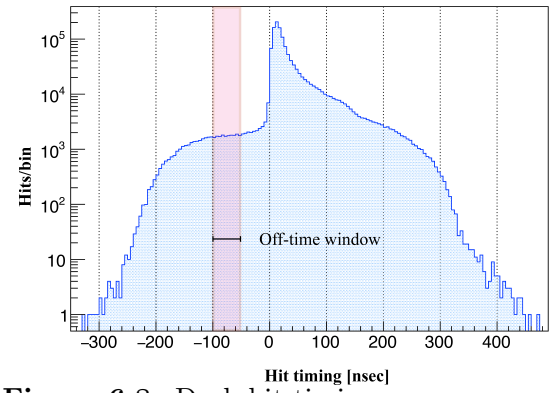

Figure 6.8: Dark hit timing
The PMT hit timings are shown. The charge sum in the off-time windows corresponds to the "dark charge".

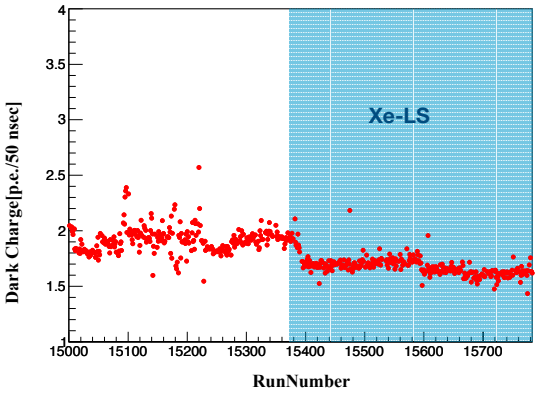

Figure 6.9: The trend of the dark charge is shown. The shaded area corresponds to the Xe-LS period, and the decreases in the dark charge are due to the HV reductions.

6.2.3 Vertex Reconstruction

There are two vertex fitters for event vertex reconstructions. First, LTVertex fitter estimates rough event positions, which are used as inputs for V2 fitter to reconstruct more precise positions. In the vertex reconstructions, hits of bad channels and hits with the charge less than 0.3 p.e. are omitted.

LTVertex Fitter

The LTVertex fitter uses i-th PMT position $R_i(x_i,y_i,z_i)$ and the PMT hit timing information T_i to reconstruct event vertex $r_{vtx}(x_{vtx},y_{vtx},z_{vtx})$. Time of flight Tof_i of the scintillation light toward the i-th PMT is described using an effective light velocity c_{eff} in the LS by $Tof_i = \frac{|R_i - r_{vtx}|}{c_{eff}}$. The emission time of the scintillation light($T_i^{\rm emit}$) detected i-th PMT is described by

$$T_i^{\rm emit} = T_i - \frac{|R_i - r_{vtx}|}{c_{eff}} \tag{6.8}$$

The distribution of $T_i^{\rm emit}$ for all PMTs with the correct vertex is the very reproduction of the scintillation light waveform. The event vertex is determined by moving the vertex step by step from $r(0,0,0)$ so that the spread of the time distribution for all PMTs will become the scintillation waveform.

V2 Fitter

The result of the LTVertex fitter is used as the initial vertex in the V2 fitter. The bad channel and dark hit tables are read in the fitter. First, T_0 is estimated by a

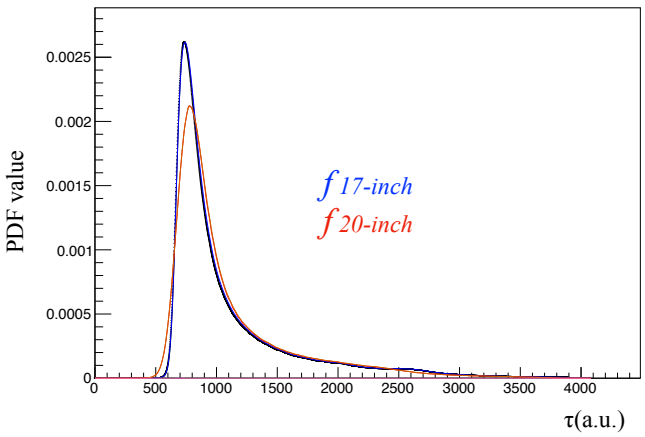

Figure 6.10: PDF function of $\tau_i(x, y, z, T_0)$ for 17-inch and 20-inch PMT
The blue histogram is the PDF for 17-inch PMTs, and the red one is that for 20-inch PMTs.

draft fit. T_0 is the time of the event occurrence.

$$T_0 = \frac{\Sigma_i (T_{pmt\ i} - Tof_{pmt\ i}) \times Q_i}{\Sigma_i Q_i} - const. \tag{6.9}$$

where, $T_{pmt\ i}$ is the i-th PMT hit timing, $\mathrm{Tof}_{pmt\ i}$ is its time of flight, and Q_i is its observed charge. Once the initial value of T_0 is determined, $\tau_i(x, y, z, T_0) = T_{pmt\ i} - Tof_{pmt\ i} - T_0$ is calculated for each PMT, and the log-likelihood is defined using probability density functions $f(\tau)$, which are created from the calibration data for 17-inch PMTs and 20-inch PMTs, respectively (See Fig. 6.10).

$$L = \Pi_i \phi_i \tag{6.10}$$

Here, ϕ_i is

$$\phi_i = \psi_i / \psi_{norm} \tag{6.11}$$
$$\psi_i = \mu \times f_i(\tau_i) + dark_i \tag{6.12}$$
$$\psi_{norm} = \mu \times C_{17\text{-}inch/20\text{-}inch} + dark_i \tag{6.13}$$

where, μ is a pulse shape determination factor, f_i is the PDF function of $\tau_i(x, y, z, T_0)$, $dark_i$ is dark hit of the i-th PMT, and $C_{17\text{-}inch/20\text{-}inch}$ are the normalization constants for the 17-inch PMT and the 20-inch PMT. The minus log likelihood is minimized using a modified Newton-Raphson method, in which x, y, z, and T_0 are moved and $\tau_i(x, y, z, T_0)$ is changed accordingly.

6.2.4 Energy Estimation

The visible energy that can be observed with KamLAND is the energy deposit of charged particles to the scintillator, which is also estimated using a likelihood method.

The expected number of p.e.(charge) for i-th PMT $\mu_{pmt\ i}$ is expressed using the visible energy($Evis$) by:

$$\mu_{\mathrm{pmt}i}(Evis) = b_{\mathrm{pmt}\ i}(x,y,z) \times Evis + d_{\mathrm{pmt}\ i}. \tag{6.14}$$

where, $d_{pmt\ i}$ is the dark noise of the i-th PMT, $b_{pmt\ i}(x,y,z)$ is a coefficient of p.e./MeV in the i-th PMT and calibrated by neutron capture event. It depends on the distance and angle between the PMT position and the event position. When the expected number of hits on i-th PMT is $\mu_{\mathrm{pmt}\ i}$, the probability of detecting j photons in i-th PMT $P_{pmt\ i,jp.e.}$ is given by the Poisson distribution.

$$P_{\mathrm{pmt}\ i,jp.e.} = \frac{(\mu_{\mathrm{pmt}\ i})^j}{j!} \exp(-\mu_{\mathrm{pmt}\ i}) \tag{6.15}$$

On the other hand, the probability for no PMT hit is given by $j = 0$, but in fact, the 1 p.e. signal cannot be acquired sometimes because the 0.3 p.e. analysis threshold is set. The probability for no PMT hits ($P_{pmti,\ nohit}$) is described using its efficiency ϵ,

$$P_{\mathrm{pmt}\ i,\mathrm{no\ hit}} = p_{0\ p.e.} + (1-\epsilon)p_{1\ p.e.} \tag{6.16}$$

When the signal is detected by the i-th PMT, what we will obtain is its charge Q_i. The probability density function of the charge distribution $f(Q_i)$ is

$$f_{\mathrm{pmt}\ i,\ j\ p.e.}(Q_i) = \frac{1}{\sqrt{2\pi j\sigma^2}} \exp(-\frac{(Q_i - j)^2}{2j\sigma^2}) \tag{6.17}$$

where, σ is the charge resolution of the 1 p.e. distribution. Finally, the likelihood(L) is defined as:

$$L = \prod_{i=0}^{\#\mathrm{of\ no\ hit\ PMT}} P_{\mathrm{pmt}\ i,\mathrm{no\ hit}} \left[\prod_{i=0}^{\#\mathrm{of\ hit\ PMT}} \left(\sum_{j=1}^{100} P_{\mathrm{pmt}\ i,j\ p.e.} f_{\mathrm{pmt}\ i,j\ p.e.}(Q_i) \right) P_{i\ \mathrm{pmt,hittime}} \right] \tag{6.18}$$

Where $P_{\mathrm{pmt}\ i,j\ pe}$ is the probability of the i-th PMT hitting j p.e., and $P_{\mathrm{pmt}\ i,\mathrm{no\ hit}}$ is the probability of no i-th PMT hit. $P_{i\ \mathrm{pmt,hittime}}$ is the hit time probability density function of i-th PMT. The PDF of hits is summed up to 100 p.e. The reconstructed energy is derived from the maximization of the likelihood function by a Newton-Raphson method.

$$\frac{\partial L}{\partial Evis} = 0 \tag{6.19}$$

The 20-inch PMTs' energy and that of 17-inch PMTs' energy are combined with a weight like:

$$Evis = (1-\alpha)E_{\text{17-inch}} + \alpha E_{\text{20-inch}}, \tag{6.20}$$

where α is a weighting factor, which is calibrated before KamLAND-Zen to obtain the best resolution.

6.2.5 Muon Reconstruction

In this sub-section, the procedure for reconstructing the muon event detected by the inner detector is described. The muon that has passed through the inner detector(ID muon) can reconstruct the muon track using the PMT hit information as follows.

1. The first hit PMT that has a sufficiently large charge and is not isolated in time is found. The intersection between a line from the first PMT position to the center of the spherical tank and the large-balloon surface is taken as the first incident point on the large-balloon.

2. Among the PMTs hit after the first hit PMT, the PMT that has the highest charge hit except for isolated PMTs in charge is determined. The intersection point between the line from the detector center to the strongest PMT and the large-balloon surface is regarded as the first exit point.

3. The entrance and exit points are corrected based on the correlation between track length and total charge, and other PMT hit timing and charge information.

4. The quality of the muon track reconstruction is checked for the following items.

   - There are the fastest hit PMT and the strongest PMT.
   - The average ID PMT hit time around the entrance point should be faster than that of around the exit point.
   - The average hit time of OD PMTs around the entrance point is earlier than that around the exit point.

The quality of the track reconstruction is quantified as "badness". A muon event with "badness" exceeding 100 is considered as a badly reconstructed muon. The reason for bad reconstruction could be multiple muons arriving at the same time or a stopped muon in the inner detector.

Muon Selection

High charge events in the ID or the OD are regarded as muon events. The muon event selection is based on the total charge of the ID 17-inch PMTs and the number of the OD PMT hits.

$$\text{Total charge ID 17-inch PMT} \geq 10,000 \text{ p.e. for ID muons}$$
$$\text{Total charge ID 17-inch PMT} \geq 500 \text{ p.e.} \cap \text{N200OD} \geq 9 \text{ hits for OD muons.}$$

6.2.6 MoGURA Neutron Reconstruction

There exist afterpulses and overshoots in the PMTs after large charge event such as muons. In order to detect neutron capture gammas after muons without event loss, the dead time free electronics MoGURA is used for the neutron capture event search. The detection of neutron capture events with MoGURA is performed as follows.

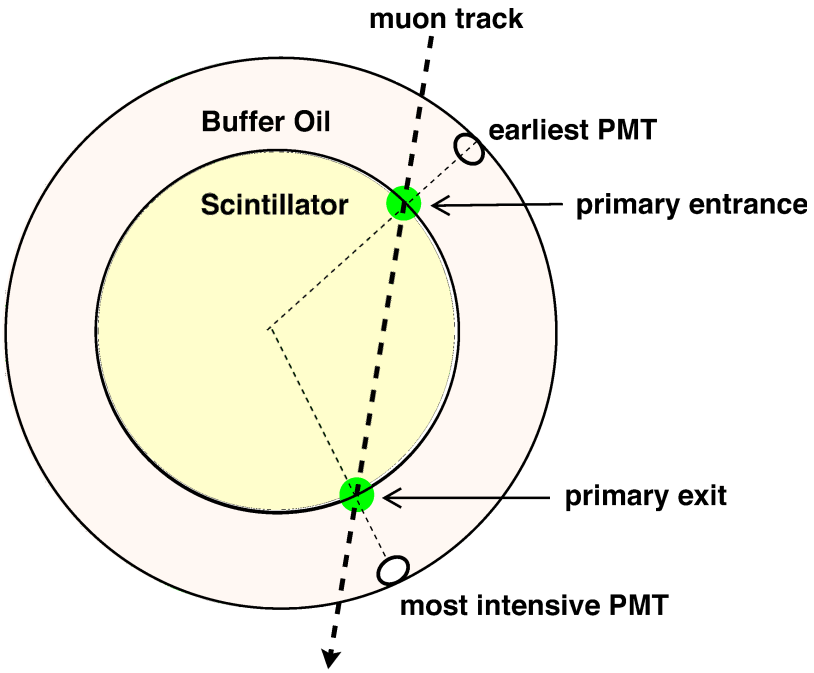

Figure 6.11: The figure shows the procedure for the muon track reconstruction.

I. Opening a 200 nsec sequence window from the beginning of the events and perform a vertex fitting. The LTVertex fitter is used.

II. Calculating Tof using results of the vertex fitting and create PMT hit timing distribution (See Fig. 6.12).

III. Calculating the signal/noise parameter N_{S}. The N_{S} is defined as

$$N_{\mathrm{S}} = N_{\mathrm{in}} - N_{\mathrm{out}} \times \frac{N_{\mathrm{S}}\ \text{window(30 nsec)}}{\text{Sequence window(200 nsec)} - N_{\mathrm{S}}\ \text{window(30 nsec)}}, \quad (6.21)$$

where N_{in} is the total number of PMT hits in the N_{S} window. N_{S} window is defined as hit peak time $\pm$15 nsec. N_{out} is the total number of PMT hits in the sequence window except for the N_{S} window.

IV. Repeating I. to III. every 20 nsec to determine the maximum N_{S}. The maximum N_{S} is used to detect neutron events and the vertex at the maximum N_{S} is defined as the neutron capture position.

Muon Neutron Vector File (MNVF)

The $0\nu\beta\beta$ decay search analysis is performed with the data of KamFEEs. The MoGURA neutron events are tagged with KamFEE muon events as followings:

1. Finding KamFFE muons by the selection in Section 6.2.5 except for fake muon events of which time distance from the last muon $>$ 10 μsec.

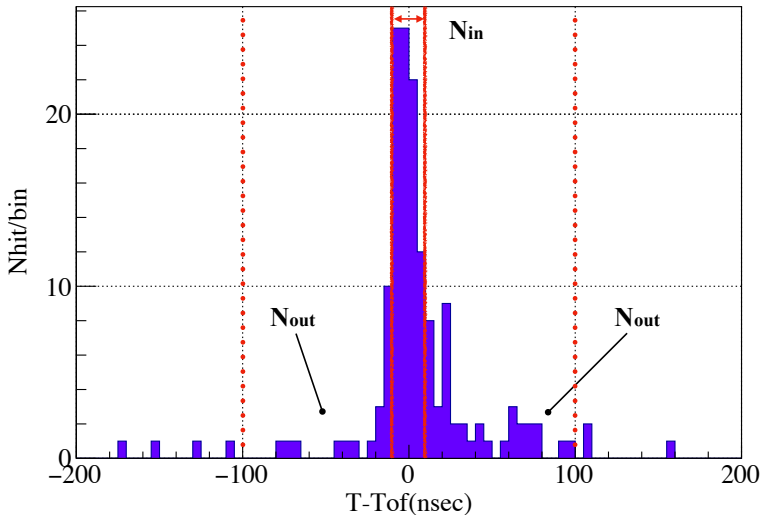

Figure 6.12: N_s calculation
The dashed red line is the sequence widow, and the solid red line is the N_s window.

2. The MoGURA events are tagged with the KamFEE muons based on the unix-time.

3. Events that are unlikely to be neutron captures are rejected based on N_S <50 or Ntotal(N_{in}+ N_{out})< 150, time distance from muon > 2500 μsec, and time distance from last event < 1 μsec.

Fig. 6.13 shows N_S vs dT distribution of the neutron candidates. The N_S value becomes smaller with short dT. The reason for the loss is thought to be the effect of afterpulses, overshoots, and ringing in the PMTs. Neutron tagging efficiency of the MoGURA DAQ is estimated by fitting the dT distribution, shown in Fig. 6.14. Events within the KamLAND LS region in the Xe-LS period were analyzed. The red line is the fitting function $f(x) = N/\tau \cdot \exp(-t/\tau)$. The integral of the function represents the production rate. The fitted neutron production rate 3333±38 /day/kton is consistent with previous works 3323±9 /day/kton [61] and 3575±462 /day/kton [66]. The neutron tagging efficiency, which corresponds to the fraction of the histogram (data) against the fitted function in the figure, is 78.6±0.8%.

Neutron Capture in Xe-LS

In the Xe-LS, the neutron production rate is higher than that of the KamLAND LS due to the presence of Xe. It was estimated to be 22% higher in KamLAND-Zen 400 [61]. The excess in KamLAND-Zen 800 was also estimated again. The neutron production rates within $r < 150$ cm for the Xe-LS period and for the KamLAND LS period were estimated. The production rates were respectively 5546 ± 279 /day/kton and 5093 ± 201 /day/kton. This result indicates that the neutron production rate in the Xe-LS is (9 ± 7)% higher than that of the KamLAND LS.

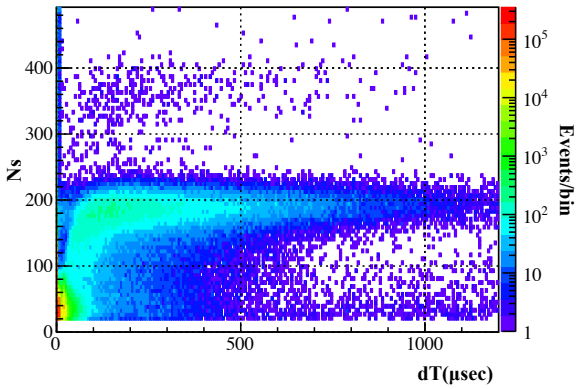

Figure 6.13: N_s vs dT distribution
The cluster around N_S ∼180 is 2.2 MeV gamma from neutron capture by H. The N_S value decreases with short dT because of the noise by the PMT afterpulses and signal loss by the PMT overshoot.

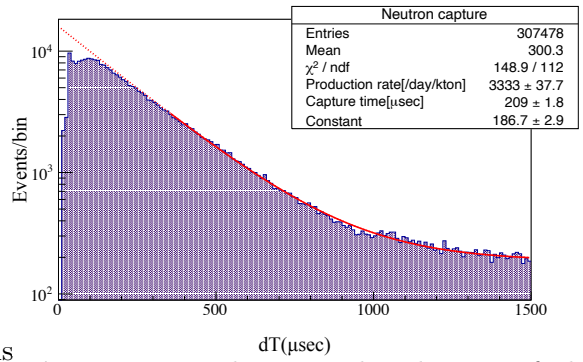

Figure 6.14: The time distribution of the neutron capture events is shown. The events were lost with short dT.

6.3 Event Selections

Event selections for $0\nu\beta\beta$ decay candidate are described in this section. The outline of the $0\nu\beta\beta$ decay search analysis was shown in Fig. 6.15. The final candidate events are narrowed down by the event selection described below using the RTQ file, the GVF, and the MNVF. Finally, $0\nu\beta\beta$ decay events are searched for by performing the energy spectrum fitting with the MC events.

6.3.1 Run Selection/Bad Data Rejection

The runs and the periods, when the data is collected normally, are selected. The following are treated as deadtime in the analysis.

- **Bad run**
  Run in which the KamFEE or HV crate has failed, too short run, and other periods when there exists a hardware problem such as a magnetic compensation coil trouble are excluded from the analysis as "bad run".

- **MoGURA off periods**
  The period when the MoGURA DAQ is not running, and the switching time of the MoGURA run or sub-run are excluded from the analysis.

- **After long deadtime veto**
  Spallation events such as ^{10}C cannot be tagged if muon is missed during a long time veto period, so it is vetoed for three minutes after a long deadtime(>1 sec), a MoGURA run change, and run start.

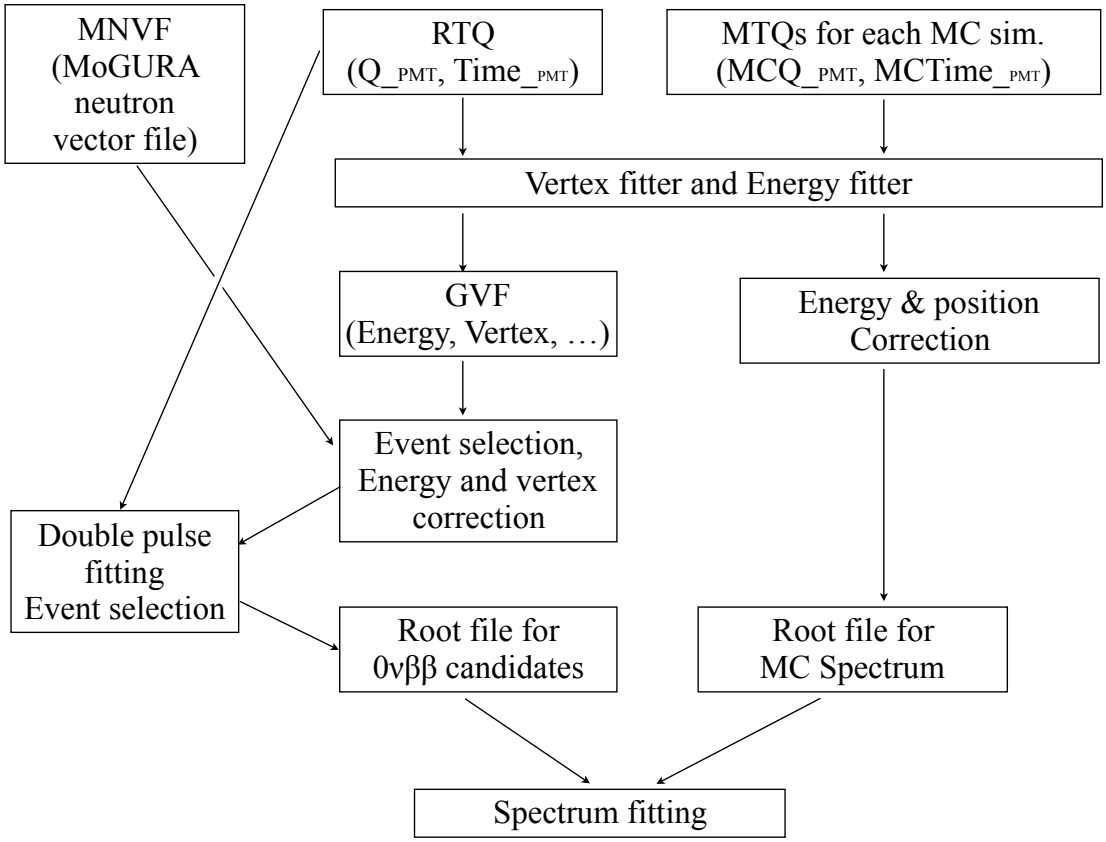

Figure 6.15: Analysis framework
The figure shows the analysis framework. The root files for real data on the $0\nu\beta\beta$ candidates were made of MNVFs and RTQs through vertex fitter, energy estimator, and event selections. The root files for MC backgrounds events and MC $0\nu\beta\beta$ decay events were made of MC RTQ files (MTQ) via the same vertex fitter and energy estimator.

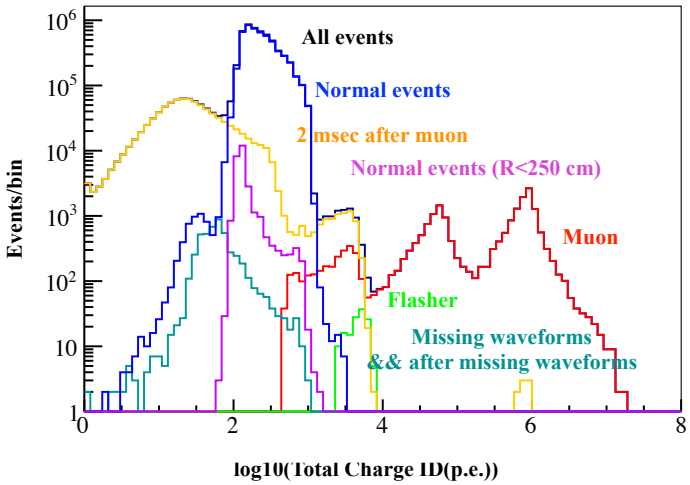

Figure 6.16: Event properties
The horizontal axis represents $\log_{10}$(Total Charge ID) in each event. The histograms are colored by event property.

- **Trigger disable veto**
  The trigger is disabled when the trigger buffer becomes almost full. Events during trigger disable time($\sim$0.4 msec) are vetoed by disable and enable triggers.

6.3.2 Unphysical Event Rejection

Some events are not related to a physical phenomenon. Flasher PMT event, missing waveform event, badly reconstructed event, and post 1 PPS trigger event are known as unphysical events. The total charge distributions in each event property are seen in Fig. 6.16. Such events are rejected by the following selections.

1. **Flasher PMT event**
   The flasher PMT event is caused by PMT light emission. The cause is not understood, but the light emission from epoxy around the breeder circuit is one possibility [67]. In most cases, the event position is reconstructed outside the outer balloon. As a characteristic of the event, one flasher PMT has the highest charge, and the neighbouring PMTs also have relatively high charges so that the next cut will eliminate such an event.

   – Total PMT charge $>$ 2500 p.e.
   – (Max PMT charge) / (Total charge) $>$ 0.6
   – Average charge among neighbouring PMTs $>$ 20 p.e.

   Fig. 6.17 shows the Max PMT charge and total charge of the flasher events and normal events. The flasher events make a cluster in the figure.

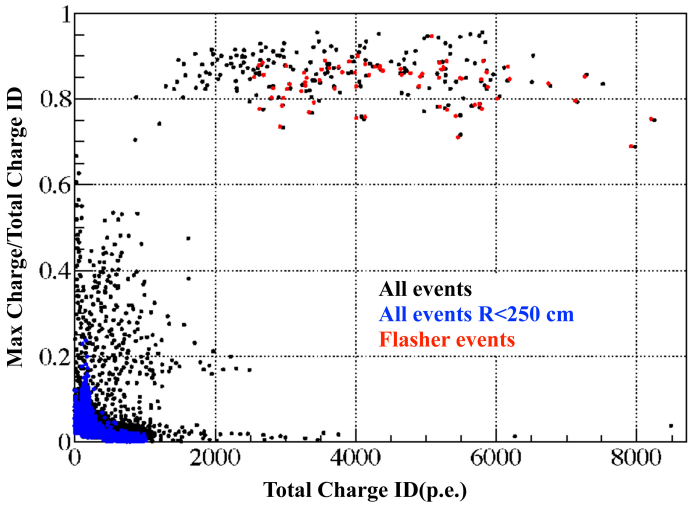

Figure 6.17: Max PMT charge and total charge of the flasher events and normal events

2. **Missing waveform event**
   A high signal rate after muon occupies the read channels, and the waveforms are not recorded. This is called "missing waveform". Since hit information remains in NsumMax, such an event can be selected by the following selection using NsumMax and Nhit17, which is the number of 17-inch hit PMTs by the waveform analysis (See Fig. 6.18a).

   – time distance from muon events $<$ 2 msec

   – Nhit17 $<$ NsumMax$\times$0.99$-$25

   The missing waveform events and subsequent events are vetoed because the waveform information may be incorrect. The veto time is 2 msec for NsumMax$>$ 200 events and 2 sec for NsumMax$>$ 1,200 events. Since the inefficiency estimated with prompt ^{214}Bi is $<$ 0.01%(See Fig. 6.18b), the inefficiency of $0\nu\beta\beta$ decay is considered to be the same level, which can be ignored.

3. **Badly reconstructed events**
   Vertex badness was parameterized as "Badness", and badly reconstructed events are rejected on this badness value (See Fig. 6.19a). The reason for the badly reconstructed events are unphysiscal noise events and pileup events.

$$\text{Badness} < 41.1 \times \exp(-7.1 \times \mathit{Evis}[\text{MeV}]) + 2.7 \tag{6.22}$$

   The inefficiency of the badness cut is estimated as 0.0064$\pm$0.0015% by the prompt ^{214}Bi events (See Fig. 6.19b).

4. **Post 1 PPS**
   100 μsec veto after 1 PPS trigger because of the trigger overlap noise (See Fig. 6.20).

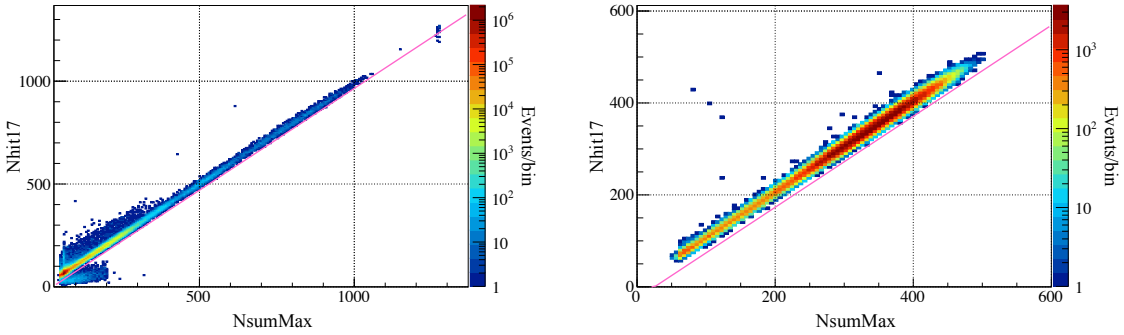

(a) Missing waveform selection for all physics events **(b)** Missing waveform selection for prompt ^{214}Bi

Figure 6.18: Missing waveform selection
The lower events than the pink line are the missing waveform events.

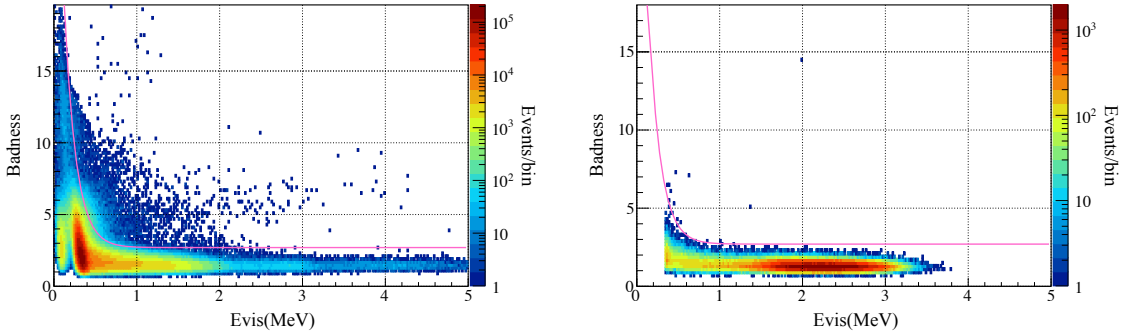

(a) Badness selection for all physics events **(b)** Badness selection for prompt ^{214}Bi

Figure 6.19: Badness selection
The upper events than the pink line are removed from the analysis.

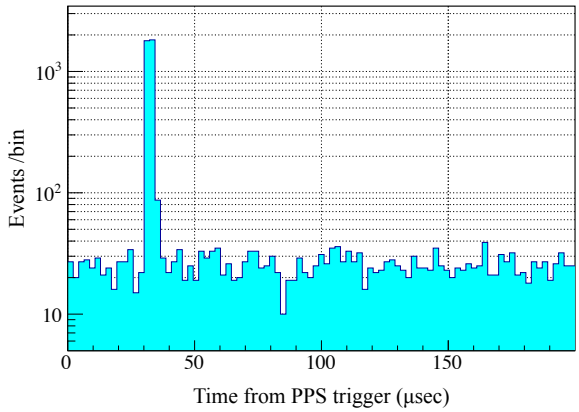

Figure 6.20: Event rate after PPS trigger
The horizontal axis represents a time interval from a PPS trigger to an event, and the event excess by the noise appeared around 30 μsec.

5. **OD event**
   The OD high hit events are also rejected to remove the fast neutron background derived from the OD muons. The events with N200OD*geq*9 hits are rejected from the $0\nu\beta\beta$ decay analysis.

6.3.3 $^{222/220}$Rn Decay and Reactor Event Veto by Delayed Coincidence

$^{214/212}$Bi-Po sequential decay from $^{222/220}$Rn decay series and anti-neutrino events are tagged with delayed coincidence measurements. They are removed from the $0\nu\beta\beta$ decay analysis.

Bi-Po Sequential Decays

$^{214/212}$Bi-Po sequential decay are respectively:

$$^{214}\mathrm{Bi} \xrightarrow[\mathrm{Q}_\beta\text{:3.272 MeV,99.979\%}]{\mathrm{T}_{1/2}=19.9\ \mathrm{min}} {}^{214}\mathrm{Po} \xrightarrow[\mathrm{Q}_\alpha\text{: 7.83MeV(Evis:0.60MeV)}]{\mathrm{T}_{1/2}=164.3\ \mu\mathrm{sec}} {}^{210}\mathrm{Pb} \tag{6.23}$$

$$^{212}\mathrm{Bi} \xrightarrow[\mathrm{Q}_\beta\text{:2.254 MeV,99.989\%}]{\mathrm{T}_{1/2}=60.55\ \mathrm{min}} {}^{212}\mathrm{Po} \xrightarrow[\mathrm{Q}_\alpha\text{: 8.954MeV(Evis:0.74MeV)}]{\mathrm{T}_{1/2}=0.299\ \mu\mathrm{sec}} {}^{208}\mathrm{Pb}. \tag{6.24}$$

Since ^{214}Po and ^{212}Po have short lives, the Bi-Po sequential decay can be selected by:

- 0.2 MeV $\leq E_d \leq$ 1.3 MeV
- distance between prompt event and delayed event $<$ 170 cm
- time interval between prompt event and delayed event $<$ 1.9 msec

The distribution of each selection of ^{214}Bi-^{214}Po events according to the criteria is shown in Fig. 6.21, within r <250 cm after the Teflon tube removal. The distribution of ^{212}Bi-^{212}Po is also shown in Fig. 6.22. dT <5 μsec was chosen for ^{212}Bi-^{212}Po events in the period after accidental ^{214}Bi-^{214}Po events derived from ^{222}Rn had fully decayed. Since the delayed ^{214}Po and ^{212}Po are quenched, they are not clearly separated by energy. In the inner-balloon, alpha does not deposit whole energy into the LS, so there are some events with energies lower than the expectation.

Anti-Neutrinos

Anti-neutrinos such as geo neutrinos and reactor neutrinos are tagged with the inverse beta decay.

$$\bar{\nu}_e + p \rightarrow e^+ + n \tag{6.25}$$

Positron energy deposit and annihilation gammas (2×0.511 MeV) are detected as the prompt signal, and 2.2 MeV neutron capture gamma is detected as the delayed signal with a mean lifetime of ∼200 μsec.

- $E_d \geq$ 1.5 MeV

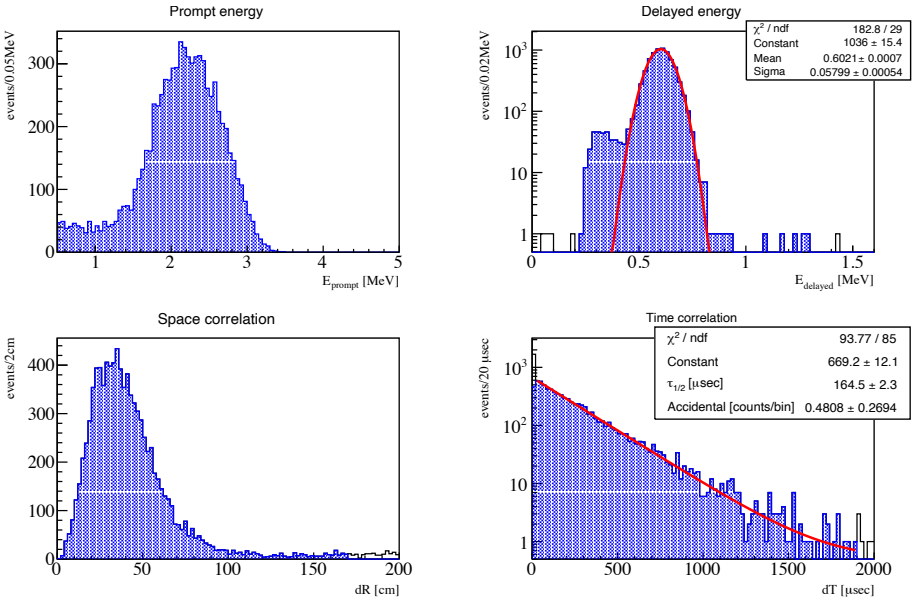

Figure 6.21: Event selections of ^{214}Bi-Po
The white histograms show (N-1) plots of each selections, and the blue histograms show the selected events. The left shoulder of the peak in the right upper figure is made by quenched film events.

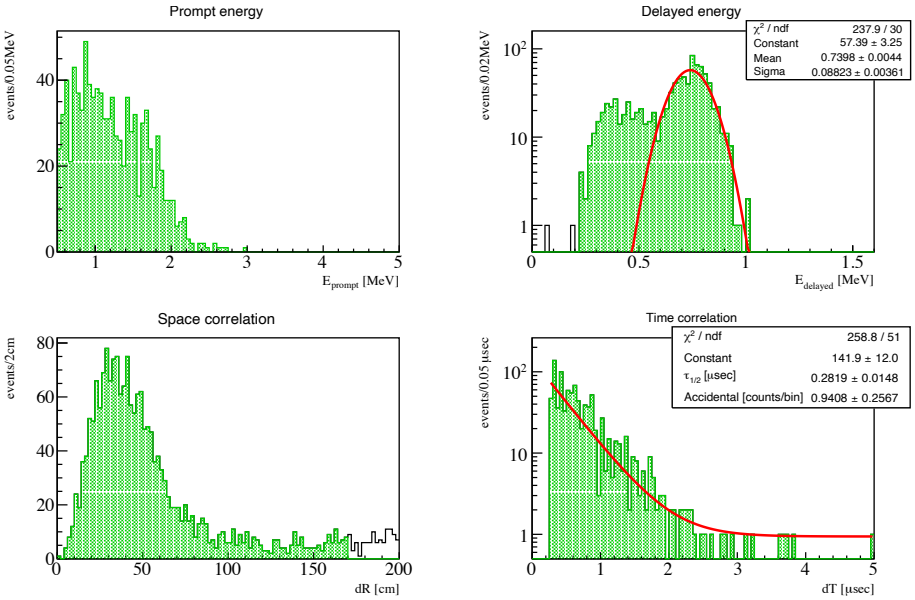

Figure 6.22: Event selections of ^{212}Bi-Po
The white histograms show (N-1) plots of each selections, and the green histograms show the selected events.

- vertex distance between the prompt event and the delayed event < 200 cm
- time interval between prompt event and delayed event < 1.0 msec

The tag efficiency is 99.14%, which is estimated in [61]. The background of $0\nu\beta\beta$ decay is miss tagged reactor neutrinos. The event rate in the reactor off period is <0.2 event/day/($V_{R=550cm}$) [63]. Considering the 250 cm fiducial radius, it will be <0.1 event/yr after tagging, and events in the ROI of $0\nu\beta\beta$ decay is much less than that, so we can ignore it.

6.3.4 Double-Pulse Fit

Pileup events of ^{212}Bi-^{212}Po could be serious backgrounds. When the time difference is large enough, it can be vetoed with the delayed coincidence measurements. When the time difference is less than about 200 nsec, ^{212}Bi and ^{212}Po events are in the same event window. Some of them are tagged with double-pulse fit developed by [68]. The double-pulse fit detects if there are double pulses in the one event window. The procedure for the double-pulse fit are followings:

- Make hit timing waveform
  Tof subtracted hit timings of 17-inch PMTs in each event are stored in 1.0 nsec bin histogram to make the hit timing waveform.
- Make a reference waveform
  A reference waveform is obtained by averaging the waveform of $2\nu\beta\beta$ decay. The event of $2\nu\beta\beta$ decay selected by energy cut from 1.4 MeV to 1.6 MeV, a radius cut $r < 160$ cm, and other event selections for $0\nu\beta\beta$ decay candidate. The event purity is >95%. The reference waveform is scaled by the energy.
- Double-pulse fitting
  Parameters used to fit the waveform are
  - prompt signal energy(E_p),
  - prompt signal timing(T_p),
  - delayed signal energy(E_d),
  - time difference from the prompt to the delayed(ΔT).

  Fitting with maximum likelihood methods is performed by minimizing χ^2 defined by

$$\chi^2 = \begin{cases} 2\sum_i \left(-(h_i - f_i) + h_i \cdot \log\frac{h_i}{f_i}\right) & (h_i > 0) \\ 2\sum_i \left(-(h_i - f_i)\right) & (y_i = 0), \end{cases} \tag{6.26}$$

  where subscript i represents i-th bin, h_i is contents of the histogram in the i-th bin. f_i is an expected value in i-th bin. The f_i is defined by

$$f_i = |E_p| \cdot R(i - T_p) + |E_d| \cdot R(i - T_p - \Delta T) + D. \tag{6.27}$$

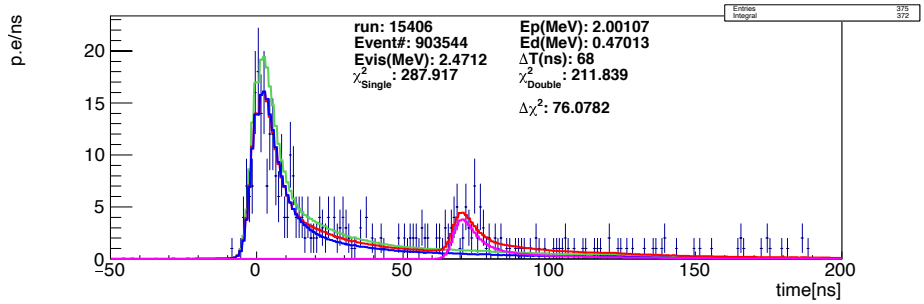

Figure 6.23: A sample of double-pulse fitting
The dots with error bars are data. The blue and pink waveforms are fitted results of the prompt and the delayed pulses. The green waveform is the fitted result with only a single pulse.

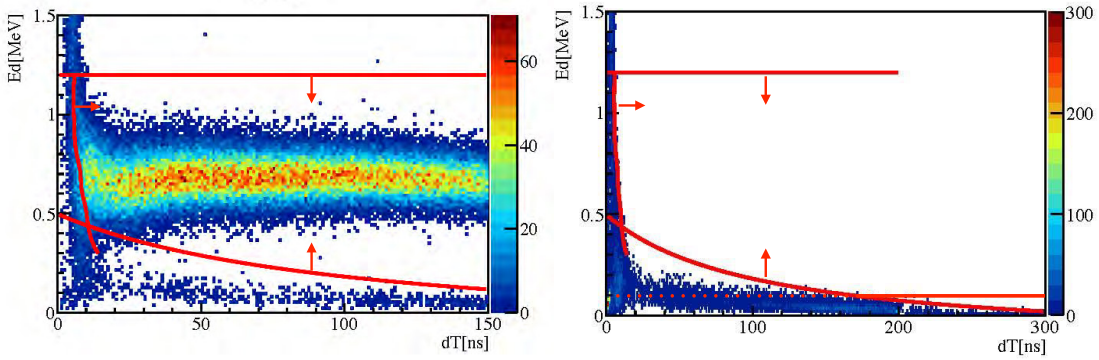

Figure 6.24: Event selection of the pileup events
The E_d and $\Delta T(dT)$ distribution of MC ^{212}Bi-^{212}Po pileup within $\Delta T < 150$ nsec (left picture) and MC $0\nu\beta\beta$ decay events (right picture) in the energy of 2 MeV $< Evis <$ 2.7 MeV are drawn. The events surrounded by the red lines are tagged events.

with a scaled reference waveform $R(i)$ and dark hits D. ΔT and T_p are scanned. E_p and E_d are floated to minimize the χ^2 by the minimization tool "ROOT Minuit". Fig. 6.23 shows a sample of the double-pulse fitting.

- Pileup events are selected with the fitting results ΔT and E_d. The selection was defined with the study of the MC simulation (See Fig. 6.24).

Double-pulse fit can not remove the pileup events in $\Delta T <\sim 10$ nsec. Pileup removal efficiency of the double-pulse fit was studied using the MC simulation. As a result, 2.3±0.5% of ^{212}Bi-Po decay remains as a background event. Also, the $0\nu\beta\beta$ decay inefficiency becomes $\sim 0.1\%$.

Connection between Delayed Coincidence and Double-Pulse

The efficiency in the joint of the delayed coincidence veto and the double-pulse fit tag around ∼200 nsec was estimated by using ^{214}Bi in the radon rich periods. Fig.

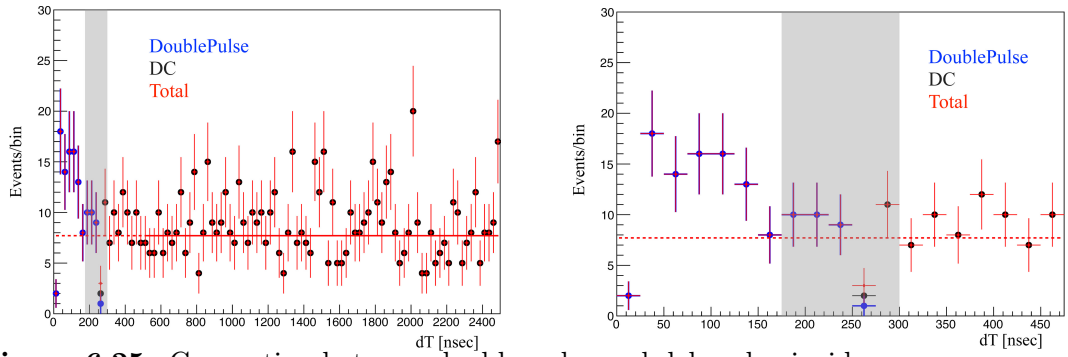

Figure 6.25: Connection between double-pulse and delayed coincidence
The each colored dots with error bars are data for double-pulse events(blue), delayed coincidence events(black), and double-pulse+delayed coincidence events(red). The shaded area is the connection part between the delayed coincidence tag and the double-pulse fit tag.

6.25 shows the dT distribution of events tagged with the delayed coincidence and the double-pulse fit. The number of events at the connection part is estimated by the fitting of the delayed coincidence events from 500 nsec to 2500 nsec. The observed (43±7) events were agreed with an expected number of event 39±2, and the efficiency of the connection part is estimated to be 112±18%. Therefore, assuming Bi-Po delayed coincidence tags are perfectly effective, the tagging efficiency of ^{214}Bi and ^{212}Bi are >99.96% and >96.7%. Also, for the pileup event, the energy fitter analysis range is ∼150 nsec window. The joint events are not detected with pileup energy. It means that the missed ^{212}Bi event in the joint part can not be a background on the $0\nu\beta\beta$ decay by its lower visible energy.

6.3.5 Spallation Veto

Post Muon Veto

There exist spallation products and neutrons after muons. All volume veto for 2 msec after all muons is applied unconditionally, and all volume veto for 150 msec is also applied after scintillation muons, of which a total 17-inch PMT charge is more than 40,000 p.e. to remove short-lived spallation events such as ^{12}B.

Muon Shower Veto

When nuclear spallation by a cosmic-ray muon occurs, a large amount of energy is locally deposited to the LS by electromagnetic and hadronic showers. The spallation event rejection by correlation with the shower position was developed in [69]. This method is also effective for events that do not involve neutrons or miss the correlated neutrons, unlike the method of tagging neutrons by the MoGURA DAQ described later. The procedure for removing spallation events is as follows.

- **Calculating muon energy deposit along with reconstructed muon track** ($\frac{dQ}{dL}$)

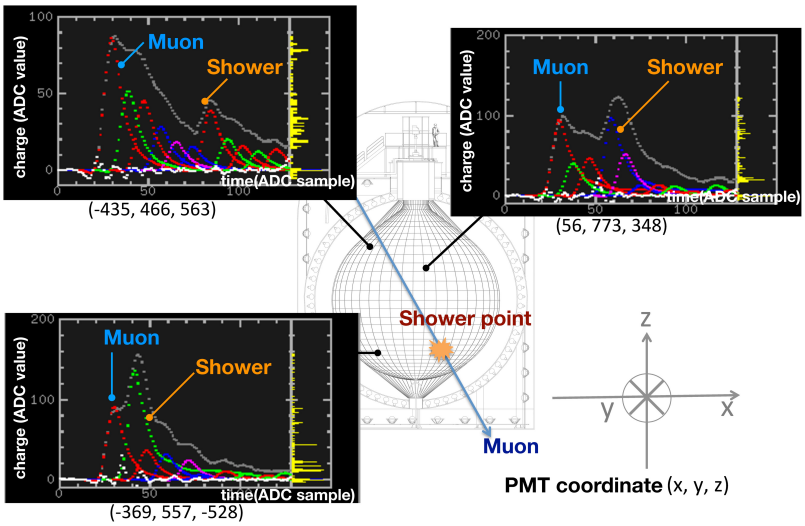

Figure 6.26: Estimation of a shower point
The original figure is from [69] and modified. Three waveform samples are shown in the figure. The waveform components are decomposed, and the first peak by muon itself and 2nd peak by the shower are seen in each PMT waveform.

The total waveform of each PMT is decomposed by the waveform fitting, and for each waveform, the emission position on the track is determined by using the muon incident time and the track geometry (See Fig. 6.26). This analysis is performed for all muons, and $\frac{dQ}{dL}$ along the track is calculated.

- **Correlation between physical events and showers**
  Whether a certain physical event is correlated with a shower is determined. The distance from the muon track (L_{trans}) and the corresponding position on the track are determined. Maximum $\frac{dQ}{dL}$ point in the $\pm$170 cm window along with the track around the corresponding position was searched for and $\frac{dQ}{dL}$ around $\pm$ 85 cm are integrated to obtain dQ value (See Fig. 6.27). Also, the time interval (dT) between the muon and the event is calculated. This analysis is performed for all muons that are 180 seconds back from the physics event time.

- **Spallation event rejection**
  Event rejection is performed by the likelihood method based on dQ, L_{trance}, and dT. The following likelihood is used.

$$\text{Likelihood} = \text{PDF}(dQ, L_{\text{trans}}) \times \text{PDF}(dT) \tag{6.28}$$

PDF for dQ and L_{trans} was created by using on-time for ^{12}B (half-life: 20.2 msec) after muon and off-time events for accidentals. In order to improve the efficiency of events that can not be tagged by the neutron tagging with the MoGURA, a likelihood function is created for events without neutrons. The events of $\log_{10}(\text{Likelihood}) >$ threshold (-1.6) was rejected. The ^{10}C tagging efficiency

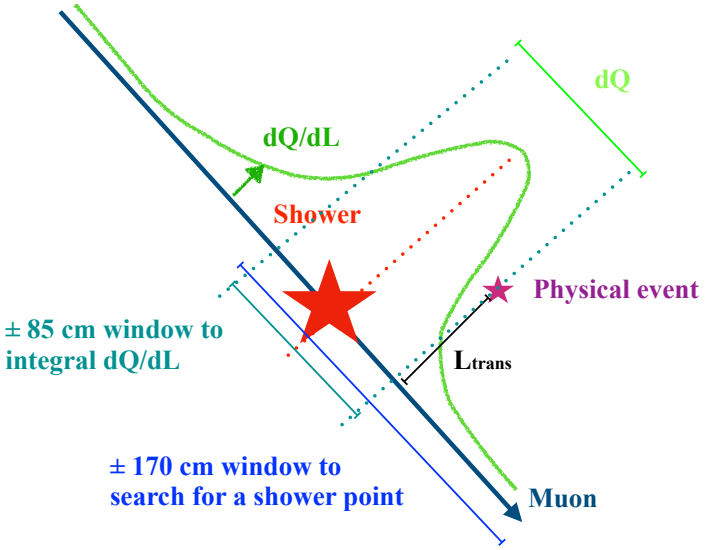

Figure 6.27: The figure shows the schematic procedure for the event correlation calculation between a muon shower point and a physical event.

by shower tag, which is one of most serious backgrounds against $0\nu\beta\beta$ decay, was estimated to be about ∼85% for neutron tagged events and ∼50% for neutron un-tagged events(See Fig. 6.28). The uncertainty by using different nuleus for the likelihood production is considered in the estimation of the production rate in Chapter 8.4.2.

MoGURA Muon Spallation Veto with Neutron Tagging

MoGURA is deadtime free DAQ system for the spallation product veto after muon events. The neutron captures are tagged with MoGURA. It is described in Section 6.2.6. Three types of the tagging are available: veto for short-lived products(mostly for ^{10}C), veto for ^{137}Xe, and veto fro long-lived products.

- **^{10}C veto**
  Volume cut for 180 sec within 160 cm radius from neutron capture events which are selected by

$$N_{\mathrm{S}} > 80 \ \cap \ dT_{\mathrm{muon}} \ < \ 30 \ \mu\mathrm{sec} \tag{6.29}$$

$$\cup \ (N_{\mathrm{S}} > 50 \ \cap \ 30 \ \mu\mathrm{sec} \ < \ dT_{\mathrm{muon}} \ < \ 1,200 \ \mu\mathrm{sec}) \tag{6.30}$$

  Here, N_S is the number of signal hit PMTs, introduced in Section 6.2.6. dT_{muon} is the neutron capture time after the primary muon.

- **^{137}Xe veto**
  The decay of ^{137}Xe (β^-, 4.2 MeV), which is made by neutron capture on ^{136}Xe, is one of serious background. It is also tagged by a triple coincidence of muon, neutron capture gamma, and the decay itself. The volume cut is applied for 27

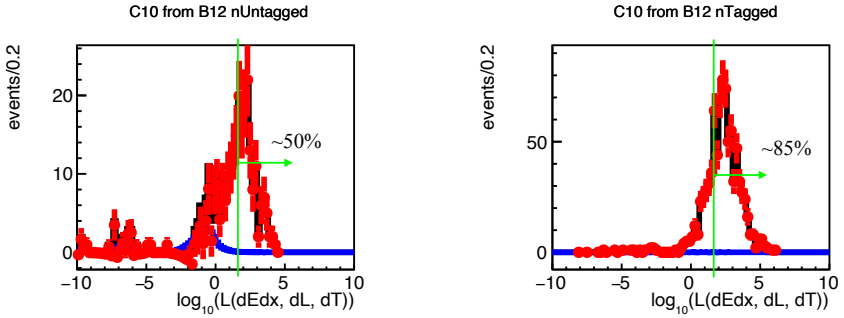

Figure 6.28: Log_{10}(likelihood) distribution for ^{10}C rejection with(right) and without(left) tagged neutron events are shown. The black dots are the data within on-time for dT scaled ^{12}B events, and blue dots are the accidental events. The red dots represents the signals((on-time)−(accidental)). The light green line is the threshold for the event rejection.

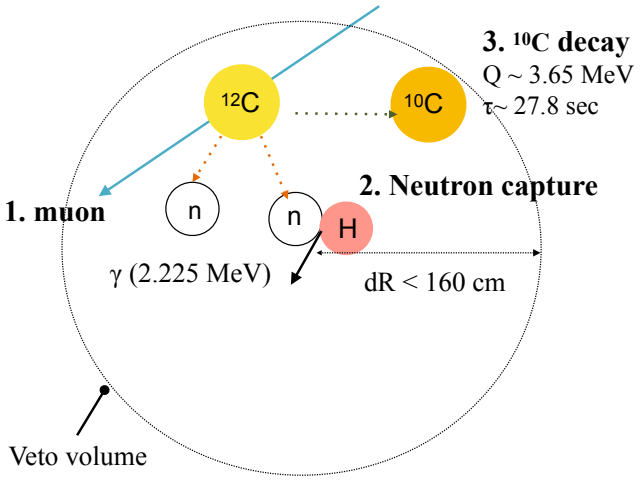

Figure 6.29: ^{10}C tagging
The figure shows the short-lived spallation event rejection by the MoGURA ^{10}C veto. The physical events within a distance of 160 cm between neutron capture events after muons are removed.

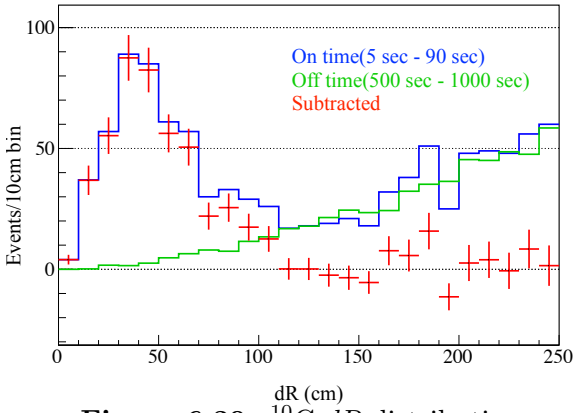

Figure 6.30: ^{10}C dR distribution
The event selections for ^{10}C were 250 cm $< r <$400 cm, 2.2 MeV $< Evis <$ 3.5 MeV. The dR selection efficiency was about 94%.

min within 160 cm radius from neutron capture events, which are selected by

$$N_{\mathrm{S}} > 240 \ \cap \ dT_{\mathrm{muon}} < 1,200 \ \mu\mathrm{sec}. \tag{6.31}$$

Neutron capture by ^{136}Xe is searched for by its high capture energy(4.0 MeV). Although neutron capture events by ^{136}Xe itself are not clearly found yet, N_{S} peak value was estimated at ∼310 (shown in Fig. 6.32) using neutron captures by ^{12}C(4.9 MeV) and H(2.2 MeV). Its inefficiency was estimated to be 74±7%. It comes from N_{S} cut efficiency and neutron tagging efficiency by H and ^{12}C. Untagged neutrons are caused by overshoot and afterpulses in short time distance($dT <\sim 50$ μsec). See Fig. 6.33.

- **Long-lived spallation products veto**
  Event rejection using the likelihood method is applied to reduce long-lived spallation products of ^{136}Xe. Their half-lives are from a few hundreds seconds to more than 10^6 sec. Neutrons are searched for by the same selections as the ^{10}C veto:

$$N_{\mathrm{S}} > 80 \ \cap \ dT_{\mathrm{muon}} < 30 \ \mu\mathrm{sec} \tag{6.32}$$

$$\cup \ (N_{\mathrm{S}} > 50 \ \cap \ 30 \ \mu\mathrm{sec} < dT_{\mathrm{muon}} < 1,200 \ \mu\mathrm{sec}) \tag{6.33}$$

Moreover, neutron multiplicity, which is the number of neutrons detected by Eq.(6.32) and Eq.(6.33) within 160 cm from the events, is used because almost all spallation products of ^{136}Xe have higher neutron multiplicity value. A likelihood function for the long-lived spallation veto is composed of a PDF of dR_{nearest} distribution and a PDF of dT distribution.

$$\mathrm{Likelihood} = \mathrm{PDF}(dR_{\mathrm{nearest}}) \times \mathrm{PDF}(dT) \tag{6.34}$$

Here, dR_{nearest} is the distance from the decay event of the spallation product to the nearest neutron (See Fig. 6.34). The likelihood value was calculated for

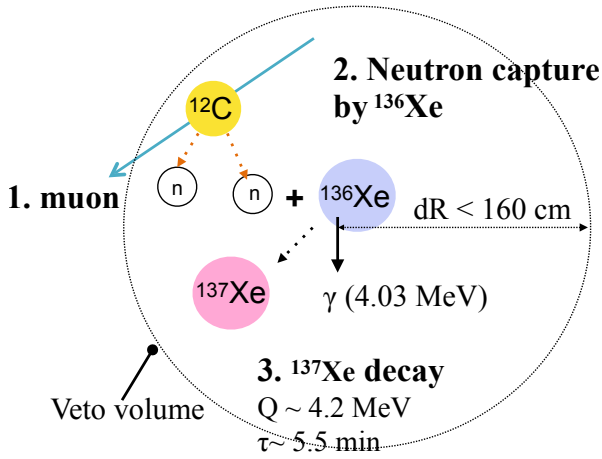

Figure 6.31: ^{137}Xe tagging
The figure shows the ^{137}Xe decay event rejection by the MoGURA ^{137}Xe veto. The physical events within a distance of 160 cm between neutron capture events by ^{136}Xe for 27 min after muons are removed.

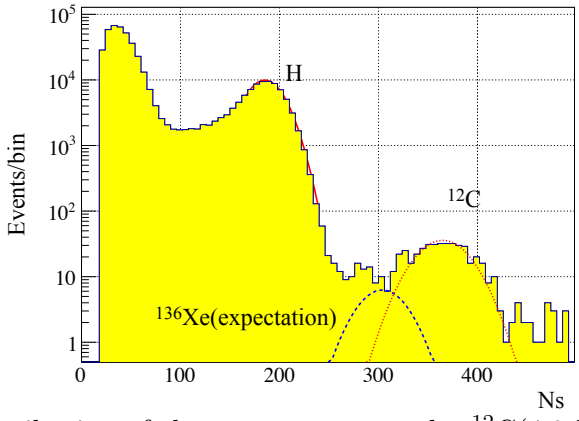

Figure 6.32: N_S distribution of the neutron capture by ^{12}C(4.9 MeV), H(2.2 MeV) and ^{137}Xe (expectation, 4.0 MeV)

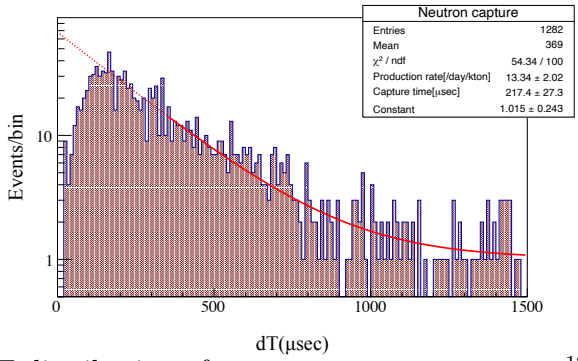

Figure 6.33: The dT distribution of neutron capture events on ^{12}C is shown. The event loss with short dT is due to the PMT afterpulses and overshoots.

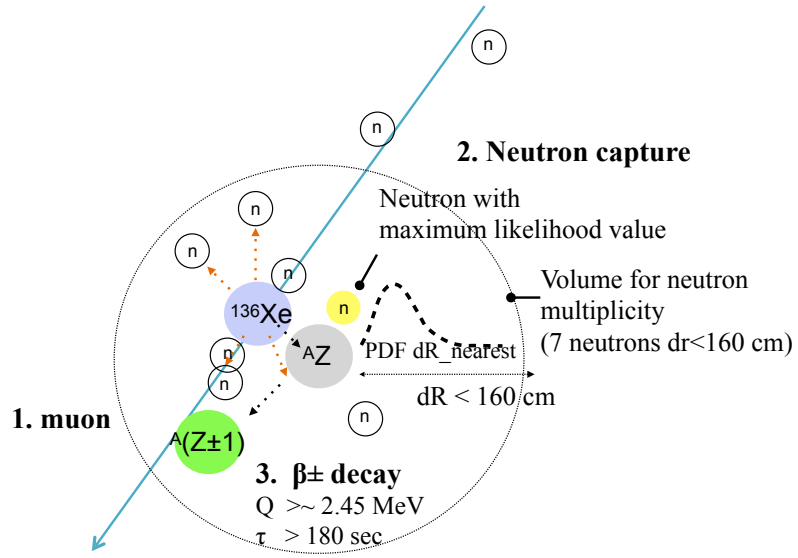

Figure 6.34: Long-lived spallation product tagging
The event rejection by the long-lived spallation veto is shown. The tagging is based on the time interval from muons to physical events, dR of the nearest neutron(yellow), and neutron multiplicity, which is the number of neutrons within a distance of 160 cm from the events.

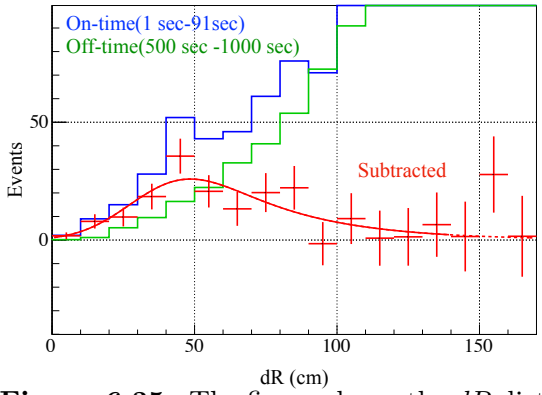

Figure 6.35: The figure shows the dR distribution of the short-lived products with a single neutron multiplicity.

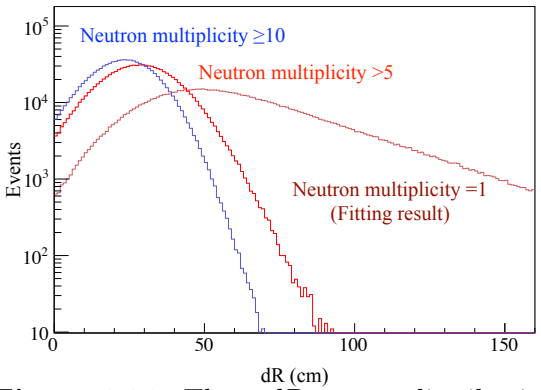

Figure 6.36: The dR_{nearest} distributions with high multiplicities made by a toy MC are shown.

all neutrons, and only the maximum one was used for the veto. The dR_{nearest} distribution was made with a toy MC simulation, which uses the measured dR distribution of the short-lived muon spallation products without neutron multiplicity (See Fig. 6.35 and Fig. 6.36). The dT distribution was made with a simulation study by FLUKA, which will be described in Chapter 8. The selection criteria are optimized with a figure of merit on $0\nu\beta\beta$ decay signal and expected long-lived spallation backgrounds.

$$\log_{10}(\mathrm{Likelihood}) > -6.95(\mathrm{Neutronmultiplicity} > 5) \tag{6.35}$$
$$\cup\log_{10}(\mathrm{Likelihood}) > -7.85(\mathrm{Neutronmultiplicity} > 30) \tag{6.36}$$

The event rejection efficiency of the long-lived products by the likelihood selections was estimated to be about 40%.

6.4 Livetime

Livetime is determined by multiplying the number of remaining events at runtime after adding the same cut as the data to the MC events generated uniformly in time and space. See Eq.(6.37). The actual event information in the run is used for cutting, such as the muon, the delayed coincidence, the 1 PPS, and the missing waveform.

$$\mathrm{Livetime} = \frac{\mathrm{Number\ of\ MC\ events\ after\ selections}}{\mathrm{Number\ of\ Generated\ MC\ events}} \times \mathrm{Runtime} \tag{6.37}$$

The deadtime ratio for each event selection is summarized in Table 6.2, which is the ratio to the KamFEE runtime. Fig. 6.37 shows the deadtime ratio for each run. The livetime ratio to runtime is 66.6%, especially large deadtimes come from the MoGURA off periods, the MoGURA ^{10}C veto, the MoGURA long-lived veto, and the shower veto.

Table 6.2: Deadtime ratio
The deadtime ratio by each event selection is shown in the table. All cuts represent the deadtime ratio after applying all event selections.

Selection	Deadtime ratio (%)
Deadtime(KamFEE)	1.53
Deadtime(MoGURA)	6.17
Missing waveform	0.001
1 PPS	0.01
Delayed coincidence(Bi-Po + $\bar{\nu}_e$)	0.02
Spallation cut	
All muon 2 msec	0.07
LS muon 150 msec	3.12
MoGURA ^{10}C	5.92
MoGURA ^{137}Xe	0.59
MoGURA long-lived	12.10
Shower tag	11.69
All cuts	33.38

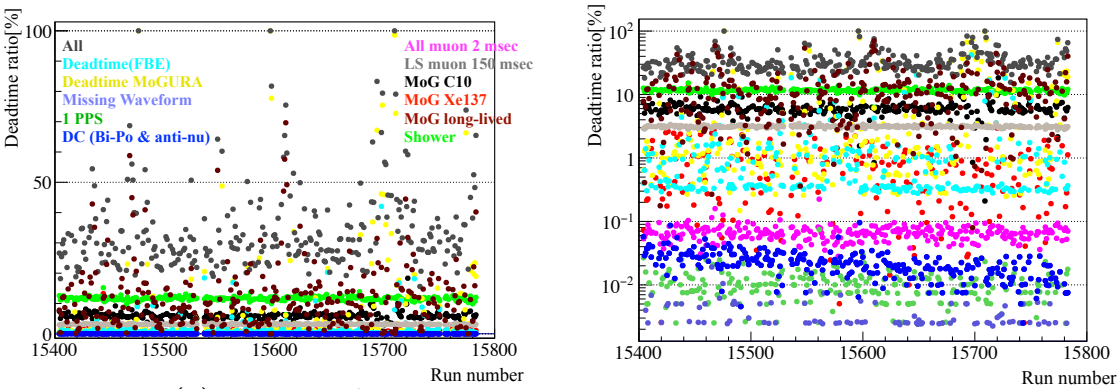

(a) Linear scale **(b)** Log scale

Figure 6.37: Deadtime ratio on each event selection
The large deadtimes in the right figure come from the MoGURA bad run and many run/sub-run changes in the MoGURA DAQ.

Chapter 7

MC Tuning and Detector Calibration

KLG4simulation is the KamLAND detector simulation based on GEANT4. Parameters in the KLG4simulation are adjusted to reproduce the data. Available calibration sources are a composite source and neutron capture gamma for the KamLAND LS, ^{214}Bi-^{214}Po, neutron capture gamma, and $2\nu\beta\beta$ decay for the Xe-LS.

7.1 Source Calibration

7.1.1 KamLAND LS Tuning

Parameters for the KamLAND LS are tuned by using data of composite source calibration campaign in January 2018 before the inner-balloon installation. A composite source containing ^{137}Cs(1γ 661.7 keV), ^{68}Ge(2γ's 551 keV) and ^{60}Co(2γ's 1173.2 keV +1332.5 keV) was installed in the KamLAND outer-balloon. The source was positioned every 50 cm from $z = -550$ cm to $z = 550$ cm using the KamLAND calibration system (MiniCal) [70]. Fig. 7.1b and Fig. 7.1a show the total charge and the number of hit PMTs of the composite source data at the KamLAND center. There are 3 peaks of gammas from ^{137}Cs, ^{68}Ge and ^{60}Co. Colored histograms represent that of MC simulation's. Birk's constant in the KamLAND LS was tuned to fit the peak positions.

Fig. 7.2 shows the position dependence of the peaks. Attenuation lengths, reemission probabilities, and scattering probabilities in both the KamLAND LS and buffer oil affect the results. Almost the same values are used in the new MC to [61]. The differences in the peaks are less than 2% within 2.5 m radius, which is the $0\nu\beta\beta$ decay analysis volume.

The difference between the actual position of the source and reconstructed vertex was shown in Fig. 7.3. The vertex difference is less than about 1% within $z = \pm 2.5$ m. This distribution in the MC could not be reproduced. The reason might be that the vertex fitter was tuned by actual data but not MC, and the fitter have many parameters to correct the reconstructed positions. It seems that these parameters reflect the

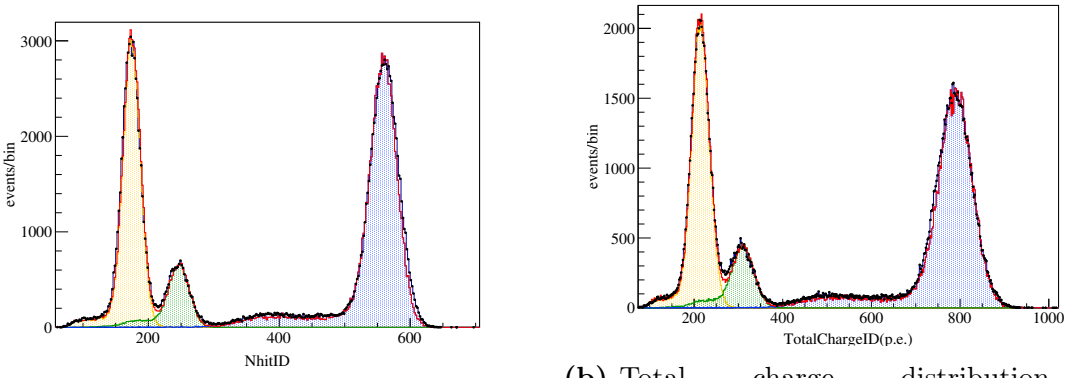

(a) Nhit distribution of ^{137}Cs^{68}Ge^{60}Co

(b) Total charge distribution of ^{137}Cs^{68}Ge^{60}Co

Figure 7.1: PMT hit and charge distribution of ^{137}Cs^{68}Ge^{60}Co
The black dots are data, orange of the composite calibration run. The colored histograms are that of MC simulations. The orange, blue, and green histograms indicate ^{137}Cs, ^{68}Ge , and ^{60}Co. All the peak positions agree with accuracy within 1% between the MC and data.

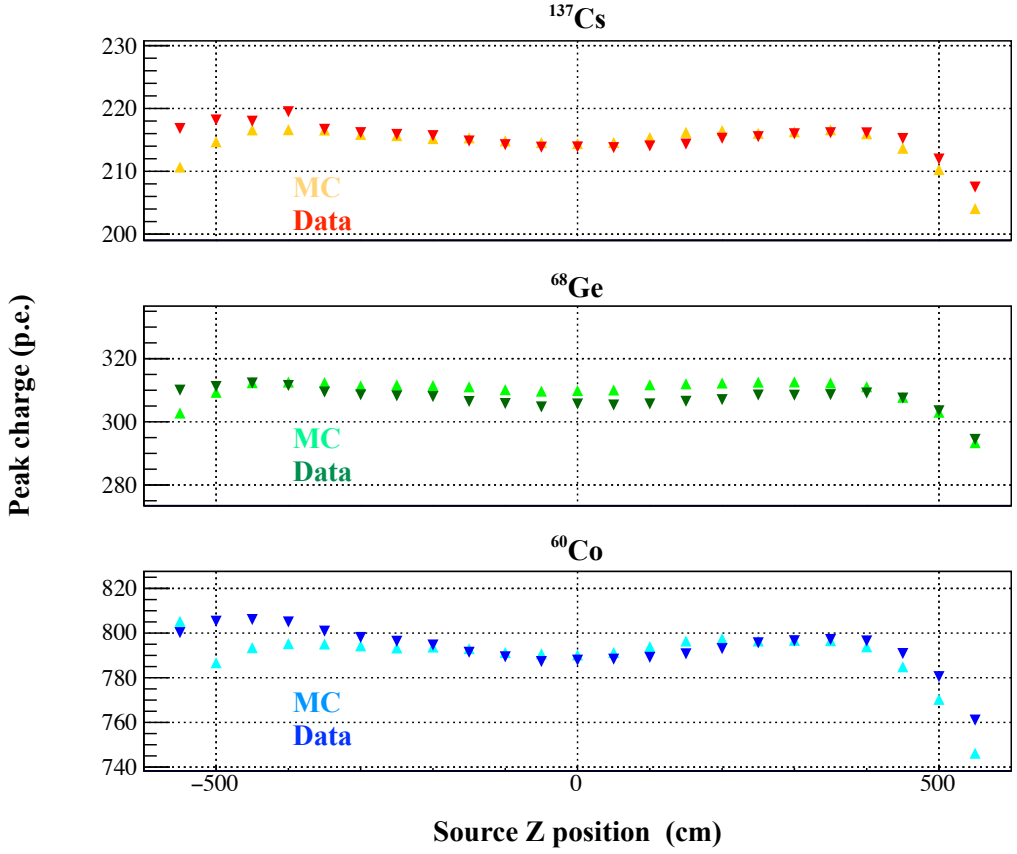

Figure 7.2: Position dependence of the ^{137}Cs^{68}Ge^{60}Co charge peaks
The differences in the charge peaks are less than 2% within the 2.5-m-radius analysis volume.

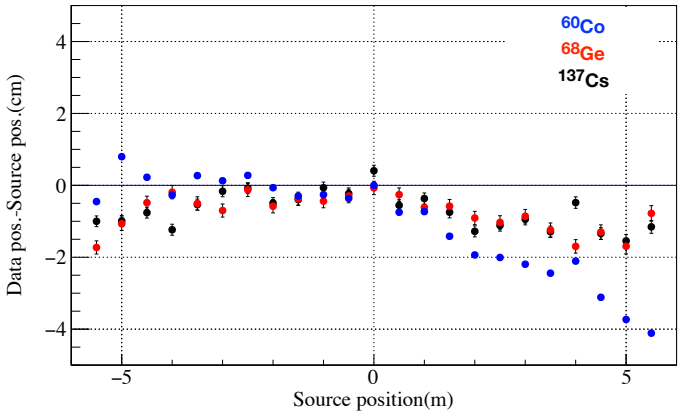

Figure 7.3: Position distribution of ^{137}Cs^{68}Ge^{60}Co
The position of ^{60}Co events was adjusted to the center. There is a deviation of about 2 cm ($\sim$ 1%) at the 250 cm radius.

difference between the actual detector and the detector made in the KLG4simulation, they might be the distortion of the balloon shape and inhomogeneous LS. The correction of the vertex bias is mentioned in Section 7.2.4.

The spread of the reconstructed vertex from the actual position was checked. It was shown in Fig. 7.4 for the center source position.

The position dependence of the vertex resolution was checked by the spread of the reconstructed z positions. It is shown in Fig. 7.5. The difference of the position dependence of the vertex resolution between the MC and the data in the KamLAND-LS was less than 0.5 cm within 250 cm radius.

The T-Q waveform, which is the distribution of PMT hit timings, was used to adjust the resolution of the vertex with MC and data. The T-Q waveform of the source at the center is shown in Fig. 7.6.

7.2 Xe-LS Tuning

The calibration campaign with composite sources has not performed after the inner-balloon installation. The source calibration in the Xe-LS will be very useful for vertex calibration and an establishment of a PID method. However, careful studies and preparation are needed, since there exists a possibility for the pollution and damage of the inner-balloon, loss of the loaded Xe gas, and contamination in the Xe-LS. Fortunately, the Xe-LS had many decay events of the ^{222}Rn coming from emanations of the tanks and pipelines. The daughter nuclei ^{214}Bi and ^{214}Po can be selected purely by the delayed coincidence selection, and they exist only inside the inner-balloon, so ^{214}Bi and ^{214}Po were available as a calibration source in the Xe-LS. Other sources are the neutron capture gamma(2.225 MeV) after muons and ^{136}Xe $2\nu\beta\beta$ decay. The camera view was also used to check the refractive index.

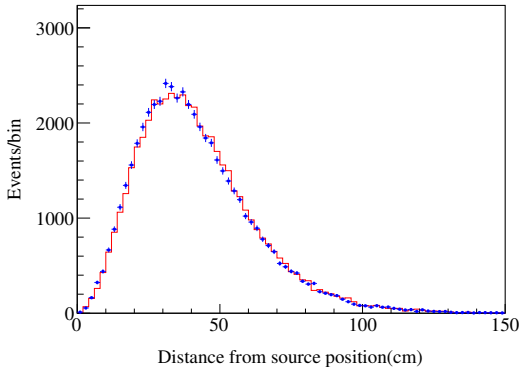

(a) ^{137}Cs

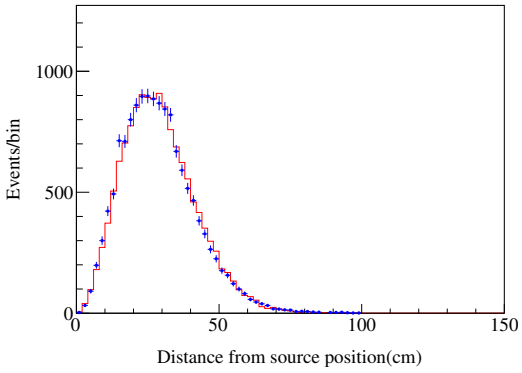

(b) ^{68}Ge

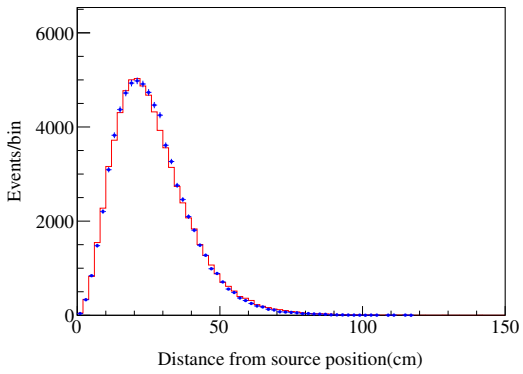

(c) ^{60}Co

Figure 7.4: Vertex distance from ^{137}Cs^{68}Ge^{60}Co source position for data(blue dots) and MC simulation(red histogram)

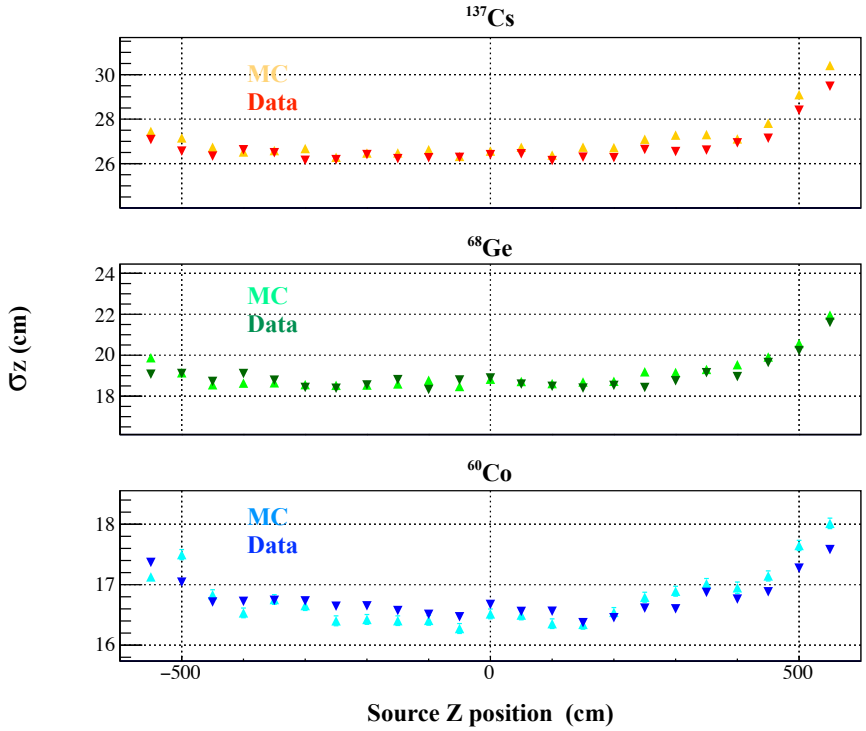

Figure 7.5: Position dependence of vertex resolution
The differences in the vertex resolution are less than 0.5 cm in the 250-cm-radius analysis volume.

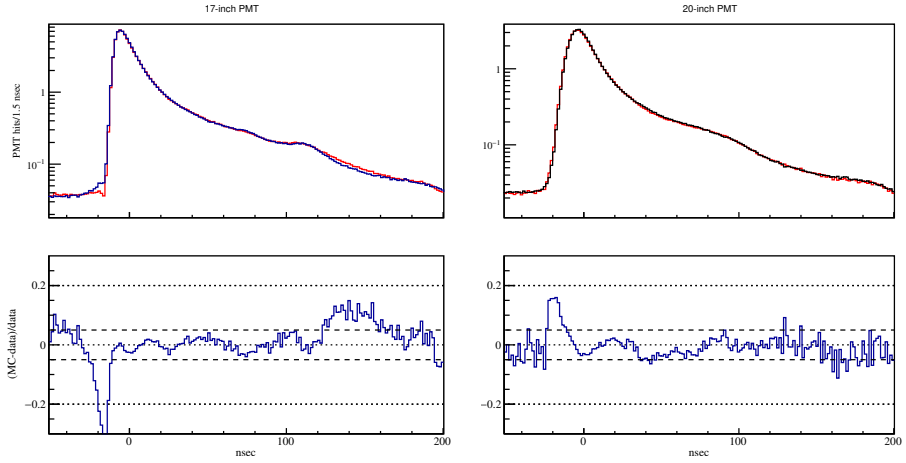

(a) ^{137}Cs

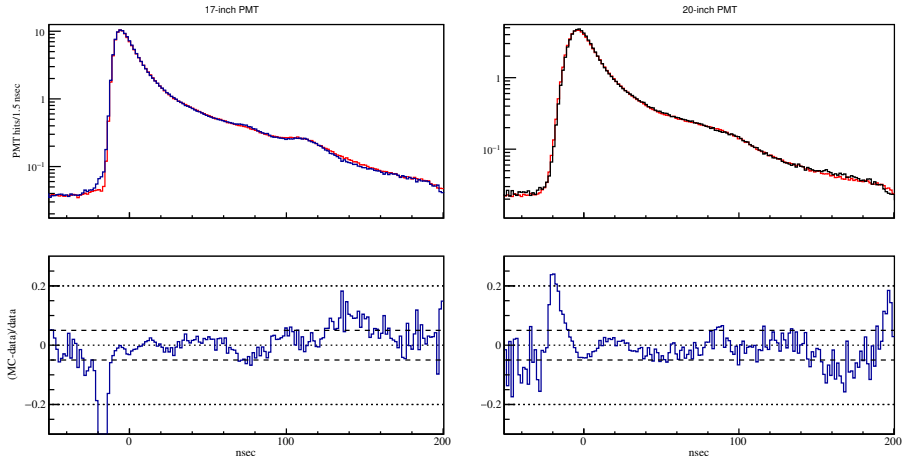

(b) ^{68}Ge

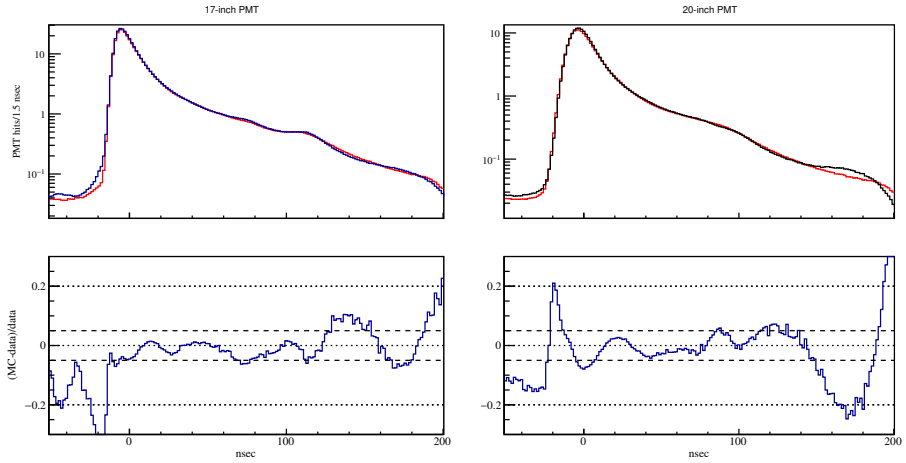

(c) ^{60}Co

Figure 7.6: T-Q waveform of the composite source
Blue and black histograms are data, and red histograms are MC simulation in the top figures. The bottom figures show the deviations.

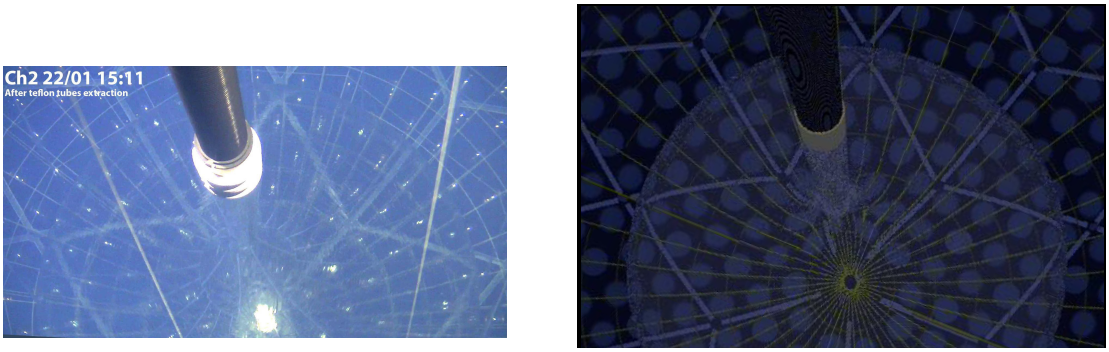

Figure 7.7: Camera view check by ray-tracing
The monitor camera view(left) and the reproduction of the view by GEANT4 ray-tracing(right) are shown. The refractive index in the Xe-LS was adjusted.

7.2.1 Camera View Check by Ray-Tracing

The refractive index in the Xe-LS was decided by comparing the camera view with the view made by ray-tracing in the KLG4simulation. The same refractive index as the KamLAND-Zen 400 MC, which is 1.45 at 400 nm, had a good agreement with the camera view (See Fig. 7.7).

7.2.2 Energy Calibration

^{214}Bi and ^{214}Po just after dissolving Xe from run015374 to run015404 until the Teflon tube was pulled out were used as calibration sources. Birk's constant, attenuation length, scattering probability, LS decay time properties, and re-emission in the MC were adjusted to match the data. Visible energy in the Xe-LS was corrected using ^{214}Po and neutron capture gamma.

Position Dependent Energy Correction

Visible energy in the Xe-LS has radius and theta-dependence. They are corrected with a function made by fitting that of the $0\nu\beta\beta$ MC simulation. The procedure is followings:

1. Radius-theta dependence in the Xe-LS of the data was confirmed with ^{214}Po data and reproduced in the KLG4simulation (See Fig. 7.8).
2. $0\nu\beta\beta$ decay events are generated in the KLG4simulation.
3. The correction function was made by fitting the MC $0\nu\beta\beta$ decay events.

Fig. 7.8 is the Q-R distribution of ^{214}Po data and MC in the XeLS. The optical parameters, such as absorption length, re-emission, and scattering, are adjusted to fit the MC to the data. Fig. 7.9 is the Q-theta distribution in each radius bin of data and MC in the Xe-LS. The asymmetry distribution can be made by the influence of bad channels and the asymmetry of the inner-balloon. This distribution was reproduced

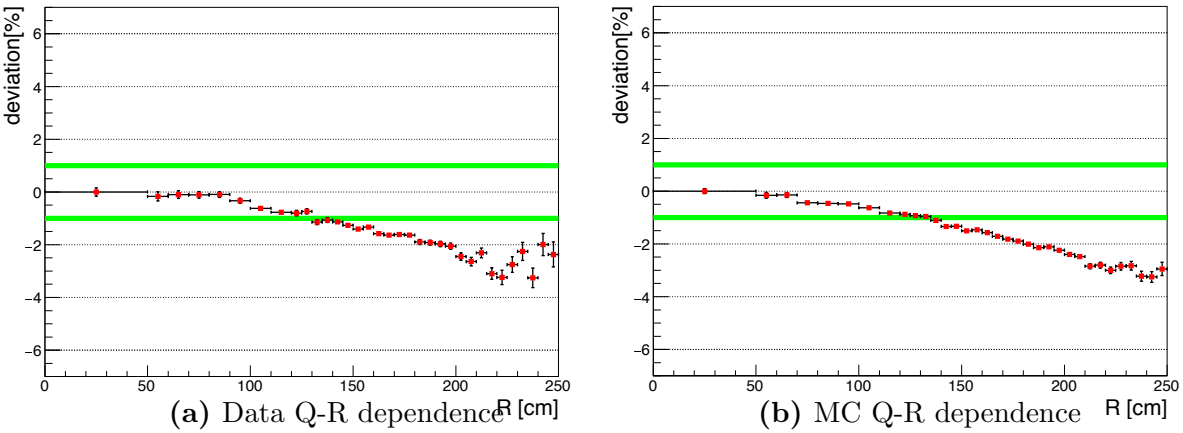

(a) Data Q-R dependence **(b)** MC Q-R dependence

Figure 7.8: Q-R dependencies of ^{214}Po in data(left) and MC(right) are shown. The Q peak values of ^{214}Po events in each position were determined by fitting the charge distribution with Gaussian functions.

in the MC except for the IB bottom position. It can be explained by the heavy PC-riched LS. The Q-R distribution of the visible energy in ^{214}Po data after correction is shown in Fig. 7.10. The deviation is within 1% for all radius bins.

Energy Non-Linearity Correction

Quenching and Cherenkov lights are the reasons for the non-linear response of the visible energy of the liquid scintillator. The quenching effect is caused by the difference in ionization density depending on the type of primary particles and their energies. The Birk's formula is usually used for describing the quenching effect as a suitable model, and used in the MC simulation.

$$\frac{dL}{dx} \propto \frac{\frac{dE}{dx}}{1 + k_B \cdot \frac{dE}{dx}} \tag{7.1}$$

where, dL/dx is light yields per distance dx, dE/dx is energy deposit per distance dx, and k_B is a constant called "Birk's constant". The effect of the Cherenkov light is also parameterized by "Cherenkov ratio"(R_C), which is the ratio of the Cherenkov light and the scintillator light. The Birk's constant in the KamLAND LS is tuned with the source calibration data. Energy non-linearity parameters in the Xe-LS were decided by comparing ^{214}Bi spectrum of the data with the ideal spectrum from a calculation (See Fig. 7.11). They are k_B=0.31 and R_C=0.02, respectively. Fig. 7.12 shows the visible energy of data and the MC simulation. The k_B and R_C in the MC simulation are tuned to fit ^{214}Bi spectrum shape of the MC to the data.

Energy Scale Correction

The energy scale was corrected using neutron capture gamma (2.225 MeV). The data was corrected so that the energy of the neutron capture in the Xe-LS would match

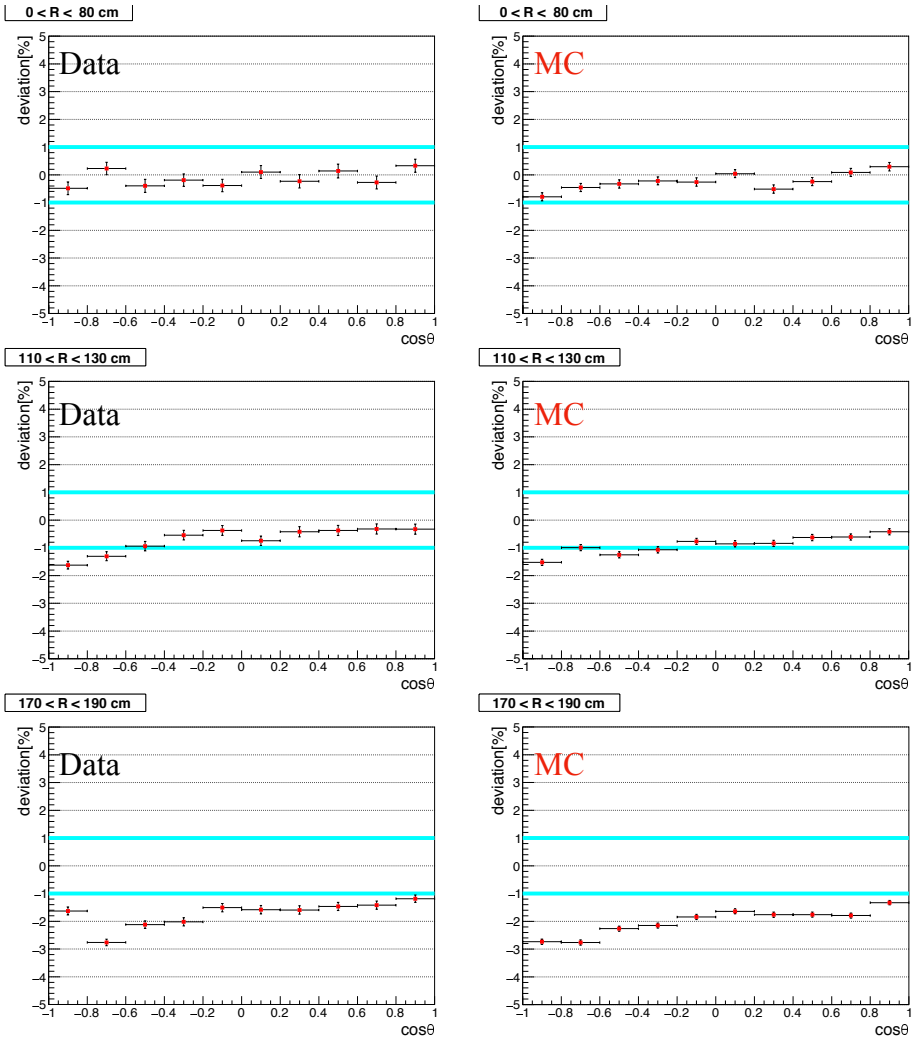

Figure 7.9: Q-theta dependence of the ^{214}Po MC and data is shown. The MC distributions reproduced well that of the data except for at the inner-balloon bottom.

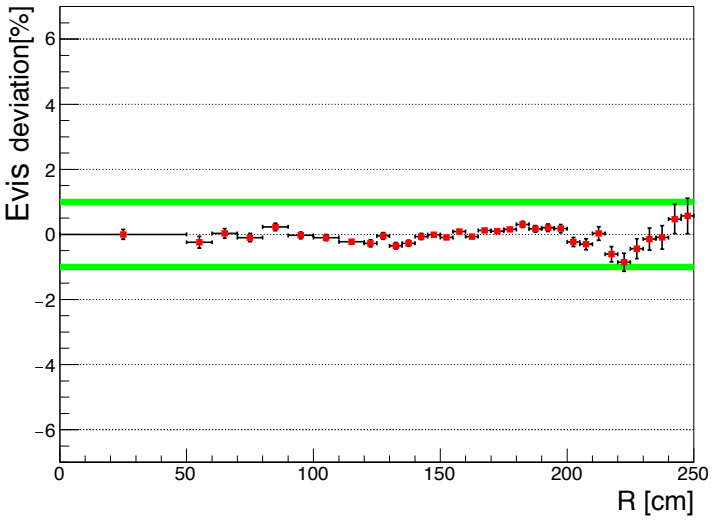

Figure 7.10: The R dependence of ^{214}Po visible energy after the correction based on the MC distribution is shown. The deviation in the visible energy by the position dependence is less than 1 %.

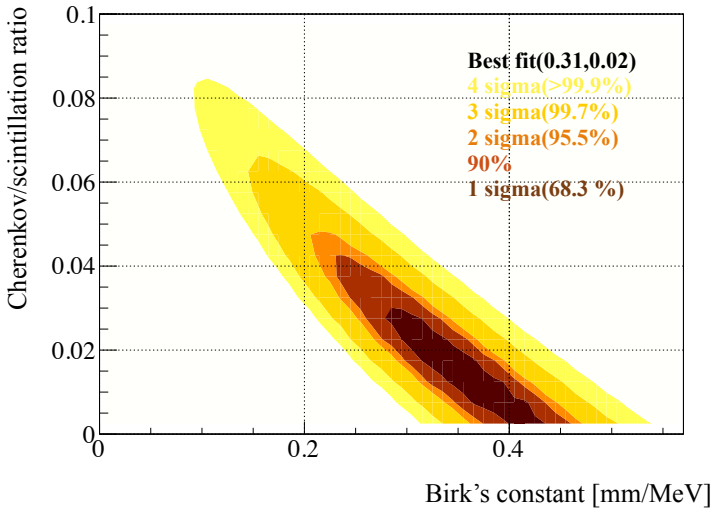

Figure 7.11: Allowed region of Birk's constant and Cherenkov/scintillation ratio of ^{214}Bi is shown. The dark brown represents the 1σ region, the 90% allowed region is the red-brown, the 2σ region is orange, the 3σ region is light orange, and the 4σ region is yellow. The best fit value was (0.31, 0.02).

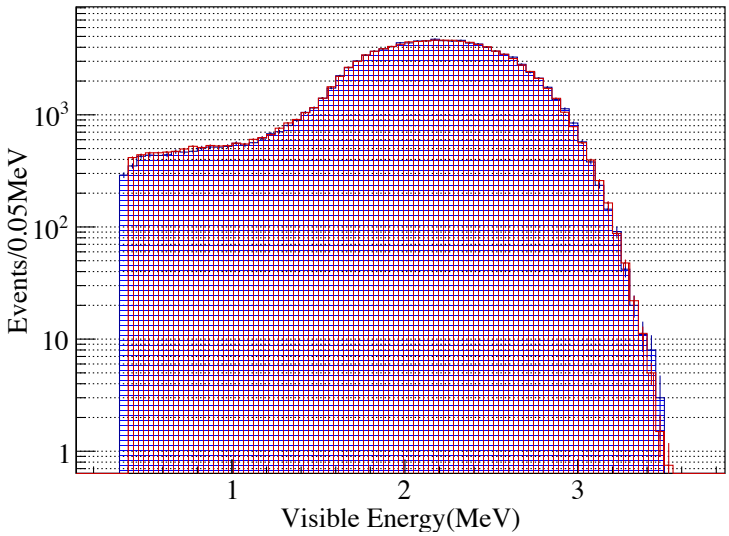

Figure 7.12: Visible energy distribution of ^{214}Bi for data and MC is shown. The MC simulation was able to reproduce high energy tail of ^{214}Bi events, which implies that the background events of the the $2\nu\beta\beta$ high energy tail is also reproduced well.

2.225 MeV (See Fig. 7.13a). The peak positions are different in the KamLAND LS and the Xe-LS. The Xe-LS contains more PPO than in the KamLAND LS, but the light yields in the Xe-LS is lower due to quenching by Xe gas. The neutron capture events were selected by $dT > 400$ μsec, since the visible energy with small dT is affected by overshoots and after-pulses in the PMTs. The ratio of light yield in the MC of the KamLAND LS and the Xe-LS was also adjusted so that the visible energy ratio of the KamLAND LS and the Xe-LS of the neutron capture event by hydrogen atoms reproduces the data. Fig. 7.13b is the visible energy of the neutron capture in the MC. The KamLAND LS is 1.11 times brighter in visible energy than the Xe-LS.

7.2.3 Vertex Calibration

The basic idea is to create a MC simulation that reproduces the data, and perform the event reconstruction in the same was as the data. The TQ waveform was checked using ^{214}Bi with large statistics. The TQ waveform of ^{214}Bi is shown in Fig. 7.14a. The deference of the TQ waveform between the MC and the data is less than 5% from 0 nsec to 50 nsec, respectively. In general, when the PPO concentration is high, the decay time constant of LS decreases, so the time constant of Xe-LS is smaller than that of KamLAND-LS. The parameters after tuning are summarized in Table 7.1. The distance between ^{214}Bi-^{214}Po events can be used to check the vertex resolution in the Xe-LS. Fig. 7.15 shows the distribution of ^{214}Bi-^{214}Po event distance with the MC and the data, respectively. It shows that there is only a slight difference, which is less than 5 cm at 120 cm distance.

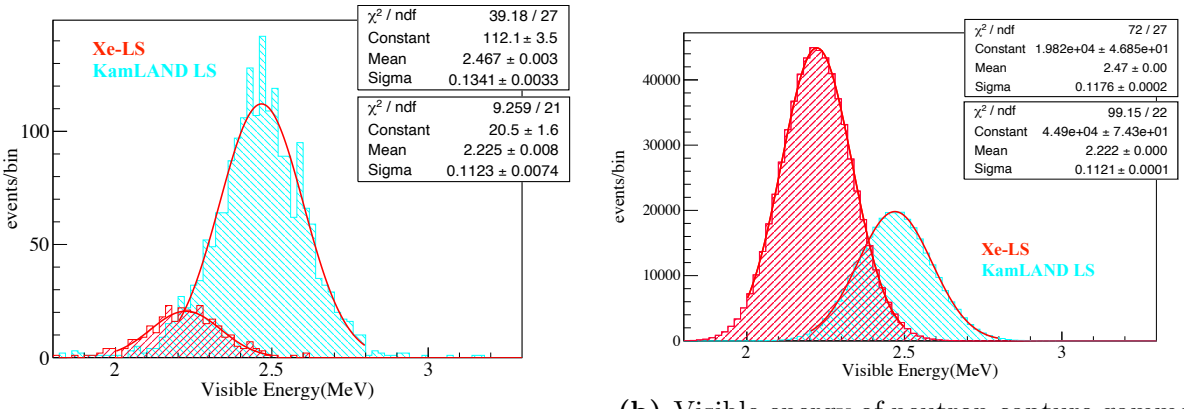

(a) Visible energy of neutron capture gamma of data in KamLAND LS and Xe-LS

(b) Visible energy of neutron capture gamma of MC in KamLAND LS and Xe-LS

Figure 7.13: Visible energies of neutron capture gamma of data(left) and MC(right) in KamLAND LS and Xe-LS are shown. The peak positions of both the KamLAND LS and the Xe-LS were reproduced well in the MC.

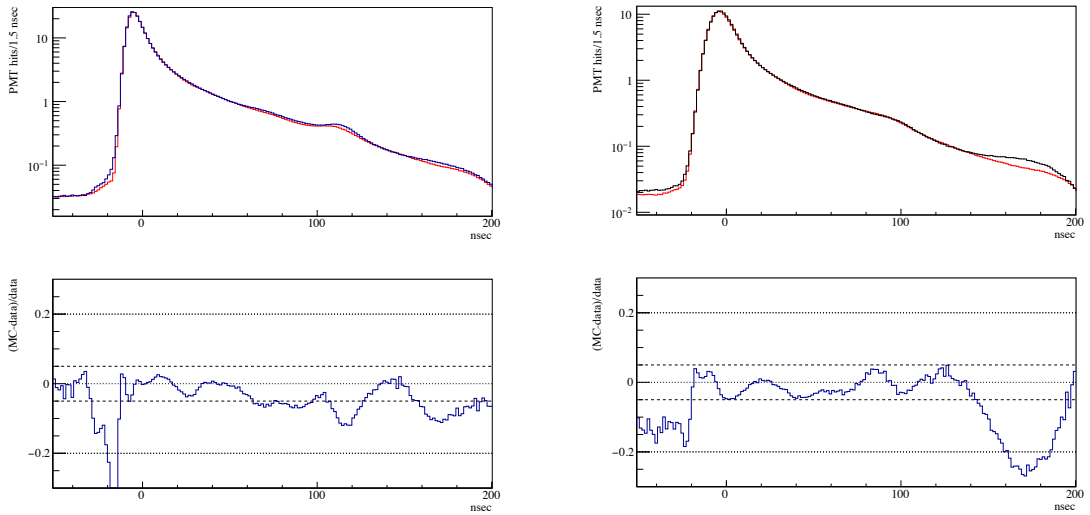

(a) TQ waveform of ^{214}Bi events in 17-inch PMT

(b) TQ waveform of ^{214}Bi events in 20-inch PMT

Figure 7.14: TQ waveforms of ^{214}Bi events in 17-inch PMTs(left) and 20-inch PMTs(right) are shown. The bottom figures show their difference between the data and the MC.

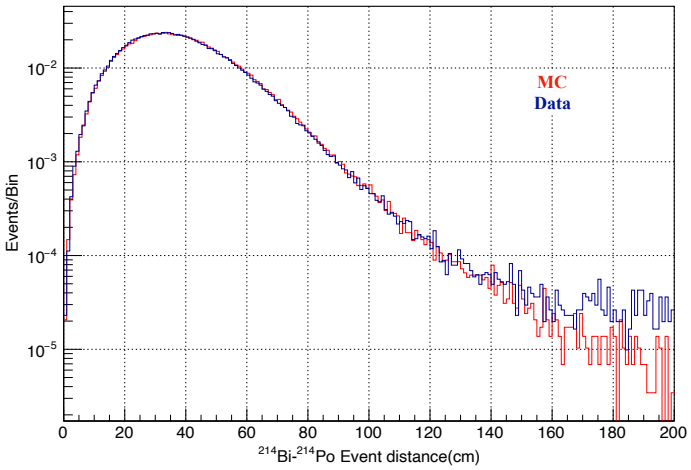

Figure 7.15: The distribution of the reconstructed event distances between prompt ^{214}Bi and delayed ^{214}Po is shown. The reproducibility of the vertex resolution can be confirmed.

Inner-Balloon Position and Xe-LS Vertex Scale

The inner-balloon is designed so that the inner-balloon center will be located at the detector center(x, y, z)=(0,0,0), but the actual inner-balloon position is not exactly the center because of the stretch of the corrugated tube, the shape difference between the design and the real, the amount of the Xe-LS, and the different tension of the IB supports. In addition, the source calibration for the Xe-LS vertex correction, which was performed in KamLAND-Zen 400, suggests that the vertex correction for the Xe-LS is necessary. Although the balloon position was confirmed by strong Cs background from the fallout of the Fukushima nuclear power plant accident, there is no strong background on the new inner-balloon this time, so the actual position of the inner-balloon and the vertex scale factor for the data are determined with the spectral fit to the background model (See Fig. 7.16). Later Chapter 8 describes the background model, and Chapter 9 explains the spectrum fit. Note that the major contribution for the spectrum fit is $2\nu\beta\beta$ decay. The position of the inner-balloon was determined to be (x, y, z)=(2.05 cm, 0.75 cm, −4.30 cm) from the KamLAND center. The vertex scale factor of the data was 1.012. The vertex difference of the inner-balloon surface is about 2.3 cm and is almost consistent with < 2 cm inside the 154-cm-radius inner-balloon of KamLAND-Zen 400, which is derived from the composite source calibration [61].

7.2.4 MC Vertex Bias

Vertex fitters were calibrated with the data but not with the MC simulation. The MC simulation has vertex bias. It was corrected with monochromatic single beta decays every 0.5 MeV from 0.5 MeV to 5.0 MeV generated in the KLG4simulation. The MC vertex correction function was made by comparing generated vertices and

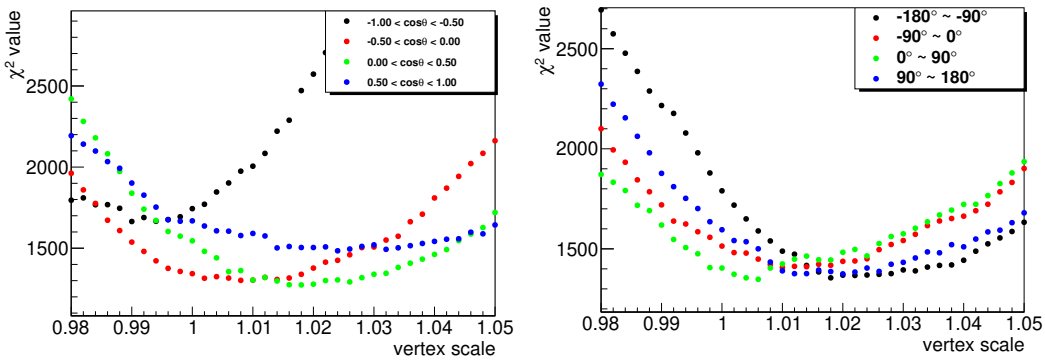

(a) Vertex scale dependence of the χ^2 values separated by 4-theta bins

(b) Vertex scale dependence of the χ^2 values separated by 4-phi bins

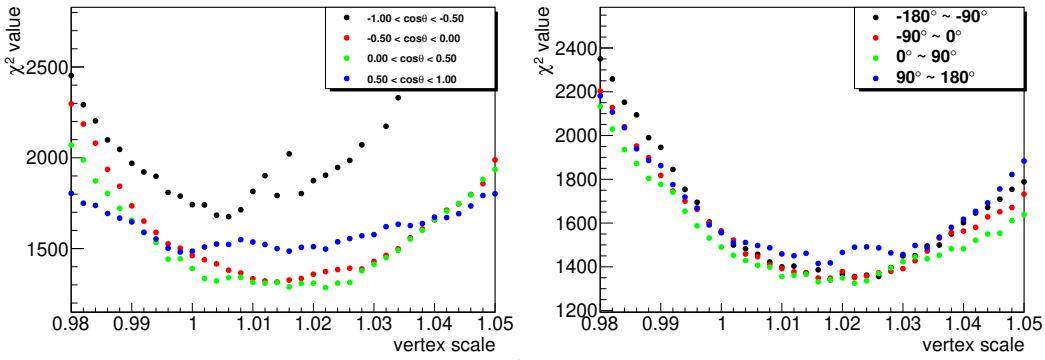

(c) Vertex scale dependence of the χ^2 values separated by 4-theta bins after position correction

(d) Vertex scale dependence of the χ^2 values separated by 4-phi bins after position correction

Figure 7.16: Vertex scale dependencies of the χ^2 values before correction(upper) and after correction(lower) are shown. The left figures show the distributions for each cosθ-bin and the right figures are for each ϕ-bin.

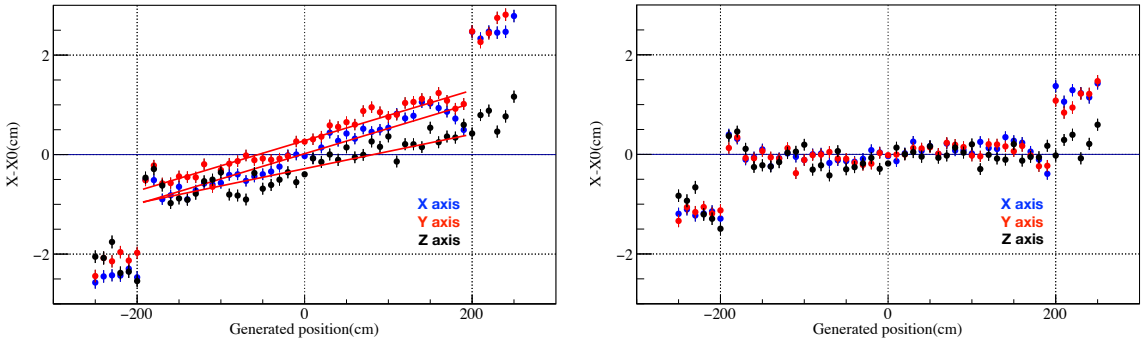

Figure 7.17: MC vertex bias correction at 2.5 MeV before correction(left) and after correction(right)

vertices through the vertex fitters. Fig. 7.17 shows the vertices before and after the correction of 2.5 MeV beta decay. The MC vertex bias is less than 1%.

7.3 Detector Stability

The detector stability is important. It has been confirmed with neutron capture events and $2\nu\beta\beta$ decay rate. Fig. 7.18 shows the energy stability of the neutron events after muons. The deviation of the neutron energy are stable within $\sim$1% in the Xe-LS. Also, Fig. 7.19 shows the $2\nu\beta\beta$ decay rate stability.

Table 7.1: MC parameter summary
The parameters for the Xe-LS, the KamLAND LS, and 17-inch and 20-inch PMTs in the KLG4simulation for KamLAND-Zen 800 are summarized. C.S represents the composite source calibration.

Material	Parameter	Value	Calibration source
KamLAND-LS	Light yield [p.e./MeV]	7909	n-capture
	Birk's [mm/MeV]	0.23	C.S.
	Absorption length at 400 nm[m]	12	C.S.
	Scattering at 400 nm[%]	49.4	C.S.
	Re-emission at 400 nm[%]	6.9	C.S.
	Scintillation time response (nsec,%)	-7.20, 79	C.S.
		-8.09, 17	C.S.
		-196, 4	C.S.
Xe-LS	Light yield [p.e./MeV]	6592	n-capture
	Birk's [mm/MeV]	0.31	^{214}Bi
	Absorption length at 400 nm[m]	15.8	^{214}Po
	Scattering at 400 nm [%]	58.9	^{214}Po
	Re-emission at 400 nm [%]	15.8	^{214}Po
	Scintillation time response for beta and gamma (nsec,%)×3	-3.7, 75	^{214}Bi
		-10.8, 21	
		-195, 4	
	Scintillation time response for alpha (nsec,%)×3	-3.8, 70	^{214}Po
		-17.2, 21	
		-185, 9	
17-inch PMT	T.T.S left [nsec]	1.8	
	T.T.S right [nsec]	2.5	
20-inch PMT	T.T.S left [nsec]	4.4	
	T.T.S right [nsec]	5.1	

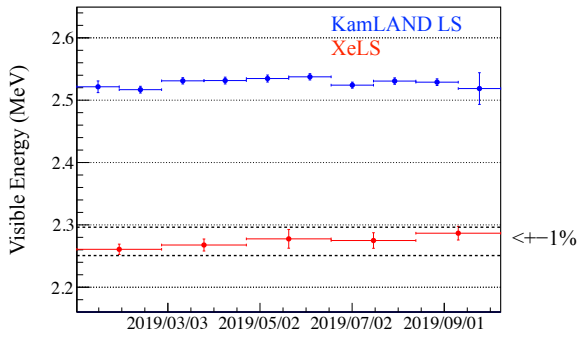

Figure 7.18: Neutron stability check
The stability in the peak of neutron capture gamma by H(2.2 MeV) is shown. The visible energy looks higher because events with short time intervals from muons are contained.

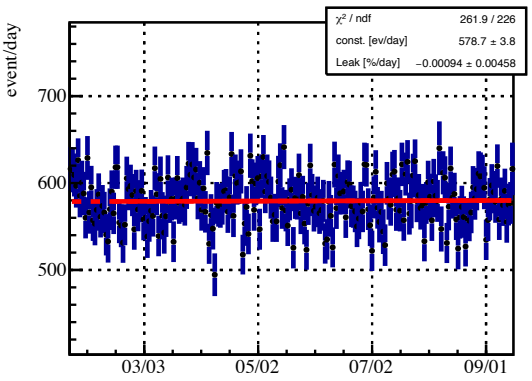

Figure 7.19: $2\nu\beta\beta$ decay rate stability
The stability of the $2\nu\beta\beta$ decay rate is shown. The decay rate was fitted with a linear function, and the leak amount was also confirmed.

Chapter 8

Background Model

8.1 Backgrounds

The background model used to fit energy spectra for $0\nu\beta\beta$ decay search was described in this chapter. Possible sources of the backgrounds are followings:

- $2\nu\beta\beta$ decay
- Natural radioactivities
  - ^{238}U series
  - ^{232}Th series
  - ^{40}K
  - ^{85}Kr
- Spallation products
- Solar neutrino
- External gammas

The source of the $2\nu\beta\beta$ decay is ^{136}Xe in the Xe-LS. Natural radioactivities are contained in all the Xe-LS, the inner-balloon film, and KamLAND LS except for ^{85}Kr, which is not included in the film because of the noble gas. The source generations in the MC simulation are separated by 3 parts the Xe-LS, the KamLAND LS, and the inner-balloon.

8.2 Natural Radioavtivities

8.2.1 ^{238}U Decay Series

^{238}U series was distinguished into the upstream and downstream of ^{230}Th, which has a relatively long life (half-life: 22.3 yr), and ^{210}Pb also has a long life. Therefore, the following ^{210}Bi decay is also considered separately.

- ^{238}U decay series 1 (US-1) $\cdots$ ^{234}Pa
- ^{238}U decay series 2 (US-2) $\cdots$ ^{214}Pb,^{214}Bi
- ^{210}Bi

Where, the branching from ^{214}Bi to ^{210}Tl was ignored because the branching ratio is 0.02%. The energy spectra of ^{238}U series are shown in Fig. 8.1. ^{214}Bi has high Q-value (Q=3.272 MeV), so it covers the energy region of interest in $0\nu\beta\beta$ decay (ROI, 2.35 MeV - 2.70 MeV). There are two types of ^{214}Bi (US-2) sources. One originates from ^{222}Rn (mean-life: 5.5 days), which is mixed in the Xe-LS during the Xe dissolving because of pipeline and tank emanations. The other comes from its upstream ^{238}U contamination. ^{222}Rn dissolved into the Xe-LS firstly decay with its half-life of 3.8 days, and its decayrate will reach the equilibrium with ^{238}U. Also, when filling LS with temperature difference by liquid circulation such as Xe dissolving and distillations, it causes convection in the KamLAND LS, and ^{222}Rn and ^{85}Kr rich LS mixes to the KamLAND LS from the top of the detector. ^{214}Bi decays originating from the equilibrium ^{238}U in the Xe-LS at the level of the order of 10^{-17} g/g can be ignored because the tagging efficiency of the delayed coincidence of ^{214}Bi-^{214}Po is high enough 99.98% [61]. Contamination of the ^{238}U is calculated with the number of the ^{214}Bi events as:

$$^{238}\mathrm{U[g/g]} = \frac{\mathrm{N}_{^{214}\mathrm{Bi}\text{-}^{214}\mathrm{Po}}[\mathrm{event}]}{\epsilon \times T[\mathrm{sec}] \times \text{Target mass[kton]} \times 12400[\mathrm{Bq/g}]}, \tag{8.1}$$

where, $\mathrm{N}_{^{214}\mathrm{Bi}\text{-}^{214}\mathrm{Po}}$ is number of detected ^{214}Bi-^{214}Po events, ϵ is the event selection efficiency, T is a livetime, Target mass is the Xe-LS or the inner-balloon mass which are calculated from 780 kg/m^3 or $\sim$1.5 kg/IB. 12400[Bq/g] is the ^{238}U activity. The unit of event rate [event/day/kton] used for the spectrum fit is

$$^{238}\mathrm{U[event/day/kton]} = \frac{\mathrm{N}_{^{214}\mathrm{Bi}\text{-}^{214}\mathrm{Po}}[\mathrm{event}]}{\epsilon \times T[\mathrm{day}] \times \text{Target mass[kton]}}. \tag{8.2}$$

The ^{238}U contamination in the Xe-LS is negligible if it is less than 2×10^{-16} g/g or $\sim$200 event/day/kton, indicating the ^{214}Bi backgrounds in the ROI is one order less than the ^{8}B solar neutrino backgrounds. The delayed coincidence tag is not efficient for the events from the inner-balloon, because the delayed α from ^{214}Po is absorbed in the film and does not deposit enough energy to the liquid scintillator. The tag efficiency for the film events is estimated to be 48$\pm$9% by comparing single event and tagged event rates. The ^{238}U contamination in the Xe-LS and the inner-balloon are $(1.5 \pm 0.4) \times 10^{-17}$ g/g and $(3 \pm 1) \times 10^{-12}$ g/g.

8.2.2 ^{232}Th Decay Series

The decay sequence of ^{232}Th series also contains a relatively long-lived daughter nucleus ^{228}Th (half-life: 1.9 yr), upstream of which is called Th series 1 (ThS-1) and downstream of it is called Th series 2 (ThS-2). Each has high decay energy nuclei as:

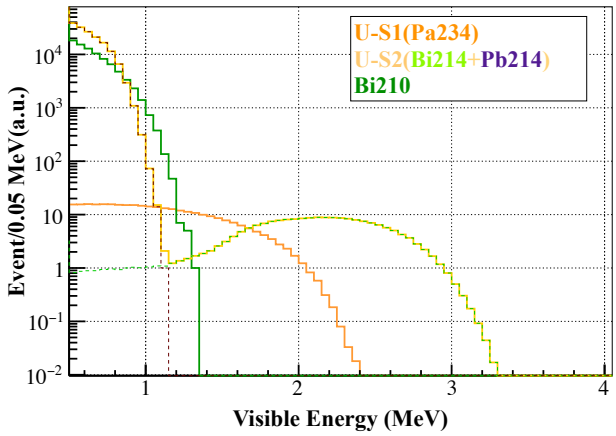

Figure 8.1: Energy spectra of ^{238}U series
The orange spectrum is ^{234}Pa, the light orange spectrum is US-2, and the green spectrum is ^{210}Bi. The dashed light green spectrum and the dashed purple spectrum are ^{214}Bi and ^{214}Pb in US-2, respectively.

- ^{232}Th decay series 1 (ThS-1) $\cdots$ ^{228}Ac
- ^{232}Th decay series 2 (ThS-2) $\cdots$ ^{212}Bi, ^{208}Tl

The energy spectra of the ^{232}Th decay series are shown in Fig. 8.2. The lead background in the ^{232}Th decay series is the pileup of the continuous decay of ^{212}Bi and ^{212}Po, which will be explained in the next section. The ^{220}Rn is also introduced during the Xe dissolving like ^{222}Rn, and it disappears with ^{212}Pb decay half-life of 10.64 hours. The ^{232}Th amount is estimated by the delayed coincidence measurements of ^{212}Bi-^{212}Po or ^{208}Tl events at the high energy region (3 MeV - 5 MeV).

$$\mathrm{Th[g/g]} = \frac{\mathrm{N}_{^{212}\mathrm{Bi}\text{-}^{212}\mathrm{Po\ or\ }^{208}\mathrm{Tl}}[\mathrm{event}]}{\epsilon \times T[\mathrm{sec}] \times \mathrm{Target\ mass[kton]} \times 4100[\mathrm{Bq/g}]} \tag{8.3}$$

The unit of event rate used for spectrum fits is

$$\mathrm{Th[event/day/kton]} = \frac{\mathrm{N}_{^{212}\mathrm{Bi}\text{-}^{212}\mathrm{Po\ or\ }^{208}\mathrm{Tl}}[\mathrm{event}]}{\epsilon \times T[\mathrm{day}] \times \mathrm{Target\ mass[kton]}}. \tag{8.4}$$

The energy selection efficiency of ^{208}Tl decay is about 80% at more than 3.0 MeV, and there are barely other background events, so the ^{208}Tl rate can be estimated by the single events. If the event rate of the ^{214}Bi is low enough, ^{212}Bi-^{212}Po can be tagged by the delayed coincidence measurements and the double-pulse fit of the pileup events. ^{232}Th contamination in the Xe-LS and the inner-balloon film were estimated to be $(30 \pm 4) \times 10^{-17}$ g/g and $(38 \pm 2) \times 10^{-12}$ g/g.

8.2.3 Pileup of ^{212}Bi-^{212}Po

Because the half-life of ^{212}Po is short (half-life: 299 nsec), it sometimes is detected as a pileup event in one event window, and the sum of decay energies of ^{212}Bi(Q=2.25

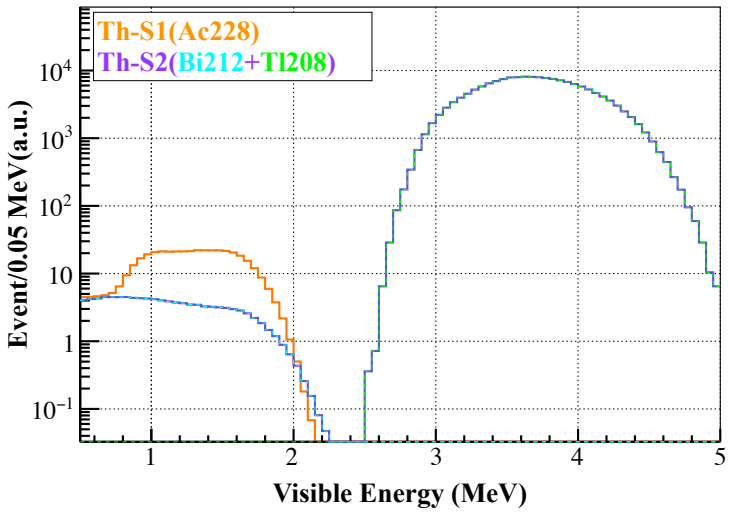

Figure 8.2: Energy spectrum of ^{232}Th series
The orange spectrum is ^{228}Ac, and the purple spectrum is ThS-2. The dashed cyan spectrum and the dashed light green spectrum are ^{212}Bi and ^{208}Tl in ThS-2, respectively.

MeV) and quenched ^{212}Po 0.73 MeV is detected if the time interval is too close. The pileup energy spectrum can overlap with the ROI of $0\nu\beta\beta$ decay (See Fig. 8.3). If the ^{232}Th contamination in the Xe-LS is less than 5×10^{-16} g/g, the pileup background in the ROI becomes less than the ^{8}B solar neutrino background ($\sim$ 0.2 events/day/kton in the ROI).

8.2.4 Others

^{40}K

^{40}K can be found everywhere in the world due to a long-lived natural radioactive nucleus like ^{238}U and ^{232}Th. ^{40}K was detected in the KamLAND LS, and in the KamLAND-Zen 400 inner-balloon, but not in the KamLAND-Zen 400 Xe-LS during Phase-II. ^{40}K is likely to be included as well in the new Xe-LS in KamLAND-Zen 800 and the new inner-balloon, although its finite value was not measured by the ICP-MS. ^{40}K has both electron capture (EC) and β^- decays (See Fig. 8.4). In the KLG4simulation, they are generated separately and added together with their branching ratio.

^{85}Kr

^{85}Kr is a radioactive noble gas. Its abundance in the atmosphere has been increasing year by year since it had been released from nuclear fuel reprocessing plants and is about $\sim$2 Bq/m^3 at present [71]. The finite value of ^{85}Kr was detected in the KamLAND LS [60]. Although the Xe gas in the Xe-LS has been purified by distillation, it is also contained in the Xe-LS. The decay rates in the KamLAND LS and Xe-LS

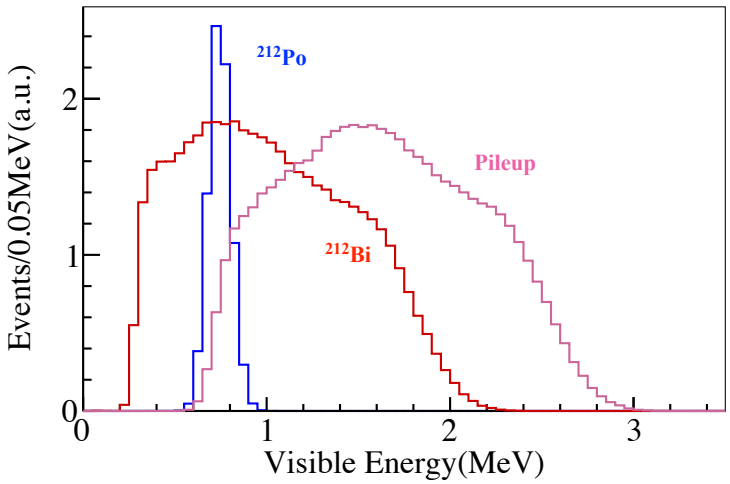

Figure 8.3: Energy spectrum of the pileup event of ^{212}Bi and ^{212}Po
The red spectrum is ^{212}Bi, and the blue spectrum is ^{212}Po. The pink spectrum is ^{212}Bi-^{212}Po pileup events with time intervals of less than 10 nsec.

depend on the period and the position. It is also possible to increase the rate by the inner-balloon installation.

^{134}Xe

^{134}Xe is also a double-beta decay nucleus. Approximately 9% of the Xe gas in the Xe-LS is ^{134}Xe. The Q-value is 0.825 MeV. The half-lives of the $2\nu\beta\beta$ decay and $0\nu\beta\beta$ decay are limited by EXO-200 [72], and the limits are respectively $T^{2\nu\beta\beta}_{1/2} > 8.7 \times 10^{20}$ yr and $T^{0\nu\beta\beta}_{1/2} > 1.1 \times 10^{23}$ yr at 90% confidence level. The $2\nu\beta\beta$ decay rate in the Xe-LS is less than 2.7×10^{4} event/day/kton. In this analysis, it was ignored because of the large backgrouds from ^{85}Kr and ^{210}Bi decays. Fig. 8.4 shows the energy spectra of ^{40}K, ^{85}Kr, and ^{134}Xe.

8.3 Inner-Balloon Contamination

8.3.1 Cleaner Inner-Balloon

The inner-balloon contains contamination of impurities such as ^{238}U, ^{232}Th, ^{40}K, and ^{210}Bi. The contamination of ^{134}Cs, ^{137}Cs, and ^{110m}Ag are assumed to be introduced by the Fukushima nuclear power plant accident, which had been observed in KamLAND-Zen 400, but not in KamLAND-Zen 800. The energy spectra for each radius in KamLAND-Zen 400 and KamLAND-Zen 800 are shown in Fig. 8.5.

The event distributions in each energy region are summarized in Fig. 8.6. The $2\nu\beta\beta$ decays of ^{136}Xe in the Xe-LS are dominant sources in the energy region from 1.2 MeV to 2.0 MeV. The ^{214}Bi decays at the film are still the main backgrounds in

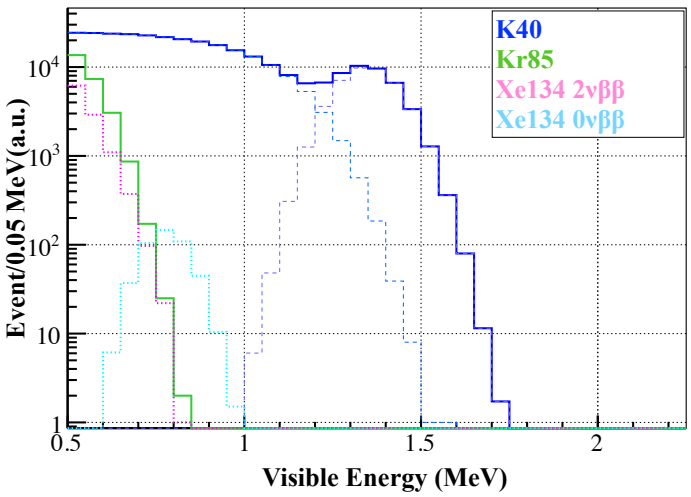

Figure 8.4: Energy spectra of ^{40}K(blue), ^{85}Kr(green), and ^{134}Xe(pink for $2\nu\beta\beta$ and cyan for $0\nu\beta\beta$) are shown.

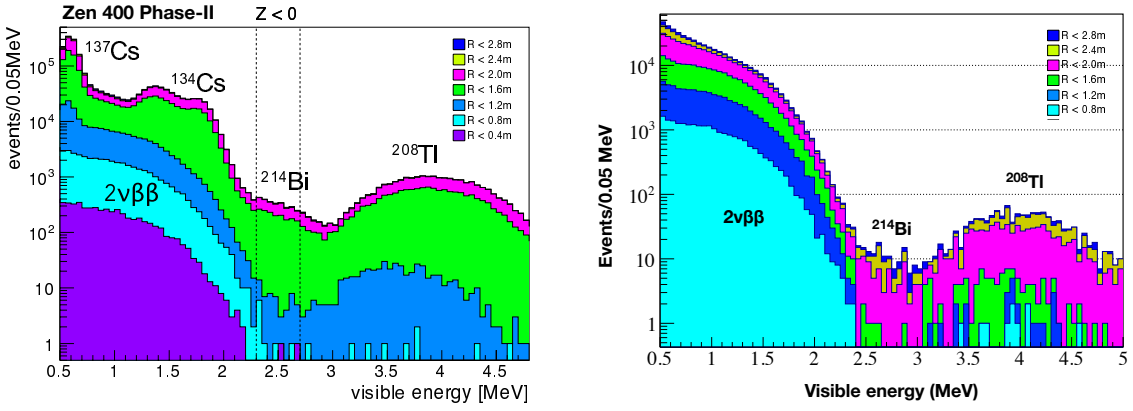

(a) KamLAND-Zen 400 Phase-II **(b)** KamLAND-Zen 800

Figure 8.5: Radius dependence of the energy spectra
The left figure is in the KamLAND-Zen 400 Phase-II from [61] and the right figure is in KamLAND-Zen 800. The peaks of ^{134}Cs and ^{137}Cs are absent in the right figure.

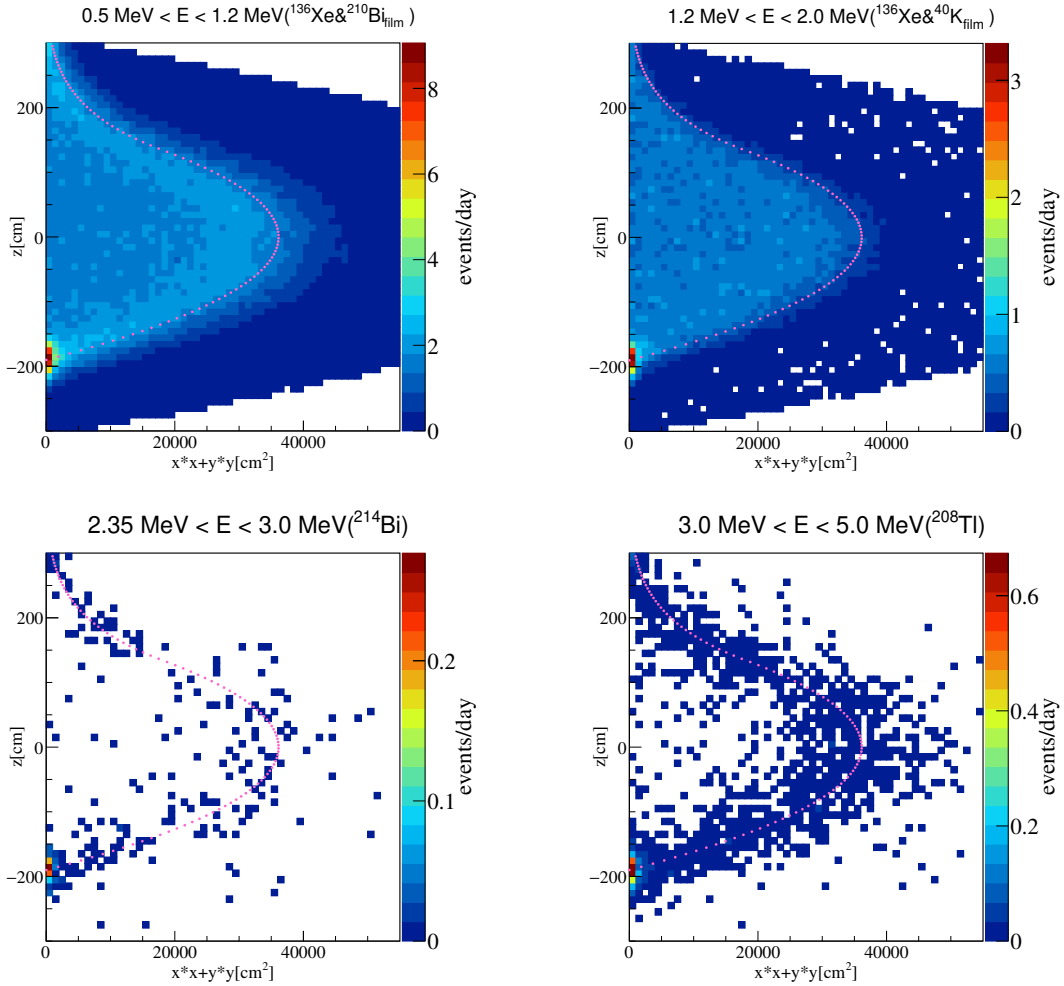

Figure 8.6: The position distributions of events for each energy region are shown. The pink dot line is the inner-balloon shape.

the ROI. There are many ^{208}Tl decays at the film in the region from 3.0 MeV to 5.0 MeV.

8.3.2 Hot Spot at IB Bottom

There exists a hot spot at the IB bottom, where the radioactivites of ^{238}U and ^{232}Th are $\sim$ 10 times higher than the others. The energy spectrum in the hot spot was confirmed, and there was no strange peak in the hot spot (See Fig. 8.7). The events within 70 cm radius from the bottom hot spot(0,0,$-$190.1 cm) were vetoed in the $0\nu\beta\beta$ decay search analysis.

8.3.3 ϕ Distribution

Except for the hot spot at the bottom region, there was no other hot point on the inner-balloon. $\cos\theta$-ϕ distribution of the inner-balloon events are shown in Fig. 8.8.

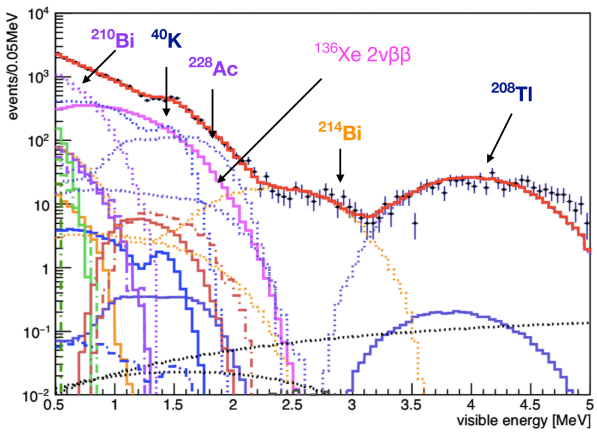

Figure 8.7: Energy spectrum of bottom hot spot is shown. The spectrum was fitted with the inner-balloon natural radioactivity backgrounds, such as ^{238}U decay series, ^{232}Th decay series, and ^{40}K.

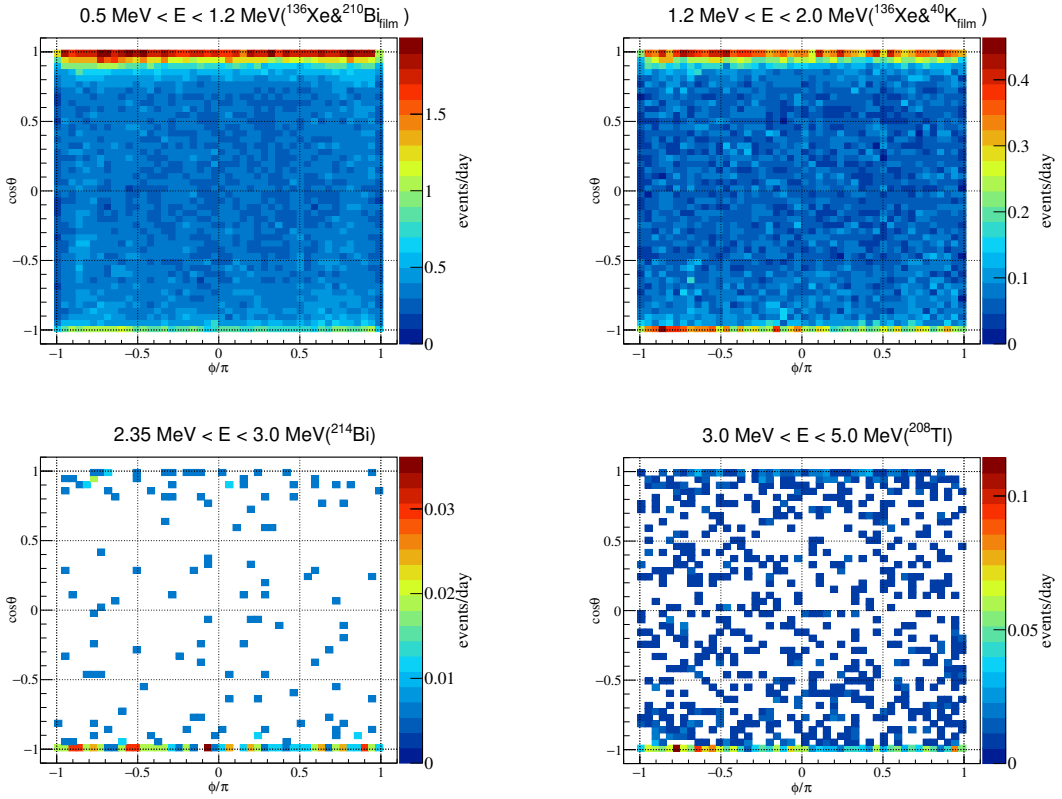

Figure 8.8: $\cos\theta$-ϕ distributions on the inner-balloon film for each energy region are shown. The film events are selected within ± 15 cm from the inner-balloon film.

Table 8.1: Neutron capture ratio
The cross-sections refer to [73] and JENDL. Natural abundance of ^{13}C 1.1% is assumed.

Nucleus	Energy [MeV]	# of atoms/g_{Xe-LS}	cross-section[mb]	capture ratio[%]
H	2.22	8.35×10^{22}	332.0	99.31
^{12}C	4.95	4.15×10^{22}	3.86	0.57
^{136}Xe	4.03	1.26×10^{20}	238	0.11
^{134}Xe	6.36	1.21×10^{19}	265.1	0.01
^{13}C	8.17	4.6×10^{20}	1.37	< 0.002

8.3.4 Non-Uniform $\cos\theta$ Distribution

Non-uniformity in $\cos\theta$ distributions for ^{214}Bi and ^{208}Tl were checked to construct the non-uniform background model in the MC simulation. The background rates were determined by fitting the r^3 distribution. The events of ^{214}Bi decays were selected by the delayed coincidence for high statistics, although the single events are better since the delayed α could be absorbed with massive particle contamination. The single events from 3 MeV to 5 MeV were selected for ^{208}Tl. The fitting result of r^3 distribution of ^{214}Bi is shown in Fig. 8.9. $\cos\theta$ dependence of ^{214}Bi and ^{208}Tl events are shown in Fig. 8.10 and Fig. 8.11, respectively.

8.4 Spallation Backgrounds

Spallation products by cosmic ray muons are one of the most serious backgrounds. They have been studied in the past [66] in the KamLAND LS. The neutron and shower tags are effective in reducing the backgrounds; they have already been described in Chapter 6.3.5. For light nuclei, the decay rates were estimated by using data in the KamLAND LS for the same analysis periods. Also, there are spallation products of ^{136}Xe in the Xe-LS. The number of background events was estimated based on studies by simulation using FLUktuierende KAskade (FLUKA) and Evaluated Nuclear Structure Data File (ENSDF).

8.4.1 Neutron Capture

The ratio of neutron capture is estimated from the number of atoms and cross-sections on the thermal neutron capture. It is summarized in Table 8.1. The number of neutrons generated by the KamLAND LS is ∼3300 /day/kton, which can be used to estimate the capture rate. However, 10-20% more capture neutrons were detected in the Xe-LS. The 22% error from [61] was taken into account in the background estimations with the KamLAND LS.

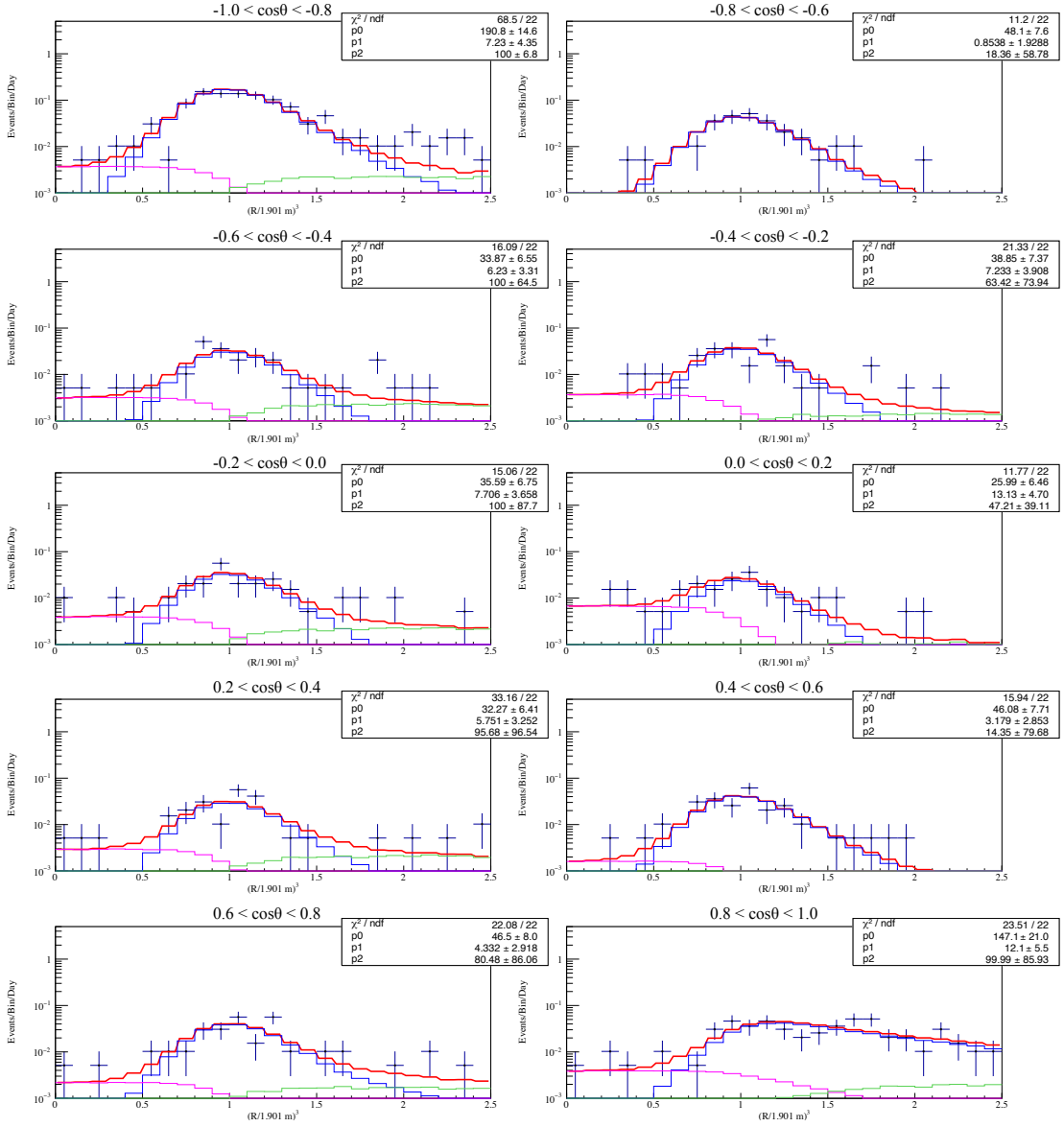

Figure 8.9: r^3 distribution for each $\cos\theta$ region is shown. The events are fitted with the distributions(red) composed of the Xe-LS(pink), the inner-balloon(blue), and the KamLAND LS(light green) made by the MC simulation.

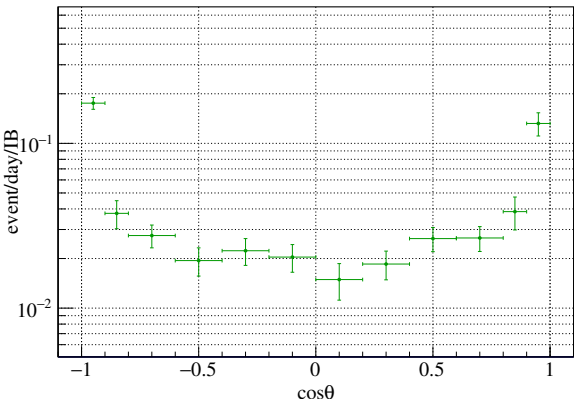

Figure 8.10: cosθ dependence of ^{214}Bi event rate is shown.

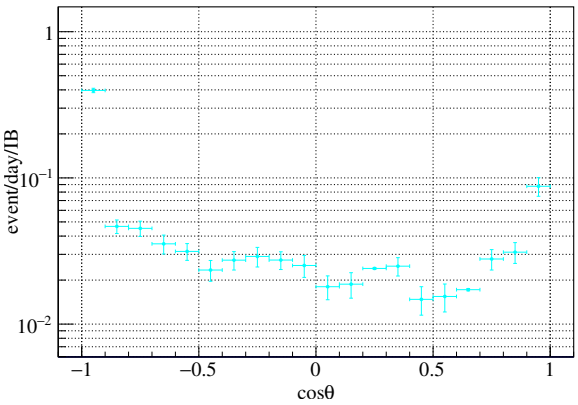

Figure 8.11: cosθ dependence of ^{208}Tl event rate is shown.

8.4.2 Light Isotopes

^{12}C nucleus spallation by muons produces unstable nuclei. Particularly, ^{10}C decay is a serious background, which can be tagged with the MoGURA neutron veto because the spallation involves many neutrons. Except for ^{11}C decay, which has a long half-life, the production rate by the muon spallation can be estimated by fitting the time interval spectrum from muons in each energy simultaneously. The event rate ($\frac{dN}{dt}$) at time t is written as

$$\frac{dN}{dt} = \sum_i N_i \times \exp(-t/\tau_i) + C, \tag{8.5}$$

where N_i is the amount of the generated product i, τ_i is its mean lifetime, and C is the accidental background rate. The data is filled into log scale bins and fitted. The results of the time spectrum fitting are shown in Fig. 8.12. The neutron-untagged and shower-tagged rate are also evaluated in the same way with neutron-untagged events. The remaining event rates were determined based on the neutron-untagged event rates and the shower tagging likelihood selection efficiency. The likelihood is created based on ^{12}B events, so the nucleus dependence of the shower likelihood selection efficiency is considered in the errors by using the neutron tagged events. The production rate and background rate of the light isotopes are summarized in Table8.2. The errors of the background rates in the Xe-LS were enlarged by the difference in the neutron production rate between the KamLAND LS and the Xe-LS.

As backgrounds for $0\nu\beta\beta$ decay search analysis, ^{11}C with many residual events and ^{6}He, ^{12}B, ^{10}C, ^{8}Li, and ^{8}B with events in the ROI were considered. However, since the residual background rates are small, the event rates were fixed at the estimated values other than ^{10}C and ^{11}C. The energy spectra are shown in Fig. 8.13.

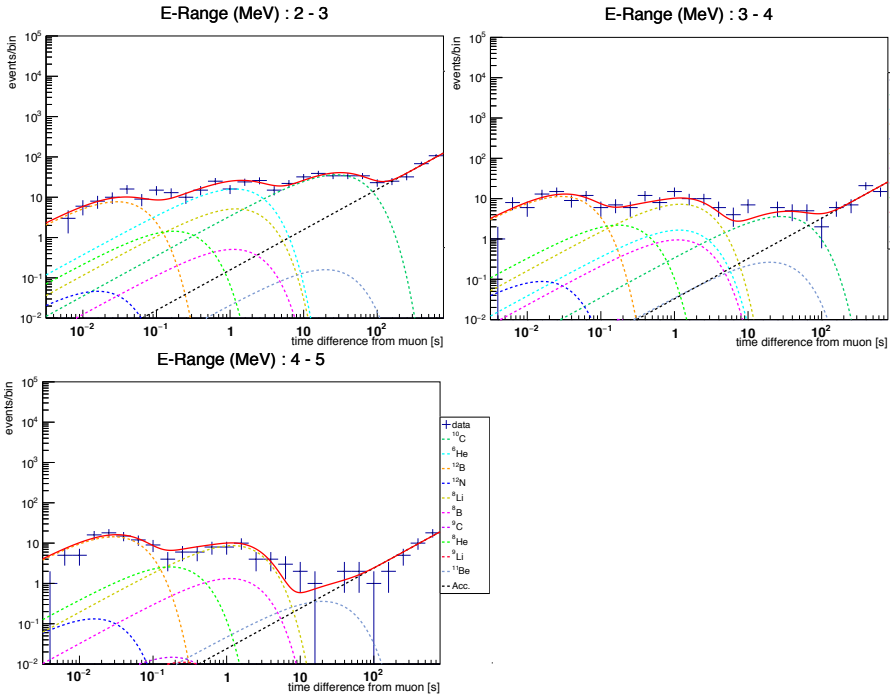

Figure 8.12: Time spectrum fitting of light isotopes
The fitting results on the estimation of the light isotope productions in each energy region are shown.

Table 8.2: Production and background rates of the light spallation isotopes are summarized. The residual rates correspond to the background rates of the residual isotopes after the event selections.

	Energy [MeV]	Mean lifetime	Estimated rate [/day/kton]	Residual rate [/day/kton]	FLUKA production [/day/kton]
^{6}He	$3.51(\beta^-)$	1.16 sec	$16.9^{+2.9}_{-2.9}$	$0.72^{+0.75}_{-0.73}$	28 ± 2
^{8}He	$10.7(\beta^-)$	171.7 msec	$3.3^{+2.1}_{-2.1}$	$0.00^{+0.03}_{-0.03}$	0.55 ± 0.04
^{8}Li	$16.0(\beta^-)$	1.21 sec	$21.3^{+2.6}_{-2.6}$	$0.00^{+0.17}_{-0.17}$	46 ± 3
^{8}B	$18.0(\beta^+)$	1.11 sec	$6.2^{+2.4}_{-2.4}$	$0.66^{+0.68}_{-0.68}$	10.7 ± 0.8
^{9}Li	$13.6(\beta^-)$	257.2 msec	$0.0^{+0.3}_{-0.3}$	$0.00^{+0.03}_{-0.03}$	4.9 ± 0.4
^{9}C	$16.5(\beta^+)$	182.5 msec	$0.00^{+1.2}_{-1.2}$	$0.00^{+0.03}_{-0.03}$	1.5 ± 0.1
^{10}C	$3.65(\beta^+)$	27.8 sec	$17.2^{+2.4}_{-2.4}$	$0.28^{+1.01}_{-0.34}$	24 ± 2
^{11}C	$1.98(\beta^+)$	29.4 min	973^{+10}_{-10}	463^{+93}_{-93}	733 ± 53
^{11}Be	$11.5(\beta^+)$	19.9 sec	$1.7^{+1.0}_{-1.0}$	$0.00^{+0.36}_{-0.36}$	1.12 ± 0.08
^{12}B	$13.4(\beta^-)$	29.1 msec	$55.3^{+2.1}_{-2.1}$	$0.016^{+0.003}_{-0.003}$	61.3 ± 4.0
^{12}N	$17.3(\beta^+)$	15.9 msec	$0.6^{+0.7}_{-0.7}$	$0.00^{+0.00}_{-0.00}$	0.73 ± 0.06

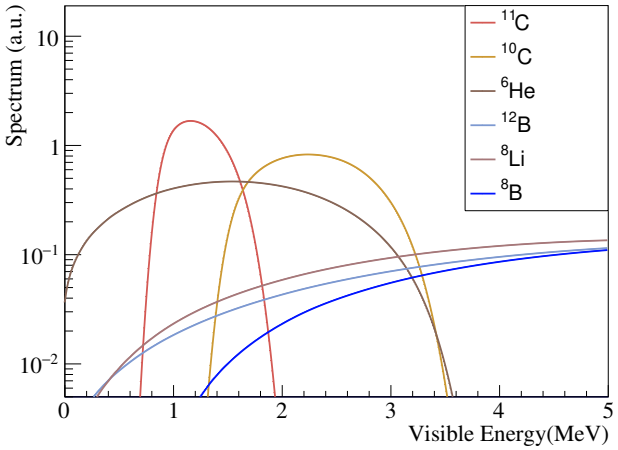

Figure 8.13: Energy spectra of light spallation isotopes in the $0\nu\beta\beta$ decay analysis energy region are shown.

8.4.3 Heavy Isotopes

A variety of heavy isotopes are produced by muon spallation of ^{136}Xe. Also, ^{136}Xe becomes ^{137}Xe by neutron capture, and the beta decay spectrum of ^{137}Xe overlaps with the ROI. The production rates of Xe spallation products with decay energy above the ROI were studied by using FLUKA.

FLUKA Simulation

FLUKA was used to simulate hadronic interactions in the Xe-LS. The muon angles and energy distributions are based on MUSIC/MUSUN simulation calibrated with the data. The geometry was simplified to a cylinder of 40 m in height and 10 m in radius. The events in the 25-m-height cylinder 5 m away from the edge is used for production yield calculation to prevent the event loss by edge effect. 10^7 events are generated each for μ^+ and μ^-, which is equivalent to about 37 years of observations with the Xe-LS. The physics list used in the simulation is the default PRECISIO(n). In addition, PHOTONIC for photon-nucleon interaction, MUPHOTON for muon-photon interaction, COALESCE(nce) for the emission of energetic light fragments, EVAPOLAT(ion):3.0 for isotope production, IONTRANS for nucleus-nucleus interaction for all energies, and EM-DISSO(ciation) for electromagnetic dissociation of heavy ions were used. The production rate of spallation products by the FLUKA simulation well reproduces the ^{12}C spallation product rates of data, which have already been observed in the KamLAND LS. Most of them are consistent within factor 2 (See Table 8.2). Fig. 8.14 shows the Z-A distribution of spallation products generated in the Xe-LS. The production rates was calculated by taking the weighted average of the μ^+ products and μ^- products, assuming μ^+ and μ^- ratio (μ^+/μ^-) to be 1.3. Although nuclei with close Z and A numbers tend to be generated more, a variety of nuclei are created. Also, neutron capture events close to the spallation products are

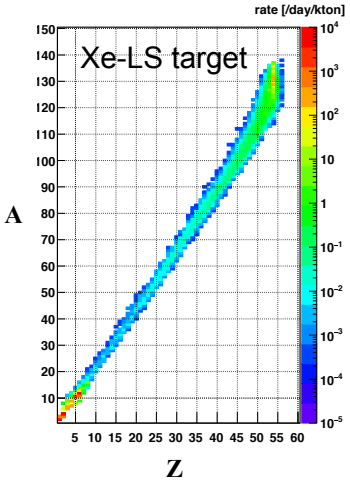

Figure 8.14: Atomic number vs mass number distribution of the Xe spallation products is shown.

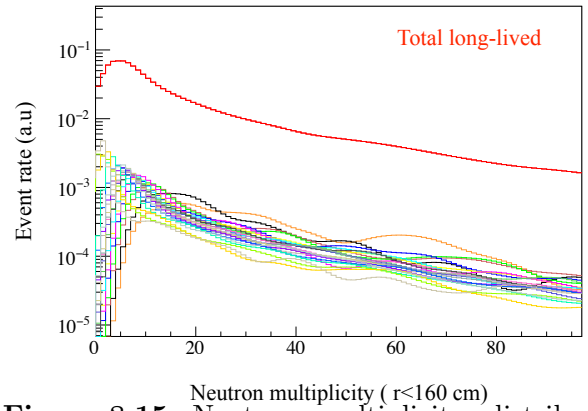

Figure 8.15: Neutron multiplicity distribution of the Xe spallation products is shown. The red line represents the sum of all products.

simulated. The Fig. 8.15 shows the neutron multiplicity distribution within 160 cm of the decay nuclei in the ROI and their parental nuclei. The neutron multiplicity in the Xe spallation products tends to be higher than that of ^{12}C spallation products.

ENSDF Database

Based on the primary particle information generated by the FLUKA simulation, the time-dependent particle decay rate was calculated with ENSDF database. The decay chains and half-lives are taking into account. It is assumed that there exists no unstable isotopes at the end of the Xe-LS filling and continuous isotope productions based on the FLUKA simulation result for 2000 days. Estimation of the decay amount for a certain nucleus is performed by following all daughter nuclei of the primary nucleus. The result revealed that each contribution is small compared to other backgrounds, but it is turned out to be non-negligible because they or their parental nuclei have relatively long half-lives, and many products are produced. Table 8.3 summarizes the Xe spallation production rates, which have decay energy in the ROI. The energy spectra produced by the decay of these nuclei are shown in Fig. 8.16. The contribution of other products, which are not shown in the table, are less than 8% in total.

The half-lives of the parental nuclei are taken into account for the analysis. The time interval distribution considering parental half-lives is created by calculating the time difference between the decay of the target nucleus at 2000 day and the time when its parent nucleus was created. The time intervals between muons and the Xe products are shown in Fig. 8.17. The remaining background rates after the long-lived veto in Table 8.3 were estimated with the neutron multiplicity distributions and the time intervals. The remaining background rate for all Xe products in the ROI

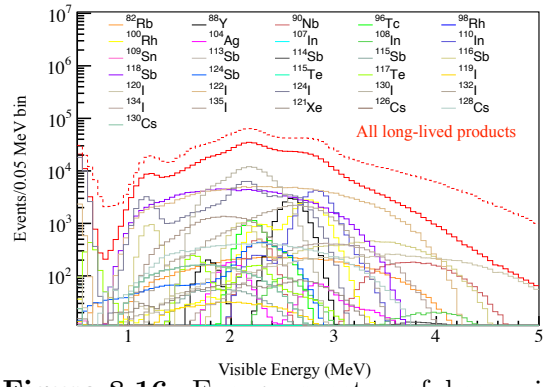

Figure 8.16: Energy spectra of heavy isotopes are shown. The solid red spectrum represents the total spectrum of the all Xe products, and the dashed red line corresponds to the total spectrum after the MoGURA long-lived spallation veto.

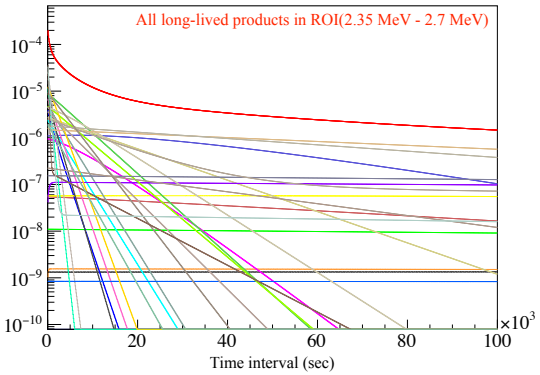

Figure 8.17: Probability distribution of time interval between muons and the heavy isotopes is shown. The red line represents all spallation products.

(2.35 MeV - 2.70 MeV) was estimated to be 1.4 events/day/kton with ∼10% muon inefficiency because of the DAQ off-time. Since most decay involves e^+, PID using gamma-rays or positronium will be highly effective.

The long-lived products were searched for using the long-lived tagging in Chapter 6.3.5. The energy spectrum fitting in the 157 cm of the tagged events after other background rejections was performed (See Fig. 8.18). The long-lived spallation rate 18.2±9.0 events/day/kton was obtained. The 40±7% tagging efficiency includes about 40% statistical error and the systematic errors of the multiplicity cut and the FLUKA dR distribution. The multiplicity cut error was estimated to be 17% by comparing the neutron-multiplicity distributions between the ^{10}C data and the PDF model (FLUKA distribution + neutron-tag efficiency) shown in Fig. 8.19. The error by using dR distribution PDF of the FLUKA simulation was checked to be 6% by replacing the PDF to the actual dR distribution of the ^{10}C.

Distortion of Long-lived Spectrum

The production ratio of long-lived products is based on the study of the FLUKA simulation, but there is no data on the ^{136}Xe spallation by muons. The error of the FLUKA simulation is evaluated by comparing the FLUKA simulation and the data of ^{136}Xe spallation by a proton in [74] and [75]. Fig. 8.20 shows the difference between the FLUKA simulation and data in the energy spectrum scaled by the production rates. The difference is introduced into the $0\nu\beta\beta$ decay analysis as a parameter for the distortion of the total long-lived energy spectrum. The difference from 500 MeV data, which has a larger difference, was used in conservative.

Table 8.3: Summary of the heavy spallation products
The background rate is the remaining rate after the long-lived spallation veto. Muon loss by deadtime was not considered in this table.

Nucleus	Q-value [MeV]	half-life[sec]	Expected rate in whole energy range (ROI) [/day/kton]	Background rate in whole energy range (ROI) [/day/kton]
^{82}Rb	4.40(β^+)	7.638	0.069(0.011)	0.069(0.011)
^{88}Y	3.62(β^+)	9.215×10^6	0.141(0.107)	0.14(0.11)
^{90}Nb	6.11(EC)	5.220×10^4	0.086(0.010)	0.05(0.005)
^{96}Tc	2.97(EC)	9.900×10^3	0.063(0.013)	0.06(0.01)
^{98}Rh	5.06(EC)	5.220×10^2	0.080(0.011)	0.00(0.00)
^{100}Rh	3.63(EC)	7.488×10^4	0.223(0.075)	0.20(0.07)
^{104}Ag	4.28(EC)	4.152×10^3	0.234(0.020)	0.02(0.001)
^{107}In	3.43(EC)	1.944×10^3	0.128(0.015)	0.00(0.00)
^{108}In	5.16(EC)	3.480×10^3	0.236(0.101)	0.01(0.00)
^{110}In	3.89(EC)	1.764×10^4	0.549(0.133)	0.23(0.06)
^{109}Sn	3.85(EC)	1.080×10^3	0.114(0.024)	0.00(0.00)
^{113}Sb	3.92(EC)	4.002×10^2	0.244(0.036)	0.00(0.00)
^{114}Sb	5.88(β^+)	2.094×10^2	0.036(0.027)	0.00(0.00)
^{115}Sb	3.03(EC)	1.926×10^3	0.774(0.030)	0.02(0.00)
^{116}Sb	4.71(EC)	9.480×10^2	1.008(0.078)	0.169(0.013)
^{118}Sb	3.66(EC)	2.160×10^2	1.426(0.185)	1.35(0.175)
^{124}Sb	2.90(β^-)	5.201×10^6	0.045(0.014)	0.04(0.013)
^{115}Te	4.64(EC)	3.480×10^2	0.124(0.014)	0.0(0.00)
^{117}Te	3.54(β^+)	3.720×10^3	0.574(0.057)	0.03(0.003)
^{119}I	3.51(EC)	1.146×10^3	0.504(0.048)	0.01(0.001)
^{120}I	5.62(EC)	4.896×10^3	0.930(0.085)	0.10(0.009)
^{122}I	4.23(EC)	2.178×10^2	2.374(0.343)	1.70(0.245)
^{124}I	3.16(EC)	3.608×10^5	1.622(0.178)	1.51(0.17)
^{130}I	2.95(β^-)	4.450×10^4	1.590(0.256)	1.03(0.16)
^{132}I	3.58(β^-)	8.262×10^3	0.427(0.146)	0.31(0.11)
^{134}I	4.18(β^-)	3.150×10^3	0.178(0.037)	0.07(0.01)
^{135}I	2.65(β^-)	2.365×10^4	0.309(0.017)	0.17(0.009)
^{121}Xe	3.75(EC)	2.406×10^3	0.518(0.072)	0.03(0.004)
^{126}Cs	4.82(EC)	9.84×10^1	0.142(0.019)	0.02(0.002)
^{128}Cs	3.93(EC)	2.17×10^2	0.319(0.043)	0.14(0.02)
^{130}Cs	2.98(EC)	1.753×10^3	0.289(0.011)	0.06(0.002)
Total	-	-	15.7(2.39)	7.5(1.2)
^{137}Xe	4.16(β^-)	2.29×10^2	3.9(0.358)	0.5(0.046)

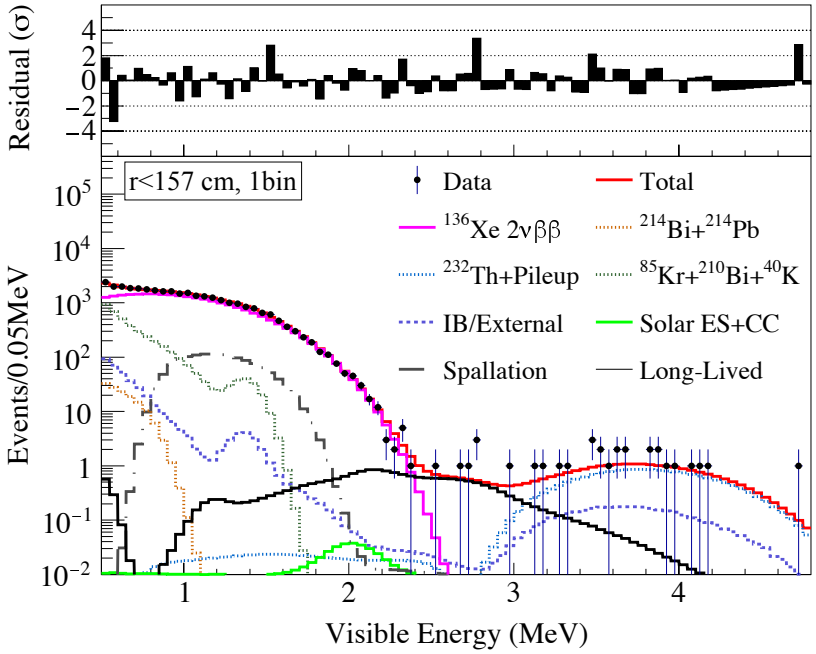

Figure 8.18: Spectrum fit for long-lived events
The events within 157 cm radius were selected by the MoGURA long-lived spallation veto, and the other background rejections were applied. The rate of the long-lived products was the free parameter.

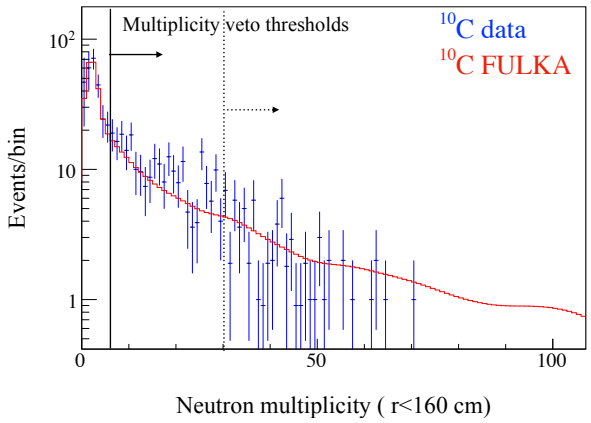

Figure 8.19: Neutron multiplicity distribution in data and FLUKA

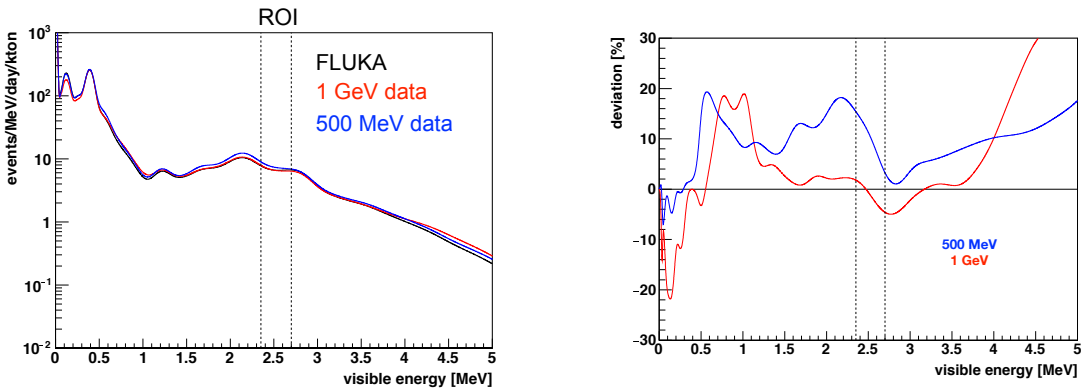

Figure 8.20: Distortion of the long-lived energy spectrum
The left figure shows scaled energy spectrum of total spallation products in the FLUKA simulation and data([74] for 500 MeV and [75] for 1 GeV). The right figure shows the difference of the energy spectra between data and the FLUKA simulation.

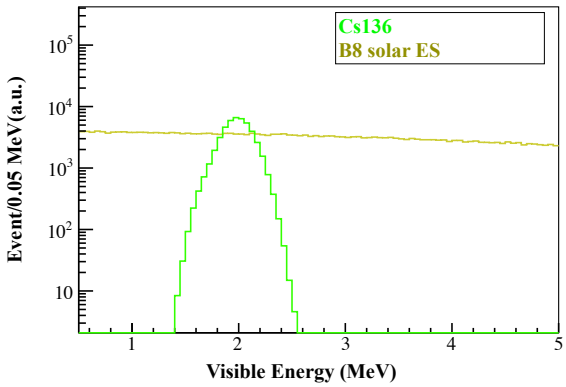

Figure 8.21: The energy spectra of Solar neutrino backgrounds are shown.

8.5 Solar Neutrino

^{8}B solar neutrino is an inevitable source of background. ^{8}B solar neutrino scatters the electrons (ES) in the detector, and its energy deposit is detected with continuous spectrum in the ROI (See Fig. 8.21). Also, solar neutrinos(pep, ^{7}Be, ^{8}B, ^{13}N, ^{15}O) turn ^{136}Xe into ^{136}Cs by the charged current [76].

$$\begin{aligned} {}^{136}\mathrm{Xe} + \nu &\rightarrow {}^{136}\mathrm{Cs} + e^{-} + \gamma \\ {}^{136}\mathrm{Cs} &\rightarrow {}^{136}\mathrm{Ba} + e^{-} + \gamma \end{aligned} \tag{8.6}$$

^{136}Cs decay(Q=2.548 MeV, half-life=13.16 days) makes a peak around the ROI (See Fig. 8.21). ^{8}B solar neutrino ES event rate can be calculated from the number of electrons and the cross-sections. ^{8}B solar neutrino ES event rate is 4.87 event/day/kton in the Xe-LS and the KamLAND LS. The CC event rate was estimated to be $\sim$ 73.4 SNU, which corresponds to 0.8 event/day/kton in the Xe-LS.

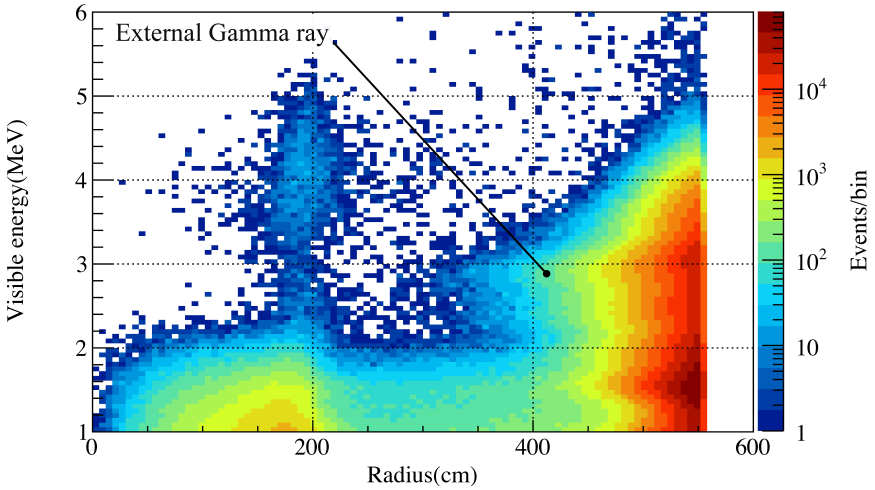

Figure 8.22: *r-Evis* distribution of the external gamma rays
The horizontal axis is event radius, and the vertical axis represents event energy. The external gamma rays from outside of the KamLAND LS can be seen.

8.6 External Background

The external gammas from impurities contained in the outside materials such as PMTs could be background.

8.6.1 External Gamma

The gamma rays emitted from radioactive impurities such as ^{238}U, ^{232}Th, and ^{40}K contained in the PMTs and acrylic panels can permeate inside the detector. Especially, the 2.6 MeV gamma from ^{208}Tl decay has an attenuation length of about $\sim$30 cm. Fig. 8.22 shows radius-Evis distribution of external gamma rays. Since the visible energy is calibrated with the neutron capture energy in the Xe-LS, the 2.6 MeV external gamma has a $\sim$ 2.8 MeV peak in the visible energy. The external background rate in the Xe-LS was determined by extrapolating the data. The distribution of the external gamma on the outside was fitted with a function of a uniform accidental($\propto r^2$) and an exponential with the parameterized attenuation($\propto \exp(r/p_{attenuation})$) for each energy (See Fig. 8.23). The fitting results provide that the external backgrounds within r <300 cm were 0.32$\pm$0.05 events/day for z >0 and 0.69$\pm$0.12 events/day for z >0. The external gamma spectrum for the $0\nu\beta\beta$ decay analysis was produced based on the fitting results (See Fig. 8.25).

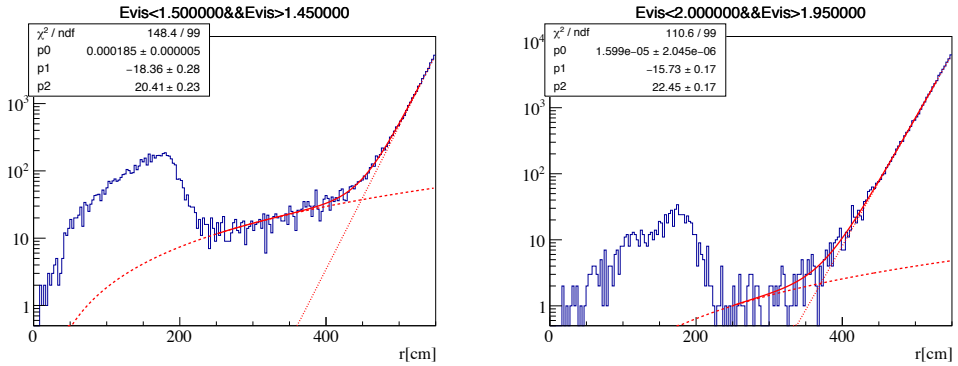

Figure 8.23: External gamma fitting
The solid red line is the fitting function. The dashed red lines are each component of accidental and external gamma.

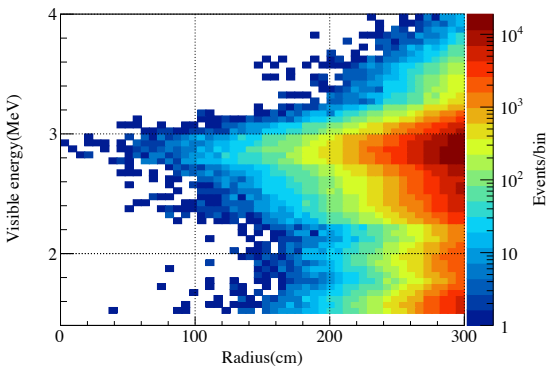

Figure 8.24: *r-Evis* distribution of external gamma made by a toy MC is shown.

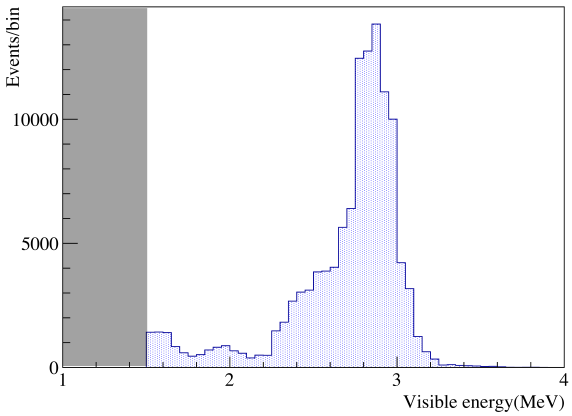

Figure 8.25: Expected external gamma spectrum within r< 250 cm
The 2.6 MeV gamma makes the peak ∼ 2.8 MeV because of the difference in the light yield between the KamLAND LS and the Xe-LS.

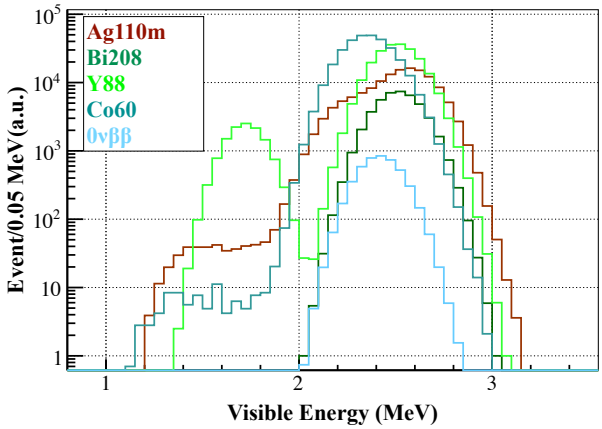

Figure 8.26: Energy spectra of potential 4 nuclei backgrounds are shown. The dark red spectrum is ^{110m}Ag, the green spectrum is ^{208}Bi, the light green is ^{88}Y, the bluish green is ^{60}Co, and the sky blue is ^{136}Xe $0\nu\beta\beta$.

8.7 Potential Backgrounds

8.7.1 4 nuclei including ^{110m}Ag

An unexpected peak was detected near ∼2.6 MeV in KamLAND-Zen 400. As candidates for a nucleus that creates the peak, ^{208}Bi(EC, Q=2.88 MeV, $\tau_{1/2}$=3.68×10^5 yr), ^{110m}Ag(β^-, Q=3.01 MeV, $\tau_{1/2}$=250 days), ^{88}Y(EC, Q=3.62 MeV, $\tau_{1/2}$= 107 days), ^{60}Co(β^-, Q=2.82 MeV, $\tau_{1/2}$=5.27 yr) were found by searching for the ENSDF database. Fig. 8.26 shows the energy spectra of the 4 nuclei. In KamLAND-Zen 400, the peak was identified to be ^{110m}Ag decay by the analysis of energy spectrum and time dependence [55]. Possible sources of the ^{110m}Ag are fallout from the Fukushima nuclear power plant accident or spallation during air transport. KamLAND-Zen 800 reuses the same Xe as used in KamLAND-Zen 400. The reused Xe does not include ^{110m}Ag because the ^{110m}Ag amount in the Phase-II was small thanks to the purification by distillation. It is also unlikely that the newly purchased Xe contains ^{110m}Ag as a background because it has been stored underground for more than 5 years and purified with the same method as KamLAND-Zen 400. If only ^{110m}Ag half-life (250 days) is considered, it will be 0.04 times the rate of KamLAND-Zen 400. Since the maximum ^{110m}Ag rate given at the KamLAND-Zen 400 Phase-II period-1 was 15.6 events/day/kton, it will be <0.3 event/day/kton in KamLAND-Zen 800. The event rate in the ROI is less than half of that, so it can be ignorable.

Chapter 9

Double Beta Decay Analysis

In this chapter, the $0\nu\beta\beta$ decay analysis is described.

9.1 Analysis Strategy

The $0\nu\beta\beta$ decay event selections were already introduced in Chapter 6.3. The energy spectrum fitting between the $0\nu\beta\beta$ candidate and background model, which was described in Chapter 8, by each radius bin was performed to determine the $0\nu\beta\beta$ decay rate and its upper limit. The strategy for the spectrum fitting was the following:

- **Pre-fitting with the background model**
  The pre-fitting using the whole single events in a 250 cm radius was performed to determine the background rates that were not observed by other analyses. The background rate with an estimation from the other analysis was constrained or fixed.

- **$0\nu\beta\beta$ decay rate scan**
  The spectrum fittings are performed while scanning the $0\nu\beta\beta$ decay rate to obtain the best fit result and a 90% confidence level upper limit. The rates of the backgrounds, which are not sensitive to $0\nu\beta\beta$ decay rate, were fixed in the $0\nu\beta\beta$ rate scan.

9.2 Xe

The Xe filling in 2019 introduced a total of 745±3 kg of the Xe gas into the inner-balloon. The composition ratio of the Xe is shown in Table 9.1 based on the quality specification sheet that the company provided, and it is well agreed with the the mass-spectrometer measurement in KamLAND-Zen 400.

The calculation using the volume of the Xe-LS 30.5±0.3 m^3 and the amount of

Table 9.1: Xe components based on the quality specification sheet are summarized.

	^{136}Xe	^{134}Xe	^{132}Xe	Others	Total
Atomic mass[u]	135.907[77]	133.905	131.904	-	135.80
Volume ratio[%]	90.85	8.82	0.17	0.16	100.0
Total mass[kg]	677.39	64.83	1.26	1.53	745.0

the Xenon gives the concentration of Xe (C_{Xe}) in the Xe-LS.

$$\begin{aligned} C_{\mathrm{Xe}} &= \frac{(\text{Xe mass in Xe-LS})}{(\text{mass of total Xe-LS})} \\ &= 745 \pm 3[\mathrm{kg}]/(30.5[\mathrm{m}^3] \times 780.13[\mathrm{kg/m}^3]) \\ &= 3.13 \pm 0.01[\%] \end{aligned} \tag{9.1}$$

Here, it is assumed that the density of the Xe-LS is equal to the density of the KamLAND LS (780.13 kg/m^3). The assumption is guaranteed by ∼0.02% because the value of the load cell that sees the density difference between the Xe-LS and the KamLAND LS is ∼40 N. Also, the value is vanished by canceling in the result on the $0\nu\beta\beta$ decay rate. The isotope abundance ($R_{^{136}\mathrm{Xe}}$) in the Xe is defined as follows.

$$\begin{aligned} R_{^{136}\mathrm{Xe}} &= \frac{(^{136}\text{Xe gas volume in Xe gas})}{(\text{volume of total Xe gas})} \\ &= 90.85[\%] \end{aligned} \tag{9.2}$$

The number of the target ^{136}Xe ($N_{^{136}\mathrm{Xe}}$) is

$$\begin{aligned} N_{^{136}\mathrm{Xe}} &= \frac{1\mathrm{kton} \times C_{\mathrm{Xe}} \times R_{^{136}\mathrm{Xe}}}{RAM_{\mathrm{Xe}}} \times N_A \\ &= ((3.13 \pm 0.01) \times 90.85[\%])/135.80 \times 6.022 \times 10^{23} \\ &= (1.261 \pm 0.004) \times 10^{29}[/\text{kton Xe-LS}] \end{aligned} \tag{9.3}$$

Here, RAM_{Xe} is the relative atomic mass number of the mixed Xe (135.80), and N_A is the Avogadro number. ^{136}Xe atoms of 3.0×10^{27} exist in the 30.5 m^3 Xe-LS, and they cause $2\nu\beta\beta$ decays about 2590 events per day. Assumed the $0\nu\beta\beta$ decay half-life to be 10^{26} years, $0\nu\beta\beta$ decay will be observed 21 events per year.

9.3 Uncertainties

Systematic errors were estimated, although they were not dominant since statistical errors were large in the $0\nu\beta\beta$ decay search analysis.

The uncertainty of the fiducial volume was estimated with the rich ^{222}Rn events mixed into the Xe-LS with Xe gas at the start of KamLAND-Zen 800. The number of uniformly distributed ^{214}Bi-^{214}Po events in the upper hemisphere of 160 cm radius (for the only inner part of the Xe-LS) and 400 cm radius (for the whole Xe-LS) was

Table 9.2: Systematic uncertainties are summarized.

	%
Fiducial volume	2.8
Enrichment	0.14
Xe amount	0.4
Detector energy scale	0.2
Detection efficiency	3.2
Total	4.3

compared. The comparison between the event number ratio and the geometric volume ratio yielded 2.8% fiducial error.

The error of the Xe amount was mentioned in Chapter 5.5.3. The uncertainty of the Xe enrichment was estimated by the difference between the value in the quality specification sheets (90.91%) and the measured ^{136}Xe enrichment (90.77±0.08%) in KamLAND-Zen 400 [61]. There was 0.14% difference.

The error of the energy scale was evaluated using the $2\nu\beta\beta$ decay rate. When the energy scale related parameters (α, k_B, and R_C) were fixed, the $2\nu\beta\beta$ decay rate was fitted to be 105525±318 event/day/kton. When they are floated, it became 105779±326 event/day/kton. The error of the $2\nu\beta\beta$ decay rate between the two analysis gives 0.2% energy scale uncertainty.

The largest uncertainty of the detection efficiency was given by the effect of non-uniformity in the neutron capture events. Notably, the detector has an inefficiency for a long time in the long-lived veto, and the difference in the livetime depending on the position made by the neutron non-uniformity creates considerable uncertainty. An error is considered by studying the livetime dependence on the radius of the cut with the MC events described in Chapter 6.4. Since the difference between the inner 100 cm radius and the 190 cm radius has a 3.2% difference of the inefficiency, this is considered as an error.

9.4 Spectrum Fitting for $0\nu\beta\beta$ Decay Search

9.4.1 Fit Data

The data used in the analysis is from run015431 to run015783, the total runtime was 218.6 days, and the livetime was 145.3 days. Fig. 9.1 shows the energy spectrum after applying each event selection to the data, and Table 9.3 shows the number of rejected events for each event selection.

Event position distribution for the final candidate events in the ROI(2.35-2.70 MeV and inner 10 radius bins r <157.49 cm), which gives the best sensitivity thanks to less the inner-balloon backgrounds, is shown in Fig. 9.2. There exist 14 events in the ROI. It is well-matched with 15.9 events, which is the expected number of events in the background model. The time dependence of the candidate events are shown in

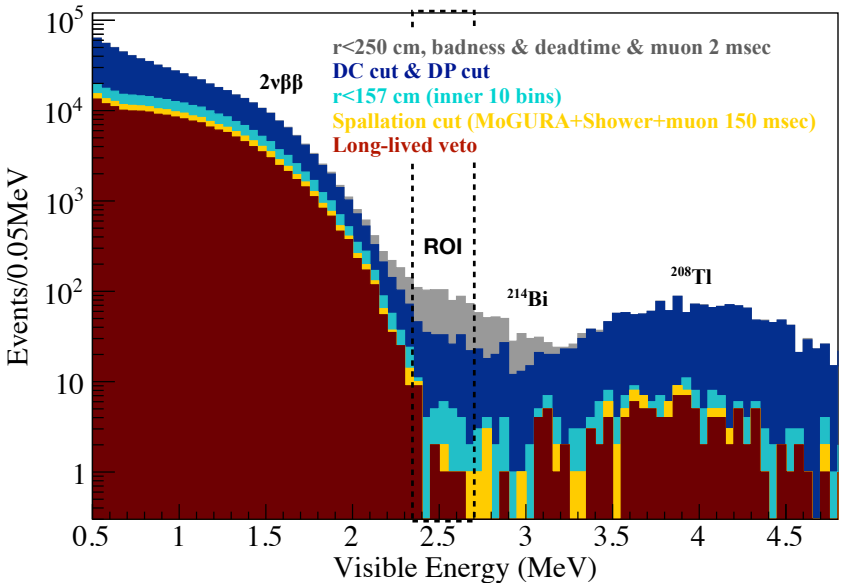

Figure 9.1: Event selections for the $0\nu\beta\beta$ decay candidate
The energy spectra of the events after each event selection are shown.

Table 9.3: Event selection
Each event selection was applied to the data after badness, deadtime, muon 2 msec veto, and DC veto.

Selection	events in ROI r <157 cm		r <250 cm	
	tag	untag	tag	untag
DC	92	41	355	287
Pileup	4	37	60	227
MoGURA ^{10}C	17	24	94	193
MoGURA ^{137}Xe	1	40	5	282
MoGURA long-lived	10	31	61	226
Shower	19	22	92	195
Muon 150 msec	2	39	16	271
Total	27	14 (exp. 15.9)	226	61

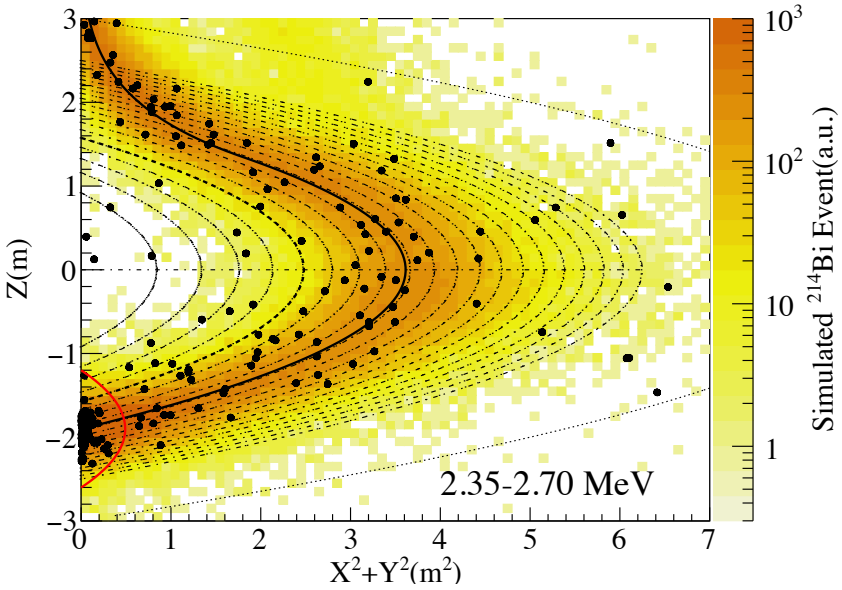

Figure 9.2: Event position distributions of the $0\nu\beta\beta$ decay candidate
The outermost thin dotted line is a 3-m-radius analysis volume cut, the inner dotted lines are the equal volume analysis bins of 2 theta bin and 20 radius bin, and inside bins of the bolder dot line are inner 10 bins. The position of the inner-balloon is drawn by the solid black line, and the solid red line shows the bottom hot spot cut region.

Fig. 9.3.

9.4.2 Fitting Method

In the spectrum fitting, the event rate of the backgrounds, the energy scale, its non-linearity parameters, and the distortion parameter of the long-lived product were optimized to minimize χ^2 value. The tool used for the minimization on the χ^2 is MINUIT, and for pre-fitting, SIMPLEX, MIGRAD, and MIGRAD were used in this order. Only MIGRAD once (or twice) was used for the $0\nu\beta\beta$ decay rate scan with the initial values of the pre-fitting results. The definition of the χ^2 was the following.

$$\chi^2 = \chi^2_{Energy} + \chi^2_{Penalty} \tag{9.4}$$

Here, each definition is as follows.

$$\chi^2_{Energy} = \begin{cases} 2\sum_i \sum_j \sum_{k\in 0.5\mathrm{MeV}\le E\le 4.8\mathrm{MeV}} [\nu_{ijk} - n_{ijk}] & (n_{ijk} = 0) \\ 2\sum_i \sum_j \sum_{k\in 0.5\mathrm{MeV}\le E\le 4.8\mathrm{MeV}} [\nu_{ijk} - n_{ijk} + n_{ijk}\log(n_{ijk}/\nu_{ijk})] & (n_{ijk} > 0) \end{cases} \tag{9.5}$$

Where, the subscripts i, j, and k represents i-th radius bin, j-th theta bin, and k-th energy bin, respectively. The energy bin was 86 equal bins by every 0.05 MeV from 0.5 MeV to 4.8 MeV. The radius bin was 20 equal volume bins within 0 cm $< r <$ 250 cm, shown in Fig. 9.2. The theta bin was 2 bins, upper($z >$0) bin, and lower($z <$0)

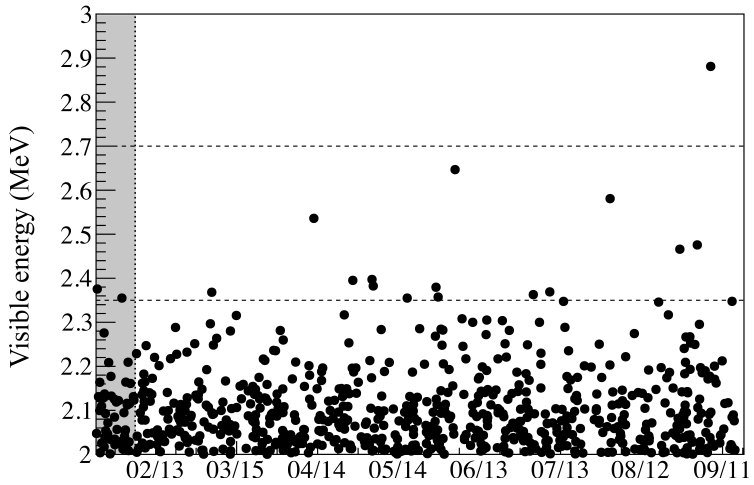

Figure 9.3: Time distribution of the $0\nu\beta\beta$ decay candidates is shown. The events in the shaded area are before the analysis period.

bin. The data were filled into one of the entire $20 \times 2 \times 48$ =3440 bins. The penalty term was a constraint on the parameter, which has an expected value from other measurements. The Pearson's χ^2 was used for it. The energy scale and non-linearity terms are also limited by the prompt ^{214}Bi energy spectrum in the radon rich period.

$$\chi^2_{Penalty} = \sum_n (\frac{E_n - O_n}{\sigma_n})^2 \tag{9.6}$$

Here, E_n is its expected value, O_n is its observed rate parameter in the fitting, and σ_n is the error of the expected value. The list of the backgrounds used for fitting and the handling of their parameters are summarized in Table 9.4. The energy scale parameter(α) is calibrated with ^{214}Bi events in the data and the MC, and the time deviation is suppressed to $\sim$ 1% by the correction with neutron capture gamma events. However, the parameter is scanned by 0.5% step from $\alpha = 1$, and the best fit is searched for each step to determine the minimum χ^2 value.

9.5 Results

9.5.1 Lower Limit on $0\nu\beta\beta$ Decay Rate

The relation between χ^2 values and $0\nu\beta\beta$ decay rates is summarized in Fig. 9.4. The best fit result gives the slightly positive $0\nu\beta\beta$ decay rate 0.2 event/day/kton. The energy spectra with the best fit results and the radius distribution in each energy region were shown in Appendix B. The upper limits on the $0\nu\beta\beta$ decay rate at the 90% confidence level (90% C.L.) is <4.1 events/day/kton Xe-LS. It can be translated to the lower limit on the half-life using the value in Eq. (9.4). The lower limit on the

Table 9.4: Summary of the fit parameter handling
IB represents the inner-balloon, and Kam-LS is the KamLAND LS.

	Material source	condition(pre-fit)	condition ($0\nu\beta\beta$ scan)
^{136}Xe $0\nu\beta\beta$	Xe-LS	non	scanned
^{136}Xe $2\nu\beta\beta$	Xe-LS	floated	floated
^{238}U S1	IB	floated	fixed
^{238}U S2	Xe-LS	constrained	constrained
	IB,Kam-LS	floated	floated
^{232}Th S1	IB	floated	fixed
^{232}Th S2	Xe-LS,IB,Kam-LS	floated	fixed
^{212}Bi-^{212}Po pileup	Xe-LS,IB	floated	constrained
^{40}K	Xe-LS,IB,Kam-LS	floated	fixed
^{210}Bi	Xe-LS,IB,Kam-LS	floated	fixed
^{85}Kr	Xe-LS,Kam-LS	floated	fixed
Solar ν CC+NC	cosmogenic	fixed	fixed
^{10}C	spallation	fixed	constrained
^{11}C	spallation	constrained	constrained
^{6}He	spallation	fixed	fixed
^{8}Li	spallation	fixed	fixed
^{12}B	spallation	fixed	fixed
Long-lived	spallation	constrained	constrained
(Spectrum distortion)		constrained	constrained
^{137}Xe	^{136}Xe n-capture	fixed	constrained
Ext. γ	PMT, acrylic panel...	fixed	fixed
Energy scale(α)		constrained	constrained
Nonliniality(k_B, R)		constrained	constrained

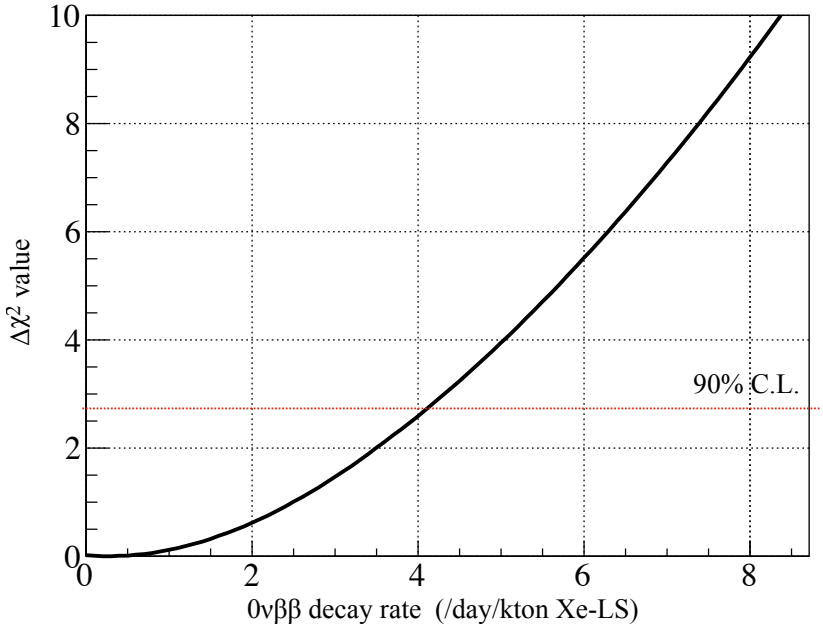

Figure 9.4: $\Delta\chi^2$ distribution for $0\nu\beta\beta$ decay rate
The black line is $\Delta\chi^2$ distribution, and the red dashed line represents 90% C.L. upper limit.

half-life of ^{136}Xe $0\nu\beta\beta$ decay rate was derived,

$$T_{1/2}^{0\nu\beta\beta} > 5.8 \times 10^{25}\text{yr (90\% C.L.)}. \tag{9.7}$$

The fit results of the pre-fitting and $0\nu\beta\beta$ decay rate scan are summarized in Table 9.5.

Fig. 9.5 shows the energy spectrum of the inner-radius 10 bins. The number of events in the ROI on the best-fit result and the expected were summarized in Table 9.6. Although the number of data points (14) in the ROI was slightly less than the expected (15.9), the best fit value on the $0\nu\beta\beta$ rate is slightly positive because the events around 2.45-2.60 MeV bins can be easily explained by the $0\nu\beta\beta$ decay spectrum.

Potential Backgrounds

The $0\nu\beta\beta$ decay rate scan with potential backgrounds (^{208}Bi, ^{88}Y, ^{110m}Ag, and ^{60}Co) was performed. Part of $0\nu\beta\beta$ decay rate was taken place with ^{60}Co, and it gave a better limit $>6.1\times10^{25}$ yr. The results without 4 nuclei was conservative.

$2\nu\beta\beta$ Decay Rate

The best fit result on $2\nu\beta\beta$ decay rate was 105779 event/day/kton. It corresponds to the half-life of $T_{1/2}^{2\nu} = 2.26 \times 10^{21}$ yr, which is consistent with the previous result in KamLAND-Zen 400 $T_{1/2}^{2\nu} = (2.21 \pm 0.02(\text{stat.}) \pm 0.07(\text{syst.})) \times 10^{21}$ yr [61] within

Table 9.5: Summary of fitting results
The pre-fitting results with MIGRAD errors, best fit results, 90% C.L. results, and constraints on the parameters are shown.

Parameter	Pre-fitting	Best fit	90% C.L.	Constraint
	Xe-LS [/day/kton]			
^{136}Xe $0\nu\beta\beta$	0(fix)	0.2	4.1	scanned
^{136}Xe $2\nu\beta\beta$	105571±338	105779	105901	free
^{238}U S2	223±38	222	222	222±38
^{232}Th S1	61±49			
^{232}Th S2	106±13	111	112	free
^{232}Th pileup	tagged to ^{232}Th S2	106	105	pre-fit±30%
^{40}K	139±179			
^{210}Bi	19517±811			
^{85}Kr	57963±1553			
Solar ν ES+CC	4.87+0.80(fixed)			
^{10}C	0.28(fixed)	0.26	0.25	$0.28^{+1.23}_{-0.33}$
^{11}C	480±80	539	541	463^{+113}_{-93}
^{6}He	0.72(fixed)			
^{8}Li	0.0(fixed)			
^{12}B	0.02(fixed)			
^{8}B	0.66(fixed)			
^{137}Xe	0.5(fixed)	0.49	0.49	0.50±0.33
Long-lived	10.0±4.0	8.04	2.50	18.2 ± 9.0
(Spectrum distortion)	0.15(σ)	0.02	-0.007	0±1
	IB [/day/IB]			
^{238}U S1	5.5±1.9			
^{238}U S2 (z <0, z >0)	4.8±0.7, 4.8±0.7	4.6, 4.7	4.5, 4.7	free
^{232}Th S1	23.3 ± 1.5			
^{232}Th S2 (z <0, z >0)	23.3±1.1, 33.5±1.9			
Pileup(z <0, z >0)	tagged to ^{232}Th S2	24.3, 31.4	24.4, 31.5	pre-fit±30%
^{40}K	157±10, 122±9			
^{210}Bi	2627 ±24, 2591 ± 23			
	Kam-LS [/day/kton]			
^{238}U S2	1479.9±132			
^{232}Th S2	13.4±6.8			
^{40}K	1501±66			
^{210}Bi (z <0, z >0)	278±103, 9481±375			
^{85}Kr (z <0, z >0)	12816±544, 11723±672			
Solar ν ES	4.87(fixed)			
^{10}C	0.28(fixed)	0.40	0.41	$0.28^{+1.01}_{-0.33}$
^{11}C	568±28	561	561	463±93
^{6}He	0.72(fixed)			
^{8}Li	0.0(fixed)			
^{12}B	0.02(fixed)			
^{8}B	0.66(fixed)			
Ext. γ (z <0, z >0)	0.28, 0.69(fixed)			
α, k_B, R_C	0.991, 0.44,0.003	0.995, 0.32, 0.03	0.995, 0.31, 0.03	

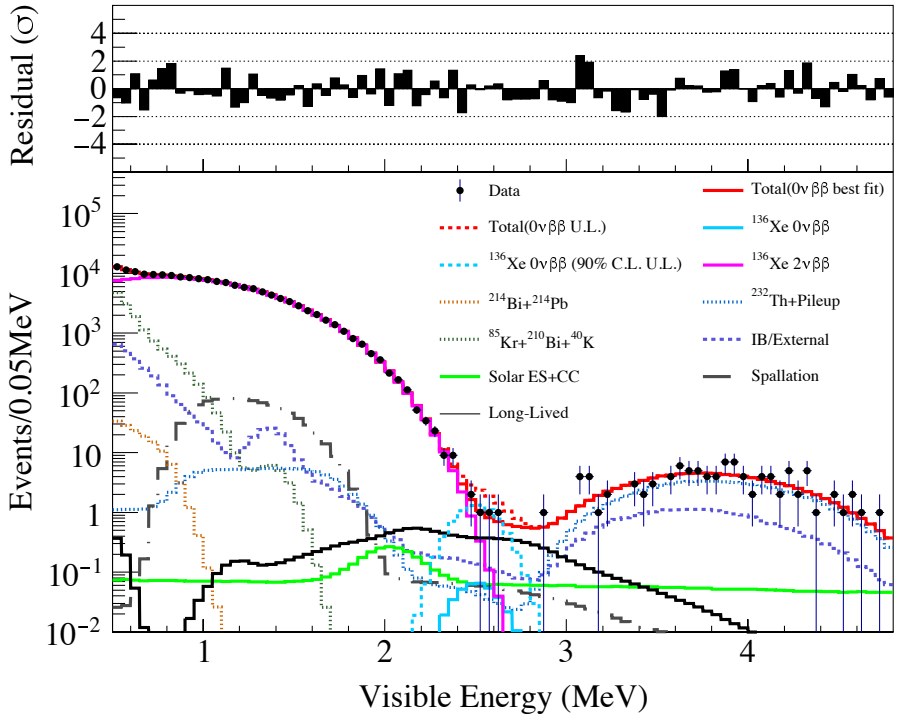

Figure 9.5: Spectrum with best fitting results and 90% C.L. $0\nu\beta\beta$ decay rate within inner 10 bins (r<157 cm)

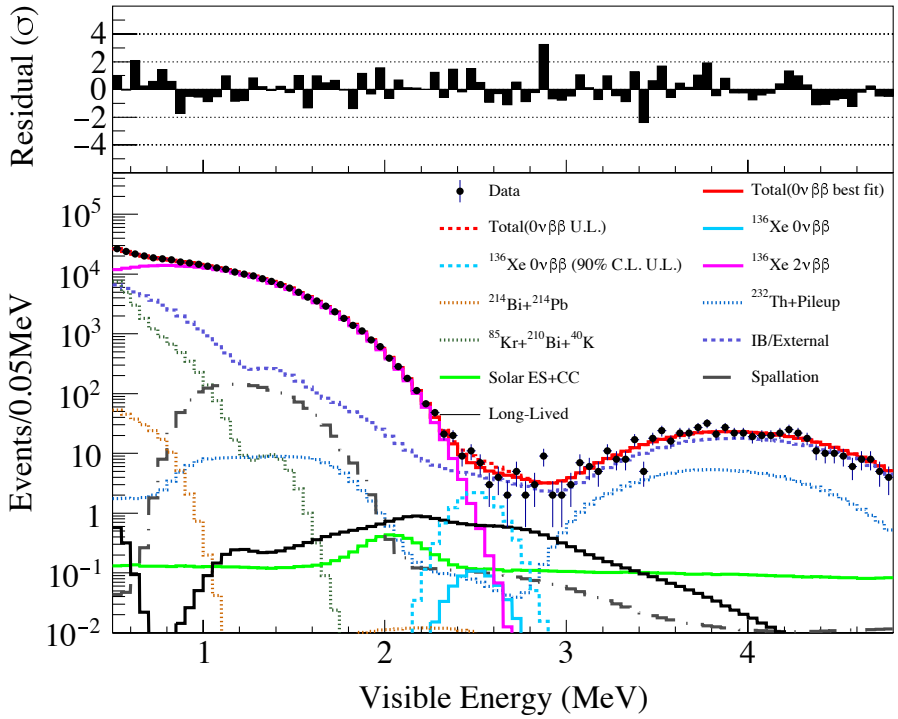

Figure 9.6: Spectrum with best fitting results and 90% C.L. $0\nu\beta\beta$ decay rate within inner 18 bins (r<192 cm)

Table 9.6: Summary of the backgrounds in the ROI
The expected and best fit event rate are shown, and the event rate within the ROI energy region are shown in parentheses. The rightmost column shows the event number within the inner 10 bins from 2.35 MeV to 2.70 MeV.

	Expected (ROI)	Best fit (ROI)	Best fit events in the ROI (1.85 day-kton)
Xe-LS[event/day/kton]			[events]
^{136}Xe $0\nu\beta\beta$	-	0.2(0.18)	0.33
^{136}Xe $2\nu\beta\beta$	107692(4.18)	105779(4.61)	8.54
^{238}U S2	222(0.022)	222(0.022)	0.04
^{232}Th S2	106(0.002)	110.5(0.001)	0.002
^{212}Bi-^{212}Po pileup	106(0.150)	106(0.154)	0.29
Solar ν NC+CC	4.87+0.80(0.238+0.006)		0.46
^{10}C	0.28(0.070)	0.26(0.067)	0.12
^{6}He	0.72(0.070)		0.13
^{12}B	0.016(0.0003)		0.001
^{8}B	0.66(0.009)		0.02
^{137}Xe	0.5(0.057)	0.5(0.056)	0.10
Long-lived	18.2(3.28)	8.0(1.457)	2.70
IB [events/day/IB]			[events]
^{238}U S2 ($z<0, z>0$)	4.8(0.249), 4.8(0.150)	4.6(0.302), 4.7(0.187)	0.56, 0.35
^{212}Bi-^{212}Po pileup ($z<0, z>0$)	31(0.003)	31.4(0.004), 24.3(0.001)	0.007, 0.002
External[events/day/V_{300cm}]			[events]
Ext. γ ($z<0, z>0$)	0.69(0.014), 0.32(0.006)	0.69(0.014), 0.32(0.006)	0.03, 0.01
Total	8.62	7.40	13.7
Observed			14

the range of systematic uncertainty 4.2% in Section 9.3. The precise measurement of $2\nu\beta\beta$ decay rate with KamLAND-Zen 800 requires improvement on the systematic uncertainties. The error of the detector efficiency can be reduced with optimization for event selection. The fiducial volume error is expected to be improved by a whole volume analysis and source calibrations.

Uncertainty of Energy Resolution

The energy resolution was estimated to be $7.2\%/\sqrt{E}$ for single beta decay and $7.5\%\sqrt{E}$ for single gamma-rays by using the KLG4 simulation. Although the MC simulation well-reproduced ^{214}Bi spectrum, it may have an uncertainty. The effect of the uncertainty in the energy resolution was confirmed. The MC simulation with $+0.4\%/\sqrt{E}$ resolution, which is the uncertainty in the KamLAND-Zen 400 source calibration [61], was fitted to the data. The limit on the $0\nu\beta\beta$ decay half-life changed $\sim$2% worse. The difference is comparable to the other uncertainties.

9.6 Sensitivity

9.6.1 Sensitivity from Toy MC Spectrum Fitting

The validity of the analysis is checked by calculating the sensitivity with the toy MC analysis based on the background model at the best fit values. The $0\nu\beta\beta$ rate is assumed to be exactly 0. The $0\nu\beta\beta$ decay rates at the 90% confidence levels are obtained in the same analysis by fitting the toy MC data. The distribution of the fit results for 500 MC trials is plotted in Fig. 9.7. The probability of obtaining results that are better than the results obtained by the data analysis was 71%, and the midian sensitivity was

$$T^{0\nu\beta\beta}_{1/2\ \mathrm{sensitivity}} > 8.1 \times 10^{25}\mathrm{yr}(90\%\ \mathrm{C.L.}). \tag{9.8}$$

This sensitivity states that KamLAND-Zen 800 is already the world highest sensitivity search for the ^{136}Xe $0\nu\beta\beta$ decay and the effective Majorana mass. The result of the data is statistically largely fluctuated because of the small observation time, and the expected number of ROI events is not large. Besides, if $0\nu\beta\beta$ decay actually exists in the data, the sensitivity on the 90% C.L limit becomes poor. The result obtained by the analysis is reasonable.

Projection of Sensitivity

The projections of the sensitivity when KamLAND-Zen 800 continues the observation was calculated based on the results of the fit. It is assumed that the constraints on the spallation backgrounds including long-lived products will be improved with the extended observation time. The sensitivity with 3 yr livetime($\sim$5 yr runtime) was

$$T^{0\nu\beta\beta}_{1/2\ \mathrm{3yrsensitivity}} > 21.5 \times 10^{25}\ \mathrm{yr.}(90\%\ \mathrm{C.L.}). \tag{9.9}$$

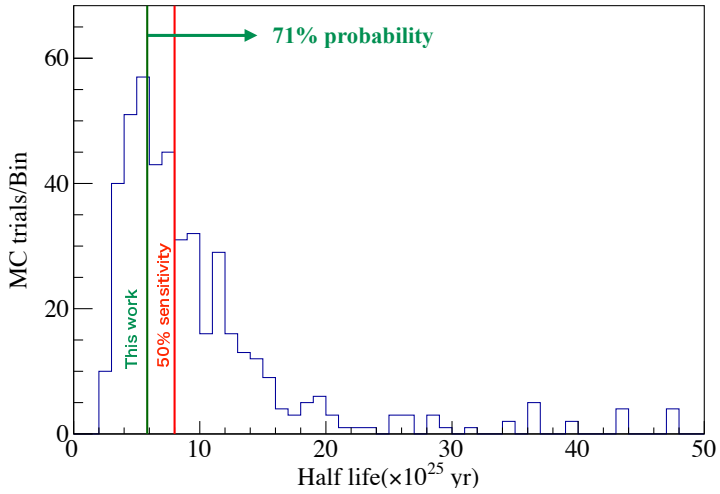

Figure 9.7: 90% C.L. sensitivity of $0\nu\beta\beta$ decay rate
The histogram is filled with the 90% upper limits of each Toy MC trial. The red line is median sensitivity, and the green line is the result obtained by the data analysis.

Since KamLAND-Zen 800 is the experiment with backgrounds, the sensitivity increases roughly on the route of the observation time. Note that possible improvements in the analysis and the hardware mentioned in the next section can improve the sensitivity. Also, determining the background rate from other investigations or other analyses will improve the limit.

9.6.2 Possible Future Improvement

Here is the summary of the possible future improvements in KamLAND-Zen 800.

- **Re-use of low gain PMT**
  Current analysis did not use the low-gain channels which have the gains less than 0.4 p.e. Such PMTs still have hit-information, and it is possible to use the information if one can determine the gain or its hit-efficiency by a careful procedure. Also, the amplification for the low gain channels are being developed and will be installed soon. The energy resolution will be improved from $7.2\%/\sqrt{E}$ to $6.6\%/\sqrt{E}$ at the maximum, and the tail of $2\nu\beta\beta$ decay will be well separated to $0\nu\beta\beta$ decay.

- **Particle identification methods**
  Double-pulse fitting and neural network analysis still have room for improvement. Also, future source calibration will help it. Gamma sources such as ^{214}Bi, ^{10}C, ^{212}Bi-Po pileup, and most of the long-lived products can be reduced.

- **Electronics upgrade (neutron capture tagging improvement)**
  The neutron tagging efficiency in the current MoGURA DAQ is about 80%.

Table 9.7: ^{136}Xe $0\nu\beta\beta$ decay 90% C.L. limits and sensitivities in the KamLAND-Zen all phases

	Phase-I	Phase-II		Zen 800	Combined
		period-1	period-2		
Rate limit (/day/kton)		<4.4	<4.8	<4.1	-
$T^{0\nu}_{1/2}$ limit (yr)	$>1.9\times10^{25}$	$>5.3\times10^{25}$	$>5.0\times10^{25}$	$>5.8\times10^{25}$	$>12.7\times10^{25}$
		$>8.9\times10^{25}$(p-1+p-2)			
Sensitivity (yr)	$>0.6\times10^{25}$	$>2.1\times10^{25}$	$>3.9\times10^{25}$	$>8.1\times10^{25}$	$>9.7\times10^{25}$ (w/o Phase-I)
		$>4.5\times10^{25}$(p-1+p-2)			

Electronics for KamLAND2-Zen, which is the next generation detector of KamLAND-Zen, is aiming to improve it to be more than 94.8% [78], and it can be installed in the KamLAND-Zen 800 phase. This will help to reduce the spallation backgrounds such as ^{10}C, ^{137}Xe, and long-lived products.

- **Neutron tagging reconstruction**
  The vertex resolution of the neutron capture event will be improved by a timing calibration of the PMTs for the MoGURA DAQ. Also, the vertex fitter may be tuned for events after muons. It can enhance the long-lived veto efficiency.

9.7 Discussion/Conclusion

9.7.1 Limits on $\langle m_{\beta\beta}\rangle$

Using the phase space factor in [30] and the NMEs in [1], the limits on the effective Majorana mass obtained by this analysis was

$$\langle m_{\beta\beta}\rangle < \text{(70-229) meV (90\% C.L.).} \tag{9.10}$$

The result only in KamLAND-Zen 800 with 145-days-livetime provided the comparable limit to the other $0\nu\beta\beta$ decay experiments (See Table 3.1).

The long-lived spallation backgrounds were not taken into account in the previous analysis for KamLAND-Zen 400 [61], and new spallation veto tools (Shower veto, ^{137}Xe veto, Muon 150 msec veto for ^{12}B, and long-lived veto) were developed this time. The new analysis methods were also applied to the KamLAND-Zen 400 Phase-II. The fitting results were shown in Appendix C. The sensitivity and results of KamLAND-Zen all phases are summarized in Table 9.7.

The χ^2 distribution including all phases of KamLAND-Zen is shown in Fig. 9.8. Combined results in the KamLAND-Zen all phases on the $0\nu\beta\beta$ decay half-life limit

$$T^{0\nu\beta\beta}_{1/2} > 1.27\times10^{26}\text{yr. (90\% C.L.),} \tag{9.11}$$

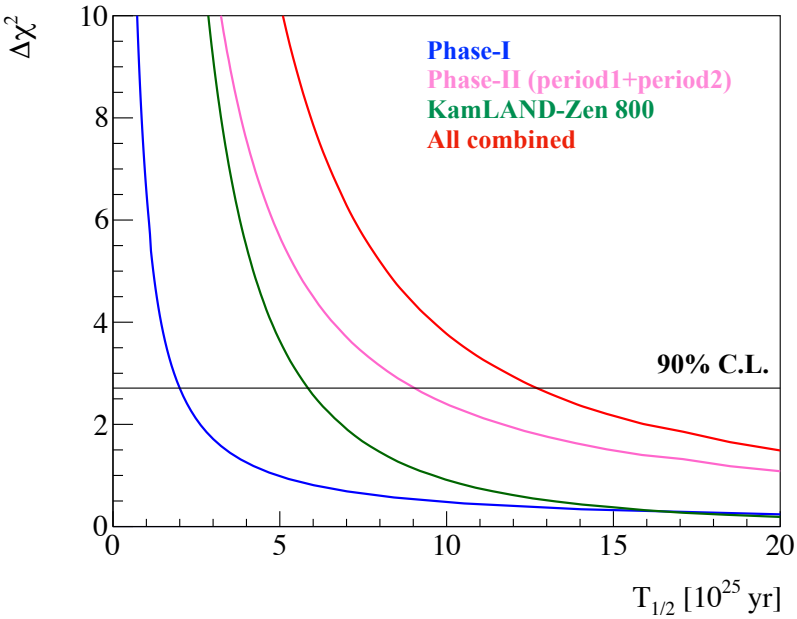

Figure 9.8: Combined results on $0\nu\beta\beta$ decay half-life are shown. The blue line represents the $\Delta\chi^2$ distribution in KamLAND-Zen 400 Phase-I, the pink line is that in KamLAND-Zen 400 Phase-II, the green line is that in KamLAND-Zen 800, and the red line is the all combined distribution.

was obtained. The results provide most stringent limit on the effective Majorana mass

$$\langle m_{\beta\beta}\rangle < \text{(49-150) meV (90\% C.L.)}. \tag{9.12}$$

The NME model dependence of the result is summarized in Table 9.8.

In Fig.9.9, the results obtained this time are projected to $\langle m_{\beta\beta}\rangle$ vs $m_{lightest}$, assuming the presence of the Majorana neutrinos and 3 generations of the neutrinos. Although the highest value of the NME may not be likely, the result have reached to the band of the inverted hierarchy region at first in the world. Also, restrictions on the lightest neutrino mass were obtained with the best fit and 3σ range in the neutrino oscillation parameters (OS), assuming the presence of Majorana neutrinos.

$$\begin{aligned} m_{\text{lightest}} &< \text{(131-427)/(175-557) meV for IH, 90\% C.L.(best/3}\sigma\text{ OS)} \\ m_{\text{lightest}} &< \text{(141-430)/(183-559) meV for NH, 90\% C.L.(best/3}\sigma\text{ OS)} \end{aligned} \tag{9.13}$$

The results of this analysis have reached a region without cosmological limits. Also, the results have higher sensitivity for neutrino masses than the distortion measurement of the beta decay endpoint at present. If the total neutrino mass is determined or strictly limited by the cosmology based on future observations, the allowed region on $\langle m_{\beta\beta}\rangle$ can be narrowed for the standard scenario of the neutrinos and the cosmology. However, note that depending on non-standard $0\nu\beta\beta$ decay mechanisms and cosmological scenarios, both observations are not always in the expected region. Complementary measurements by multiple experimental methods are important for searching for beyond the standard model physics.

Table 9.8: NME model dependence of the effective Majorana mass with the obtained half-life: $T^{0\nu\beta\beta}_{1/2} > 1.27 \times 10^{26}$yr. (90% C.L.) is shown.

Model	Value	90% C.L. limit on $\langle m_{\beta\beta} \rangle$
Shell model (SM Mi)[79]	2.19	106
Shell model (SM St-M)[80]	1.63/1.76	143/132
QRPA-Tu [81]	2.18/2.44	107/96
QRPA-Jy [82]	2.91	80
QRPA-CH [83]	1.55	150
IBM-2 [84]	3.05	76
REDF[85]	4.32	54
NREDF[86]	4.77	49

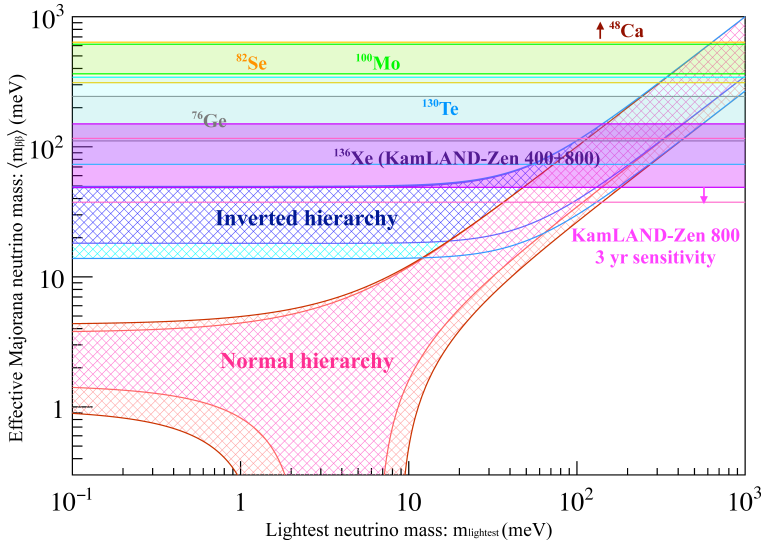

Figure 9.9: Effective Majorana mass and lightest neutrino mass with the results from KamLAND-Zen 800
The blue band represents the inverted mass hierarchy and the red band is the normal mass hierarchy. Light colors mean 3σ from the current global oscillation analysis [57]. The results in Table 3.1, the result and sensitivity of KamLAND-Zen 800 are drawn.

Chapter 10

Conclusions

This dissertation presents the first results with 219-days-runtime (145-days-livetime) on ^{136}Xe $0\nu\beta\beta$ decay search from KamLAND-Zen 800. Ton scale experiments are necessary to cover the inverted hierarchy region (15 meV $< \langle m_{\beta\beta} \rangle <$ 50 meV). The KamLAND-Zen 800 introduced more than half ton isotopes (677 kg) for the first time in the world by doubling the scale of KamLAND-Zen 400, which had used the most isotope ($\sim$350 kg) in the world. KamLAND-Zen 800 has achived to fabricate and install the 10 times cleaner inner-balloon (IB) as that of KamLAND-Zen 400.

Thanks to Xe purification and LS distillation campaigns, there was no unexpected ^{110m}Ag backgrounds, and ^{212}Bi-Po pileup backgrounds form ^{232}Th are reduced to less than solar neutrino background level. Also, the analyses for removing the spallation background events have been improved. ^{10}C decay of the spallation backgrounds, which was considered as a dominant background in KamLAND-Zen 400, was rejected by more than 90%. The study on Xe spallation products, which have been appeared as a result of the intense background rejections, was also performed by using FLUKA simulation and ENSDF database. The veto tools for the Xe spallation products have been developed.

The results for the $0\nu\beta\beta$ decay half-life from KamLAND-Zen 800 yields $T^{0\nu}_{1/2} > 5.8 \times 10^{25}$ yr (90% C.L.). The sensitivity of the observation was $T^{0\nu}_{1/2} > 8.1 \times 10^{25}$ yr (90% C.L.), and it was the highest-sensitivity search for the $0\nu\beta\beta$ decay in the world. The combined results with KamLAND-Zen 400 provides the strictest limit on the $0\nu\beta\beta$ decay half-life in the world, $T^{0\nu}_{1/2} > 1.27 \times 10^{26}$ yr (90% C.L.). Assuming 3 generation neutrinos and light Majorana neutrino exchange, the result corresponds to the limit on the effective Majorana mass: $\langle m_{\beta\beta} \rangle <$ (49-150) meV. The result is the most stringent limit of all double-beta decay experiments.

It is demonstrated with the sensitivity study based on the analysis in this dissertation that KamLAND-Zen 800 will have already sensitivity to $T^{0\nu}_{1/2} > 2.15 \times 10^{26}$ in 3 years livetime, and it will be ameliorated by updating analysis tools and DAQ hardware.

Appendix A

Trigger Type

The types of data acquisition triggers of KamFEE are listed.

Table A.1: List of KamFEE data acquisition triggers

Trigger Type	Description	Trigger Type	Description
0x000,000,001	ID singles trigger	0x001,000,000	ID delayed trigger
0x000,000,002	ID history trigger	0x002,000,000	ID prompt trigger
0x000,000,008	1PPS trigger	0x004,000,000	OD to ID trigger
0x000,000,0X0	Acquire Trigger	0x008,000,000	ID to OD trigger
0x000,000,100	ID prescale trigger	0x010,000,000	OD top history trigger
0x000,000,200	GPS trigger	0x020,000,000	OD middle history trigger
0x000,100,000	OD top singles trigger	0x040,000,000	OD bottom history trigger
0x000,200,000	OD middle singles trigger	0x080,000,000	OD global history trigger
0x000,400,000	OD bottom singles trigger	0x400,000,000	Disable trigger
0x000,800,000	OD global singles trigger	0x800,000,000	Enable trigger

- **GPS Trigger**
  - **1PPS trigger:** A trigger without external trigger issue based on 1PPS of GPS.
  - **1PPS global acquisition trigger:** A forced DAQ trigger for all ID and OD based on 1PPS of GPS.
  - **GPS trigger:** A forced DAQ trigger issued every 32 seconds.
- **ID Nusm Trigger**
  - **ID singles trigger:** A DAQ trigger for the entire ID issued when the number of ID hits (N_{ID}) exceeds the threshold of the ID singles trigger threshold, which was set to 60 in the runs of KamLAND-Zen 800.

  - **ID prompt trigger:** A DAQ trigger for the entire ID issued when the number of ID hits (N_{ID}) exceeds the threshold of ID prompt trigger threshold, which is also 60 in KamLAND-Zen 800. Then, the DAQ accept ID delayed trigger for the variable delayed time window, which was set to $\sim$ 1.2 msec in KamLAND-Zen 800.
  - **ID delayed trigger:** A DAQ trigger for the entire ID issued when the number of ID hits (N_{ID}) exceeds the threshold of the ID delayed trigger threshold in the delayed time window.
  - **ID prescale trigger:** A DAQ trigger for the entire ID issued when the number of ID hits (N_{ID}) in the prescale time after 1PPS trigger (*sim* 10 msec) exceeds the threshold of the ID prescale trigger threshold.
  - **OD to ID trigger:** A DAQ trigger for the entire ID issued when one of OD Nsum triggers is issued.

- **OD Nusm trigger**
  - **OD top singles trigger:** A DAQ trigger for the entire OD issued when the number of OD top PMT hits (N_{top}) exceeds the threshold of OD top singles trigger threshold.
  - **OD middle singles trigger:** A DAQ trigger for the entire OD issued when the number of OD middle PMT hits (N_{middle}) exceeds the threshold of OD middle singles trigger threshold.
  - **OD bottom singles trigger:** A DAQ trigger for the entire OD issued when the number of OD bottom PMT hits (N_{bottom}) exceeds the threshold of OD bottom singles trigger threshold.
  - **OD global singles trigger:** A DAQ trigger for the entire OD issued when the number of entire OD PMT hits (N_{global}) exceeds the threshold of OD global singles trigger threshold.
  - **ID to OD trigger:** The DAQ trigger for the entire OD issued when one of ID Nsum triggers is issued.

- **History Trigger**
  - **History trigger:** A trigger for trigger recording without external trigger issue for up to 8 clocks (200 nsec) while the number of ID hits (N_{ID}) exceeds the threshold of the ID history threshold.
  - **OD top history trigger:** A trigger for trigger recording without external trigger issued for up to 8 clocks (200 nsec) while the number of OD top PMT hits exceeds the threshold of OD top history trigger threshold.
  - **OD middle history trigger:** A trigger for trigger recording without external trigger issued for up to 8 clocks (200 nsec) while the number of OD middle PMT hits exceeds the threshold of OD middle history trigger threshold.

- **OD bottom history trigger:** A trigger for trigger recording without external trigger issued for up to 8 clocks (200 nsec) while the number of OD bottom PMT hits exceeds the threshold of OD bottom history trigger threshold.
- **OD global history trigger:** A trigger for trigger recording without external trigger issued for up to 8 clocks (200 nsec) while the number of OD global PMT hits exceeds the threshold of OD global history trigger threshold.

Appendix B

Energy Spectra and Radius Distribution

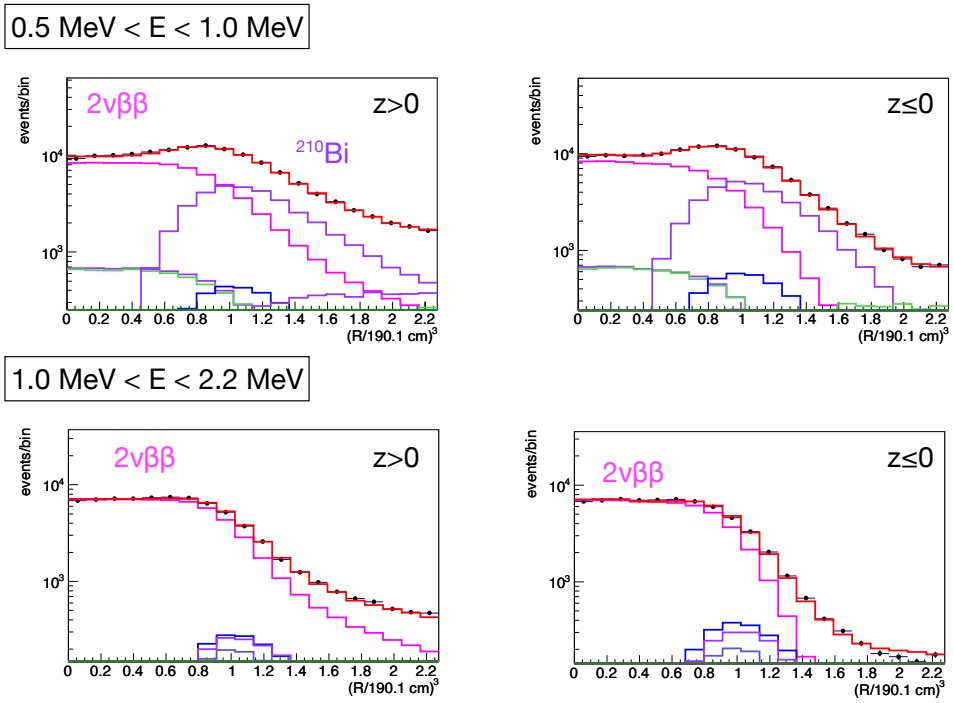

Figure B.1: Radius distribution in each energy region (1)

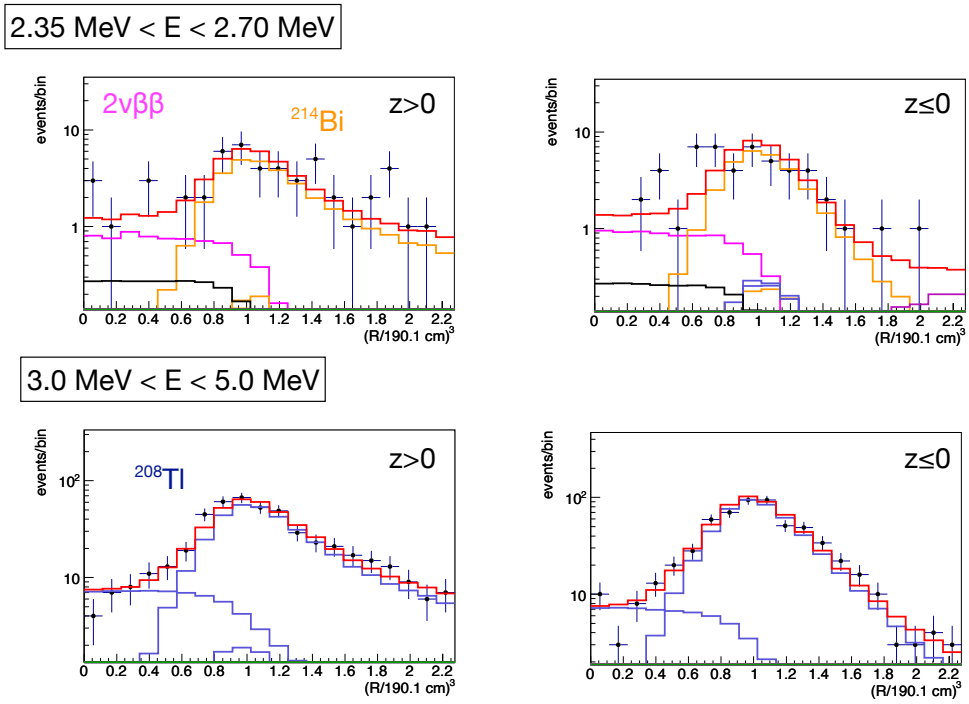

Figure B.2: Radius distribution in each energy region (2)

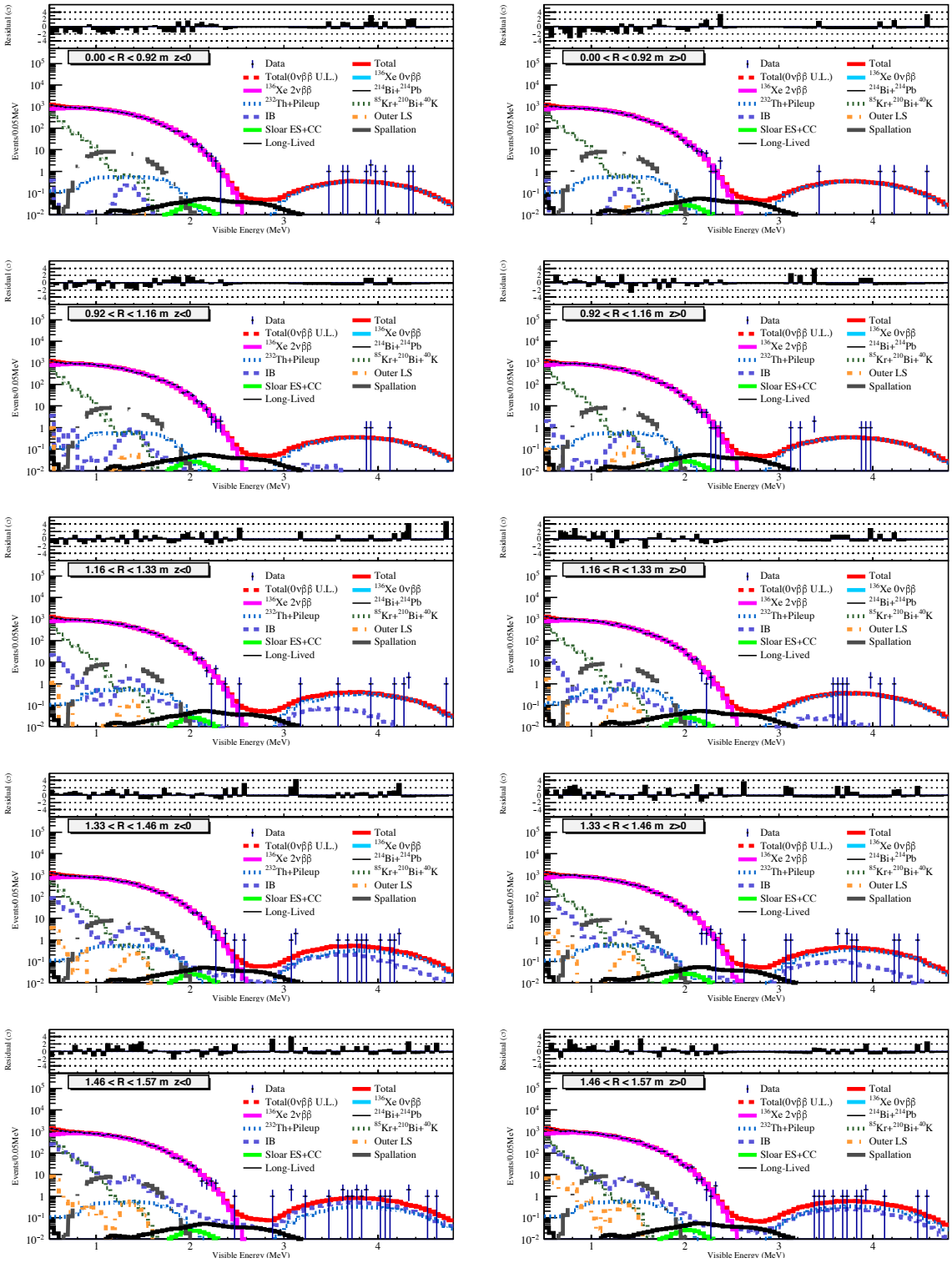

Figure B.3: Energy spectrum in each radius-theta bin (1)

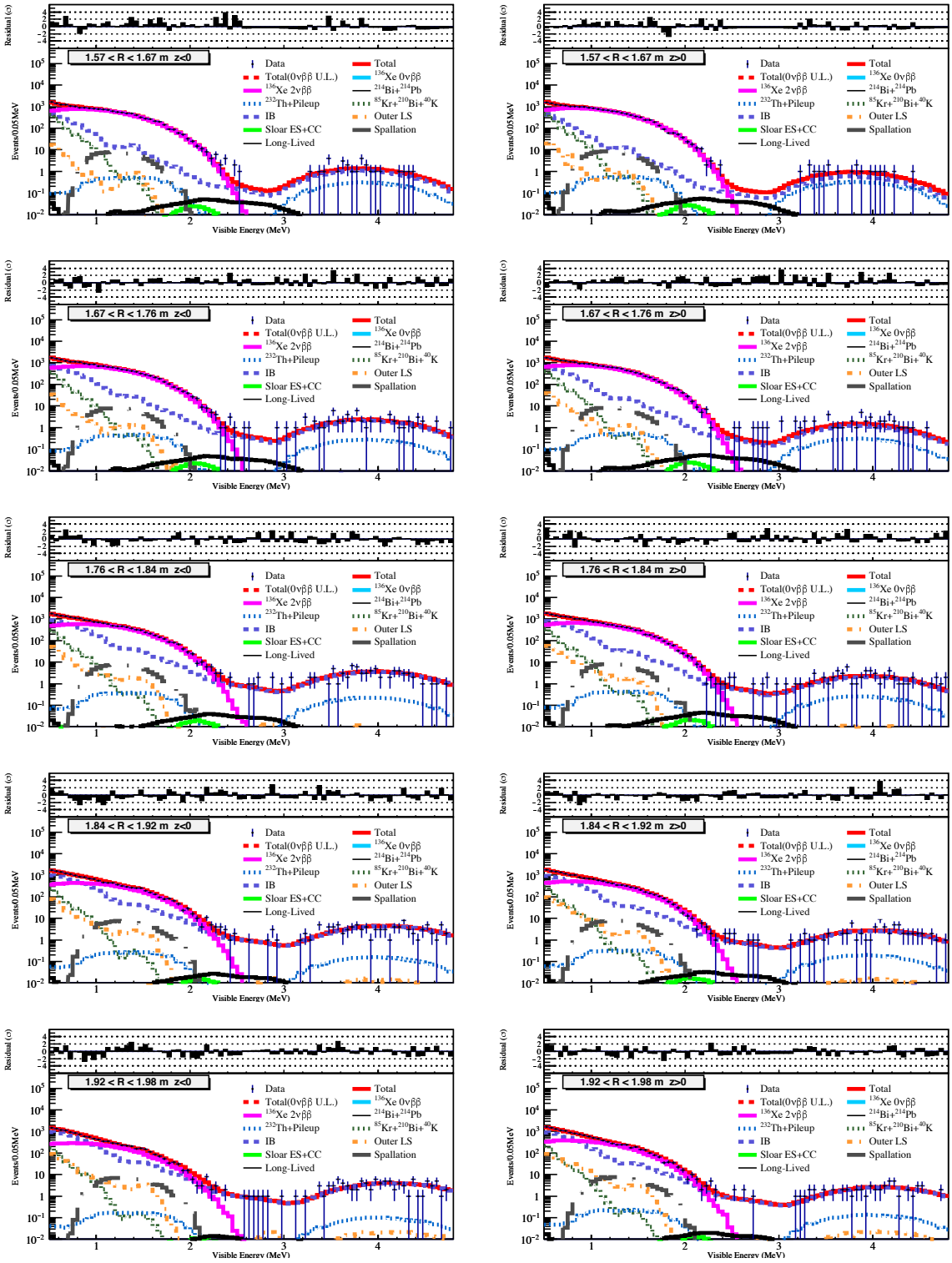

Figure B.4: Energy spectrum in each radius-theta bin (2)

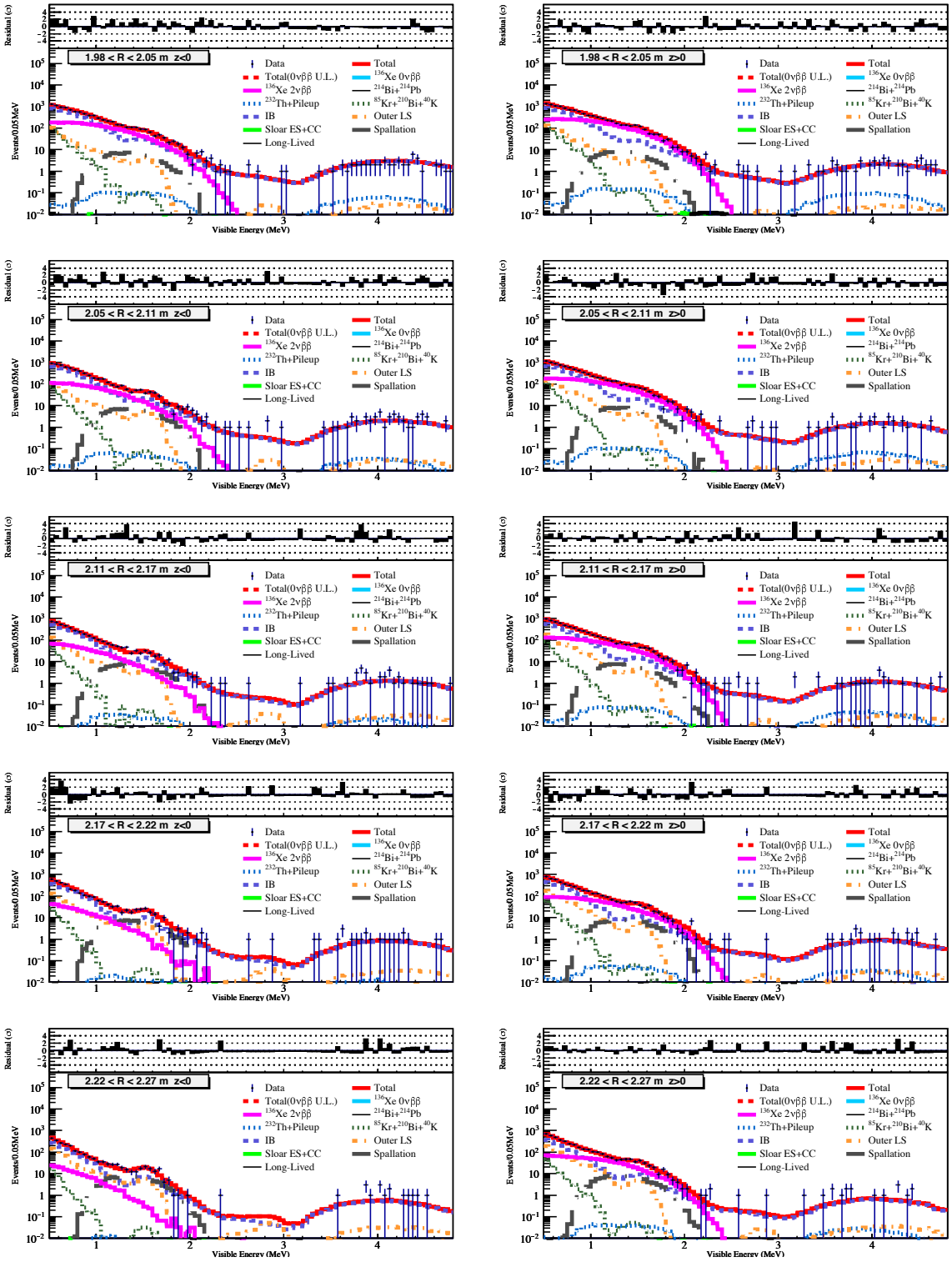

Figure B.5: Energy spectrum in each radius-theta bin (3)

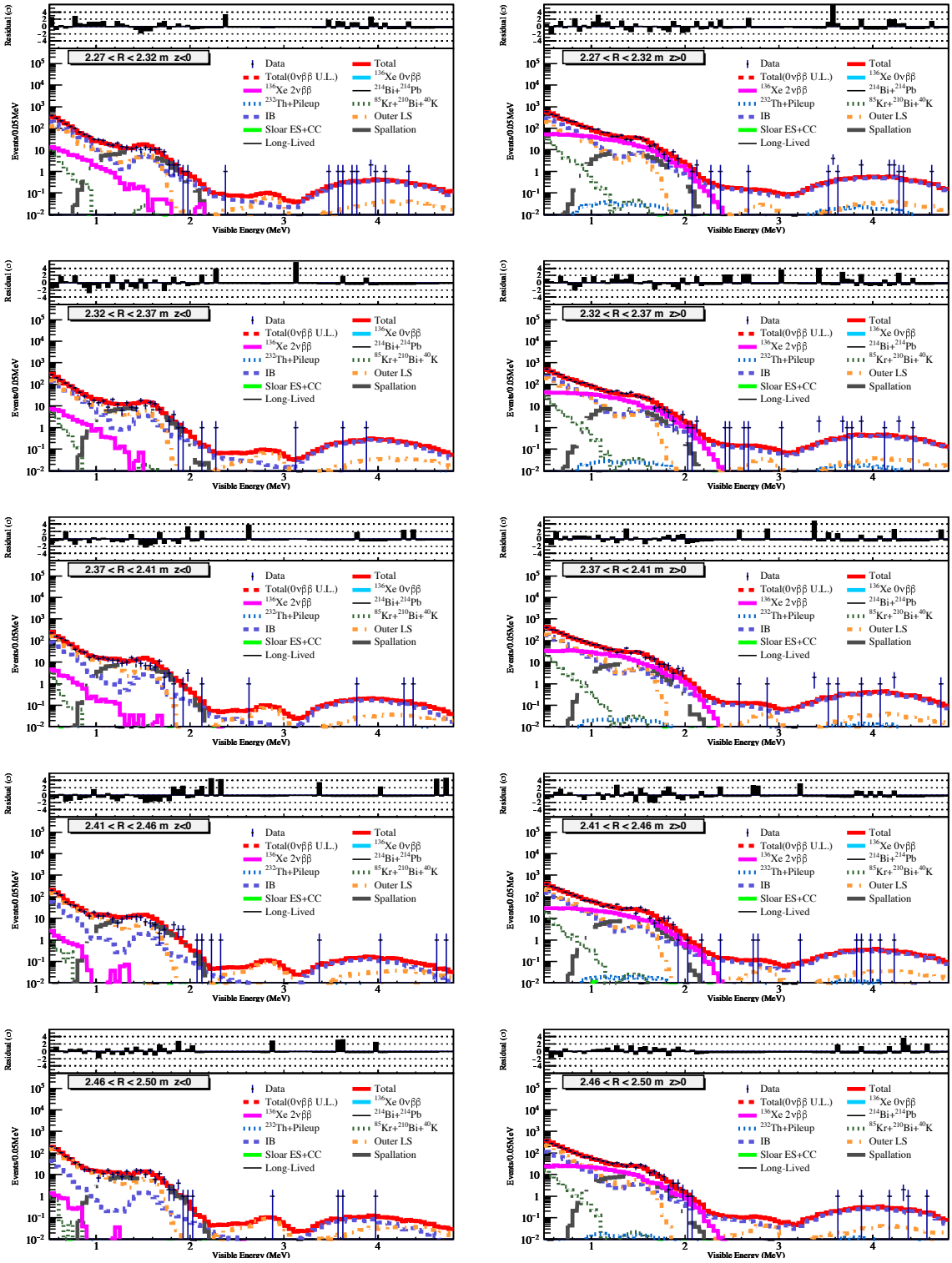

Figure B.6: Energy spectrum in each radius-theta bin (4)

Appendix C

Results in KamLAND-Zen 400

The reanalysis of the KamLAND-Zen 400 Phase-II was performed. The differences from the previous work in [61] and published paper [18] are the following tools,

- Shower tag
- MoGURA ^{137}Xe tag
- MoGURA long-lived tag
- 150 msec veto after LS muons

Also, the contribution of the long-lived spallation product was newly added. The constraint of the long-lived product was not from the tagged event in KamLAND-Zen 800. The value estimated from the FLUKA simulation and the rejection efficiency was used with a 100 % error. The backgrounds and the $0\nu\beta\beta$ decay at the best fit is summarized in Table C.1. The energy spectra in the fiducial volume are shown in Fig. C.1 for period-1 and Fig. C.2 for period-2.

Table C.1: Summary of the backgrounds in the ROI
(2.35 MeV<Energy<2.70 MeV, r <1.06 m for z <0 and r <1.26 m for z >0)

	period1		period2	
	Best fit (ROI)	Best fit events in the ROI	Best fit (ROI)	Best fit events in the ROI
	Xe-LS			
	[event/day/kton]	[events]	[event/day/kton]	[events]
^{136}Xe0$\nu\beta\beta$	0	0	0	0
^{136}Xe2$\nu\beta\beta$	103142(2.52)	2.58	102417(2.95)	2.97
^{238}U S2	3475(0.34)	0.36	381.09(0.04)	0.04
^{232}Th S2	25.6(0.001)	0.001	15.5(0.001)	0.001
^{110m}Ag	14.82(8.48)	8.71	0.52(0.30)	0.30
^{10}C	0.04(0.01)	0.01	0.02(0.00)	0.00
^{6}He	0.39(0.04)	0.04	0.39(0.04)	0.04
^{12}B	0.01(0.00)	0.0	0.01(0.00)	0.0
^{137}Xe	0.50(0.06)	0.058	0.50(0.06)	0.06
Long-lived	160.7(1.67)	1.72	143.0(1.49)	1.50
	IB			
	[event/day/IB]	[events]	[event/day/IB]	[events]
^{238}U S2 lower	33.7(2.78)	2.86	31.3(2.57)	2.59
^{238}U S2 upper	25.3(1.49)	1.53	25.1(1.47)	1.49
^{232}Th S2 lower	135.9(0.02)	0.02	140.9(0.02)	0.02
^{232}Th S2 upper	112.5(0.01)	0.01	113.5(0.01)	0.01
^{110m}Ag S2 lower	0.00(0.00)	0.00	0.00(0.00)	0.00
^{110m}Ag S2 upper	0.36(0.18)	0.18	0.11(0.05)	0.06
Total	-	18.9	-	9.9
Observed	-	17	-	7

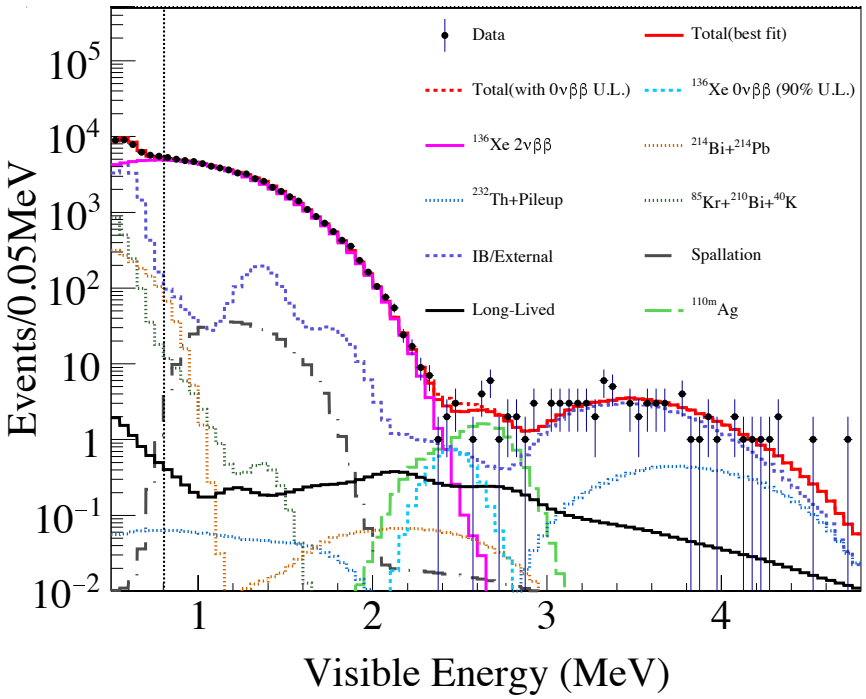

Figure C.1: Energy spectrum in the KamLAND-Zen 400 Phase-II period1 in the inner radius bins $r < 1.26$ m for $z > 0$ and $r < 1.06$ m for $z < 0$

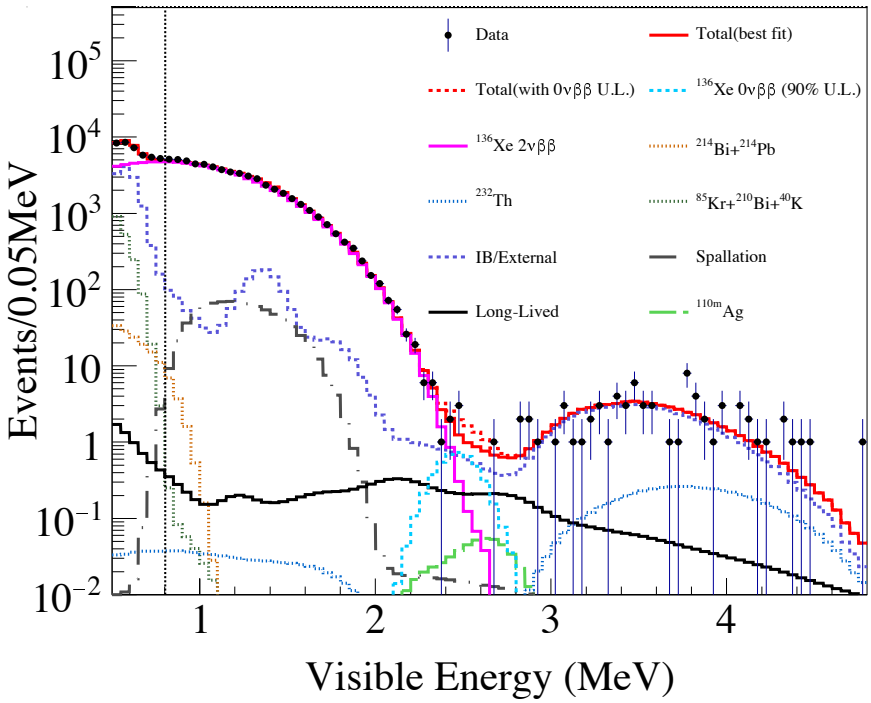

Figure C.2: Energy spectrum in the KamLAND-Zen 400 Phase-II period2 in the inner radius bins $r < 1.26$ m for $z > 0$ and $r < 1.06$ m for $z < 0$

Bibliography

[1] J. Engel, J. Menéndez, Status and future of nuclear matrix elements for neutrinoless double-beta decay: a review, *Reports on Progress in Physics* 80 (4) (2017) 046301. doi:10.1088/1361-6633/aa5bc5.

[2] T. Yanagida, Horizontal Symmetry and Masses of Neutrinos, *Prog. Theor. Phys.* 64 (1980) 1103. doi:10.1143/PTP.64.1103.

[3] M. Fukugita, T. Yanagida, Baryogenesis Without Grand Unification, *Phys. Lett.* B174 (1986) 45–47. doi:10.1016/0370-2693(86)91126-3.

[4] Fukuda Y. *et al.*(Super-Kamiokande Collaboration), Evidence for Oscillation of Atmospheric Neutrinos, *Phys. Rev. Lett.* 81 (1998) 1562–1567. doi:10.1103/PhysRevLett.81.1562.

[5] Q. R. Ahmad *et al.*, Direct evidence for neutrino flavor transformation from neutral-current interactions in the sudbury neutrino observatory, *Phys. Rev. Lett.* 89 (2002) 011301. doi:10.1103/PhysRevLett.89.011301.

[6] K. Eguchi *et al.*(KamLAND Collaboration), First Results from KamLAND: Evidence for Reactor Antineutrino Disappearance, *Phys. Rev. Lett.* 90 (January 2003) 021802,pp.1–6.

[7] M. A. Acero *et al.*, First measurement of neutrino oscillation parameters using neutrinos and antineutrinos by nova, *Phys. Rev. Lett.* 123 (2019) 151803. doi:10.1103/PhysRevLett.123.151803.

[8] K. Abe *et al.*, Search for *cp* violation in neutrino and antineutrino oscillations by the t2k experiment with 2.2×10^{21} protons on target, *Phys. Rev. Lett.* 121 (2018) 171802. doi:10.1103/PhysRevLett.121.171802.

[9] E. Akhmedov, S. Esposito, Majorana neutrinos and other Majorana particles: theory and experiment, Cambridge University Press, 2014, p. 303–353. doi:10.1017/CBO9781107358362.015.

[10] E. Majorana, Teoria simmetrica dell'elettrone e del positrone, *Il Nuovo Cimento (1924-1942)* 14 (4) (1937) 171. doi:10.1007/BF02961314.

[11] M. Gell-Mann, P. Ramond, R. Slansky, Complex Spinors and Unified Theories, *Conf. Proc.* C790927 (1979) 315–321. arXiv:1306.4669.

[12] P. Minkowski, $\mu \to e\ \gamma$ at a rate of one out of 109 muon decays?, *Physics Letters B* 67 (4) (1977) 421 – 428. doi:https://doi.org/10.1016/0370-2693(77)90435-X.

[13] K. Abe *et al.*, Atmospheric neutrino oscillation analysis with external constraints in super-kamiokande i-iv, *Phys. Rev. D* 97 (2018) 072001. doi:10.1103/PhysRevD.97.072001.

[14] M. Aker et al., An improved upper limit on the neutrino mass from a direct kinematic method by KATRINarXiv:1909.06048.

[15] P. A. R. Ade *et al.*(Planck Collaboration), Planck 2015 results. XIII. Cosmological parameters, *arXiv:1502.01589v3*.

[16] M. M. Ivanov, M. Simonović, M. Zaldarriaga, Cosmological parameters and neutrino masses from the final planck and full-shape boss data (2019). arXiv:1912.08208.

[17] K. N. Abazajian et al., CMB-S4 Science Book, First EditionarXiv:1610.02743.

[18] A. Gando *et al.*(KamLAND-Zen Collaboration), Search for Majorana Neutrinos Near the Inverted Mass Hierarchy Region with KamLAND-Zen, *10.1103/PhysRevLett.117.082503* (August 2016) pp.1–6.

[19] P. F. de Salas *et al.*, Neutrino mass ordering from oscillations and beyond: 2018 status and future prospects, *Frontiers in Astronomy and Space Sciences* 5. doi:10.3389/fspas.2018.00036.

[20] S. Dell'Oro, S. Marcocci, F. Vissani, New expectations and uncertainties on neutrinoless double beta decay, *Physical Review D* 90. doi:10.1103/PhysRevD.90.033005.

[21] V. Kuzmin, V. Rubakov, M. Shaposhnikov, On anomalous electroweak baryon-number non-conservation in the early universe, *Physics Letters B* 155 (1) (1985) 36 – 42. doi:https://doi.org/10.1016/0370-2693(85)91028-7.

[22] R. H. Cyburt *et al.*, Big bang nucleosynthesis: Present status, *Rev. Mod. Phys.* 88 (2016) 015004. doi:10.1103/RevModPhys.88.015004.

[23] P. A. R. Ade et al., Planck 2015 results. XIII. Cosmological parameters, *Astron. Astrophys.* 594 (2016) A13. arXiv:1502.01589, doi:10.1051/0004-6361/201525830.

[24] A. D. Sakharov, Violation ofCPin variance,casymmetry, and baryon asymmetry of the universe, *Soviet Physics Uspekhi* 34 (5) (1991) 392–393. doi:10.1070/pu1991v034n05abeh002497.

[25] K. Hamaguchi, Cosmological baryon asymmetry and neutrinos: Baryogenesis via leptogenesis in supersymmetric theories, Ph.D. thesis, Tokyo U. (2002). arXiv:hep-ph/0212305.

[26] N. Aghanim et al., Planck 2018 results. VI. Cosmological parametersarXiv:1807.06209.

[27] K. Moffat *et al.*, Three-flavored nonresonant leptogenesis at intermediate scales, *Phys. Rev. D* 98 (2018) 015036. doi:10.1103/PhysRevD.98.015036.

[28] M. Goeppert-Mayer, Double beta-disintegration, *Phys. Rev.* 48 (1935) 512–516. doi:10.1103/PhysRev.48.512.

[29] W. H. Furry, On transition probabilities in double beta-disintegration, *Phys. Rev.* 56 (1939) 1184–1193. doi:10.1103/PhysRev.56.1184.

[30] M. Mirea, T. Pahomi, S. Stoica, Values of the phase space factors involved in double beta decay, *Romanian Reports in Physics* 67 (2015) 872–889. doi:10.1063/1.4934913.

[31] J. Kotila, F. Iachello, Phase-space factors for double-β decay, *Phys. Rev. C* 85 (2012) 034316. doi:10.1103/PhysRevC.85.034316.

[32] D. c. v. Štefánik *et al.*, Reexamining the light neutrino exchange mechanism of the $0\nu\beta\beta$ decay with left- and right-handed leptonic and hadronic currents, *Phys. Rev. C* 92 (2015) 055502. doi:10.1103/PhysRevC.92.055502.

[33] J. Schechter, J. W. F. Valle, Neutrinoless Double beta Decay in SU(2) x U(1) Theories, *Phys. Rev.* D25 (1982) 2951, [,289(1981)]. doi:10.1103/PhysRevD.25.2951.

[34] M. Hirsch, S. Kovalenko, I. Schmidt, Extended Black box theorem for lepton number and flavor violating processes, *Physics Letters B* 642 (1) (2006) 106 – 110. doi:https://doi.org/10.1016/j.physletb.2006.09.012.

[35] F. Deppisch *et al.*, Neutrinoless Double Beta Decay and the Baryon Asymmetry of the Universe, *Physical Review D* 98. doi:10.1103/PhysRevD.98.055029.

[36] P. Gysbers *et al.*, Discrepancy between experimental and theoretical β-decay rates resolved from first principles, *Nature Physics* 15 (2019) 1. doi:10.1038/s41567-019-0450-7.

[37] L.-J. Wang, J. Engel, J. M. Yao, Quenching of nuclear matrix elements for $0\nu\beta\beta$ decay by chiral two-body currents, *Phys. Rev. C* 98 (2018) 031301. doi:10.1103/PhysRevC.98.031301.

[38] J. Menéndez, D. Gazit, A. Schwenk, Chiral two-body currents in nuclei: Gamow-teller transitions and neutrinoless double-beta decay, *Phys. Rev. Lett.* 107 (2011) 062501. doi:10.1103/PhysRevLett.107.062501.

[39] F. Šimkovic *et al.*, Improved description of the $2\nu\beta\beta$-decay and a possibility to determine the effective axial-vector coupling constant, *Phys. Rev. C* 97 (2018) 034315. doi:10.1103/PhysRevC.97.034315.

[40] A. Gando *et al.*, Precision analysis of the ^{136}Xe two-neutrino $\beta\beta$ spectrum in kamland-zen and its impact on the quenching of nuclear matrix elements, *Phys. Rev. Lett.* 122 (2019) 192501. doi:10.1103/PhysRevLett.122.192501.

[41] First result of the CANDLES III experiment searching for double beta decay of 48Ca. doi:10.5281/zenodo.1300737.

[42] R. Arnold *et al.*, Measurement of the double-beta decay half-life and search for the neutrinoless double-beta decay of ^{48}Ca with the nemo-3 detector, *Phys. Rev. D* 93 (2016) 112008. doi:10.1103/PhysRevD.93.112008.

[43] M. Agostini et al., Probing Majorana neutrinos with double-β decay, *Science* 365 (2019) 1445. arXiv:1909.02726, doi:10.1126/science.aav8613.

[44] GERDA Collaboration *et al.*, Results on $\beta\beta$decay with emission of two neutrinos or majorons in ^{76}ge from gerda phase i, *The European Physical Journal C* 75 (9) (2015) 416. doi:10.1140/epjc/s10052-015-3627-y.

[45] R. Arnold *et al.*, Final results on ^{82}Se double beta decay to the ground state of ^{82}Kr from the NEMO-3 experiment, *The European Physical Journal C* 78 (10) (2018) 821. doi:10.1140/epjc/s10052-018-6295-x.

[46] O. Azzolini *et al.*, Final result of cupid-0 phase-i in the search for the ^{82}Se neutrinoless double-β decay, *Phys. Rev. Lett.* 123 (2019) 032501. doi:10.1103/PhysRevLett.123.032501.

[47] O. Azzolini et al., Evidence of Single State Dominance in the Two-Neutrino Double-β Decay of Se-82 with CUPID-0arXiv:1909.03397.

[48] R. Arnold *et al.*, Results of the search for neutrinoless double-β decay in ^{100}Mo with the nemo-3 experiment, *Phys. Rev. D* 92 (2015) 072011. doi:10.1103/PhysRevD.92.072011.

[49] R. Arnold *et al.*, Detailed studies of ^{100}Mo two-neutrino double beta decay in NEMO-3, *The European Physical Journal C* 79 (5) (2019) 440. doi:10.1140/epjc/s10052-019-6948-4.

[50] C. Alduino *et al.*, First results from cuore: A search for lepton number violation via $0\nu\beta\beta$ decay of ^{130}Te, *Phys. Rev. Lett.* 120 (2018) 132501. doi:10.1103/PhysRevLett.120.132501.

[51] C. Collaboration *et al.*, Improved limit on neutrinoless double-beta decay in ^{130}Te with CUORE (2019). arXiv:1912.10966.

[52] G. Anton *et al.*, Search for Neutrinoless Double-β Decay with the Complete EXO-200 Dataset, *Phys. Rev. Lett.* 123 (2019) 161802. doi:10.1103/PhysRevLett.123.161802.

[53] S. Hayashida, Search for Neutrinoless Double-Beta Decay with KamLAND-Zen Applying Advanced Spallation Background Reduction, *Ph.D. thesis(2019)*.

[54] B. Schmidt *et al.*, First data from the cupid-mo neutrinoless double beta decay experiment (2019). arXiv:1911.10426.

[55] A. Gando, First Results of Neutrinoless Double Beta Decay Search with KamLAND-Zen, *Ph.D. thesis(2012)*.

[56] A. Gando *et al.*, Limit on neutrinoless $\beta\beta$ decay of ^{136}Xe from the first phase of kamland-zen and comparison with the positive claim in ^{76}Ge, *Phys. Rev. Lett.* 110 (2013) 062502. doi:10.1103/PhysRevLett.110.062502.

[57] I. Esteban *et al.*, Global analysis of three-flavour neutrino oscillations: synergies and tensions in the determination of θ23, δCP, and the mass ordering, *Journal of High Energy Physics* 2019 (1) (2019) 106. doi:10.1007/JHEP01(2019)106.

[58] M. Agostini, G. Benato, J. A. Detwiler, Discovery probability of next-generation neutrinoless double-β decay experiments, *Phys. Rev. D* 96 (2017) 053001. doi:10.1103/PhysRevD.96.053001.

[59] V. M. Gehman, S. R. Elliott, Multiple-isotope comparison for determining $0\nu\beta\beta$ mechanisms, *Journal of Physics G: Nuclear and Particle Physics* 34 (4) (2007) 667–678. doi:10.1088/0954-3899/34/4/006.

[60] A. Gando *et al.*, ^{7}Be solar neutrino measurement with KamLAND, *Phys. Rev. C* 92 (2015) 055808. doi:10.1103/PhysRevC.92.055808.

[61] S. Matsuda, Search for Neutrinoless Double-Beta Decay in ^{136}Xe after Intensive Background Reduction with KamLAND-Zen, *Ph.D. thesis(2016)*.

[62] H. Ozaki, J. Shirai, Refurbishment of KamLAND Outer Detector, *PoS* ICHEP2016 (2017) 1161. doi:10.22323/1.282.1161.

[63] S. Obara, A Search for Supernova Relic Neutrinos with KamLAND during Reactor-Off Period, *Ph.D. thesis(2018)*.

[64] H. Yoshida, Limit on Majorana Neutrino Mass with Neutrinoless Double Beta Decay from KamLAND-Zen, *Ph.D. thesis(2014)*.

[65] H. Sambonsugi, Kamland-zen 800: Xe concentration measurement in liquid scintillator of kamland, *JPS 2019 Autumn Meeting*.

[66] S. Abe *et al.*(KamLAND Collaboration), Production of radioactive isotopes through cosmic muon spallation in KamLAND, *Phys. Rev. C* 81 (2010) 025807. doi:10.1103/PhysRevC.81.025807.

[67] Y. Abe *et al.*, Characterization of the spontaneous light emission of the PMTs used in the double chooz experiment, *Journal of Instrumentation* 11 (08) (2016) P08001–P08001. doi:10.1088/1748-0221/11/08/p08001.

[68] T. Hachiya, Study on Background Reduction Using Waveform Information in KamLAND-Zen, *Master's thesis(2016)*.

[69] Y. Karino, Improvement of Background Rejection for Cosmic Muon Spallation in KamLAND-Zen, *Master's thesis(2017)*.

[70] T. Banks *et al.*, A compact ultra-clean system for deploying radioactive sources inside the KamLAND detector, *Nuclear Instruments and Methods in Physics Research Section A: Accelerators, Spectrometers, Detectors and Associated Equipment* 769 (2015) 88 – 96.

[71] N. Momoshima *et al.*, An improved method for ^{85}Kr analysis by liquid scintillation counting and its application to atmospheric ^{85}Kr determination, *Journal of Environmental Radioactivity* 101 (8) (2010) 615–621. doi:10.1016/j.jenvrad.2010.03.009.

[72] J. B. Albert *et al.*, Searches for double beta decay of ^{134}Xe with exo-200, *Phys. Rev. D* 96 (2017) 092001. doi:10.1103/PhysRevD.96.092001.

[73] J. B. Albert *et al.*, Measurement of neutron capture on ^{136}Xe, *Phys. Rev. C* 94 (2016) 034617. doi:10.1103/PhysRevC.94.034617.

[74] G. Lydie *et al.*, Isotopic production cross sections of the residual nuclei in spallation reactions induced by ^{136}Xe projectiles on proton at 500 A MeV, *Nuclear Physics A* 899 (2013) 116–132. doi:10.1016/j.nuclphysa.2012.12.119.

[75] P. Napolitani *et al.*, Measurement of the complete nuclide production and kinetic energies of the system ^{136}Xe+hydrogen at 1 GeV per nucleon, *Phys. Rev. C* 76 (2007) 064609. doi:10.1103/PhysRevC.76.064609.

[76] H. Ejiri, S. R. Elliott, Charged current neutrino cross section for solar neutrinos, and background to $\beta\beta(0\nu)$ experiments, *Phys. Rev. C* 89 (2014) 055501. doi:10.1103/PhysRevC.89.055501.

[77] M. Redshaw *et al.*, Mass and double-beta-decay q value of ^{136}Xe, *Phys. Rev. Lett.* 98 (2007) 053003. doi:10.1103/PhysRevLett.98.053003.

[78] A. Takeuchi, Study on ^{10}C Tagging Efficiency for KamLAND2-Zen, *Master's thesis(2019)*.

[79] M. Horoi, A. Neacsu, Shell model predictions for ^{124}Sn double-β decay, *Phys. Rev. C* 93 (2016) 024308. doi:10.1103/PhysRevC.93.024308.

[80] J. Menéndez *et al.*, Disassembling the nuclear matrix elements of the neutrinoless $\beta\ \beta$ decay, *Nuclear Physics A* 818 (3) (2009) 139 – 151. doi:https://doi.org/10.1016/j.nuclphysa.2008.12.005.

[81] F. Šimkovic *et al.*, $0\nu\beta\beta$ and $2\nu\beta\beta$ nuclear matrix elements, quasiparticle random-phase approximation, and isospin symmetry restoration, *Phys. Rev. C* 87 (2013) 045501. doi:10.1103/PhysRevC.87.045501.

[82] J. Hyvärinen, J. Suhonen, Nuclear matrix elements for $0\nu\beta\beta$ decays with light or heavy majorana-neutrino exchange, *Phys. Rev. C* 91 (2015) 024613. doi:10.1103/PhysRevC.91.024613.

[83] M. T. Mustonen, J. Engel, Large-scale calculations of the double-β decay of ^{76}**Ge**, ^{130}**Te**, ^{136}**Xe**, and ^{150}**Nd** in the deformed self-consistent skyrme quasi-particle random-phase approximation, *Phys. Rev. C* 87 (2013) 064302. doi:10.1103/PhysRevC.87.064302.

[84] J. Barea, J. Kotila, F. Iachello, $0\nu\beta\beta$ and $2\nu\beta\beta$ nuclear matrix elements in the interacting boson model with isospin restoration, *Phys. Rev. C* 91 (2015) 034304. doi:10.1103/PhysRevC.91.034304.

[85] J. M. Yao *et al.*, Systematic study of nuclear matrix elements in neutrinoless double-β decay with a beyond-mean-field covariant density functional theory, *Phys. Rev. C* 91 (2015) 024316. doi:10.1103/PhysRevC.91.024316.

[86] N. L. Vaquero, T. R. Rodríguez, J. L. Egido, Shape and pairing fluctuation effects on neutrinoless double beta decay nuclear matrix elements, *Phys. Rev. Lett.* 111 (2013) 142501. doi:10.1103/PhysRevLett.111.142501.